Controlled Synthesis and Photo-Physical Properties of Graphene Quantum Dots and Its Heterostructures for Visible Light Photocatalysis and Bio-Imaging Applications

A Dissertation submitted to

Indian Institute of Technology Guwahati
For the Degree of

Doctor of Philosophy

By

Gone Rajender

Department of Physics
Indian Institute of Technology Guwahati
Guwahati-781039

January 2018

Dedicated to my Parents and my Wife

&

To my Teachers

DEPARTMENT OF PHYSICS

INDIAN INSTITUTE OF TECHNOLOGY GUWAHATI

Guwahati- 781039, Assam, INDIA

Phone: +91 361 2582703, Fax: +91 361 2582749

STATEMENT

The work contained in the dissertation entitled **"Controlled Synthesis and Photo-Physical Properties of Graphene Quantum Dots and Its Heterostructures for Visible Light Photocatalysis and Bio-Imaging Applications"** has been carried out by me at Indian Institute of Technology Guwahati under the supervision of **Prof. P. K. Giri,** *Professor*, Department of Physics, Indian Institute of Technology Guwahati. This work has not been submitted elsewhere for the award of any degree.

Gone Rajender

Roll No. -11612122

Senior Research Scholar

Department of Physics

Indian Institute of Technology Guwahati

Guwahati-781 039, India

Prof. P. K. Giri

Professor

Department of Physics and Centre for Nanotechnology

Indian Institute of Technology Guwahati

Guwahati- 781 039, Assam, INDIA

Phone: +91 361 2582703, Fax: +91 361 2582749

Email: giri@iitg.erent.in

CERTIFICATE

This is certify that the work contained in the dissertation entitled **"Controlled Synthesis and Photo-Physical Properties of Graphene Quantum Dots and Its Heterostructures for Visible Light Photocatalysis and Bio-Imaging Applications"** has been carried out by *Mr. Gone Rajender* at Indian Institute of Technology Guwahati under my supervision. This work has not been submitted elsewhere for the award of any degree.

(Prof. P. K. Giri)

Thesis Supervisor

Acknowledgements

The research work presented here is the results of hard work and dedication. It is my pleasure and I would consider this opportunity to acknowledge the people who are involved directly or indirectly to complete my thesis work.

Working towards a goal and satisfying the teacher is the secret of success for a student. Prior to everything, I would like to express my deep sense of gratitude to my inspiration and my thesis supervisor Prof. P. K. Giri. I am thankful to him for granting me the opportunity to work in his research group. I am thankful for his guidance, enthusiasm and patience throughout my thesis work. His moral and intellectual support kept me alive during the difficulties of my research work. I am very grateful to him for giving me a complete freedom in research.

I would like to thank my doctoral committee members, Prof. A. Perumal, Prof. P. S. Robi and Dr. Subhash Thota for their regular review and suggestions on the progress of my research work. I would like to thank my former doctoral committee member Prof. D. K. Goswami.

I am thankful to the Head of the Department of Physics and other faculty members, Centre for Nanotechnology, Central Instrumental Facilities and members, for providing me the research friendly domain and up-to-date research facilities. I am grateful to Indian Institute of Technology Guwahati for providing the research fellowship, good accommodation and various facilities in the pleasant campus. I am grateful to the scientific and technical officers, Dr. Sidananda Sarma, Dr. Dolly Gogoi, Dr. Babulal Das, Mr. Indrajit Talukdar, Mr. Chandan Borgohain, Mr. Diganta Kumar Hira and Mr. Dhiren Huzuri, for their support to complete my research work. I would express thanks to Prof. Siddhartha Sankar Ghosh and Ms. Upashi Goswami for help in bio-imaging studies. I would like to thank Prof. M. Fujii, Kobe University, Japan for X-ray photoelectron spectroscopy measurements.

I express my sincere thanks to my seniors, Dr. Batakrushna Santara, Dr. Biroju Ravikumar, Dr. Ramesh Ghosh and Dr. Sk. Md Obaidulla, and Dr. Biswajit Choudhury, for their valuable suggestions in early days of my research work. I would like to thank our group members, Mr. Kamal Kr. Paul, Ms. Larionett P. L. Mawlong, Mr. Somorjit Singh,

Ms. Ruma Das, Mr. Joydip Ghosh, Mr. Kaustubh Acharyya, Ms. Sumaiya and Ms. Abhilasha for their assistance and good research atmosphere in the lab.

I wish to appreciate my friends Suresh and Chary. A special thanks to my friend Harikrishna, for his nice company and moral support. I would like to thank all of my friends in Department of Physics.

I would like to express thanks to my college teachers, Prof. N. Gopikrishna and Dr. A. Lakshminarayana, who are my inspiration to choose physics as my major subject. I am thankful to my school teachers Sarangapani Sir and Yesu Sir, for their motivation and financial support during my school days.

I do not have sufficient words to express my gratitude to my parents, for their love, affection and encouragement. I would like to acknowledge my sisters and my brother for their motivation and support. I wish to acknowledge my brother-in-laws support. Words are not sufficient to acknowledge my wife for her immense love and care for me and my daughter.

Gone Rajender

IIT Guwahati

CONTENTS

SYNOPSIS

After the invention of 2D prototype sp^2 hybridized graphene, lots of efforts have been made for synthesis, fundamental understanding and applications of 2D materials. However, absence of band gap and high transparency to UV-visible light impede the efficient utilization of graphene in optoelectronic applications. Graphene quantum dot (GQD) has emerged as an interesting class of 0D materials that possesses attractive properties, such as tunable band gap, highly luminescent properties that are suitable for various commercial applications. When the graphene is cut into small pieces, it possesses interesting features, such as edge sites (zigzag and armchair) and oxygenated functional groups. It is interesting to note that due the ultra-fine size of GQDs, the ratio of edge to basal plane carbon atoms is high resulting in the dominance of the edge states, which could not be realized in the bulk form of graphene functional materials. Controlling of the edge/surface states of GQDs is the key to its ensuing applications in various areas of nanoscience and nanotechnology. Photoluminescence (PL) is the one of the intriguing property of the GQDs that has drawn considerable attention of researchers worldwide. Interestingly, GQDs are considered to be a promising alternative over the conventional quantum dots (QDs) owing to its excellent solubility, less toxicity, bright and tuneable PL. These properties enable them to use in various applications ranging from sensing, bio-imaging, energy conversion and environmental cleaning etc.

There are several methods for the synthesis of graphene functional materials. The most commonly used one is the modified Hummers method. On the other hand, the novel GQDs synthesis techniques are mainly categorized into two approaches. The first one is the top down method, where the GQDs are synthesized by cutting of the bulk graphene based materials. This method includes the cutting of the carbon fibers, carbon nanotubes, graphene oxide and carbon black etc. However, understanding the formation mechanism at the early stage of cutting from graphene materials is not well understood. In the present thesis, the formation mechanism of nearly circular cross section GQDs during the cutting of graphene oxide is studied. The second one is the bottom up method, where the small organic molecules are used as a precursor material. In this case the organic molecules are carbonized to form the GQDs. Among these, hydrothermal and solvothermal (top down) techniques are cheap and versatile for large scale production of high quality GQDs. In the present thesis work, hydrothermal and solvothermal methods are employed for the synthesis and functionalization of GQDs. Hydrothermal reactions are performed at 12 and 24 hr duration using two different precursor materials. Further, we studied the effect of *in-situ* chemical functionalization on GQDs by using the polyethelenglycol (PEG). To study the effect of solvent on structural and optical properties of GQDs, we have performed solvothermal reactions using two different solvents, namely dimethlyformamide (DMF) and dimethyl sulfoxide (DMSO), by keeping the temperature and time unchanged. After controlled synthesis and functionalization of GQDs, we explore its photophysical properties and then study the bio-imaging application of solvent assisted synthesized GQDs. We further explore the GQDs and GQDs based heterostructures for visible light photocatalytic application.

As compared to the pristine GQDs, the hybrid nanostructures of GQDs possess superior optical and electronic properties. Note that the optical and electronic properties

of hybrid nanostructures strongly depend on the choice of materials. Thus, it is necessary to design the hybrid structures before it is explored for the desired applications. Using the low cost synthesis technique, the production of high quality hybrid nanostructures is another challenging task. Recently, the study of plasmonic nanoparticles (NPs) has gained significant attention due to the strong visible light absorption caused by the surface plasmon resonance. In the present thesis, an *in-situ* chemical synthesis is adopted to prepare the hybrid nanostructure of plasmonic Au NPs functionalized GQDs and graphitic carbon nitride (GCN) nanosheets. We also fabricated the heterojunction of GQDs and TiO_2 nanoparticles using the ultrasonication process. To understand the formation mechanism of the TiO_2-GQD heterojunction, a series of controlled experiments were performed. To lend support to the proposed mechanism of heterojunction formation, we have carried out density functional theory (DFT) calculations using the *Material studio* software and it shows close agreement with the experimental results.

One of the main focuses of the present thesis is the study of the origin of PL from GQDs thin films, as opposed to the GQDs in dispersion commonly reported in the literature. Despite sustained efforts, the exact origin of PL from GQDs is not well understood by the research community. There is considerable debate in understanding the PL from GQDs, as there are competing effects of intrinsic state and defect state PL emissions. In the present thesis, we have studied the origin of PL from GQD thin films by controlled annealing experiments in the presence of oxygen or hydrogen gas environment. Next, in order to understand the broad Raman spectrum from the GQDs samples, we have deconvoluted the spectra and the significance of different new peaks is studied in details. We have made a correlation between the PL signature and the Raman modes for the first time. To study the impact of solvent on the PL of GQDs in liquid media, we have performed the GQDs dispersion in different solvents, such as water, DMSO and tetrahydrofuran. Interestingly, the PL spectrum of GQD sample exhibited different PL behavior in different solvents. After studying the origin of PL for differently prepared GQDs, we go on to demonstrate the bio-imaging applications of GQDs. Since the GQDs show bright blue PL emission, using the GQDs as fluorescent markers, the bio-imaging of two different human cancer cells is studied.

Next we explore the photocatalytic application of GQDs. Photocatalytic dye degradation using semiconductor based catalyst has assumed greater significance in recent times due to the environment and water pollution caused by the ever growing industrial developments. The issue needs to be resolved in an environmental begin manner. The major two limitations of the conventional materials are very low visible light absorption due to their large band gap and high recombination rate of the charge carriers. To overcome these limitations, the hetero-junction approach has proved to be very powerful. Recently graphitic carbon nitride (GCN) has been considered as a promising material for visible light photocatalytic applications, since it possess a band gap due to the electronegativity difference between the carbon and nitrogen atoms. To achieve the enhanced visible light photocatalytic degradation of a model organic dye methylene blue (MB), we have fabricated the plasmonic NP functionalized 2D-0D system of GCN and GQDs. In another system of GQD-TiO_2 heterojunction has been fabricated and the evaluation of dye degradation performance in different catalyst samples was studied. In addition, to understand the reactive species (free radicals) involvement in different

catalyst samples, a series of scavenge experiments were conducted. The absorption and photoluminescence measurement techniques are adopted to probe the free radicles presence and the mechanism of enhanced photocatalytic degradation.

In essence, this thesis presents a systematic study on the controlled synthesis, origin and tunability of PL from GQDs and its application in bio-imaging, and finally it's visible light photocatalytic application. The entire thesis is divided into the seven chapters. It starts with the recent advances in the research on GQDs and its composites for different applications and motivation for the present thesis. Next, the controlled synthesis and *in-situ* chemical functionalization on GQDs is discussed. To understand the role of in-plane functional groups on GQDs synthesis, two different precursor materials are prepared and their results are compared. We propose a new mechanism for the formation of GQDs and studied their edge sites conversion using the PL and Raman spectroscopy techniques, for the first time. The role of solvents on the synthesis and visible PL emission from GQDs are studied. We have achieved a PL quantum yield of 32% from GQDs. Further, the advantageous bright visible PL of GQDs is used as bio-marker to study the bio-imaging of human cancer cells. The plasmonic Au NPs functionalized GQD-GCN hybrid nanostructures are fabricated to study the visible light photocatalytic activity of MB. We have achieved enhanced degradation of MB after Au NPs decoration on the GQD-GCN hybrid system due the interfacial charge transfer between the GQD-GCN hybrids to Au NPs. Next, a hybrid of GQD and TiO_2 NPs is prepared using ultrasonication process and the photocatalytic degradation of MB in different catalyst samples was studied. We find that TiO_2-GQD hybrid prepared under ultra-sonication yields higher MB degradation as compared to the hybrid prepared under stirring. We proposed the formation mechanism of TiO_2-GQD hybrid through the C-O-Ti bonds, for the first time, and the conclusions are supported by DFT calculation. The important and noteworthy results of this thesis are listed below chapter wise.

Chapter 1 provides a brief overview of the recent advances in synthesis, properties and applications of GQDs and its heterostructures. A comparison of the properties of GQDs and other conventional QDs and the characteristic Raman features of GQDs is presented. The important advantages of GQDs and GQD based hybrid nanostructures, and improvement in desired applications, such as sensing, bio-imaging, energy and environmental cleaning are presented. The motivation for the present thesis work is discussed at the end of the chapter.

Chapter 2 contains details of the experimental techniques and characterization tools used for the synthesis and study of the morphological, structural and optical properties, and applications of the pristine and hybrid nanostructures of GQDs. This chapter provides the working principle and applicability of the techniques for the GQD research.

Chapter 3 presents the size controlled synthesis and chemical functionalization of GQDs grown by a hydrothermal method. By synthesizing the GQDs from two different precursor materials, we infer that the in-plane epoxy functional groups play a significant role on the formation of the GQDs. In this chapter, we proposed a new mechanism on the formation of GQDs by studying its early stages of growth through cutting of the graphene oxide sheets. Further, we studied the origin of PL from GQDs thin films before and after thermal annealing in the controlled gas flow of oxygen or hydrogen environment. The

thermal annealing enables the conversion of edge sites and functional groups in GQDs thin films as probed by the PL and Raman techniques. From these studies, we identified each of the PL bands to specific states of GQDs, for the first time. It is concluded that the blue PL emissions (~407 and ~442 nm) arise from the edge sites and the green PL bands (~490 and ~529 nm) originate from the oxygenated functional groups of GQDs.

Chapter 4 presents results on the effect of solvents on the synthesis, PL emission and bio-imaging applications of GQDs. The PL measurements of GQDs in liquid media exhibit strong blue PL emission. We studied the origin of PL emission of GQDs in liquid media and elucidated the PL mechanism on the basis of change in the dielectric constant of solvents and free electrons sites of the edge sites and oxygen functional groups of GQDs. We have achieved PL quantum yield of 32% from GQDs. The bio-imaging of human cancer cell lines, such as A-375 and HeLa cells are probed with GQDs. The incorporation of GQDs into the cancer cells results in the bright blue PL inside cell lines. In order to understand the role GQDs on bio-imaging, we performed the bio-imaging on normal cells (HEK-293), which do not show any PL under the confocal imaging. Further, we study the cell viability of GQDs on the cancer cells using MTT (3-(4,5-dimethylthiazol-2-yl)-2,5-diphenyltetrazolium bromide) dye assay and the results show very good biocompatibility of the as-prepared GQDs.

In Chapter 5, we discuss the effect of plasmonic Au NP decoration on the hybrid nanostructure of GQD-GCN and then evaluate the visible light photocatalytic activity of the hybrid catalyst using MB as a model dye. A striking enhancement in the intensity of Raman G band is observed in Au functionalized GQD-GCN due to the surface plasmon resonance. Under visible light illumination, we have achieved a significantly high ~86 % degradation of MB in presence of the hybrid Au@GQD-GCN catalyst. Plasmon resonance mediated enhancement of solar absorption and efficient charge transfer at the interface of Au and GQD-GCN results in the enhanced MB degradation. Free radical scavenger experiments prove the dominance of $^{\bullet}OH$ radical generation and the consequent the dye degradation.

In Chapter 6, the mechanism of heterojunction formation of GQDs and TiO_2 NP hybrid system and its application in photocatalytic degradation of MB is investigated. TiO_2 NPs with high oxygen vacancies were prepared by ball milling. We propose that the heterojunction formation is facilitated by the C-O-Ti bond formation through the oxygen vacancy sites in TiO_2 and in-plane epoxy functional groups in GQDs. We introduce the concept of in-plane epoxy functional groups rearrangement in GQDs in order to form C-O-Ti bonds in TiO_2-GQD, for the first time. Evidence for C-O-Ti bonds in hybrid is probed by the FTIR, XPS and Raman analysis. The DFT based simulation results confirm the enhanced visible light absorption in TiO_2-GQD hybrid as a result of C-O-Ti bonds. The heterojunction exhibited the enhanced photocatalytic degradation (97%) of MB due to the facile interfacial charge transfer from GQD to TiO_2. The degradation rate constant (first order) for TiO_2-GQD hybrid is 5.2 times higher than that of the bare TiO_2. Our controlled studies on the free radical experiments revealed that that $^{\bullet}OH$ radical played a major role in MB degradation as compared to $O_2^{\bullet -}$ radical.

Chapter 7 summarizes the important findings of the thesis on synthesis, origin and tunability of PL emission, and mechanism of heterojunction formation for different GQD

based hybrid nanostructures. The significant new findings on the bio-imaging and visible light photocatalytic activities of pristine and hybrids of GQDs are enumerated. The future scope of works on the synthesis of GQDs using different precursor materials, the fabrication of hybrid nanostructures and expected applications from these materials are presented at the end.

List of Publications

The important findings of this thesis work have been published in international peer reviewed journals and conference proceedings as listed below.

A. Publications in International Peer Reviewed Journals:

1. **Gone Rajende**r, Jitendra Kumar and P. K. Giri, "*Interfacial Charge Transfer in Oxygen Deficient TiO_2-Graphene Quantum Dot Hybrid and Its Influence on the Enhanced Visible Light Photocatalysis,"* **Applied Catalysis B: Environmental 224, 960-972 (2018).**
2. Ruma Das, **Gone Rajender** and P. K. Giri**,** "Anomalous Fluorescence Enhancement and Fluorescence Quenching of Graphene Quantum Dots by Single Walled Carbon Nanotubes", **Phys. Chem. Chem. Phys. 20, 4527-4537 (2018).**
3. **Gone Rajender,** B. Choudhury and P. K. Giri, *"In-Situ Decoration of Plasmonic Au Nanoparticles on Graphene Quantum Dots-Graphitic Carbon Nitride Hybrid and Evaluation of its Visible Light Photocatalytic Performance"* **Nanotechnology 28, 395703 (2017).**
4. **Gone Rajender** and P. K. Giri, "*Formation Mechanism of Graphene Quantum Dots and Their Edge States Conversion Probed by Photoluminescence and Raman Spectroscopy",* **J. Mater. Chem. C 4, 10852 (2016).**
5. **Gone Rajende**r and P. K. Giri, "S*train Induced Phase Formation, Microstructural Evolution and Bandgap Narrowing in Strained TiO_2 Nanocrystals Grown by Ball Milling",* **J. Alloys Comp. 676, 591-600 (2016).**
6. Ravi K. Biroju, **Gone Rajender,** P. K. Giri, *"On the Origin and Tunability of Blue and Green Photoluminescence from Chemically Derived Graphene: Hydrogenation and Oxygenation Studies",* **Carbon 95, 228 (2015).**
7. Ravi K. Biroju, Nikhil Tilak, **Gone Rajender**, S. Dhara, P. K. Giri, "*Catalyst Free Growth of ZnO Nanowires on Graphene and Graphene Oxide and Its Enhanced Photoluminescence and Photoresponse"*, **Nanotechnology *26,* 145601 *(2015)*.**

B. Manuscripts under Preparation:

8. **Gone Rajender,** Upashi Goswami, Siddhartha Sankar Ghosh and P. K. Giri "*Solvent Assisted Synthesis of Highly Fluorescent Graphene Quantum Dots and Its Application in Bio Imaging of Cancer Cells*".
9. **Gone Rajender,** Ravi K. Biroju and P. K. Giri, "*Effect of Precursor Material and Thermal Annealing On The Synthesis of Luminescent Graphene Quantum Dots*".

10. **Gone Rajender** and P. K. Giri, "*Graphene Quantum Dots and ZnO Nanostructures Hybrids: Structural and Optical Properties*".

11. **Gone Rajender** and P. K. Giri, "*Optical and Magnetic Properties of Undoped and Cr Doped TiO_2 Nanoparticles".*

C. Conference Presentations:

1. **Gone Rajender,** Upashi Goswami, Siddhartha Sankar Ghosh and P. K. Giri, "*Highly Fluorescent Graphene Quantum Dots and Its Hybrid Nanostructures for Bio-Imaging of Cancer Cells and Visible light Photocatalytic Applications"* International Conference on Advanced Nanomaterials and Nanotechnology (ICANN-2017), December 18-21, 2017, IIT Guwahati, India.

2. Ruma Das, **Gone Rajender** and P. K. Giri, *"Study of Fluorescence Enhancement and Fluorescence Quenching of Graphene Quantum Dots by Single Walled Carbon Nanotubes in Aqueous Medium",* International Conference on Advanced Nanomaterials and Nanotechnology (ICANN-2017), December 18-21, 2017, IIT Guwahati, India.

3. **Gone Rajender** and P. K. Giri, "*Graphene Quantum Dots and TiO_2 Nanoparticle Hybrid for Enhanced Photocatalytic Application*", Annual Physics Meet, January 27-28th, 2017, IIT Guwahati, India.

4. **Gone Rajender** and P. K. Giri, *"Study of Graphene Quantum Dot-TiO_2 Nanoparticle Heterojunction and Interfacial Charge Transfer for Visible Light Photocatalytic Application",* Research Conclave 2017 (RC-17), March 16-19th, 2017, IIT Guwahati, India.

5. **Gone Rajender** and P. K. Giri, *"Graphene Quantum Dots and TiO_2 Nanoparticle Hybrid: An Efficient Photocatalyst for Environmental Applications",*The Fourth International Conference on Frontiers on Nanoscience and Nanotechnology (Cochin Nano-2016), Feb 20-23rd, 2016, Cochin, India. ***(Best Poster Award).***

6. **Gone Rajender** and P. K. Giri , "*Effect of Functional Groups and Edge States On The Visible Photoluminescence From Graphene Quantum Dots*", 4th International Conference on Advanced Nanomaterials and Nanotechnology (ICANN-2015), Dec 08-11th, 2015, IIT Guwahati, India.

7. **Gone Rajender**, Ravi K. Biroju and P. K. Giri, "*On the Origin of Strong Blue and Green Emission from Edge Functionalized Graphene Quantum Dots*", 6th International Conference on Advanced Nanomaterials (ANM 2015), July 20-22nd, 2015, Aveiro, Portugal.

8. P. K. Giri, **Gone Rajender** and Ravi K. Biroju, "*Tunable Photoluminescence from Functionalized Graphene Quantum Dots and Graphene-ZnO Nanowires Hybrid*", 3rd International Conference on Nanoscience and Nanotechnology (ICONN 2015), Feb 4-6th, 2015, Chennai, India.

9. **Gone Rajender,** Ravi K. Biroju and P. K. Giri, *"Strong Visible Luminescence from Edge Functionalized 0-Dimenstional Graphene Quantum Dots",* National Conference

on Transport Properties in Low Dimensional Systems: Experiment and Simulation (TransLES-2014), December 11-13th, 2014, Guwahati, India.

10. **Gone Rajender,** Ravi K. Biroju and P. K. Giri, "*Effect of Reduction and Oxidation Treatment On The Photoluminescence of Edge Functionalized Graphene Quantum Dots",* First International Conference on Emerging Materials: Characterization and Application (EMCA-2014), December 4-6th, 2014, Kolkata, India.

11. **Gone Rajender,** Batakrushna Santara and P. K. Giri, *"Control of Defects and Defect Mediated Room Temperature Ferromagnetism In Undoped TiO_2 Nanoparticles Grown By Ball Milling Method",* International Conference on Nanoscience and Engineering Applications (ICONSEA-14), June 26-28th, 2014, Hyderabad, India.

12. **Gone Rajender**, Ravi K. Biroju and P. K. Giri, *"One Step Solvothermal Synthesis of Graphene Quantum Dots: Structural and Optical Studies",* National Conference on Nanotechnology and Renewable Energy (NCNRE-2014), April 28-29th, 2014, New Delhi, India.

13. Batakrushna Santara, **Gone Rajender** and P. K. Giri, *"Fabrication of 1-D and 3-D Flower-Like Complex Structures of TiO_2 Nanotubes And Nanorods With Tunable Architectures On Various Substrates",* Indo-Singapore Joint Physics Symposium on Physics and Advanced Materials (ISJPS 2013), February 25-27th, 2013, IIT Kharagpur, India.

D. Workshops/Seminars Attended:

1. *INUP Familiarization workshop on nano fabrication technologies,* September 28-29th, 2012, IIT Guwahati, India.
2. *IVCr workshop on X-ray Diffraction systems and related applications,* September 11-12th, 2014, IIT Guwahati, India.
3. *National workshop on MEMS/NEMS and Theranostic devices*, March 16-17, 2015, IIT Guwahati, India.
4. *Surface Characterization Workshop*, April 14-15th, 2015, IIT Kharagpur, West Bengal, India.
5. *National workshop on Advanced Probing Techniques in TEM***,** February 15-16, 2016, IIT Guwahati, India.
6. *National workshop on MEMS/NEMS and Theranostic devices*, March 21-22, 2016, IIT Guwahati, India.
7. *National workshop on MEMS/NEMS and Theranostic devices*, February 21-23, 2017, IIT Guwahati, India.

List of Symbols and Abbreviations

Symbol	Description
0D	Zero dimensional
DMF	Dimethylformamide
DRS	Diffuse Reflectance Spectroscopy
EDX	Energy Dispersive X-ray Analysis
FESEM	Field Emission Scanning Electron Microscopy
ESR	Electron Spin Resonance
FTIR	Fourier Transform Infrared Spectroscopy
GCN	Graphitic Carbon Nitride
GO	Graphene Oxide
GQD	Graphene Quantum Dot
HRTEM	High Resolution Transmission Electron Microscopy
MB	Methylene Blue
NP	Nanoparticle
OGO	Oxidized Graphene Oxide
PC	Photocatalytic
PL	Photoluminescence
QY	Quantum Yield
rGO	reduced Graphene Oxide
SERS	Surface Enhanced Raman Scattering
SPR	Surface Plasmon Resonance
τ	Carrier Life Time
TGA/DTG	Thermogravimetric analysis/ Differential Thermogravimetry
TRPL	Time Resolved Photoluminescence
UV-visible	Ultraviolet visible
XPS	X-ray Photoelectron Spectroscopy
XRD	X-ray Diffraction

Chapter 1

Introduction

1.1. Preface

Carbon, in nature, forms different types of allotropes depending on the electronic configuration and it renders to hybridize into sp, sp^2 and sp^3. The various hybridization and arrangement of carbon atoms in different allotropes allow formation of hybrids with foreign materials that may have interesting properties and they play an important role in diverse range of applications. The most widely known allotropes are graphite, diamond, fullerene and carbon nanotubes (CNTs). **Fig. 1.1** shows a schematic of the various allotropes of carbon. Graphite is a 3-dimensional (3D), sp^2 hybridized carbon black opaque soft material and made up of stacked layers that are held together by van der Waals interactions. CNT is another form of 1D sp^2 carbon material. In this form, carbon atoms are rolled up into cylindrical tubes, which was discovered by Iijima [1, 2]. Depending on the numbers of rolled layers, these materials are divided into single, double and multi walled CNTs. Diamond is another allotrope of carbon, in which carbon atoms are sp^3 hybridized [3]. Diamond is a transparent electrical insulator and the hardest known material. Buckminsterfullerene or fullerene is the 0D form of sp^2 carbon. The carbon atoms in fullerene (C60) are bonded through the pentagons and hexagons, where each C60 molecule consists of 60 sp^2 carbon atoms[4]. Graphene is a monolayer of graphite, which was isolated by Novoselov and Andre Geim in 2004, while doing some groundbreaking experiments on the ultra-thin material [5]. Different dimension allotropes of carbon such as graphite, single walled CNT, diamond, fullerene, graphene are shown **Fig. 1.1(a-e),** respectively. The invention of graphene opened the revolution in 2D materials research and greatly attracted the scientific community. Meanwhile, absence of band gap and high transparency to UV-visible light impede the efficient utilization of graphene in optoelectronic applications.

1.2. Graphene Quantum Dots

Graphene quantum dot (GQD) has emerged as an interesting class of 0D materials of sp^2 carbon, with lateral dimension less than 100 nm and it consists of a few layer graphene[6, 7]. GQDs are graphene core smaller polycyclic aromatic hydrocarbon molecules (PAHs).

GQD possesses attractive properties, such as tunable band gap, high yield photoluminescence that are suitable for various commercial applications. When the graphene is cut into small pieces, it exhibits interesting features, such as edge sites (zigzag and armchair type) and oxygenated functional groups. It is interesting to note that due the ultra-fine size of GQDs, the ratio of edge to basal plane carbon atoms is high resulting in the dominance of the edge states and edge oxygen functional groups [7-9]. **Fig. 1.1(f)** shows a schematic of a GQD with edge sites and oxygen functional groups. Photoluminescence (PL) is the one of the intriguing properties of the GQDs that has drawn considerable attention of researchers worldwide. GQDs show the characteristic optical transitions in the ultraviolet-visible region and it shows an absorption peak in the deep UV region 250-290 nm due to π– π* transition of aromatic C=C bonds [6]. Another absorption tail extended from UV to visible region is assigned to n– π* transition of oxygen functional groups [6, 10]. The Raman spectrum of GQDs usually exhibits the characteristic Raman D and G bands.

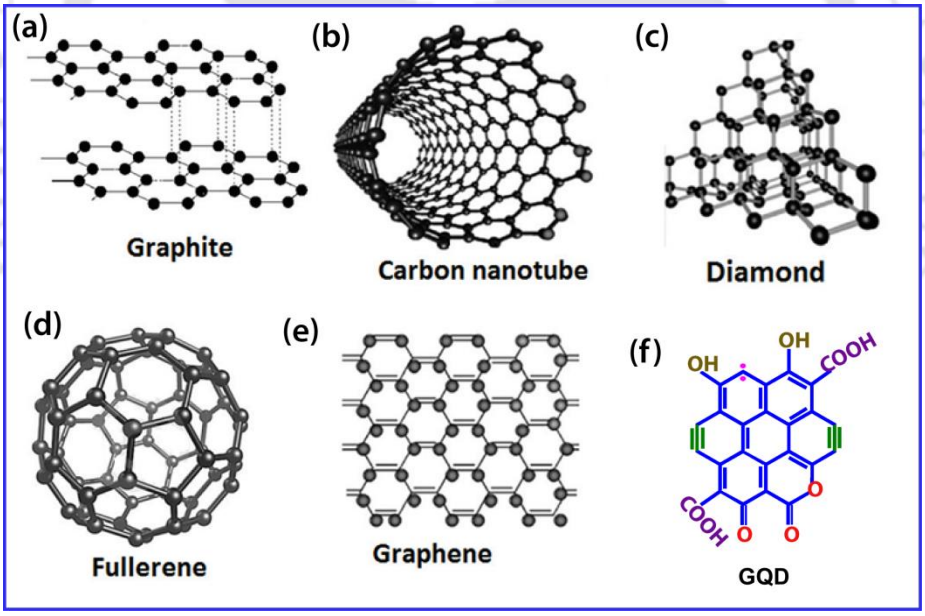

Figure 1.1: Various forms of carbon nanomaterial. Adapted from **Ref. [2]**

1.3. Comparison of GQDs and Semiconductor QDs

The term Quantum dot (QD), first coined by Mark Reed [11], originally referred to semiconductor nanoparticles (NPs) of sizes in the quantum-confined region. It means that the when the size of the material is comparable or less than the exciton Bohr radius of the material, the excitons in these particles are confined in spatial dimensions. GQDs possess

a high excitonic binding energy (0.8 eV for GQDs having the diameter of 2 nm), which is much larger than the conventional QDs, such as CdSe or CdS with similar size [12, 13]. The merits of GQDs, such as chemical stability, dispersibility in common solvents, good biocompatibility and low toxicity, make them new-generation luminescent materials superior to conventionally used fluorescent organic dyes and luminescent semiconductor QDs [14].

1.4. Raman Spectroscopy of Carbon Nanomaterial

Raman spectroscopy is a very important and established tool for the characterization of carbon materials [15]. It has been widely explored over the last decades for characterizing different forms of carbon materials, including the graphene [16-20]. In particular, it provides valuable information about the crystallinity/disorder, strain, degree of hybridization, edge defects and the extent of chemical modification in graphitic structures [15, 21-24].

1.4.1. Raman Spectrum of Graphene and GQDs

1.4.1.1 Graphitic Band

The characteristic of graphitic carbon atom lattice vibrations exhibit the graphitic (G) band, which appears at 1580 cm^{-1} in the Raman spectrum. This band originates from the in-plane stretching vibrations of sp^2 carbon atoms and is associated with the doubly degenerate (iTO and iLO) phonon vibrations at Γ point [25]. The G band is present in all forms of sp^2 carbon materials, such as graphite, graphene, CNTs, amorphous carbon and including other pi conjugated materials. **Fig. 1.2(a)** shows the Raman spectrum of defected and defect- free graphene. The important Raman bands of graphene are marked in the figure. **Fig. 1.2(b)** shows the Raman spectrum of GQDs. The G band peak position in carbon material, not only suggest the characteristics sp^2 carbon but also reveals the strain, if the peak position is deviated from the characteristic peak. For highly crystalline carbon materials, the G peak is very sharp and when the material contains lots of defects the G peak becomes broad. In addition, the D' band (explanation provided below) appears close to the G band in Raman spectrum of GQDs when it contains a lot of defects. The details of the origin of defects bands of graphene and GQDs are discussed below.

1.4.1.2. Disordered Band

Another important characteristic band of GQDs is the D band, which is known as disordered band. It comes from iTO phonons around the Brillouin zone corner K, and it is

active by symmetry involving phonons near the K zone boundary [26, 27]. This mode is forbidden in perfect graphite and becomes active only in the presence of disorder [26]. The D mode is dispersive, it varies with photon excitation energy [15]. A comparative Raman spectrum of defected and defect-free graphene is shown in **Fig. 1.2(a).** The D band is strongly present in the defective graphene, while it is absent for graphene. The D band intensity is very sensitive to the edges of graphitic carbon[22, 23, 28]. The D band intensity is low for zigzag edges, while it is high for armchair edges [22, 23, 28]. **Fig. 1.2(b)** shows the Raman spectrum of GQDs [29]. Besides the D band, another disorder band, known as D' band, it appears in the region 1610-1620 cm^{-1} [30]. This band is partially merged with the G band, as discussed above. The explanation given for the appearance of this band is that in graphite, there is a nonzero phonon density of states above the G band; such phonons, which are usually Raman-inactive, become active due to phonon confinement caused by the defects. Such defects includes the carbon vacancies and defects composed of two pentagonal rings and one octagonal ring and is usually referred to as the 5-8-5 defect. In addition to such 5-8-5 defects, the common 5-7-7-5 rings, that is, the so-called Stone-Wales (SW) defects [31-34] also contribute to the resultant Raman spectrum. The second order 2D and 2D' bands and other combinational bands such as D+D' (~2930 cm^{-1}) and 2D' (~3220-3240 cm^{-1}) of graphene are labelled in **Fig. 1.2(a).** It is well-known that except for the G band, all the defect bands and second order Raman modes, including the combinational modes are dispersive in nature [15, 22, 23]. However, these bands are relatively very weak in GQDs due to the inter layer distortion of the graphite during the exfoliation and attachments of various oxygenated functional groups [30].

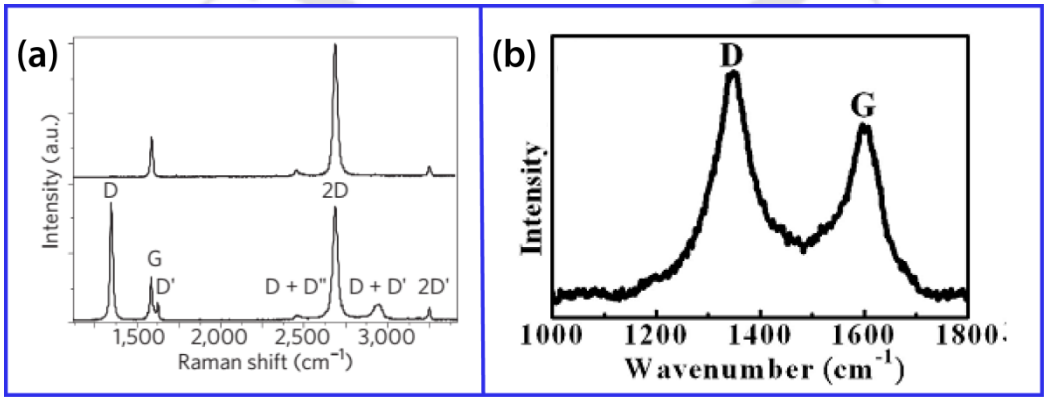

Figuree 1.2: (a) Raman spectra of pristine (top) and defected (bottom) graphene. The main peaks are labelled. Adapted from **Ref. [15]** (c) Raman spectrum of GQDs. Adapted from **Ref. [29]**

1.5. Methodologies for Synthesis of GQDs

The synthesis strategy of GQDs is classified into two main groups: top-down and bottom-up methods. Top down approach refers to cutting of a bulk material to get nano sized particle. Bottom up approach includes the building up of nano materials atom by atom, molecule by molecule or cluster by cluster. Both approaches play very important role in modern industry and as well as the different fields in nanotechnology. There are advantages and disadvantages in both approaches. Below we discuss the most commonly used synthesis methods of GQDs.

1.5.1. Top down Method

Hydrothermal route is a good example of top down approach and it is a suitable and the simplest way to produce the GQDs from the aqueous precursor solution. In this process, the parameters like degree of oxidation of precursor, temperature and reaction duration play important role in cutting of the bulk carbon materials into small dimensions of few nanometer GQDs. The first attempt on hydrothermal synthesis of GQDs is reported by Pan et al. [35]. In this report, they synthesized the GQDs using micrometre oxidized graphene sheets (OGSs) at 200 °C and 24 h. The size of the GQDs is distributed between 5 to13 nm (average diameter: 9.6 nm) and GQDs consists of 1-3 layers of graphene. The synthesized GQDs emitted the blue PL and the PL quantum yield (QY) of GQDs was 6.9% [35]. They proposed a formation mechanism of GQDs through the C-C line cutting of graphene sheets, as shown in **Fig. 1.3(a).** GQDs were also prepared in alkaline medium ammonia ($NH_3.H_2O$) with deionised water and OGSs as precursor materials at temperature 200 °C and duration for 10 h [36]. This group have achieved a nearly uniform size of GQDs (1.5 to 5 nm) with a mean size of 3 nm and GQDs consisted of the 2-3 graphene layers. In this case, the GQDs showed the bright green PL emission and the PL QY was 7.5% [36]. Shen et al. reported on the functionalization of GQDs [37]. In their experiment, GOs and Polyethylene glycol (PEG1500N) were used as precursor and surface passivation agent, respectively and the reaction duration and temperature was maintained at 120 °C for 24 h [37]. The diameters of GQDs were mainly distributed in the range of 5–19 nm and mean size was 13.3 nm. In another study, functionalization of GQDs was carried out with PEG 10000 [38]. GO and PEG 10000 (0.2 g) was mixed with water and the then transferred into a Teflon-lined stainless-steel autoclave and heated at

200 °C for 24 h. The size of the GQDs was in the range from 5–25 nm and mean diameter was 13.0 nm. The PL QY was low for bare GQDs (13.1%) and for PEG functionalized GQD the PL QY was increased to 28.0% [38]. It was suggested that the improvement in PL QY yield originated from the stabilization effect of excitons in the GQDs after passivation by PEG [39, 40] .

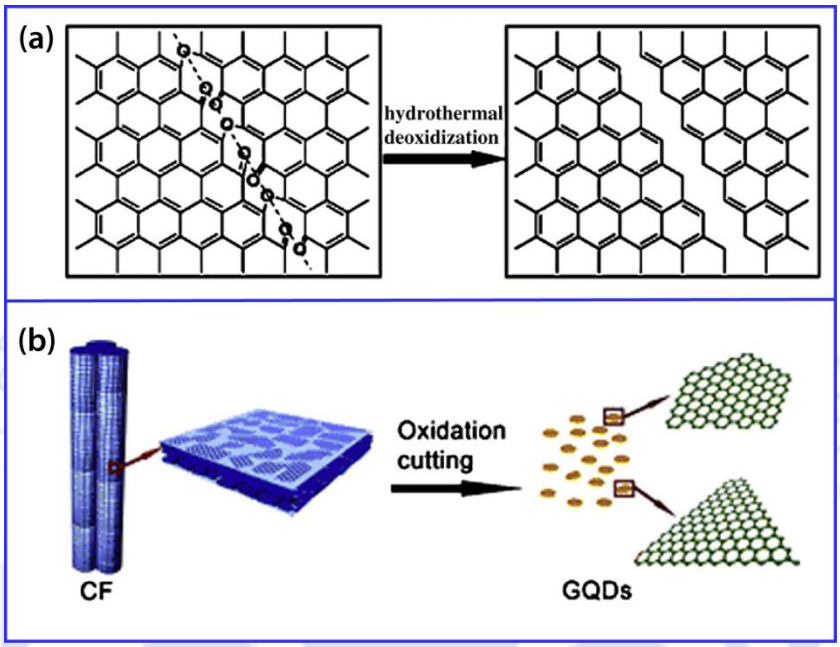

Figure 1.3: (a) Mechanism for the hydrothermal cutting of oxidized GSs into GQDs. Adapted from **Ref. [35]** and (b) schematic of oxidation cutting of CFs into GQDs. Adapted from **Ref. [41]**

Top down method of GQDs synthesis is not limited to the precursor of only GO. GQDs were also synthesised from the different other precursor materials, such carbon fibres [41], coal [42], MWNCTs [43-45] , electrolysis of the graphite rod [46], refluxing the XC-72 carbon black in concentrated HNO_3 [47] and chemical exfoliation of graphite [48]. For different precursor materials, the reaction duration or temperature is varied for GQDs synthesis. For example, Peng et al. [41] prepared the GQDs from carbon fibres (CFs) by varying the reaction temperature. **Fig. 1.3(b)** shows the oxidative cutting of CFs under acidic condition. First, the pitch CFs were added into a mixture of concentrated H_2SO_4 (60 mL) and HNO_3 (20 mL). This solution was sonicated for two hours and stirred for 24 hours at different temperatures of 80, 100, and 120 °C. Based on the different reaction temperatures, different sized GQDs were achieved. The GQD sizes lie in the range 7-11 nm for reaction temperature of 80 °C, 4-8 nm for 100 °C, and 1-4 nm for 120 °C and the GQDs contained 1-3 graphene layers. The GQDs synthesized at temperature 80, 100, and 120 °C resulted in the yellow, green and blue PL emission, respectively.

Besides the hydrothermal method, solvothermal method is also used for the synthesis of GQDs. In this process the solvents play a major role to get the high quality and uniform size GQDs. Zhu et al. [49] reported on strongly green fluorescent GQDs prepared by solvothermal method using GO as a precursor and dimethylformamide (DMF) as a solvent. The average diameters of GQDs were 5.3 nm and consist of single or bi-layer graphene. In another study, GO and DMF were used for the GQDs synthesis and after the synthesis the GQDs were separated by the column chromatography on silica, from which GQDs with different degree of oxidation were separated [50]. The diameter of the GQDs was 3–5 nm and the GQDs contain single layer to bi-layer graphene. Based on the degree of oxidation, different PL evolution and distinct PL QYs, such as 4.1, 9.9 and 12.2%, were noticed. In another study, organic solvents, such as ethylene glycol, DMF, dimethyl sulfoxide (DMSO) and N-Methyl-2-pyrrolidone were used for the synthesis of GQDs from GO after 24 h reaction [51]. In this process, the oxidation degree of precursor material, solvent, reaction temperature and duration played important roles in the GQDs synthesis. One need to customize the appropriate precursor materials, optimize the reaction temperature and reaction duration in order to achieve highly photo luminescent GQDs according to the requirement.

1.5.2. Bottom up Method

In the bottom up process, the organic materials are mainly used as precursors for the GQDs synthesis. Tang et al. [52] first reported a facile microwave-assisted hydrothermal method for the production of GQDs with glucose as the starting material. A formation mechanism of GQDs was proposed as shown in **Fig. 1.4(a)**. It was proposed that first the glucose molecules dehydrate to form the nucleus of GQDs that is composed of C=C. Next, the growth of GQD occurred at the spherical surface (edge growth), and with increasing heating time, the additional glucose molecules reach the surface of the GQD and generate new C=C by dehydration. The resultant C=C is orderly arranged and assists the growth of crystalline GQDs as shown in **Fig. 1.4(a)**. The diameter of the GQDs can be increased by increasing the microwave heating time. It was reported that the size of the GQDs can be tuned from 1.65 to 21 nm by simply prolonging the heating time from 1 to 9 min. In another study, Dong et al. [53] prepared blue luminescent GQDs as well as GO by tuning the carbonization degree of citric acid (CA). According to the report, the carbonization time of 30 min for CA yields the GQDs having the sheet like structure with

15 nm in size. Prolonged carbonizations for 2 h gave the sheet of GO. It was confirmed that the GQDs were well passivated due to the incomplete carbonization of CA, as shown in **Fig. 1.4(b).** From the precursor of glucose and CA for GQDs synthesis, these studies suggested that the precursor containing C, H, and O in the ratio of 1:2:1could be used for the GQDs preparation. All the carbohydrates containing the H and O exists in the forms of hydroxyl, carboxyl or carbonyl groups, which may dehydrate under hydrothermal conditions.

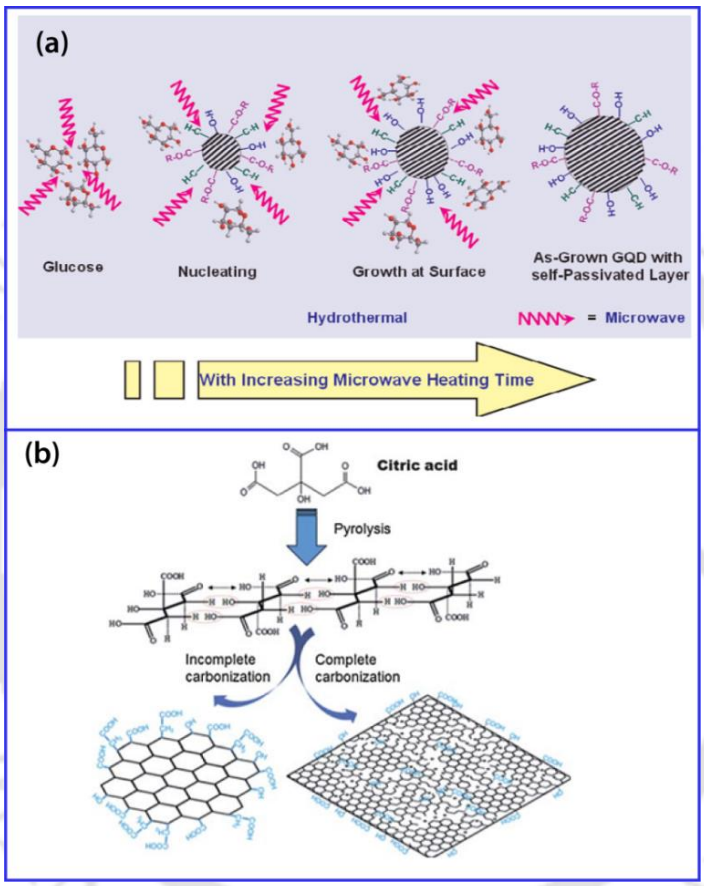

Figure 1.4: (a) Schematic representation of GQD formation by microwave assisted hydrothermal method, Adapted from **Ref. [52]** (b) Schematic for the synthesis of GQDs and GO, the black dots in the GO represents oxygen atoms, Adapted from **Ref. [53]**

Liu et al. [54] prepared the GQDs from hexa-peri-hexabenzocoronene (HBC), a polycyclic aromatic hydrocarbon. They produced monodisperse disk-like GQDs of size ~60 nm and thickness 2–3 nm. HBC was pyrolyzed, oxidized, functionalized and then reduced, which could be considered as nano scaled fragments of graphene that stack via interactions. GQDs were also synthesised using Ruthenium-catalysed cage-opening of C60 molecules [55], Glycerol [56] and natural amino acid, L-glutamic acid [57] as the precursor materials.

In addition to the chemical methods, GQDs preparation has been reported using the physical methods, such as lithography techniques and chemical vapour deposition [7, 58, 59]. Certainly these methods are very expensive and yield a low scale preparation of GQDs. The chemical methods offer to prepare well controlled, high quality and industrial scale GQDs that are suitable for various commercial applications. The advantage of GQDs synthesis using the top-down approach is that GQDs shows the well crystalline graphene lattice and abundant functional groups. In the bottom up approach, the organic materials are carbonized to yield the GQDs and understanding the surface chemistry of the formation mechanism of GQDs needs to be studied more thoroughly.

1.6. Fabrication of GQDs Based Heterostrucutres

GQDs opened up a new dimension to graphene research and there has been much hype on the potential applications of GQDs. The free electron sites (edges) and oxygen functional groups defects in GQDs allows the formation of heterostructures with various materials with different dimensions ranging from 0D to 3D. In addition, GQDs exhibiting excellent solubility and low toxicity enables them in solution processed optoelectronic devices and biological applications [60, 61]. Moreover, the intriguing PL of GQDs offers to explore a wide range of applications. Thus, the design of suitable hybrid nanostructure of GQDs, low cost processing and large scale production of materials are essential for industrial applications. The versatile GQDs and its heterostrucutres are categorized into (i) 0D-0D such as NPs [62, 63], (ii) 0D-1D hybrids, such as nanorods, nanowires, nanofibres, and nanotubes[64-67], (iii) 0D-2D hybrids [68, 69], and (iv) 0D-3D hybrids [70].

Plasmonic metal NPs has gained significant attention due to the strong visible light absorption caused by the surface plasmon resonance (SPR) [71, 72]. Recently, plasmonic NP functionalized GQD is one of the emerging fields of research interest. The integration of plasmonic NPs on graphitic materials has endowed the improved photocatalytic performance in the degradation of organic dyes by the utilization of localized SPR [71, 72]. The SPR absorption in the visible region can monitor the visible PL emission of GQDs that can produce the turn on or turn off PL for selective sensing applications [73-77]. The graphitic carbon nitride (g-C_3N_4, GCN) is a 2D material and it possesses a bandgap, in contrast the zero bandgap graphene due to the electronegativity difference between carbon and nitrogen. In a recent theoretical study, Ma *et al.* studied the strong interfacial

electron coupling in GQD hybridized with GCN [68]. The heterojunction of GQD-GCN facilitates charge carrier separation at the interface making the hybrid a better photocatalyst. There are numerous reports on the ultrasonic synthesis of TiO_2-graphene based hybrid nanostructures [69, 78, 79]. The hybrid of TiO_2 and GQDs has some advantages over conventional semiconductor QDs to cross the Shockley–Queisser limit, where the hot charge carriers are the sources in solar to electric energy conversion process [80]. TiO_2 nanotubes array and GQDs hybrids are good candidates for UV and visible light photocatalysis [81, 82], and GQD-TiO_2 hallow nanowire hybrid was studied for photoelectrochemical (PEC) hydrogen fuel production [83].

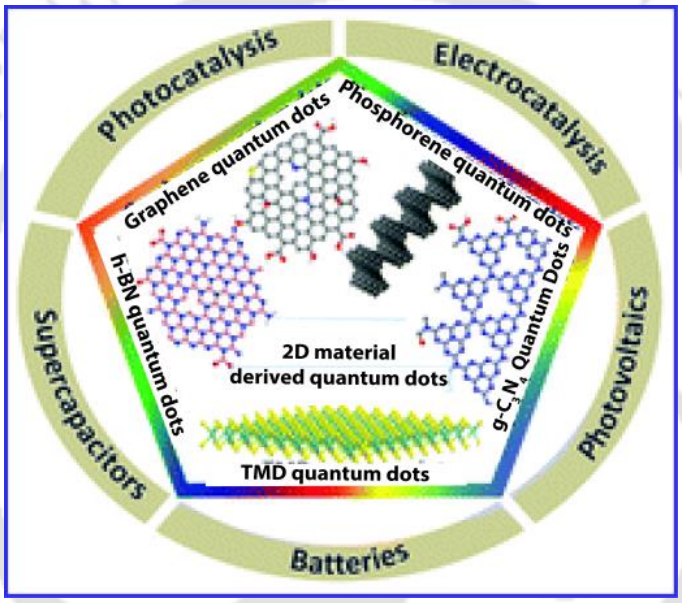

Figure 1.5: Schematic of representation of QDs derived from 2D materials and their applications. Adapted from **Ref. [86]**

GQDs possess some attractive properties as compared to the bulk form of graphene, which open the new path ways for exploring the potentials of QDs derived from other 2D materials. The 2D materials family, such as transition metal dichalcogenides (TMDs), phosphorene, hexagonal boron nitride (h-BN), GCN and oxides of transition metal etc. are some of the interesting 2D materials [84, 85]. Research on the QDs based on 2D materials is in infant stage and is one of the emerging research interests of the nanomaterials research community. A recent perspective has been devoted to the QDs derived from 2D materials [86]. **Fig. 1.5** shows a library of QDs derived from 2D materials and their potential applications. GQD heterostructures with other 2D materials may give rise to new properties. This may pave the way for studying and designing the

low cost, industrial scale devices made of 2D materials for various applications ranging from sensors, biological, optoelectronic, energy and environment.

1.7. Applications of GQDs and Its Heterostrucutres

1.7.1. Sensing Applications

The most important feature of GQDs is their optical performance, especially the intriguing PL emission. As novel fluorescent probes, GQDs are highly sensitive to minute perturbations, providing great potential for sensing applications. Meanwhile, the high photo stability, low toxicity, good biocompatibility and excellent dispersion of GQDs result in high sensitivity, selectivity and security as compared with traditional organic dyes and semiconductor QDs. Based on the very bright & high QY of PL from GQDs, various sensing applications are designed. Some of the fluorescence based applications are discussed below.

1.7.1.1. Metal Ions Detection

Based on the PL of GQDs, various sensors have been fabricated recently with either signal-off or signal-on processes. Sun et al. [87] fabricated the amino-functionalized GQDs (af-GQDs) to sense the copper ions. They suggested that the Cu^{2+} ions have a higher binding affinity and faster chelating kinetics with N and O on the surface of af-GQDs than other transition-metal ions. The PL quenching effect was suggested due the static and dynamic phenomena. Wang et al. [88] developed a blue PL emitting GQD as a sensing probe for the detection of Hg^{2+}. The PL intensity of the GQDs decreases with increasing concentration of Hg^{2+}. The PL quenching effect was ascribed to two reasons, such as aggregation induced quenching and electron transfer quenching. The aggregation induced quenching is due to the affinity of mercury ions for carboxyl groups at GQD edges and reduced electron/hole recombination due to the effective of electron transfer. The PL based analytical technique is also utilized for detection of other metal ions such as Ni^{2+}, Mn^{2+}, Co^{2+}, Cu^{2+}, Fe^{3+} and Cd^{2+} etc. [89-92].

1.7.1.2. Chemicals Sensing

The bright PL of GQDs is advantageous for detecting the chemical compounds. Fan et al. reported that GQDs could serve as an effective and simple PL sensing platform for ultrasensitive detection of 2,4,6-trinitrotoluene (TNT) in solution. They suggested that the PL quenching and detection of TNT is due to fluorescence resonance energy transfer (FRET) between the GQD and TNT [93]. The TNT species could specifically be attached

onto the fluorescent GQDs by the π– π stacking interaction between GQDs and aromatic rings. The attached TNT could strongly suppress the PL emission by the FRET from GQDs donor to the TNT acceptor through intermolecular polar–polar interactions at spatial proximity. Yang et al. found that the PL intensity of GQDs decreased with the increasing concentration of pyrocatechol [94]. They proposed that the oxygen-containing groups in GQDs enabled noncovalent interaction between GQDs and pyrocatechol through electrostatic interaction, π– π stacking or hydrogen bonding. This interaction leads to the energy transfer and further PL quenching of GQDs. In another study, GQDs were assembled on an Au electrode using cysteamine as a crosslinker [77]. The resultant covalently assembled GQD/Au electrode detected the H_2O_2 with good stability and reusability. The GQD/Au electrode displayed a rapid amperometric response to H_2O_2. Similarly, the PL of GQDs is used to detect the ascorbic acid, Melamine and Gallic acid[95-97].

1.7.1.3. Detection of Bio-Molecules

The low toxicity, excellent solubility, and biocompatibility of GQDs have facilitated their promising application in biological sensors. A novel glucose-sensing system was designed based on combining affinity sensing and electrostatic attraction between anionic fluorescent GQDs and a cationic boronic acid-substituted bipyridinium salt (BBV) [98]. **Fig. 1.6(a)** shows the electrostatic attraction between GQDs and BBV and glucose sensing. The PL quenching in this case is due to the excited-state electron transfer from the GQDs to BBV. After addition of glucose to the GQD-BBV system, tetrahedral anionic glucoboronate esters formed. Meanwhile the glucose effectively neutralized the net charge of the cationic bipyridinium, and recovered the fluorescence intensity of the GQDs. The plasmonic NPs based GQDs hybrids are attractive for sensitive and selective detection of bio-molecule. For example, taking the advantage of the PL quenching of GQDs, a turn-off sensor for Ag^+ and biothiol detection was developed [73]. This sensor was designed based on the formation of the AgNP/ GQD hybrids following the attachment of Ag^+ onto the surface of the GQDs via electrostatic interaction. In this process, the addition of biothiols caused a further turn-off phenomenon through the formation of an Ag-S bond. Further, a biosensor for trypsin detection was designed on the basis that cytochrome c (Cyt c, rich in Fe^{3+}) induced remarkable fluorescence quenching in self-assembled GQDs [99]. **Fig. 1.6(b)** shows that the electrostatic attraction between GQDs and

Cyt c. The presence of phenolic hydroxyl group in the GQDs and Fe^{3+} could bind to the GQDs using electrostatic interactions, and completely quenched the fluorescence of GQDs through electron transfer. When trypsin was present, Cyt c cleaved into smaller fragments on the c-terminal side of arginine and lysine residues, and the Fe^{3+} in Cyt c was possibly reduced to Fe^{2+} using a digestive enzyme. However, the trypsin-cleaved peptide bonds of Cyt c to the lysine and arginine residues could reduce the GQDs into reducing-GQDs and, as a result, the fluorescence of the GQDs was restored.

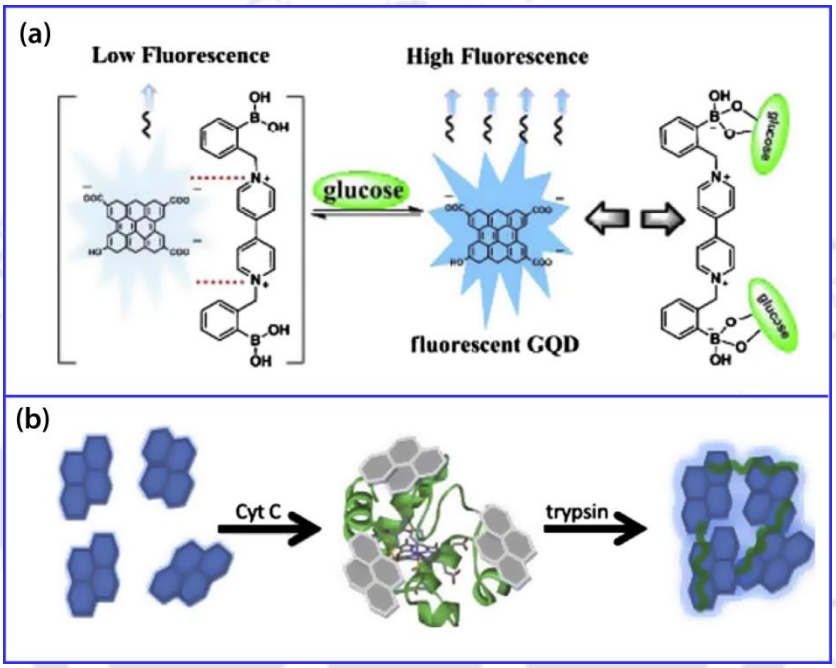

Figure 1.6: (a) Glucose-sensing mechanism based on boronic acid-substituted bipyridinium salt (BBV) receptor and GQDs. Adapted from **Ref. [98]** (b) The fluorescent biosensor for trypsin based on self-assembled GQDs. Adapted from **Ref. [99]**

1.7.2. Bio-Imaging

The bio-imaging of cancer cells by using semiconductor QDs, such as CdSe or CdS and their core–shell NPs, have been used in various in vitro or in vivo optical imaging experiments [100, 101]. The toxicity is a natural concern for bio-applications. These QDs have prompted serious health and environmental concerns due to the heavy metal elements in them [101]. The tunable and very strong PL emission of GQDs is more advantageous than the semiconductor QDs due to the low toxicity and eco-friendly nature of GQDs. These features make them excellent fluorescent markers for bio-imaging. The toxicity of GQDs over the different cells lines was investigated. To understand the cytotoxicity of different cell lines, MTT ((3-(4,5-dimethylthiazol-2-yl)-2,5-diphenyltetrazolium bromide) assay

experiments were done. Peng et al. [41] evaluated the cytotoxicity of blue and green fluorescent GQDs using two different human breast cancer cell lines MDAMB-321 and T47D with MTT viability assay. They measured the cytotoxicity of GQDs concentration upto 50 μg/ml. It was found that GQDs did not show any considerable toxicity on two cell lines and the GQDs entered into the cyto plasma on these cell lines. High PL QY of GQDs shows the very low cytotoxicity than the pristine GQDs. Sun et al. [61] performed the photo reduction of cGQDs under UV light, the photo reduced GQDs (pGQDs) exhibited the 3.7 fold high PL QY than the pristine GQDs. They studied the bio-imaging

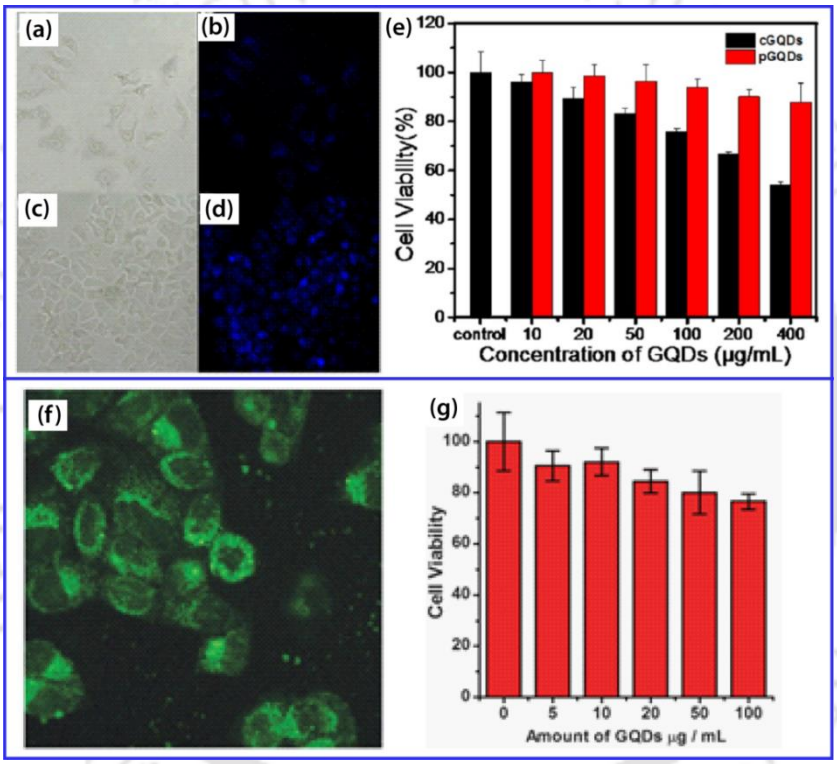

Figure 1.7: Cellular imaging of cGQDs: (a, b) under bright field and fluorescence, respectively, Cellular imaging of pGQDs: (c, d) under bright field and fluorescence, respectively. (e) Cytotoxicity studies of the pGQDs and cGQDs on A549 cell line. Adapted from **Ref. [61].** (f) Fluorescence of A549 cells with GQDs, (g) Cell viability assays of A549 cells treated with GQD at different concentrations. Adapted from **Ref. [48].**

and cytotoxicity of two different GQDs on A549 cell lines [61]. **Fig. 1.7(a-d)** shows the bright field and blue fluorescence images of A549 cell lines by using two different GQDs. **Fig. 1.7(e)** shows the toxicity results of two GQDs on A549 cell lines. The pGQDs show good biocompatibility than the cGQDs for concentration upto 400 μg/mL. In another work, the bio-imaging of the same cell lines were studied by green emitting GQDs [48]. **Fig. 1.7(f)** shows the green fluorescence image of GQDs labelled in A549 cell lines. **Fig.**

1.7(g) shows the toxicity results of GQDs on A549 cell lines. The viability of the cells treated by GQDs was close to 90% at low concentrations (<10μg /mL) and this value decreases to about 80% at a high concentration of 100 μg/mL[48].

1.7.3. Solar Cells

One of the renewable energy resource, solar light conversion into electricity is immensely important research in the field of photovoltaic device. Interestingly, GQDs are very attractive and promising materials for photovoltaic applications due to its extraordinary properties, such as light absorption characteristic in the visible region, excellent solubility and tunable bandgap, which are beneficial features for photovoltaic device applications [102]. GQDs were used as a sensitizer for dye-sensitized solar cells fabricated by using nanocrystalline TiO_2. The open-circuit voltage and fill factor are comparable to those of solar cells sensitized by ruthenium complexes, suggesting that the possible replacement of the traditionally used sensitizer with GQDs [102]. GQDs dispersed in conjugated polymers enhances the efficiency of organic solar cells and light emitting diodes as compared to the use of graphene sheets, due to improved morphological and optical characteristics [103]. The device performance can be further enhanced by employing other polymers or different types of functionalization with foreign materials, where functionalized GQD acts as electron selective layer [104]. In another case, GQDs acted well as the hole transport layer material for organic solar cells with a structure of glass/ITO/HTLs/PEDOT:PSS/LiF/Al [105]. A Recent reports suggest that the GQDs and Si nanowires based heterostructure solar cells have high efficiency [106, 107]. These results suggest the important role of GQDs in solar cell applications and endow for further research on ultrahigh efficiency photovoltaic cells in the future.

1.7.4. Supercapacitors

GQD based supercapacitor has attracted tremendous research interest due to the unique properties, such as larger specific surface area, high electro-chemically active sites, ease of integration with other nanomaterials, and being more amenable to solution-based processes [65, 108]. From the electrode material aspect, various nanostructure materials, such as CNTs [109], RuO_2 [110], MnO_2 [111] and polypyrrole [112] have been utilized as electrode materials for micro-supercapacitors. However, their performances are still unsatisfactory for the practical application of micro-supercapacitors due to the mechanical degradation, low power response and low stability. To overcome these issues and implement the

practical supercapacitor applications, GQDs based heterostructures are designed. Liu et al. [113] assembled a GQD-based symmetric micro-supercapacitor and they obtained a high rate performance, fast power response, and good cycling stability (97.8% retention after 5000 cycles). At the current density of 15 μA cm^{-2}, a specific capacity of 534.7 μF cm^{-2} with an energy density of 0.074 μW h cm^{-2} and a power density of 7.5 μW cm^{-2} was obtained. In another study, to obtain the high capacitance, Hu et al. [67] fabricated GQD/CNT composite film which exhibited a capacitance of 44 mF cm^{-2} , which was 200% more than the capacitance of bare CNT film. **Fig. 1.8(a)** shows a schematic of preparation of GQD and CNT hybrid, where GQDs are deposited on the horizontal aligned CNTs, and **(b)** shows the charge–discharge curve. In order to increase the potential window, asymmetric micro-supercapacitors have been fabricated with one electrode coated with GQDs and another functionalized with highly pseudocapacitive nanomaterials (e.g., MnO_2, PANI). Liu et al, [65] designed GQDs as negative active material and polyaniline (PANI) nanofibers as positive active material. The GQDs//PANI asymmetric micro-supercapacitor has more excellent rate capability (up to 1000 V s^{-1}) than previously reported electrode materials, as well as faster power response capability (very short relaxation time constant =115.9 μs). In another study, Mondal et al.[114] synthesized GQD-modified PANI nanotubes with a high aspect ratio and a surface-to-volume ratio, and obtained a high specific capacity of 1044 F g^{-1} at the current density of 1 A g^{-1}. They suggested the high specific capacity of the GQDs due to its abundant ion-interacting edges, defect, and chemical moiety sites. These findings suggest that GQDs is a highly promising material in high-performance energy-storage devices.

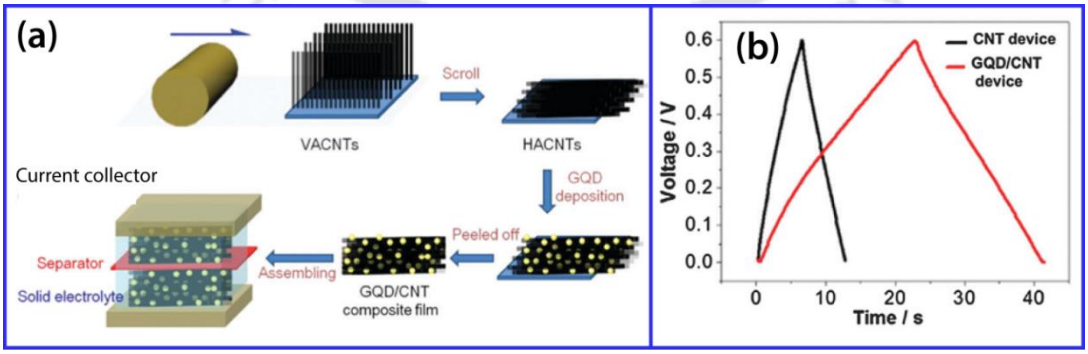

Figure 1.8: (a) Fabrication of a supercapacitor based on a GQD/CNT composite film and (b) galvanostatic charge–discharge curve at 700 μAcm^{-2}. Adapted from **Ref. [67]**

1.7.5. Visible light Photocatalysis

The photocatlytic (PC) degradation of dye effluents is essential for water purification, since the dye effluents greatly affect the environmental eco system [115, 116]. TiO_2 is the most widely used photocatalyst in dye degradation due to the long-term thermodynamic stability, strong oxidizing power, and relative nontoxicity and charge carrier transport etc.[117, 118]. **Fig. 1.9(a)** shows the energy band diagram, charge carries recombination and free radical generation in TiO_2. Limitations of TiO_2 in visible light photocatalysis includes the light absorption in the UV region and high recombination rate of charge carriers etc. [119]. The band gap narrowing and separation of charge carriers are some of the important factors in PC dye degradation. Hybrids of GQD with plasmonic NPs and semiconductors nanostructures play significant role in photocatalytic applications[74, 82, 120]. The hybrid of GQD-GCN was studied in photocatalytic H_2 evolution and it was reported that the incorporation of GQD on the GCN nano sheet improves the H_2 generation [69]. In another study, Au NPs loaded GCN hybrid was studied in photocatalytic degradation of methyl orange (MO) under visible-light irradiation [121]. The photocatlytic activity of GQD-TiO_2 is fifteen times higher than that of the bare TiO_2 on MO degradation [122]. There are other reports that discussed the role of GQDs based hybrid nanostructures in degradation of different dyes, such as MO [122], methylene blue (MB) [81]. Hybrid of TiO_2-GQDs show a photocurrent enhancement of ~70% for water oxidation compared to pristine TiO_2 [83]. **Fig. 1.9(b)** shows a schematic of the charge transfer in heterojunction of GQD-TiO_2 hallow nanowire hybrid for hydrogen fuel production [83].

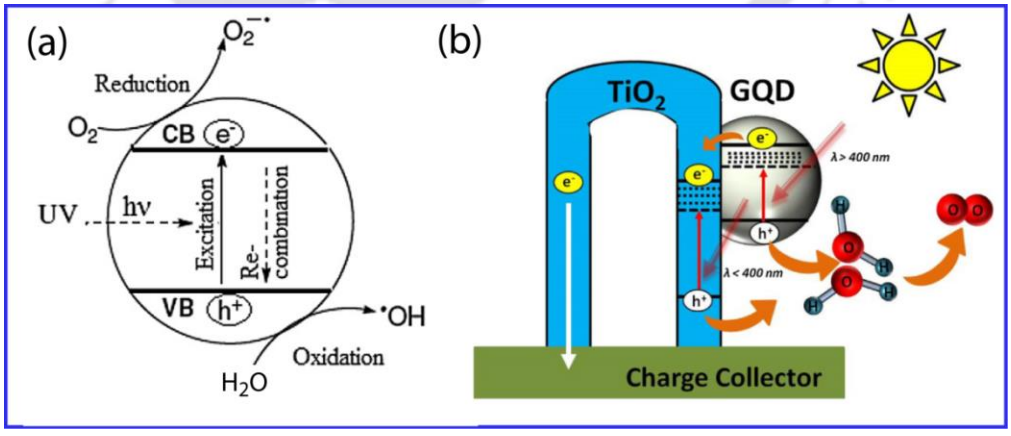

Figure 1.9: (a) Schematic diagram illustrating the principle of TiO_2 photocatalysis. Adapted from **Ref. [119]** (b) Photoexcitation charge carriers generated at GQDs/TiO_2 interfaces. Adapted from **Ref. [83]**

1.8. Motivation and Focus of the Present Thesis

Despite extensive studies, the role of in-plane epoxy functional groups on the synthesis of high quality GQDs from different precursor materials and understanding the mechanism of formation of circular shaped GQDs have not been addressed in the literature. Understanding the the origin of PL from GQDs thin films, as opposed to the GQDs in dispersion commonly reported in the literature, is still lacking. Despite sustained efforts made on understanding the blue and green PL emission of GQDs, assignment of particular PL emission bands and the relation between the PL and Raman spectral band are not well understood by the research community. Achieving the high PL QY GQDs and its influence on the bio-imaging of cancer cell lines is important. Fabricating the high quality GQDs and its heterostructures with low cost synthesis technique and exploration of its application is a challenging task. Understanding the formation mechanism of GQDs and its heterojunction with other materials, in particular with graphitic material and metal oxide semiconductor is important for ensuing applications. Mechanism of charge transfer between GQDs and its hybrid nanostructures and its consequence on visible light PC degradation of organic pollutants is very important. Free radicals generation and their critical role on dye degradation is important for eco-friendly environmental system.

This thesis focuses on the controlled synthesis, elucidating the formation mechanism of GQDs and its heterostructures, tuning its optical properties and exploring its applications in bio-imaging and visible light photocatalysis. We propose a new formation mechanism for circular shaped GQDs, by studying the critical role of in-plane epoxy functional groups on the formation of GQDs. Further, we investigate the origin of visible PL emission of GQDs, in particular the specific PL bands, through the controlled annealing experiments, from which we made an important correlation between the PL and Raman studies. Furthermore, we performed the PL measurements of GQDs in different solvent media, which confirm the contribution of surface state in the PL of GQDs. After controlled synthesis and studying the origin of PL from GQDs, we explored the GQDs and its heterostructures in bio-imaging and visible light photocatalytic applications. Bio–imaging and cell viability test results revealed that GQDs are highly bio-compatible for the cancer cell lines, such as A-375 and HeLa. An *in-situ* chemical synthesis is adapted to prepare the hybrid nanostructure of plasmonic Au NPs functionalized GQDs and graphitic carbon nitride (GCN) nanosheets. We demonstrate the efficient charge transfer

from the GQD-GCN hybrid to Au, which accelerate the PC degradation of MB. We fabricated the heterojunction of GQDs and TiO_2 NPs using the ultrasonication process, and for the first time, we proposed C-O-Ti bond formation mechanism in GQD-TiO_2 heterojunction by controlled experiment and DFT based simulation results. We discussed about the free radical scavenger test, generation of free radicals and mechanism of MB degradation in detail in hybrids of GQDs.

First, we concentrate on the controlled synthesis and understanding the formation mechanism of GQDs. Hydrothermal and solvothermal methods are employed for the synthesis as well the functionalization of GQDs. Hydrothermal reactions were performed using oxidized GO as a precursor material and for different reaction duration (12 and 24 h) by keeping the temperature constant. The higher reaction duration yields the ultrafine size ~ 5nm GQDs. Further, to understand the role of in-plane epoxy functional groups on the formation of GQDs, we have synthesized the GQDs by using reduced GO as a precursor material. Interestingly, no proper formation of GQDs was seen in this reaction. Based on thermogravemetric analysis (TGA) and differential TGA, UV-Vis absorption and FTIR studies, we proposed a new formation mechanism of GQDs. Our studies suggested that the in-plane epoxy functional groups play important role on the formation of circular shaped and highly crystalline GQDs. Furthermore, we studied the effect of *in-situ* chemical functionalization on GQDs by using the polyethelenglycol (PEG). To understand the origin of PL of GQDs, we fabricated the GQDs thin films by spin coating technique and annealed under controlled flow of oxygen or hydrogen gas environments. In general, the PL spectrum of GQDs is broad and we have noticed a change in the PL spectrum of GQDs before and after annealing in both gases. To understand the change in PL spectrum of GQDs, we have deconvlouted the spectrum into multiple peaks. The evolution of different peaks with annealing allows us to assign specific peaks to a particular species in spectral evolution of GQDs thin films. Similarly, we also observed changes in the Raman spectrum of GQDs after annealing. Based on the Raman spectrum of GQDs before and after annealing, we have monitored the spectral bands to elucidate the PL origin of GQDs. Based on the PL, Raman, FTIR and XPS studies, we identified each of the PL bands to specific states of GQDs, for the first time. We have made a correlation between the PL signature and the Raman modes for the first time. We discussed the significance of different new peaks in addition to the characteristic peaks of

GQDs. It is concluded that the blue PL emissions (~407 and ~442 nm) arise from the edge sites and the green PL bands (~490 and ~529 nm) originate from the oxygenated functional groups of GQDs. To know the effect of solvent on GQDs synthesis, we performed the solvothermal reactions by using oxidized GO as precursor and DMF or DMSO as solvents by keeping the temperature and time unchanged. We also performed the PL measurement on GQDs dispersed in liquid media, such as water, DMSO and tetrahydrofuran. The PL spectrum of GQDs strongly depends on the solvents. This further elucidates the fact that PL of GQDs mainly arises from the surface states. We discussed the evolution of PL of GQDs in terms of interaction between the lone pair electrons of GQDs and dielectric media of the solvents. We have achieved PL quantum yield of 32% from GQDs.

After controlled synthesis and functionalization of GQDs, we explore its photophysical properties in bio-imaging of cancer cells and then study the GQD and its heterostructures for visible light photocatalytic application. Since GQDs emit very bright blue PL emission, we have taken its advantage in bio-imaging application. At first, we measured the cancer cell lines viability in presence of different concentration of GQDs in order to find out the bio-compatibility of GQDs on cancer cell lines, such as A-375 and HeLa cells. The GQDs showed very good bio-compatibility over the cell lines. To prove that the GQDs indeed show the bright blue PL emission inside the cancer cell, we recorded the confocal image of normal cell line HEK-293 using GQDs as fluorescent markers. Note that we did not find any PL contrast in the confocal imaging of normal cell lines. This suggested important role of GQDs in the bio-imaging application.

Next, we explore the visible light photocatlysis application of GQDs and its hybrid nanostructures. As a case, we first prepared a ternary hybrid of plasmonic Au NPs functionalized GQD and graphitic carbon nitride (GCN) for degradation of MB. An *in-situ* chemical synthesis is adapted to prepare the hybrid nanostructure of Au NPs decorated GQD and GCN (Au@GQD-GCN). We have utilized various experimental tools to study the properties of pristine as well as the hybrid samples. We noticed a strong enhancement of Raman G band intensity of GQDs after decoration of the Au NPs. The SPR absorption of the Au NPs on the hybrid of GQD-GCN gives the high efficiency of MB degradation as compared to the other catalysts. The mechanism of interfacial charge transfer and role of SPR on the enhanced PC degradation of MB is discussed. Further, the

fluorescence based technique is utilized to study and prove the existence of free radical generation and their involvement and pathways for MB degradation is presented. In another case study, we have fabricated the heterojunction of GQDs and TiO_2 NPs using a low cost synthesis technique. We have performed a series of experiments to propose a formation mechanism of GQD-TiO_2 heterojunction. We elucidated the formation mechanism of GQD-TiO_2 heterojunction in terms of ultra-sonication induced oxygen vacancy defects in TiO_2 and in-plane epoxy functional groups in GQDs as active channels for the hybrid formation. The formation mechanism of TiO_2-GQD hybrid is explained through the formation of C-O-Ti bonds, for the first time. The hybrid of GQD-TiO_2 possesses the extended visible light absorption, which is beneficial for the visible light photocatalysis applications. These results are corroborated with density functional theory (DFT) calculations using the *Material studio* software. The strong interaction between the GQD-TiO_2 and existence of C-O-Ti bonds were proved from the Raman, XPS and FTIR studies. The preparation of GQD-TiO_2 hybrid by mixing and ultrasonication of GQD-TiO_2 and their distinct interaction were analyzed from the TGA analysis. The GQD-TiO_2 hybrid exhibited high degradation efficiency of MB as compared to the bare counterparts. The free radical generation and mechanism of MB degradation is discussed.

1.9. Organization of the Thesis

The complete thesis work is presented in seven chapters. The present chapter has provided motivation and focus of the work including the introduction, synthesis and properties of GQDs and its heterostrucutres, and their important applications in different fields of nanoscience and nanotechnology. The **Chapter 2** provides an account of the experimental techniques used for synthesis, characterization & applications of GQDs and its heterostucutres. **Chapter 3** is devoted to the controlled synthesis and exploring the formation mechanism of GQDs. It also deals with the edge state conversion and origin of various PL bands from GQD thin films. Next, the solvent assisted synthesis of GQDs, PL evolution of GQDs in liquid media and bio-imaging application of GQDs are discussed in **Chapter 4.** In **Chapter 5,** we present the in-situ chemically prepared ternary hybrid of GQDs-Au NPs-GCN and its use in visible light photocatalytic application. A possible path way for the formation of heterojunction of GQD-TiO_2 NPs and their influence on the visible light photocatalytic activity is presented in **Chapter 6** through experimental and

simulation results. The last chapter, **Chapter 7,** summarises the important findings and noteworthy results of the present thesis and recommendations for the future work.

References

1. S. Iijima, *Nature*, 1991, **354**, 56.
2. Q.-L. Yan, M. Gozin, F.-Q. Zhao, A. Cohen and S.-P. Pang, *Nanoscale*, 2016, **8**, 4799-4851.
3. J. Robertson, *Materials Science and Engineering: R: Reports*, 2002, **37**, 129-281.
4. H. W. Kroto, J. R. Heath, S. C. O'Brien, R. F. Curl and R. E. Smalley, *Nature*, 1985, **318**, 162.
5. A. K. Geim and K. S. Novoselov, *Nature Materials*, 2007, **6**, 183-191.
6. G. W. Lingling Li, Guohai Yang, Juan Peng, Jianwei Zhao and Jun-Jie Zhu, *Nanoscale*, 2013, **5**, 4015-4039.
7. L. A. Ponomarenko, F. Schedin, M. I. Katsnelson, R. Yang, E. W. Hill, K. S. Novoselov and A. K. Geim, *Science*, 2008, **320**, 356-358.
8. L. R. Radovic, *Journal of the American Chemical Society*, 2009, **131**, 17166-17175.
9. Y. Li, Y. Zhao, H. Cheng, Y. Hu, G. Shi, L. Dai and L. Qu, *Journal of the American Chemical Society*, 2012, **134**, 15-18.
10. G. Rajender and P. K. Giri, *Journal of Materials Chemistry C*, 2016, **4**, 10852-10865.
11. M. A. Reed, J. N. Randall, R. J. Aggarwal, R. J. Matyi, T. M. Moore and A. E. Wetsel, *Physical Review Letters*, 1988, **60**, 535-537.
12. G. D. Scholes and G. Rumbles, *Nat Mater*, 2006, **5**, 683-696.
13. L.-s. Li and X. Yan, *The Journal of Physical Chemistry Letters*, 2010, **1**, 2572-2576.
14. Z. Wang, H. Zeng and L. Sun, *Journal of Materials Chemistry C*, 2015, **3**, 1157-1165.
15. A. C. Ferrari and D. M. Basko, *Nat Nano*, 2013, **8**, 235-246.
16. A. Sadezky, H. Muckenhuber, H. Grothe, R. Niessner and U. Pöschl, *Carbon*, 2005, **43**, 1731-1742.
17. T. Jawhari, A. Roid and J. Casado, *Carbon*, 1995, **33**, 1561-1565.

18. E. B. Barros, N. S. Demir, A. G. Souza Filho, J. Mendes Filho, A. Jorio, G. Dresselhaus and M. S. Dresselhaus, *Physical Review B*, 2005, **71**, 165422.
19. D. Dresselhaus M.S, G. Eklund, P.C. Laszlo Nemes, *Academic Press, Inc., New York,* , 1996, **5**, 627-628.
20. A. C. Ferrari and J. Robertson, *Philosophical Transactions of the Royal Society of London. Series A: Mathematical, Physical and Engineering Sciences*, 2004, **362**, 2477-2512.
21. K. N. Kudin, B. Ozbas, H. C. Schniepp, R. K. Prud'homme, I. A. Aksay and R. Car, *Nano Letters*, 2008, **8**, 36-41.
22. L. G. Cançado, M. A. Pimenta, B. R. A. Neves, M. S. S. Dantas and A. Jorio, *Physical Review Letters*, 2004, **93**, 247401.
23. C. Casiraghi, A. Hartschuh, H. Qian, S. Piscanec, C. Georgi, A. Fasoli, K. S. Novoselov, D. M. Basko and A. C. Ferrari, *Nano Letters*, 2009, **9**, 1433-1441.
24. B. Ryan, C. Luiz Gustavo and N. Lukas, *Journal of Physics: Condensed Matter*, 2015, **27**, 083002.
25. M. Lazzeri, C. Attaccalite, L. Wirtz and F. Mauri, *Physical Review B*, 2008, **78**, 081406.
26. F. Tuinstra and J. L. Koenig, *The Journal of Chemical Physics*, 1970, **53**, 1126-1130.
27. A. C. Ferrari and J. Robertson, *Physical Review B*, 2000, **61**, 14095-14107.
28. D. Bischoff, J. Güttinger, S. Dröscher, T. Ihn, K. Ensslin and C. Stampfer, *Journal of Applied Physics*, 2011, **109**, 073710.
29. T. N. Lin, M. R. Inciong, S. R. M. S. Santiago, T. W. Yeh, W. Y. Yang, C. T. Yuan, J. L. Shen, H. C. Kuo and C. H. Chiu, *Scientific Reports*, 2016, **6**, 23260.
30. S. Claramunt, A. Varea, D. López-Díaz, M. M. Velázquez, A. Cornet and A. Cirera, *The Journal of Physical Chemistry C*, 2015, **119**, 10123-10129.
31. M. J. McAllister, J.-L. Li, D. H. Adamson, H. C. Schniepp, A. A. Abdala, J. Liu, M. Herrera-Alonso, D. L. Milius, R. Car, R. K. Prud'homme and I. A. Aksay, *Chemistry of Materials*, 2007, **19**, 4396-4404.
32. G.-D. Lee, C. Z. Wang, E. Yoon, N.-M. Hwang, D.-Y. Kim and K. M. Ho, *Physical Review Letters*, 2005, **95**, 205501.
33. A. J. Stone and D. J. Wales, *Chemical Physics Letters*, 1986, **128**, 501-503.

34. H. C. Schniepp, J.-L. Li, M. J. McAllister, H. Sai, M. Herrera-Alonso, D. H. Adamson, R. K. Prud'homme, R. Car, D. A. Saville and I. A. Aksay, *The Journal of Physical Chemistry B*, 2006, **110**, 8535-8539.

35. D. Pan, J. Zhang, Z. Li and M. Wu, *Advanced Materials*, 2010, **22**, 734-738.

36. D. Pan, L. Guo, J. Zhang, C. Xi, Q. Xue, H. Huang, J. Li, Z. Zhang, W. Yu, Z. Chen, Z. Li and M. Wu, *Journal of Materials Chemistry*, 2012, **22**, 3314-3318.

37. J. Shen, Y. Zhu, C. Chen, X. Yang and C. Li, *Chemical Communications*, 2011, **47**, 2580-2582.

38. J. Shen, Y. Zhu, X. Yang, J. Zong, J. Zhang and C. Li, *New Journal of Chemistry*, 2012, **36**, 97-101.

39. S. N. Baker and G. A. Baker, *Angewandte Chemie International Edition*, 2010, **49**, 6726-6744.

40. L. Tian, D. Ghosh, W. Chen, S. Pradhan, X. Chang and S. Chen, *Chemistry of Materials*, 2009, **21**, 2803-2809.

41. J. Peng, W. Gao, B. K. Gupta, Z. Liu, R. Romero-Aburto, L. Ge, L. Song, L. B. Alemany, X. Zhan, G. Gao, S. A. Vithayathil, B. A. Kaipparettu, A. A. Marti, T. Hayashi, J.-J. Zhu and P. M. Ajayan, *Nano Letters*, 2012, **12**, 844-849.

42. R. Q. Ye, C. S. Xiang, J. Lin, Z. W. Peng, K. W. Huang, Z. Yan, N. P. Cook, E. L. G. Samuel, C. C. Hwang, G. D. Ruan, G. Ceriotti, A. R. O. Raji, A. A. Marti and J. M. Tour, *Nature Communications*, 2013, **4**, 1-6.

43. L. Minati, S. Torrengo, D. Maniglio, C. Migliaresi and G. Speranza, *Materials Chemistry and Physics*, 2012, **137**, 12-16.

44. D. B. Shinde and V. K. Pillai, *Chemistry – A European Journal*, 2012, **18**, 12522-12528.

45. L. Lin and S. Zhang, *Chemical Communications*, 2012, **48**, 10177-10179.

46. M. Zhang, L. Bai, W. Shang, W. Xie, H. Ma, Y. Fu, D. Fang, H. Sun, L. Fan, M. Han, C. Liu and S. Yang, *Journal of Materials Chemistry*, 2012, **22**, 7461-7467.

47. Y. Dong, C. Chen, X. Zheng, L. Gao, Z. Cui, H. Yang, C. Guo, Y. Chi and C. M. Li, *Journal of Materials Chemistry*, 2012, **22**, 8764-8766.

48. Y. Sun, S. Wang, C. Li, P. Luo, L. Tao, Y. Wei and G. Shi, *Physical Chemistry Chemical Physics*, 2013, **15**, 9907-9913.

49. S. Zhu, J. Zhang, C. Qiao, S. Tang, Y. Li, W. Yuan, B. Li, L. Tian, F. Liu, R. Hu, H. Gao, H. Wei, H. Zhang, H. Sun and B. Yang, *Chemical Communications*, 2011, **47**, 6858-6860.
50. S. Zhu, J. Zhang, X. Liu, B. Li, X. Wang, S. Tang, Q. Meng, Y. Li, C. Shi, R. Hu and B. Yang, *RSC Advances*, 2012, **2**, 2717-2720.
51. V. Štengl, S. Bakardjieva, J. Henych, K. Lang and M. Kormunda, *Carbon*, 2013, **63**, 537-546.
52. L. Tang, R. Ji, X. Cao, J. Lin, H. Jiang, X. Li, K. S. Teng, C. M. Luk, S. Zeng, J. Hao and S. P. Lau, *ACS Nano*, 2012, **6**, 5102-5110.
53. Y. Dong, J. Shao, C. Chen, H. Li, R. Wang, Y. Chi, X. Lin and G. Chen, *Carbon*, 2012, **50**, 4738-4743.
54. R. Liu, D. Wu, X. Feng and K. Müllen, *Journal of the American Chemical Society*, 2011, **133**, 15221-15223.
55. J. Lu, P. S. E. Yeo, C. K. Gan, P. Wu and K. P. Loh, *Nature Nanotechnology*, 2011, **6**, 247.
56. Z. Huang, Y. Shen, Y. Li, W. Zheng, Y. Xue, C. Qin, B. Zhang, J. Hao and W. Feng, *Nanoscale*, 2014, **6**, 13043-13052.
57. X. Wu, F. Tian, W. Wang, J. Chen, M. Wu and J. X. Zhao, *Journal of materials chemistry. C, Materials for optical and electronic devices*, 2013, **1**, 4676-4684.
58. J. Lee, K. Kim, W. I. Park, B.-H. Kim, J. H. Park, T.-H. Kim, S. Bong, C.-H. Kim, G. Chae, M. Jun, Y. Hwang, Y. S. Jung and S. Jeon, *Nano Letters*, 2012, **12**, 6078-6083.
59. X. Ding, *Journal of Materials Chemistry C*, 2014, **2**, 3717-3722.
60. Q. Zhang, J. Jie, S. Diao, Z. Shao, Q. Zhang, L. Wang, W. Deng, W. Hu, H. Xia, X. Yuan and S.-T. Lee, *ACS Nano*, 2015, **9**, 1561-1570.
61. H. Sun, L. Wu, N. Gao, J. Ren and X. Qu, *ACS Applied Materials & Interfaces*, 2013, **5**, 1174-1179.
62. D. I. Son, B. W. Kwon, J. D. Yang, D. H. Park, W. S. Seo, H. Lee, Y. Yi, C. L. Lee and W. K. Choi, *Nano Research*, 2012, **5**, 747-761.
63. J. Wang, X. Xin and Z. Lin, *Nanoscale*, 2011, **3**, 3040-3048.
64. D. Chao, C. Zhu, X. Xia, J. Liu, X. Zhang, J. Wang, P. Liang, J. Lin, H. Zhang, Z. X. Shen and H. J. Fan, *Nano Letters*, 2015, **15**, 565-573.

65. W. Liu, X. Yan, J. Chen, Y. Feng and Q. Xue, *Nanoscale*, 2013, **5**, 6053-6062.
66. T. Majumder and S. P. Mondal, *Journal of Electroanalytical Chemistry*, 2016, **769**, 48-52.
67. H. Yue, Z. Yang, L. Gewu, C. Nan, Z. Zhipan, L. Hui, S. Huibo and Q. Liangti, *Nanotechnology*, 2013, **24**, 195401.
68. Z. Ma, R. Sa, Q. Li and K. Wu, *Physical Chemistry Chemical Physics*, 2016, **18**, 1050-1058.
69. J.-P. Zou, L.-C. Wang, J. Luo, Y.-C. Nie, Q.-J. Xing, X.-B. Luo, H.-M. Du, S.-L. Luo and S. L. Suib, *Applied Catalysis B: Environmental*, 2016, **193**, 103-109.
70. Q. Chen, Y. Hu, C. Hu, H. Cheng, Z. Zhang, H. Shao and L. Qu, *Physical Chemistry Chemical Physics*, 2014, **16**, 19307-19313.
71. Z. Xuming, C. Yu Lim, L. Ru-Shi and T. Din Ping, *Reports on Progress in Physics*, 2013, **76**, 046401.
72. S. V. Boriskina, H. Ghasemi and G. Chen, *Materials Today*, 2013, **16**, 375-386.
73. X. Ran, H. Sun, F. Pu, J. Ren and X. Qu, *Chemical Communications*, 2013, **49**, 1079-1081.
74. B. Park, S. J. Kim, J. S. Sohn, M. S. Nam, S. Kang and S. C. Jun, *Nano Research*, 2016, **9**, 1866-1875.
75. S. Chen, X. Hai, X.-W. Chen and J.-H. Wang, *Analytical Chemistry*, 2014, **86**, 6689-6694.
76. R. K. Biroju, B. Choudhury and P. K. Giri, *Catalysis Science & Technology*, 2016, **6**, 7101-7112.
77. Y. Zhang, C. Wu, X. Zhou, X. Wu, Y. Yang, H. Wu, S. Guo and J. Zhang, *Nanoscale*, 2013, **5**, 1816-1819.
78. M. Xing, F. Shen, B. Qiu and J. Zhang, *Scientific Reports*, 2014, **4**, 6341.
79. S. Umrao, S. Abraham, F. Theil, S. Pandey, V. Ciobota, P. K. Shukla, C. J. Rupp, S. Chakraborty, R. Ahuja, J. Popp, B. Dietzek and A. Srivastava, *RSC Advances*, 2014, **4**, 59890-59901.
80. K. J. Williams, C. A. Nelson, X. Yan, L.-S. Li and X. Zhu, *ACS Nano*, 2013, **7**, 1388-1394.
81. B. K. Gupta, G. Kedawat, Y. Agrawal, P. Kumar, J. Dwivedi and S. K. Dhawan, *RSC Advances*, 2015, **5**, 10623-10631.

82. A. Qu, H. Xie, X. Xu, Y. Zhang, S. Wen and Y. Cui, *Applied Surface Science*, 2016, **375**, 230-241.

83. P. Sudhagar, I. Herraiz-Cardona, H. Park, T. Song, S. H. Noh, S. Gimenez, I. M. Sero, F. Fabregat-Santiago, J. Bisquert, C. Terashima, U. Paik, Y. S. Kang, A. Fujishima and T. H. Han, *Electrochimica Acta*, 2016, **187**, 249-255.

84. G. R. Bhimanapati, Z. Lin, V. Meunier, Y. Jung, J. Cha, S. Das, D. Xiao, Y. Son, M. S. Strano, V. R. Cooper, L. Liang, S. G. Louie, E. Ringe, W. Zhou, S. S. Kim, R. R. Naik, B. G. Sumpter, H. Terrones, F. Xia, Y. Wang, J. Zhu, D. Akinwande, N. Alem, J. A. Schuller, R. E. Schaak, M. Terrones and J. A. Robinson, *ACS Nano*, 2015, **9**, 11509-11539.

85. A. K. Geim and I. V. Grigorieva, *Nature*, 2013, **499**, 419.

86. X. W. Wang, G. Z. Sun, N. Li and P. Chen, *Chemical Society Reviews*, 2016, **45**, 2239-2262.

87. H. Sun, N. Gao, L. Wu, J. Ren, W. Wei and X. Qu, *Chemistry – A European Journal*, 2013, **19**, 13362-13368.

88. B. Wang, S. Zhuo, L. Chen and Y. Zhang, *Spectrochimica Acta Part A: Molecular and Biomolecular Spectroscopy*, 2014, **131**, 384-387.

89. H. Huang, L. Liao, X. Xu, M. Zou, F. Liu and N. Li, *Talanta*, 2013, **117**, 152-157.

90. T. V. Tam, N. B. Trung, H. R. Kim, J. S. Chung and W. M. Choi, *Sensors and Actuators B: Chemical*, 2014, **202**, 568-573.

91. A. Ananthanarayanan, X. Wang, P. Routh, B. Sana, S. Lim, D.-H. Kim, K.-H. Lim, J. Li and P. Chen, *Advanced Functional Materials*, 2014, **24**, 3021-3026.

92. L.-L. Li, J. Ji, R. Fei, C.-Z. Wang, Q. Lu, J.-R. Zhang, L.-P. Jiang and J.-J. Zhu, *Advanced Functional Materials*, 2012, **22**, 2971-2979.

93. L. Fan, Y. Hu, X. Wang, L. Zhang, F. Li, D. Han, Z. Li, Q. Zhang, Z. Wang and L. Niu, *Talanta*, 2012, **101**, 192-197.

94. F. Yang, M. Zhao, B. Zheng, D. Xiao, L. Wu and Y. Guo, *Journal of Materials Chemistry*, 2012, **22**, 25471-25479.

95. S. Benítez-Martínez and M. Valcárcel, *Sensors and Actuators B: Chemical*, 2014, **197**, 350-357.

96. L. Li, G. Wu, T. Hong, Z. Yin, D. Sun, E. S. Abdel-Halim and J.-J. Zhu, *ACS Applied Materials & Interfaces*, 2014, **6**, 2858-2864.

97. H. Liu, W. Na, Z. Liu, X. Chen and X. Su, *Biosensors and Bioelectronics*, 2017, **92**, 229-233.

98. Y.-H. Li, L. Zhang, J. Huang, R.-P. Liang and J.-D. Qiu, *Chemical Communications*, 2013, **49**, 5180-5182.

99. X. Li, S. Zhu, B. Xu, K. Ma, J. Zhang, B. Yang and W. Tian, *Nanoscale*, 2013, **5**, 7776-7779.

100. X. Gao, L. Yang, J. A. Petros, F. F. Marshall, J. W. Simons and S. Nie, *Current Opinion in Biotechnology*, 2005, **16**, 63-72.

101. R. Hardman, *Environmental Health Perspectives*, 2006, **114**, 165-172.

102. X. Yan, X. Cui, B. Li and L.-s. Li, *Nano Letters*, 2010, **10**, 1869-1873.

103. V. Gupta, N. Chaudhary, R. Srivastava, G. D. Sharma, R. Bhardwaj and S. Chand, *Journal of the American Chemical Society*, 2011, **133**, 9960-9963.

104. H. B. Yang, Y. Q. Dong, X. Wang, S. Y. Khoo and B. Liu, *ACS Applied Materials & Interfaces*, 2014, **6**, 1092-1099.

105. M. Li, W. Ni, B. Kan, X. Wan, L. Zhang, Q. Zhang, G. Long, Y. Zuo and Y. Chen, *Physical Chemistry Chemical Physics*, 2013, **15**, 18973-18978.

106. P. Gao, K. Ding, Y. Wang, K. Ruan, S. Diao, Q. Zhang, B. Sun and J. Jie, *The Journal of Physical Chemistry C*, 2014, **118**, 5164-5171.

107. M.-L. Tsai, W.-C. Tu, L. Tang, T.-C. Wei, W.-R. Wei, S. P. Lau, L.-J. Chen and J.-H. He, *Nano Letters*, 2016, **16**, 309-313.

108. Z. Zhang, J. Zhang, N. Chen and L. Qu, *Energy & Environmental Science*, 2012, **5**, 8869-8890.

109. M. Kaempgen, C. K. Chan, J. Ma, Y. Cui and G. Gruner, *Nano Letters*, 2009, **9**, 1872-1876.

110. C. B. Arnold, R. C. Wartena, K. E. Swider-Lyons and A. Pique, *Journal of The Electrochemical Society*, 2003, **150**, A571-A575.

111. I. Nam, G.-P. Kim, S. Park, J. Park, N. D. Kim and J. Yi, *Nanoscale*, 2012, **4**, 7350-7353.

112. W. Sun and X. Chen, *Microelectronic Engineering*, 2009, **86**, 1307-1310.

113. W.-W. Liu, Y.-Q. Feng, X.-B. Yan, J.-T. Chen and Q.-J. Xue, *Advanced Functional Materials*, 2013, **23**, 4111-4122.

114. S. Mondal, U. Rana and S. Malik, *Chemical Communications*, 2015, **51**, 12365-12368.

115. D. Özer, G. Dursun and A. Özer, *Journal of Hazardous Materials*, 2007, **144**, 171-179.

116. R. S. Blackburn, *Environmental Science & Technology*, 2004, **38**, 4905-4909.

117. A. Fujishima and K. Honda, *Nature*, 1972, **238**, 37-38.

118. T. A. Kandiel, A. Feldhoff, L. Robben, R. Dillert and D. W. Bahnemann, *Chemistry of Materials*, 2010, **22**, 2050-2060.

119. H. Dong, G. Zeng, L. Tang, C. Fan, C. Zhang, X. He and Y. He, *Water Research*, 2015, **79**, 128-146.

120. J. Xue, S. Ma, Y. Zhou and Q. Wang, *RSC Advances*, 2015, **5**, 88249-88257.

121. N. Cheng, J. Tian, Q. Liu, C. Ge, A. H. Qusti, A. M. Asiri, A. O. Al-Youbi and X. Sun, *ACS Applied Materials & Interfaces*, 2013, **5**, 6815-6819.

122. D. Y. Pan, J. K. Jiao, Z. Li, Y. T. Guo, C. Q. Feng, Y. Liu, L. Wang and M. H. Wu, *ACS Sustainable Chemistry & Engineering*, 2015, **3**, 2405-2413.

Chapter 2

Experimental Techniques

The present chapter describe the methodologies for synthesis of samples, characterization techniques and data analysis. The instrumental techniques involved in the controlled growth and processing of grapehene quantum dots (GQDs) and its heterostructures are discussed first. Next, various microscopic and spectroscopic tools adapted for understanding the morphological and structural evolution of GQDs and GQDs based heterostructures are discussed and a brief account on the line shape analysis of the spectroscopic data in understanding the defects evolution of GQDs is presented. The details on visible light photocatalysis and bio-imaging applications of GQDs and its heterostructures are presented at the end.

2.1. Synthesis Techniques of GQDs and Its Heterostructures

In the present work, hydrothermal/solvothermal reactions were performed for the synthesis and functionalization of the graphene quantum dots (GQDs). Different solvents, and reaction durations were used for the GQDs synthesis. Planetary ball milling is used for the preparation of TiO_2 nanoparticles (NPs) from TiO_2 powders. For the heterostructures of GQDs, an *in-situ* chemical reaction and ultrasonic process are employed.

2.1.1. High Pressure Reactor for the Hydrothermal/Solvothermal Reactions

For the GQD synthesis, the commonly used techniques are classified as top down and bottom up methods. The top down method generally involves the cutting of bulk graphene sheets into pieces. In bottom up method, the organic precursor (small molecules) materials are used for growing the GQDs. In the present thesis work, the top down approach is adapted for the syntheses of GQDs. Hydrothermal/solvothermal reactions are performed on different precursor materials to understand the mechanism of GQD formation. The hydrothermal/sovothermal reactions are performed in a high pressure reactor. For solvothermal reactions, dimethylformamide (DMF) and dimethyl sulfoxide (DMSO) solvents are used. The reactions are performed at constant temperature and for different reaction durations. A photograph of our laboratory reactor (Autoclave) (Bergof-100, Germany) is shown in **Fig. 2.1.** The autoclave consists of mainly four major

components, such as reaction vessel, a lid having parts for controlling the reactions, hot plate and a rectangular box. Inside the stainless steel vessel a Teflon vial is mounted. The desired reaction solution is placed inside the Teflon vial. The use of Teflon vial prevents the contamination of the sample during the synthesis. A Teflon O-ring is placed on the top of vessel to prevent the leakage between lid and the vessel. The reaction vessel and the lid are fixed with a stainless steel clamp. The lid has the facilities to immerse the thermal sensor (convenient for measuring the reaction temperature), to monitor the pressure and to purge some gases during/after the reactions. The thermal sensor is immersed in a tube and other end is connected through a cable to the PID controller to measure the exact temperature of the reaction. The reaction pressure is measured with the help of a manometer and other additional features of the lid are shown in **Fig. 2.1.** The third component is the hot plate, which provides the heating to the system. Further, the last one is the rectangular box. This helps to prevent from the heat loss with the surroundings. There are two knobs, in the base unit, one is used to setting the desired temperature and other for controlling the stirring of the solution.

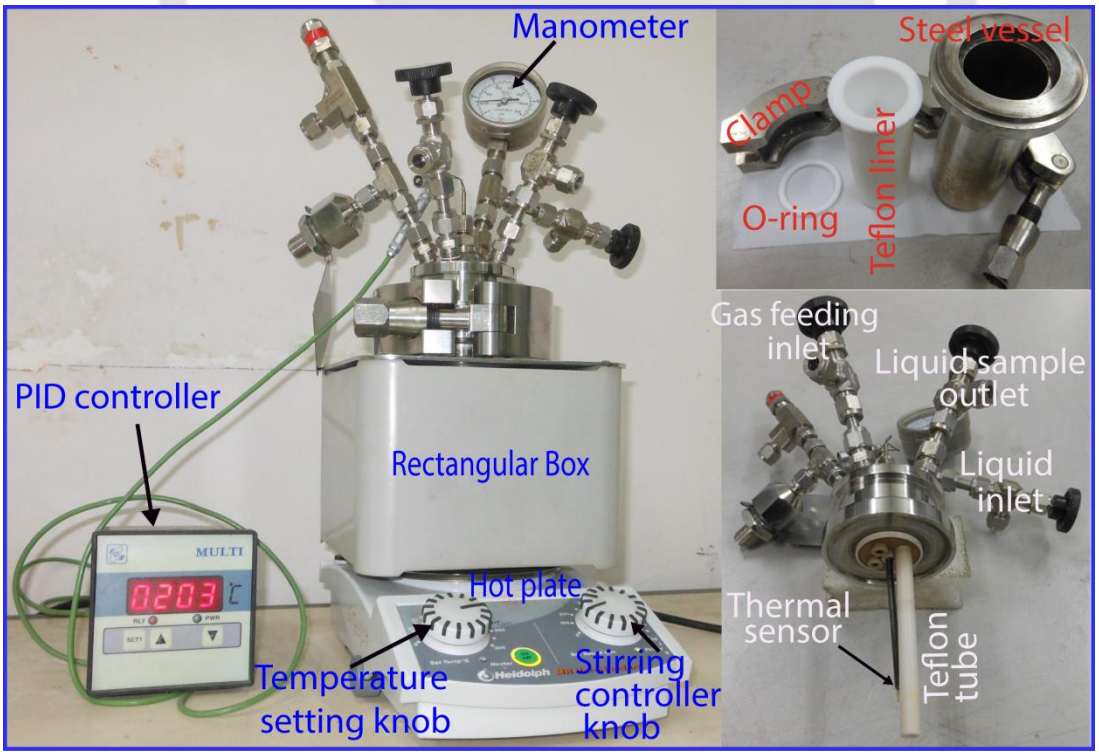

Figure 2.1: Photograph of high pressure reactor (autoclave) (Berghof, BR-100; Germany) with its components

2.1.2. High Temperature Furnace

A high temperature split-type furnace (Indfurr, India) is used for the preparation of graphitic carbon nitride (GCN) sample. The furnace consists of SiC heating elements and a cylindrical alumina tube. It can reach a max temperature up to 1200 °C and a programmable PID controller is used for setting and monitoring the parameters, such as heating rate, time and temperature. The photograph of our laboratory furnace is shown in **Fig. 2.2**. For the GCN preparation, urea was taken in silica crucible and covered with a lid. This was kept in the centre of the furnace and heated to 550 °C for 3h with the heating rate of 5 °C/min. After natural cooling of the furnance, the GCN was collected from the silica crucible.

Figure 2.2: Photograph of high temperature furnace (Indfurr, India) and temperature controller unit.

2.1.3. Planetary Ball Milling

Planetary ball milling method is used to prepare the TiO_2 NPs from TiO_2 powder as a precursor. The photograph of the ball milling instrument is shown **Fig. 2.3**. The ball milling unit (PM 100, Retsch,) consists of a control panel and a planetary platform (grinding station). In the control panel setting, we can monitor the rotation speed, time duration and halt time of the machine for longer period of run. The grinding station is having a scale bar and a vial, which is made of ceramic material zirconia (ZrO_2). We also used ZrO_2 balls for the grinding purpose. A photograph of the ZrO_2 balls is shown in the

inset of **Fig. 2.3.** This ensures that the ball milling is contamination free in the preparation of TiO_2 NPs. For TiO_2 NPs preparation, first the TiO_2 powder is ground in a ceramic mortar for 10 minutes. Then the ground powder is put inside the ZrO_2 vial (powder: ball = 1:10) and set at 350 rpm for 16 h [1]. We varied the milling time duration to tune the size of the TiO_2 NPs [1].

Figure 2.3: .Photographs of the planetary ball-mill machine (Retsch, PM 100), grinding station and zirconia balls.

2.1.4. Spin Coater

Spin coating is a process of coatings a flat surface by a thin liquid film. This process is widely used in industry for depositing uniform films on substrates. A spin coater (APEX, spin NXG) is used for the deposition of GQD thin films on transparent and opaque substrates. A photograph of our laboratory spin coater is shown in **Fig. 2.4(a).** Before fabricating the films, the substrates were cleaned following a proper protocol and GQDs are dispersed in water and sonicated for a few minutes for achieving the uniform solution. The GQDs solution is drop casted on the fixed substrate using a micro-pipette. The average speed of the rotor is maintained at ~3000 rpm. The GQD dispersion spreads outwards to the edge of the substrate and forms a thin film of a relatively uniform thickness. The thickness and uniformity of the films can be tuned by the concentration of

the liquid, spinning speed and time. We fabricated all the GQD thin films under ambient condition.

2.1.5. Ultra-Sonicator

Ultrasonic process is a low cost technique for the preparation of nanomaterials. When the ultrasonic waves (frequency >20 kHz) are generated in a liquid medium, a huge number of micro bubbles form, grow and collapse in very short times [2, 3]. These micro bubbles or so-called hot spots have enough energy to disturb the sample surfaces [2, 3]. In the present thesis work, the ultrasonicator (Jeiotech, UC-10) is of 300 W power and operates at 40 kHz frequency. The photograph of our lab ultrasonicator is shown in **Fig. 2.4(b)**. TiO_2 and GQD heterojunction is prepared via ultrasonication process and the results are discussed in **Chapter 5.**

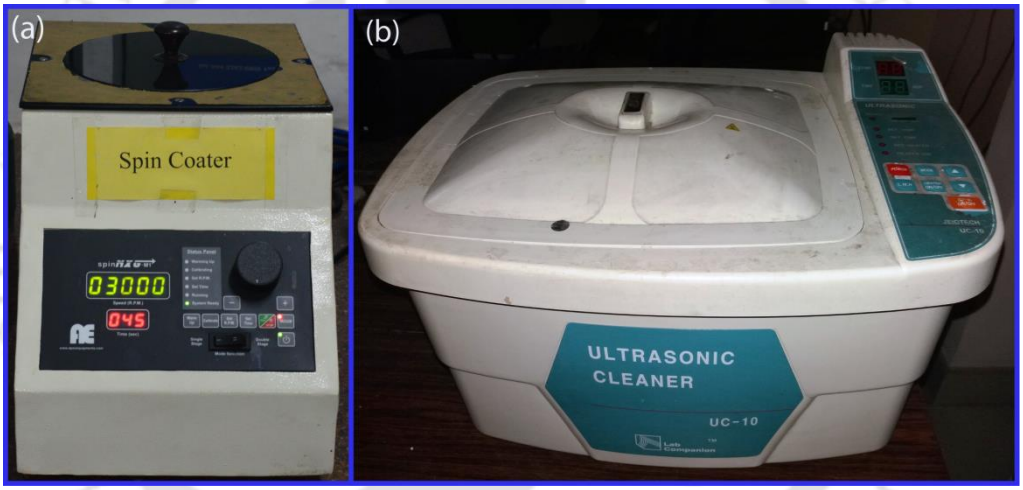

Figure 2.4: Photographs of (a) spin coater (APEX, spin NXG) and (b) ultrasonicator (Jeiotech, UC-10).

2.2. Characterization Techniques

Several characterization tools are used to study the nature of samples and their characteristic properties. Morphological, compositional and lattice defects are analysed with electron microscopes, such as field emission scanning electron microscopy (FESEM) and high resolution transmission electron microscopy (HRTEM). X-ray diffraction study is utilized to study the phase, crystallinity and composition of the samples. For structural defects and optical property studies, characterization techniques such as micro-Raman, Fourier transform infrared (FTIR) spectroscopy, x-ray photoelectron spectroscopy (XPS), electron paramagnetic resonance (EPR), optical absorption, steady state photoluminescence (PL) and time resolved PL are used. In the

following sections, we provide a brief account of these instruments, including sample preparation and data analysis.

2.2.1. Microscopy Techniques

2.2.1.1. Field Emission Scanning Electron Microscopy (FESEM)

FESEM is an electron microscopy technique used for imaging of the materials with a resolution micro-nano meter range. The use of electrons in microscope has two main advantages as compared to the conventional microscopy (optical). Much larger magnifications are possible here, since electron wavelengths are much smaller than photon wavelengths and the depth of field is much higher. The electron wavelength depends on the electron velocity or the accelerating voltage expressed as,

$$\lambda = \frac{h}{mv} = \frac{h}{\sqrt{2qmV}} = \frac{1.22}{\sqrt{V}} \text{ nm} \quad \ldots\ldots\ldots\ldots\ldots\ldots \quad (2.1)$$

In the FESEM, electrons are emitted from a field emission source under extreme vacuum. The vacuum allows the electrons movement along a column without scattering, which helps to prevent discharges inside the instrument. The field emission source is a tungsten filament (cathode) with sharp tip, which is placed in a huge electrical potential gradient. The significance of extremely thin and sharp tip (diameter 10-100 nm) is that an electric field can be concentrated to an extreme level so that the work function of the material is lowered and electrons can leave from the cathode. After emission, the electrons are accelerated by the two anodes. An accelerating voltage (0.5-30 kV) between the cathode and anode is commonly used. This voltage combined with the beam diameter determines the resolution of the image. As the voltage increases, better point-to-point resolution can be achieved. Because of the smaller beam size of the electron source, the beam produced by this emitter is about 1000 times smaller in diameter than that in a standard SEM, which markedly improves the image resolution. The beam is collimated by electromagnetic condenser lenses, focused by an objective lens, and scanned across the surface of the sample by electromagnetic deflection coils. The primary imaging method is by collecting emitted secondary electrons that are released by the sample. A secondary electron detector is placed near to the specimen. By correlating the sample scan position with the resulting signal, an image is formed on the screen that is strikingly similar to what would be seen through an optical microscope. The FESEM is equipped with a

special objective or focusing lens that projects the magnetic field below the lens. Very high resolution is obtained by shortening the specimen–lens distance and using a specially designed in-lens. The distance is shortened by placing the specimen in the lens magnetic field. In this case, secondary electron detector is placed above the objective in-lens (called as in-lens detector), which makes difference in the image compared to the conventional image of the secondary electron detector. Very high resolution and contrast can be obtained by using in-lens detector. Interaction of the primary electron beam with atoms in the material results in the shell transitions. This process leads to the emission of X-ray. The emitted X-ray has an energy characteristic of the parent element. Detection and measurement of the energy permits elemental analysis by means of Energy Dispersive X-ray Spectroscopy (EDS). EDS provides rapid qualitative, or with adequate standards, elemental composition with a sampling depth of 1-2 microns. FESEM (Sigma Zeiss, Germany) is used in the present study. The resolution of the FESEM instruments is 1nm. FESEM characterization of Au NPs decorated GQD-GCN sample was done for imaging as well as the compositional analysis.

2.2.1.2. High Resolution Transmission Electron Microscopy (HRTEM)

TEM is one of the advanced imaging techniques for nanoscale materials characterization. HRTEM is well known for studying the structural information, lattice imaging (defects or dislocations) and the morphology of the nanostructured samples. In case of a crystalline material, electron diffraction will occur only at specific angles, which are the characteristic features for the crystal structures present. In the present thesis, TEM and HRTEM are extensively used to study the morphology and crystallinity of GQD and GQDs based heterostructures. TEM works on the principle of optical projection; when an object is placed in front of a light source, its image is enlarged and a shadow is created on the screen placed far distance behind this object. Electrons emitted from an electron gun are accelerated to high voltages (typically 100 to 400 kV) and focused on the sample by a number of condenser lenses. Lanthanum hexaboride (LaB_6) crystal is used for generation of thermionic electron emission. The emitted electrons pass through a series of lenses to be focused and scanned across the sample. The static beam has a diameter of a few microns. The sample must be sufficiently thin (a few tens to a few hundred nm) to be transparent to electrons. The transmitted and forward scattered electrons form a diffraction pattern in the back focal plane and a magnified image in the image plane. With

additional lenses, either the image or the diffraction pattern is projected onto a fluorescent screen for viewing or photographic recording.

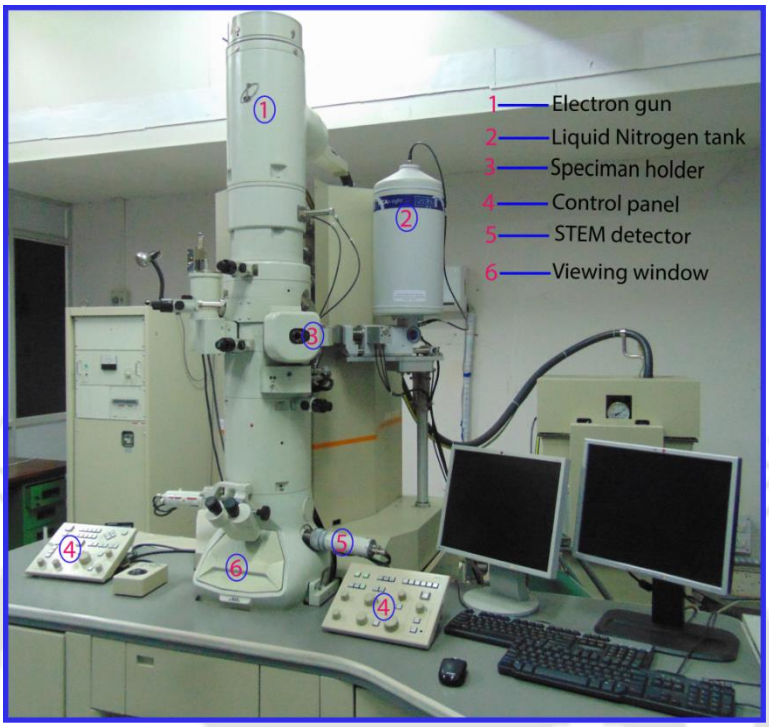

Figure 2.5: photograph of the TEM (JEM 2100, JEOL, Japan) used for the present study. Some of the components are marked in image.

In our present study, a TEM (JEM2100, JEOL, Japan) operating at 200 kV with a high resolution CCD camera (Gatan, USA) is used for the TEM and HRTEM imaging. A photograph of the TEM instrument is shown in **Fig. 2.5**. Some components of the TEM instrument are labelled in the figure. For TEM imaging, the powder samples were dispersed in methanol solvent and sonicated for a few minutes. The GQD or GQD heterostructure in solvent sample is drop casted on a copper grid having 400 mesh size (Pacific Grid, USA). After normal drying for a prolonged time, this grid is used for the TEM imaging. Improved resolution of the lattice image is obtained after processing of inverse fast Fourier transformation (IFFT) image using a *'Digital Micrograph'* (Gatan, USA) image analysis software. TEM imaging is a powerful tool for analysing the shape of the nanostructures. In the present thesis, TEM analysis is used for studying the size of GQDs and understanding the formation of GQDs at different stages of reaction using two different precursor materials.

2.2.2. Spectroscopic Techniques

In this section we discuss the different spectroscopy methods and interpretation of spectral data of GQDs and GQDs based heterostructures.

2.2.2.1. Raman Spectroscopy

Raman spectroscopy is an established non-destructive tool for the characterization of semiconductor nanostructures and graphitic materials. It provides valuable information about the crystallinity/disorder, degree of hybridization, defects and the extent of chemical modification in nanostructures. In particular, in case of carbon materials Raman spectra gives direct information about the graphitic nature, nature of edges and the degree of oxidation [4-7]. Raman effect is an inelastic scattering of light from the material. In the Raman spectroscopy measurement, an intense laser beam is incident on the sample through a commercial microscope with spot size about a few microns. The weak back-scattered light or signal is passed through a double monochromator to reject the Raleigh scattered signal and the only the Raman is signal detected by a photodetector or CCD detector. The nature of the Raman spectrum depends on the amount of crystalline and amorphous phases present in the sample. For crystalline or amorphous nature of the sample can be understood by observing the sharpness or broadness of the various vibrational modes of materials, respectively. Besides, the nature of strain can be determined by observing the blue shift or red shift, which indicates compressive strain or tensile strain, respectively.

In the present study, a high resolution micro-Raman (LabRAM HR-800, Jobin Yvon, USA) instrument with a liquid nitrogen cooled CCD detector is used for the characterization of GQDs and GQD based heterostructures. **Fig. 2.6** shows the photograph of micro-Raman set up used to measure the Raman spectrum. Raman measurements are carried out at room temperature using different excitation wavelengths 488, 514 nm (Ar+ laser), 632.8 nm (He-Ne laser) and approximately 1 mW laser power was used to avoid the laser heating effects.

In order to understand the broad Raman spectra of the samples, we deconvluted it into multiple peaks. The Raman spectrum is deconvlouted into Gaussian and Lorentzian peaks using the following expressions. We measured the spectral profile of the Raman bands using a peak fit software.

$$y = y_0 + Aexp\left[-\left(\frac{(x-x_c)^2}{2w^2}\right)\right] \quad \ldots\ldots\ldots\ldots\ldots\ldots \quad (2.2)$$

$$y = y_0 + \frac{2A}{\pi}\left[\left(\frac{w}{4(x-x_c)^2+x^2}\right)\right] \quad \ldots\ldots\ldots\ldots\ldots\ldots \quad (2.3)$$

Equations 2.2, 2.3 represents the Gaussian function and Lorentzian functions, respectively. Here, 'y_0' is the offset constant, 'x_c', 'w' and 'A' are the peak centre, full width at half maximum (FWHM) and area, respectively. In case of GQDs, the Raman D and G bands are well known to the research community. The Raman D band intensity is very sensitive to the edge disorder. In addition to characteristic Raman bands, we have deconvloted Raman spectra of GQDs into other bands, which are assigned to the oxygen functional groups. The details of the Raman peak assignments are discussed in **Chapter 3.**

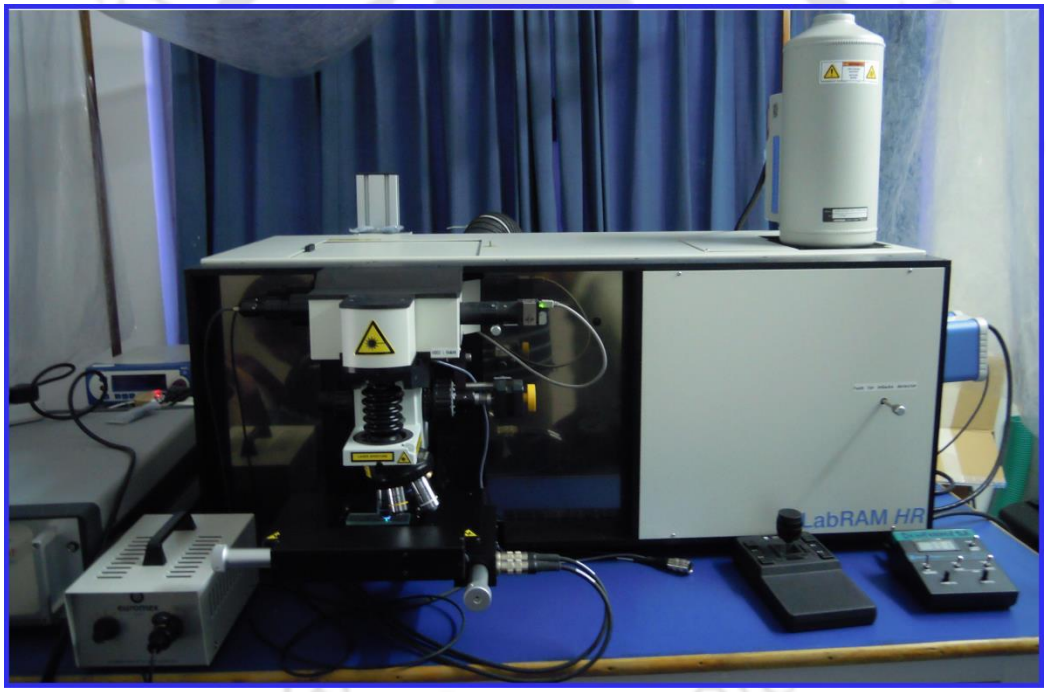

Figure 2.6: Photograph of the micro-Raman spectrometer (LabRAM HR-800, Jobin Yvon, USA).

2.2.2.2. Ultraviolet-Visible Absorption Spectroscopy

The Ultraviolet-Visible (UV-Vis) absorption spectroscopy provides useful information about the interaction of light with a material by measuring the reflection, absorption or transmission properties when light passes through the sample surface. When we excite the sample with light of different wavelengths, the material absorb the light corresponding to the energy of band gap or any state intermediate to the band gap. The absorption band of a material depends on its band gap and gives the information about its characteristics. In

the present study, we have performed the UV-vis absorption measurements to understand the optical absorption of GQDs and its hybrids. **Fig. 2.7** shows the photograph of the UV-Vis spectrometer (Shimadzu, UV3101PC) used in the present study. In phatocatlytic (PC) degradation studies of organic dye, the same instrument is used for measuring the change in absorption intensity of dye in different catalyst samples for different irradiation time.

Figure 2.7: Photograph of the UV-Vis absorption spectrometer (Shimadzu, UV3101PC).

2.2.2.3. Diffuse Reflectance Spectroscopy (DRS)

DRS is a technique generally used to record the reflectance or absorbance spectra of the semiconductor thin film / powders, from which one can estimate the band gap of the material. Understanding the band gap of a material is very important for application point of view. Based on the band gap of the material, one can design its application in UV light sensitive, visible light photocatalysis, and photovoltaic devices etc. The optical reflectance or absorbance is a result of interaction of light with the material. The basic principle is that UV, visible or near infrared (NIR) light is used to excite electrons from the valence band to the empty conduction band. A sharp increase (decrease) in absorption (reflection) at energy close to the band gap that manifests the absorption edge (reflectance threshold) in the UV-visible-NIR absorbance (reflectance) spectra. This technique is mostly applicable to powder samples and thin films. In our study, some of the powder samples, which are not well dispersed in liquid media, are used for the DRS measurements. The light from sample surface is reflected back in two ways, such as specular reflection and diffuse reflection. In specular reflection, the reflection beam makes the same angle with respect to the angle of incident beam on the sample surface with respect to the normal plane. In case of diffused refection, the incident ray is reflected at multiple angles from the sample surface due to the uneven surface. Integrating spheres

are used for samples with a significant diffuse reflectance component such as powders and other 'rough' materials. Samples are placed at the back of the sphere and the light is reflected back off the sample and collected by the sphere. The theory which makes possible to use diffuse reflectance spectra to calculate the absorbance was proposed by Kubelka and Munk [8]. The absorbance can be calculated using Kubelka-Munk (K-M) formula as

$$F(R_\infty) = \frac{(1-R_\infty)^2}{2R} = \frac{k}{s} \qquad \ldots\ldots\ldots\ldots\ldots\ldots \quad (2.3)$$

Where $F(R_\infty)$ is called the K-M function, and $R_\infty = \frac{R_{sample}}{R_{standard}}$. k is K-M absorption coefficient and s is K-M scattering coefficient.

The photograph of Perkin Elmer (LAMBDA 750) spectrophotometer used for the DRS measurements is shown in **Fig. 2.8.** It performs the measurement in the UV/visible/ NIR (i.e., 200 – 2500 nm wavelength range) region. Two light sources deuterium and tungsten halogen are provided to perform the measurements in the UV/Visible/NIR region. An integrating sphere along with PMT (photomultiplier), InGaAs and PbS detectors is used to collect the diffused light reflected from the sample in all direction.

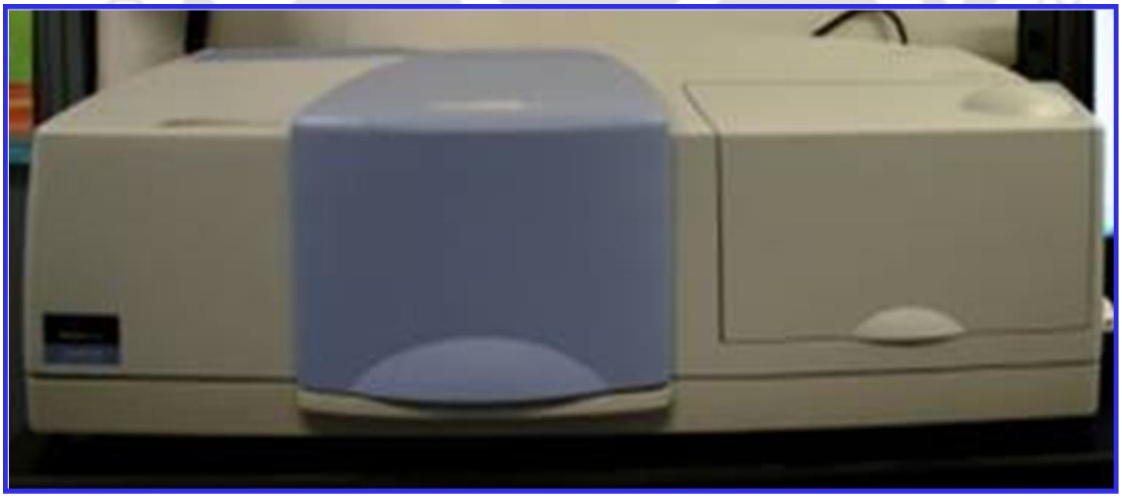

Figure 2.8: Photograph of the diffuse reflectance spectrometer (Perkin Elmer, LAMBDA 750).

2.2.2.4. Photoluminescence (PL) Spectroscopy

PL spectroscopy is a non-destructive method of probing the electronic structure of a material. Some excitation energy is required to excite the electrons from a lower energy level (ground state) to a higher energy level (excited state). However, the electrons are not stable in the higher energy excited states. The electrons come back to the intermediate

state or original state by releasing the energy in terms of photons. This phenomenon is known the PL. The energy of the emitted light relates to the difference in energy levels between the two electronic states involved in the transition between the excited state and the ground state. The quantity of the emitted light is related to the relative contribution of the radiative process between the various excited states and the ground states. The emission spectrum of the sample strongly depends on the band gap energy, impurity level/ defect level.

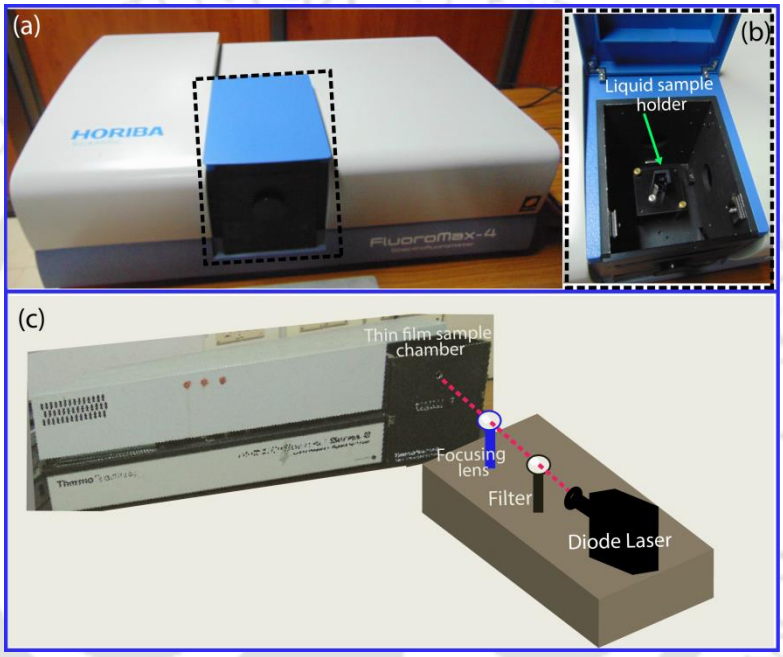

Figure 2.9: Photograph of the (a) PL spectrometer (Fluromax-4, Horiba) and (b) magnified view of sample loading chamber showing the liquid sample holder. (c) Schematic showing the arrangements for thin films sample PL measurement (AB2, Thermo spectronic), using diode laser as an excitation source.

Fig. 2.9(a) shows the photograph of PL spectrometer (Fluromax-4, Horiba) and the region marked with the dotted line shows the sample loading chamber. The magnified portion of dotted line (sample chamber open view) is shown in **2.9(b),** where the liquid sample holder is shown with an arrow. A quartz cuvette (4 mL) is used for all the PL measurements in liquid media. The PL spectra of GQDs thin film samples are obtained with the PL spectrometer (AB2, Thermo spectronic) with 355nm external diode laser source. The GQD thin film PL analysis is presented in **Chapter 3**. A schematic of the PL measurements on GQDs thin films is shown in **Fig. 2.9(c).** In order to achieve better PL response from TiO_2 powder samples, PL measurements are carried out with a 405 nm

external laser as an excitation source and a single grating monochromator (Triax 550) coupled to a cooled CCD detector (Jovin Yvon). The use of CCD detector gives better response than the PMT detector. Further, in the present study to understand the broad PL spectrum of GQDs thin films, the PL spectrum is deconvoluted into multiple Gaussian peaks. The fitted spectral bands give the information about the nature of defect states (edge sites and functional groups) and its evolution in different GQDs samples.

2.2.2.5. Time Resolved Photoluminescence (TRPL) Spectroscopy

TRPL characterization is performed to understand the charge carrier recombination dynamics in GQDs and its heterostructures. The short pulse of light excitation generates the electron-hole pairs (excitons) in the sample and these excitations decay to lower energy levels. The emitted light is composed of a set of wavelengths corresponding to transition energies of the sample. Measurement of the optical spectrum as a function of time provides the transition energies and their lifetimes. The measurement basically counts the number of photons at a fixed wavelength with time. The emitted photon is analysed by a spectrometer and detected by a micro-channel-plate photomultiplier tube (MCP-PMT) detector. A Multi-Channel Analyzer (MCA) board in the computer analyses the output pulse voltages into various channels, which correspond to different times. In this way, the MCA can record each photon arriving at the MCP–PMT at a particular time. The number of output pulses from the MCP–PMT is directly proportional to the number of incident photons. Averaging over millions of photons, the measurement creates a histogram, which shows how long the excitons "live" after being created by the laser pulse. Thus, the carrier dynamics occurring during these processes provides not only information about the position of the peak emission, as in a normal steady state PL experiment, but also the lifetime of the excitons involved in the recombination. The photograph of the TRPL instrument (LifeSpec II, Edinburgh Inst., UK) used in the present study is shown in **Fig. 2.10.** We used adjustable nanosecond pulsed pump lasers 375 and 405 nm to measure the PL decay of the defects related visible emission in GQD and GQDs heterostructures. This instrument has a time resolution of ~50 ps. The TRPL data usually follow an exponential decay behaviour or combination of such function depending upon the number of decay channels present in the sample. The PL decay equation is expressed as

$$I(t) = A_1 e^{-t/\tau_2} + A_2 e^{t/\tau_2} + \ldots\ldots\ldots\ldots + I_0 \quad \ldots\ldots\ldots\ldots\ldots \quad (2.4)$$

Where, I(t) is the PL intensity count and τ_1, τ_2….. are the components of lifetime and A_1, A_2…. are the amplitudes and *t* is the instantaneous time and I_0 corresponds to the background noise. The average life time of the sample is calculated using the following equation.

$$\tau_{avg} = \sum \frac{A_i \tau_i^2}{A_i \tau_i} \quad \ldots\ldots\ldots\ldots\ldots\ldots\ldots \quad (2.5)$$

Figure 2.10: Photograph of the TRPL spectrometer (LifeSpec II, Edinburgh Inst., UK).

2.2.2.6. Fourier Transform Infrared (FTIR) Spectroscopy

FTIR spectroscopy is one of the powerful spectroscopic tools generally used to study the information of structural bonding and chemical functional groups present in the sample. FTIR is based on the phenomena "Michelson interference" combined with Fourier transformation of the source spectrum[9]. FTIR interferogram consists of spectral information of the source along with the transmittance characteristic of the sample. We performed all the FTIR measurements at room temperature and transmittance mode of operation to study the GQDs and GQD based heterostructures as well the characteristic vibrations of GQDs functional groups and other samples. The FTIR measured range is 400-4000 cm^{-1} with resolution of 2 cm^{-1}. A photograph of the FTIR instrument (Perkin Elmer, Spectrum BX) used in the present thesis work is shown in **Fig. 2.11**. All the spectra were taken after background corrections. For the FTIR measurement, very small quantity of the powder sample is mixed with KBr and ground in a ceramic mortar and the pellets of 10 mm diameter was prepared using KBr press and die. Transparent quartz substrates are directly used for FTIR measurements in the transmittance mode.

Figure 2.11: Photograph of the FTIR spectrometer (Perkin Elmer, Spectrum BX).

2.2.2.7. Electron Paramagnetic Resonance (EPR) Spectroscopy

ESR spectroscopy is a very powerful tool for studying the elements with unpaired electrons. When a molecule or compound, which is having an unpaired electron is placed in a strong magnetic field, the spin of the unpaired electron can align in two different ways creating two spin states, $m_s = \pm ½$. The alignment can either be along the direction (parallel) or anti parallel to the applied magnetic field. The two alignments have different energies and this difference in energy lifts the degeneracy of the electron spin states. The energy difference is given by:

$$\Delta E = E_+ - E_- = h\nu = g\mu_B H \quad \text{.....} \quad (2.6)$$

Where, E_+ and E_- are the energies of electron in spin up and spin down state, respectively and h is Plank's constant, ν is the frequency of radiation and μ_B is dipole moment of the electron (Bohr magneton). The values of h and μ_B are equals to the 6.626 x 10^{-34} J s^{-1} and 9.274 × 10-24 JT^{-1}, respectively. H is the applied magnetic field and g is dimensionless constant known as electron g-factor, and its value for a free electron is 2.0023. In an EPR experiment, the field of the spectrometer magnet is swept linearly to excite some of electrons in the lower energy level to the upper energy level while the sample is exposed to fixed microwave irradiation. The free or unpaired electrons have a small magnetic field and orient themselves parallel to the larger field produced by the spectrometer's magnet. At a particular magnetic field strength, the microwave irradiation will cause some of the free electrons to "flip" and orient against the external magnetic

field. This separation between the lower and the higher energy level is exactly matched with the energy corresponding to the applied microwave frequency. The condition where the magnetic field and the microwave frequency are "just right" to produce an EPR resonance (or absorption), known as the resonance condition, is detected by the spectrometer.

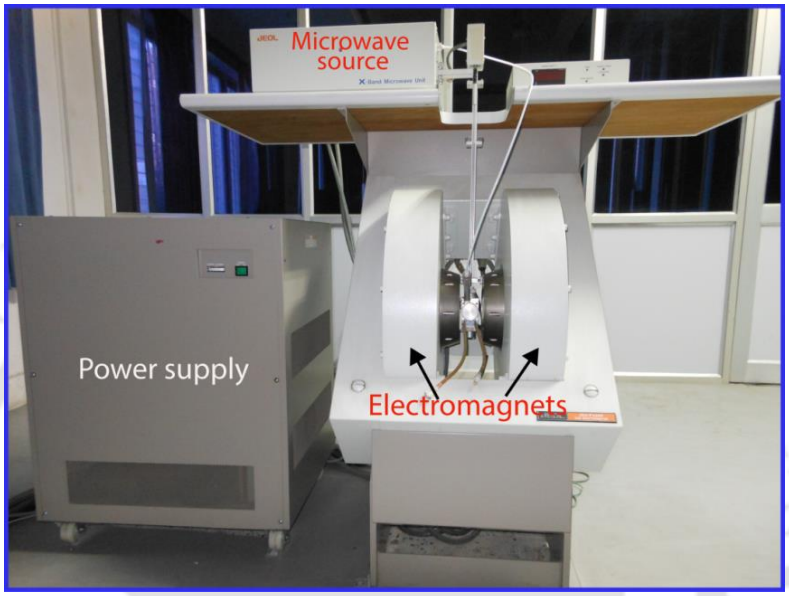

Figure 2.12: Photograph of the Electron Spin Resonance spectrometer (JEOL, JES-FA200).

EPR spectrometers working at frequencies ranging from several hundred MHz to several hundred GHz are in use. The frequencies are 1-2 GHz (L-band), 2-4 GHz (S-band), 8-10 GHz (X-Band), 35 G GHz (Q-band) and 95 GHz (W-band). The most commonly used EPR spectrometer is in the range of 9-10 GHz (X-band). In this work, EPR measurements were performed using a JEOL (JES-FA200) instrument operating in the X-band. The photograph of the EPR instrument used in the present study is shown **Fig. 2.12**. The microwave source is a Gunn oscillator operating at a frequency of 9.4 GHz (X-band). We used this technique to study the unpaired electron spin in GQD, TiO_2 and its heterostructures.

2.2.2.8. X-ray Photoelectron Spectroscopy (XPS)

XPS is a surface characterization technique, which combines surface sensitivity with the ability to quantitatively obtain both elemental and chemical bonding information. In particular, XPS is a widely used spectroscopic tool due to its high sensitivity to sample surface (10 nm from the sample surface). The nature of XPS spectrum strongly depends on the local environment of the sample, such as composition, bonding and ionic state of

elements. The photon is absorbed by an atom of the sample, leading to emission of a core (inner shell) electron. Based on the binding energy of the electrons, ejected from the sample surface the ionic state of the elements and their composition is analysed. For each element there is a characteristic binding energy of the core electrons.

Figure 2.13: Photograph of the X-ray photoelectron spectrometer (ULVAC-PHI, Inc.).

In the present study, XPS measurements were carried out with a PHI X-Tool automated photoelectron spectrometer (ULVAC-PHI, Inc.) using Al Kα X-ray beam (1486.6 eV) with a beam current of 20 mA. A photograph of the XPS instrument used for the present work is shown in **Fig. 2.13.** In case of the GQDs and GQDs hybrids, chemical bonding and functional groups are analysed using the XPS data. To understand the broad XPS spectrum the peaks are fitted with Gaussian line-shape using a XPS peak fit software and peak centre, area and FWHM are extracted from the data.

2.2.3. Analytical Techniques

2.2.3.1. X-ray Diffraction (XRD)

XRD is the most important non–destructive technique for studying the phase and crystallinty of materials. In XRD, a collimated beam of X–rays, with wavelength λ = 0.5–2.0 Å, are incident on a sample and is diffracted by the atoms of the crystalline phases in the sample according to 'Bragg's law',

$$2dsin\theta = n\lambda \quad \ldots\ldots\ldots\ldots\ldots\ldots \quad (2.7)$$

where d is the spacing between the atomic planes in the crystalline phase, θ is the angle of incidence of the X–ray beam with the atomic plane, n represents the order of diffraction. We consider only the first order diffraction n =1, because the second order peaks are mostly difficult to detect experimentally.

Figure 2.14: A photograph of the X-ray diffractometer (Rigaku RINT 2500, TTRAX III).

The diffracted X–ray beam intensity is measured as a function of the diffraction angle 2θ. For powder samples, the diffracted X-ray beam originates from the differently orientated crystallites giving reflections from all possible planes. In the XRD pattern, the position and intensity of the diffraction peaks represents the characteristic of crystallographic structure and the atomic composition of the material. Similarly, for multi-phase samples, each diffraction peak position indicates their characteristic crystallographic structure. Phase identification of the samples can be done by matching with standard XRD pattern. Owing to the huge data bank available from JCPDS Powder Diffraction Files [10] covering practically every phase of every known material, crystal phase of the sample is identified from the peak positions of the diffractogram. Homogeneous or uniform elastic strain in the (hkl) direction can also be calculated from

the shift in the diffraction peak positions, and the $d_{(hkl)}$ spacing of the unstrained crystal. A photograph of our laboratory X-ray Diffractometer (Rigaku RINT 2500, TTRAX III) used in the present study is shown in **Fig. 2.14**. XRD pattern of GQD and GQD based heterostructures are obtained using a Cu $K_{\alpha 1}$ (λ = 1.5406 Å) radiation.

2.2.3.2. Thermo Gravimetric Analysis (TGA)

TGA is a method for studying the thermal analysis of the samples. In TGA, the mass of a sample is measured over time as the temperature changes. This measurement provides information about physical phenomena, such as phase transitions, as well as chemical phenomena including chemisorption and physisorption, thermal decomposition of the functional groups. TGA is conducted on an instrument referred to as a thermogravimetric analyzer. A thermogravimetric analyzer continuously measures mass while the temperature of the sample is changed over time. Mass, temperature, and time in TGA are considered as base parameters while other additional parameters may be derived from these base quantities. A typical thermogravimetric analyzer consists of a precision balance with a sample pan located inside a furnace with a programmable control temperature. The temperature is generally increased at constant rate to incur a thermal reaction. The first derivative of the TGA curve (the DTG curve) is plotted to determine inflection points useful for in-depth interpretations of thermal analysis.

Fig. 2.15 shows the photograph of TGA instrument (STA7200 HITACHI, Thermal analyser) used in the present study. This instrument can reach maximum temperature up to 1100 °C. The important components and arrangements for the TGA are labeled in **Fig. 2.15.** The gas flow rate is controlled by a rotameter as indicated by "1" in **Fig. 2.15**. The dotted rectangular box shows the furnace chamber and the sample loading stage is immersed into the furnace. The TGA/DTG was done by purging the high purity oxygen gas (99.999%) with flow rate of 100 mL/min and heating rate was 5 °C/min. The initial weight of the sample was taken as 5 mg in each experiment. The TGA/DTG studies of GQDs provide information about the decomposition (loss) of the different oxygen functional groups that are binded at edge and in-plane carbon atoms in GQDs. The TGA characterization results also suggest the type of adsorption of GQDs with other materials and hybrid formation. Some of the TGA/DTG measurements are done with TGA instrument (STA 449 F3 Jupitar, Netzsch, Germany) in the presence of Ar gas atmosphere and these results are presented in **Chapter 3**.

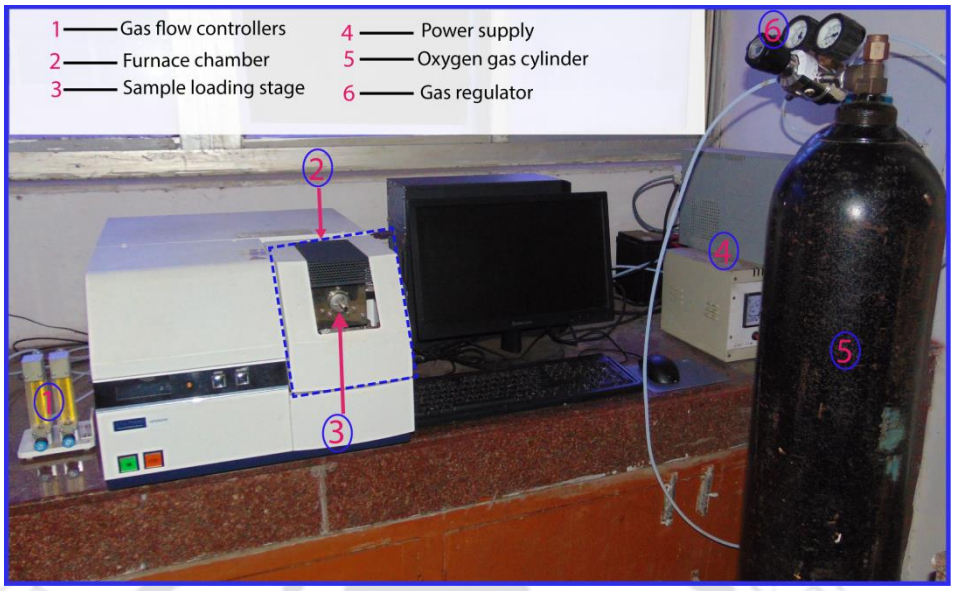

Figure 2.15: A photograph of the TGA (STA7200 HITACHI, Thermal analyser) instrument shown along with additional arrangements for TGA measurements.

2.3. Visible Light Photocatalysis

Visible light photocatalytic degradation of organic dye (methylene blue, MB) is performed with an in-house developed photocatalysis set up. A photograph of the in-house developed visible light PC setup is shown in **Fig. 2.16**. The set up consists of a Xe lamp (Oriel instruments, 450 Watt), a mirror for beam refection and a UV light cut off filter (Hoya Filter, Japan). The UV light cut off filter is placed in front of the beam of light. This beam is further reflected by a mirror such that the light is illuminated on the MB solution. A magnetic stirring stage is used for stirring the MB-catalyst solution during the irradiation of light for different time. During the visible light irradiation, cold water was circulated to the lamp to maintain it at room temperature. At certain interval of time, a portion of the solution l is measured.

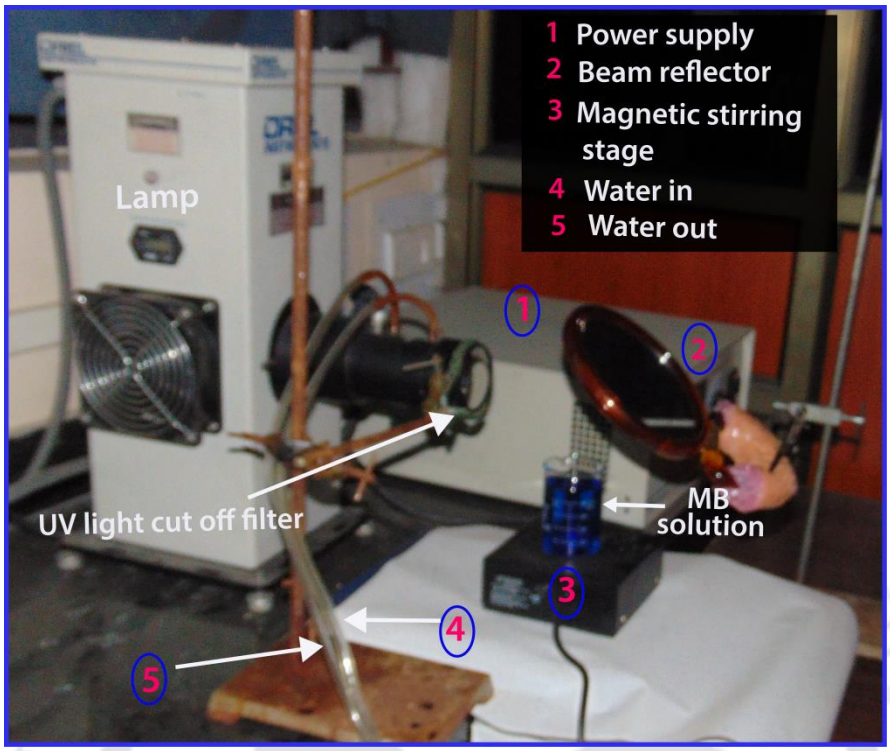

Figure 2.16: A photograph of the in-house developed visible light photocatalysis set up. The components are labelled in the image.

2.4. Bio-Imaging of Cancer Cells

2.4.1. Culture of Cells

GQDs showed very bright visible PL emission. Thus, we considered GQDs as florescent markers for the bio-imaging of cancer cells. The three different cell lines i.e. HeLa cells (human cervical carcinoma), A-375 (human malignant melanoma cells) and HEK-293 (human embryonic kidney cells) were obtained from National Center for Cell Sciences (NCCS), Pune, India. The HeLa cells were cultured in Dulbecco's modified Eagle's medium supplemented with L-glutamine (4 mM), 10,000 units penicillin, streptomycin (10 mg/mL), and 10% (v/v) fetal bovine serum (obtained from PAA Laboratories, Austria). This was incubated in 5% CO_2 humidified incubator at 37 °C for 24h. Note that the A-375 cell lines are cultured using the similar procedure. **Fig. 2.17(a)** shows the photograph of the CO_2 humidified incubator (Thermo scientific, HERA cell 150i) used for the culturing the cell lines.

2.4.2. Cytotoxicity

The effect of different GQDs on viability of cells lines were assessed by using a MTT (3-(4,5-dimethylthiazol-2-yl)-2,5-diphenyltetrazolium bromide) dye assay. For this study, 5 × 10^3 of HeLa cells/well were seeded in a 96-well microtiter plate (Eppendorf Microplates). A photograph of the 96-well microtiter plate is shown in **Fig. 2.17(b).** Further these cells were allowed to grow overnight by maintaining the same medium and condition as discussed in the previous section. The resulting intracellular purple formazan crystals are solubilized in DMSO. The solution has an absorbance at 570 nm. The absorption measurements were performed with a commercial micro plate reader (TECAN, Infinite M200 PRO)**.** A photograph of the instrument is shown in Fig. **2.17(c).** Note that similar procedure is followed for MTT assay studies of A-375 cell lines using different GQDs samples.

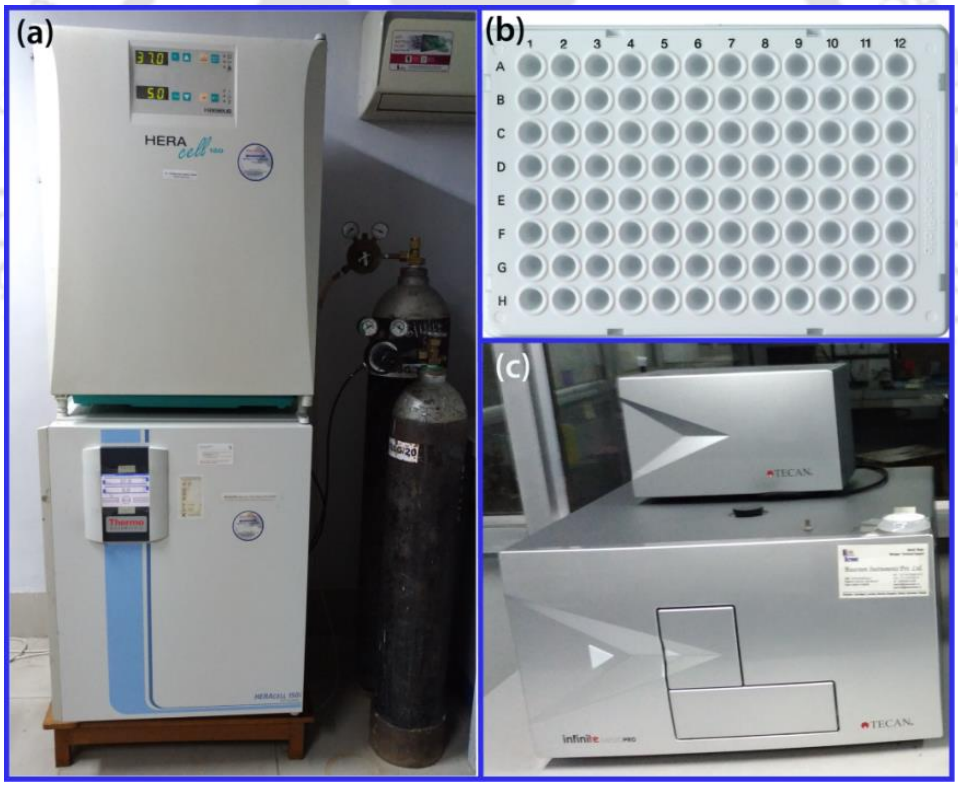

Figure 2.17: Photographs of (a) CO_2 humidified incubator (Thermo scientific, HERA cell 150i), (b) 96-well microtiter plate, and (c) micro plate reader (TECAN, Infinite M200 PRO) for absorption measurements.

2.4.3. Confocal Microscopy Imaging

Confocal microscopy is an optical imaging technique for increasing the optical resolution and contrast of a micrograph. This can be achieved by means of using a spatial pinhole to

block out-of-focus light in image formation. This technique is used extensively in the scientific and industrial communities and typical applications are in life sciences, semiconductor inspection and materials science. In the present study, confocal imaging of GQDs is performed on different biological cells. The basic difference between the conventional and confocal microscopy is that, in conventional microscope the light travels through a sample as far into the specimen as it can penetrate. This results in all parts of the specimen in the optical path excited at the same time and the resulting fluorescence is detected (including a large unfocused background part) by the microscope's photo detector or camera. On the other hand, confocal microscope only focuses a smaller beam of light at one narrow depth level at a time. The use of point illumination and a pinhole in an optically conjugate plane in front of the detector to eliminate out-of-focus signal gives rise to a better resolution image. A schematic of the working principle of confocal microscopy is shown in **Fig. 2.18(a)**. The light intensity is detected by a sensitive detector, usually a photomultiplier tube (PMT) transforming the light signal into an electrical one that is recorded by a computer.

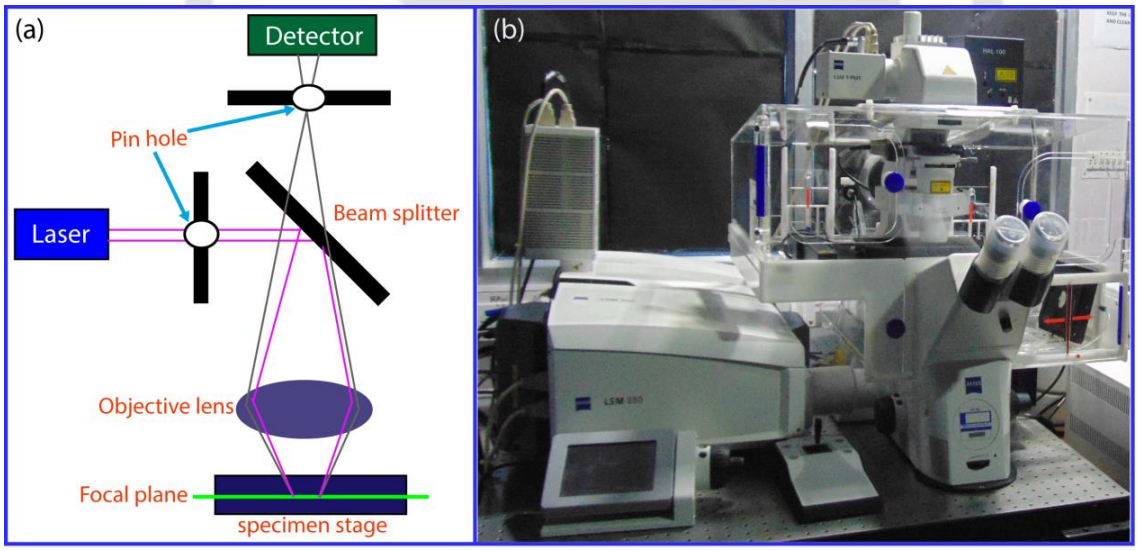

Figure 2.18: (a) A schematic of working principle of confocal microscope. (b) A photograph of the confocal microscope (Zeiss LSM 880) used in the present study.

In the present study, confocal microscopy imaging of cell lines with GQDs is performed. For this, 1×10^5 cells (HeLa or A-375 or HEK-293) were grown on a coverslip in a 35 mm culture dish plate and incubated in a 5% CO_2 humidified incubator (37 °C for 24 h). Thereafter, the cells were treated with different GQDs for 4h. After the

treatment, the cells were fixed with 70% chilled ethanol. Then the coverslips were taken out with the help of the twisers and mounted onto glass slides and the sides were sealed. In the present study, a confocal microscope (Zeiss LSM 880) is used for the fluorescence imaging of the GQD. The photograph of the instrument is shown in **Fig. 2.18(b).** The samples are excited with 405nm wavelength laser.

References

1. G. Rajender and P. K. Giri, *Journal of Alloys and Compounds*, 2016, **676**, 591-600.
2. K. S. Suslick, *Science*, 1990, **247**, 1439-1445.
3. S. You, M.-W. Chen, D. D. Dlott and K. S. Suslick, *Nature Communications*, 2015, **6**, 6581.
4. A. C. Ferrari and D. M. Basko, *Nat Nano*, 2013, **8**, 235-246.
5. S. Claramunt, A. Varea, D. López-Díaz, M. M. Velázquez, A. Cornet and A. Cirera, *The Journal of Physical Chemistry C*, 2015, **119**, 10123-10129.
6. D. Bischoff, J. Güttinger, S. Dröscher, T. Ihn, K. Ensslin and C. Stampfer, *Journal of Applied Physics*, 2011, **109**, 073710.
7. G. Rajender and P. K. Giri, *Journal of Materials Chemistry C*, 2016, **4**, 10852-10865.
8. G. Kortüm, W. Braun and G. Herzog, *Angewandte Chemie International Edition in English*, 1963, **2**, 333-341.
9. W. M. Doyle, *Technical Note AN–906 Rev. C*, 1992, 1-24.
10. *"The International Centre for Diffraction Data" retived* **www.icdd.com**.

Chapter 3

Formation Mechanism of Graphene Quantum Dots During Hydrothermal Growth and Its Edge State Conversion by Annealing

In this chapter, we present the controlled synthesis and investigation on the formation mechanism of graphene quantum dots (GQDs) from two different precursor materials. We study the inter-conversion of edge states during thermal annealing of GQD thin films through various microscopic and spectroscopic tools. Our studies reveal that the in-plane epoxy (C-O-C) functional groups are essential for cutting of graphene materials in to GQDs during the hydrothermal reaction. To understand the broad spectra of Raman and photoluminescence (PL) from GQD thin films, we have deconvoluted the spectra in each case and the significance of each band is elucidated. The deconvolution allowed us to assign the origin of particular PL emission from GQDs samples. Further, we discuss a correlation between the Raman and PL studies, for the first time. Based on our experimental results, we unambiguously assign the blue PL emissions at~407 and ~440 nm to zigzag and armchair free edge states in GQD, respectively, for the first time. On the other hand, the green emission bands at ~490 and ~530 nm are attributed to COOH/C-OH and C=O/C-O edge functional groups, respectively.

3.1. Introduction

Graphene is a one-atom thick covalently bonded sp^2 carbon prototype 2D material, while graphene oxide (GO) is known to be the functionalized few layered graphene with functional groups that are attached on the basal plane, and the reduced graphene oxide (rGO) is commonly known to be more conductive form of GO due the removal of basal plane functional groups from the sp^2 conjugated carbon network. Graphene quantum dot (GQD) is an emerging class of zero-dimensional (0D) material that show pronounced quantum confinement effect, plenty of edge states and functional groups [1-4]. When the size of the graphene is reduced to smaller the ~100 nm, it possesses strong edge effects and quantum confinement [5]. Interestingly, the edges of GQDs are more reactive than the

basal plane because of the high ratio of edge to basal plane carbon atoms [6]. A lot of efforts have been made to prepare the GQDs through the top down and bottom up approaches. Top down techniques include the cutting of bulk sp^2 bonded carbon materials (such as carbon fibres, graphite, or graphene nanosheets, carbon black etc.) through the solvothermal [7], hydrothermal [8], chemical exfoliation [9], oxidative cutting [10] etc. On the other hand, bottom-up approaches make use of the self-assembly of organic materials as a precursor, including intermolecular dehydrolysis of citric acid [11], microwave assisted heating of glucose [12] , and thermal plasma jet etc. [13, 14]. In some cases, the formation of GQDs was studied on the basis of longitudinal unzipping of carbon nanotubes (CNTs) and resulting GQDs had irregular shapes [15]. The pathway leading to the formation of the GQDs with nearly circular cross-section from GO has not been addressed properly.

Next, the intriguing mechanism of PL from GQD has been poorly understood. Most of the PL studies on GQDs have been performed in aqueous solution or GQDs dispersed in a solvent medium, which may have contribution to the measured PL. Previous studies reveal that the PL emission arises mainly from the size effect, edge sites and oxygenated functional group defects. Generally, the PL mechanism from GQDs is explained on the basis of intrinsic states (blue PL) and defect states emission (green PL). The intrinsic states arise from the size/edge defects where the recombination of electron-hole pairs takes place, while the defects states correspond to the attachment of functional groups [7, 10, 16-19]. Previous studies investigated the origin of the PL emission from GQDs [3, 20, 21]. Jianglin et al. [22] investigated the effect of functional groups on the PL evolution, and Yoon et al. [23] concentrated on the intrinsic state PL emission from GQDs. However, direct monitoring of intrinsic states, defect state evolution and the identification/ assignment of edge states in GQDs thin films through a combined PL and Raman study is not reported in the literature. Further, controlling the edge states and functional groups in GQDs is extremely important for their future optoelectronic and biomedical applications. Generally, the first order Raman spectra of GQDs in the region 1000-1815 cm^{-1} is very broad [17, 18, 23, 24]. To the best of our knowledge, Raman deconvolution for intrinsic and functional group defects states in GQDs and its manipulation through controlled annealing has not been addressed in the literature. Non-destructive evaluation of edge states and functional groups in GQDs through PL and Raman studies constitutes an

important milestone for their successful application in various emerging areas of science and technology. In this chapter, we discuss the formation mechanism of circular shaped GQDs during hydrothermal reaction and its edge state conversion during annealing probed through various experimental tools. We deconvolute the PL and Raman spectra of GQDs to gain insight into the origin of PL emission from GQDs. In the following sections we discuss the experimental details for samples preparation, characterization of different samples and formation mechanism of GQDs as well as the PL and Raman spectral deconvolution and its correlation for understanding the structural evolution of GQDs.

3.2. Experimental Details

The precursor materials for the synthesis of GQDs are prepared by chemical exfoliation methods and the GQDs are synthesized by hydrothermal reactions. The further details are discussed below.

3.2.1. Preparation of GO and rGO

GO was synthesized by a well-known modified Hummers method [25]. Expandable graphite flakes (purity 99%) were used as the precursor material for the synthesis of GO. First, 3 g of expandable graphite flakes were poured into a beaker and 1.5 g of $NaNO_3$ was added. To this solution, 69 mL of concentrated H_2SO_4 was added and stirred for 2 h to obtain a uniform solution. Next, the solution was transferred into an ice bath and 9 g of $KMnO_4$ was subsequently added drop wise under stirring to avoid the explosion. The mixture was stirred at 35 °C for 4 h to allow the oxidation. Deionized (DI) water was slowly added and stirred at 98 °C for 15 min. Further, the solution was diluted with DI water (700 mL) before being quenched with 15 mL of 30% H_2O_2. Additional DI water was added to get the aqueous solution. Subsequently, the final solution was centrifuged at 10000 rpm for 10 min and the process was repeated for 3 cycles to separate the exfoliated flakes. Later it was filtered with a 0.22 µm polytetrafluroethylene (PTFE) membrane and dried at 100 °C in an oven to obtain the GO powder.

In order to study the role of functional groups on the GQD synthesis, the rGO was synthesized using hydrazine monohydrate (Alfa Acer, 99%) as a reducing agent. In this experiment, GO powder (50 mg) was mixed with 50 mL DI water and this was

transferred to the ultra-sonication bath and was sonicated for 10 min to form uniform solution. Further, 500 µL of hydrazine monohydrate was then added to the solution and heated in an oil bath at 100 °C for 24 h [26]. During the heating, the black solid was gradually precipitated. Then this precipitate was separated from the solution, washed several times with DI water and methanol. Finally, filtered product was dried in an oven to obtain the rGO powder.

3.2.2. Size reduction of GO

In order to reduce the size of the GO sheets, the as-synthesised GO sheets were further oxidized with concentrated H_2SO_4 and HNO_3 mixture (volume ratio 1:3) with 1 mg of GO. The resulting product is referred to as oxidized GO (OGO).

3.2.3. Synthesis of GQDs

GQDs were synthesised by a hydrothermal method using OGO as the precursor material. In a typical experiment, 50 mg of OGO powder was mixed with 50 mL of DI water and was sonicated for a few minutes to achieve a uniform dispersion. Next, the solution was transferred into a Teflon lined autoclave (100 mL) and heated at 200 °C for different reaction durations (12 and 24 h). The reaction temperature was fixed based on the TGA/DTG result of OGO, discussed later. The TGA profile suggests the decomposition temperature as ~200 ℃ for the OGO through the loss of in-plane epoxy functional groups (shown later). For the convenient of discussion, 12 and 24 h reaction grown GQDs samples are named as S12 and S24, respectively.

3.2.4. Functionalization of GQDs

In situ chemical functionalization of GQDs was performed to achieve edge modification with oxygen functional groups. During the hydrothermal reaction, 3mg of ploy (ethylene glycol) (PEG, average molecular weight 1500) was added and the protocol followed for functionalization is same as that of the GQDs synthesis discussed above. GQDs functionalized for 12 and 24 h are named as S12F and S24F, respectively.

3.2.5. Synthesis of GQDs from rGO

To understand the role of in-plane oxygen functional groups on GQDs synthesis, we have performed the GQDs synthesis using rGO as a precursor material. For this experiment, 50 mg of rGO powder was mixed with 50 mL of DI water and sonicated for a few minutes to

achieve a uniform dispersion. Next, the dispersed solution was transferred into a Teflon lined autoclave (100 mL) and heated at 200 °C for 12 h.

3.2.6. Fabrication of GQDs Thin Films

As synthesized GQD powder was re-dispersed into DI water and sonicated for a few minutes. Prior to the fabrication of GQD thin films, the Si and quartz substrates were cleaned with 2-propanal, acetone and DI water for a few minutes to remove the dust and organic impurities. Next, the GQD dispersion is spin coated on to the Si and quartz substrates to obtain GQD thin films.

3.2.7. Hydrogenation and Oxygenation Studies of GQDs Thin Films

To understand the mechanism of intriguing PL originating from the edge states and functional groups of GQDs, we conducted thermal annealing of GQDs under different gas environment. Thermal annealing was conducted at 620 °C [27] under H_2 (purity 99.9%) or O_2 (purity 99.999%) gas environment for 2 hours in each case. The thin film samples were kept in an alumina boat and loaded into a tubular quartz chamber, which is mounted inside a muffle furnace. GQDs spin coated on to the Si and quartz substrates were annealed under identical conditions. Initially, the chamber was pumped down to a base pressure of 5.0×10^{-4} mbar, and the temperature was ramped up to 620 ℃ with a heating rate 5 ℃ min^{-1}. The temperature was maintained at 620 ℃ and the gas flow rate was maintained at 150 SCCM (standard cubic centimetres per minute) for the duration of 2 h. We believe that the edge sites can be more reactive with certain gas environment and subsequently attach/detach edge oxygen functional groups depending upon the gas environment, and it leads to the functionalization with the edge carbon atoms. Note that the sample codes used for the hydrogenated and oxygenated samples are represented by a suffix ‘H’ and ‘O’, respectively. For example, S12H refers to hydrogenated S12, and S12O refers to oxygenated S12 etc.

3.3. Morphology, Structural and Optical Properties of OGO and rGO

3.3.1. TEM Imaging Analysis

Prior to the GQDs synthesis, the as-prepared precursor materials are characterized by different techniques. **Fig. 3.1** shows the morphological features of the GO, OGO and rGO. **Fig. 3.1(a)** and **(b)** represents the TEM images of the GO and OGO, respectively. It

is evident from the **Fig. 3.1(a)** and **(b)** that the flake size of GO is larger than that of OGO. The upper insets in **Fig. 3.1(a)** and **(b)** depicts the optical photographs captured when the GO is in water and with the acid (H_2SO_4+HNO_3) treatment, respectively. These images further support the changes of the GO flakes before and after treatment with the acid. In **Fig. 3.1,** the lower insets shows the SAED pattern recorded for the respective samples and signifies the crystalline nature of hexagonal sp^2 carbon sheet. As compared to the SAED pattern of OGO, the rGO showed highly crystalline behaviour. This is due to the loss of oxygen functional groups from rGO and these results in the rearrangement of sp^2 carbon atoms on the basal plane in order to form the honey comb lattice.

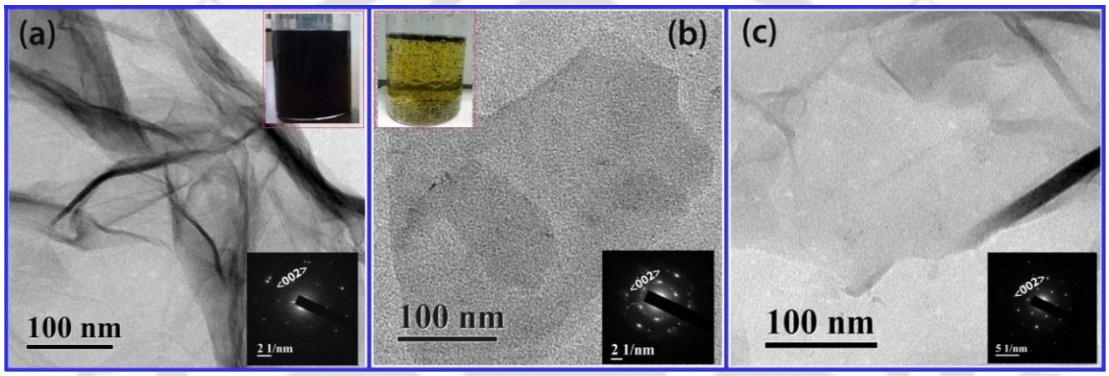

Figure 3.1: TEM imaging of the graphene samples. (a) GO, (b) OGO and (c) rGO. The upper inset in (a) and (b) represents the digital photographs of GO; in water and oxidation with H_2SO_4 and HNO_3 mixture, respectively. The lower insets in each case show the SAED pattern of sp^2 carbon hexagonal structure for GO, OGO and rGO, respectively.

3.3.2. Optical Absorption and TGA Studies

Next, we study the optical and structural changes in the OGO and rGO by using UV-Vis absorption, FTIR and TGA/DTG techniques and the results are portrayed in **Fig. 3.2. Fig. 3.2(a)** shows the UV-Vis absorption characteristics of OGO. The absorption spectrum appearing in the n-π* region (UV-vis wavelength) from OGO is due to the in-plane oxygen functional groups [28]. **Fig. 3.2(b)** shows a comparison of FTIR spectra of OGO and rGO. The vibrational mode at 1384 cm^{-1} in OGO is due to the epoxy deformation [9], the broad peak in the region 3100-3600 cm^{-1} is attributed to the attachment of hydroxyl groups and two other modes at 1580, 1650 cm^{-1} are due to the in-plane stretching vibrations of sp^2 bonded carbon atoms and COOH functional groups, respectively [29]. The additional FTIR bands due to the in-plane epoxy in OGO strongly suggest the presence of

in-plane epoxy functional groups on the basal plane of OGO, while it is absent in rGO. **Fig. 3.2(c)** and **(d)** show the TGA/DTG profile of OGO and rGO, respectively. It is evident from the **Fig. 3.2(c)** that the OGO shows ~60% weight loss at ~200 ℃ due to loss of in-plane functional groups. Inset in **Fig. 3.2(c)** shows the DTG profile of OGO. In contrast to OGO, the TGA/DTG profile of rGO shows very low weight loss (%) at 200 ℃ as compared to the OGO, likely due to the lack of in-plane oxygen functionalities. In addition, it showed additional DTG peaks at 230, 307, 436, and 812 ℃, which are due to the presence of residual epoxy/C-O (ether), COOH and C=O functional groups and sp^2 hybridized carbon, respectively [29].

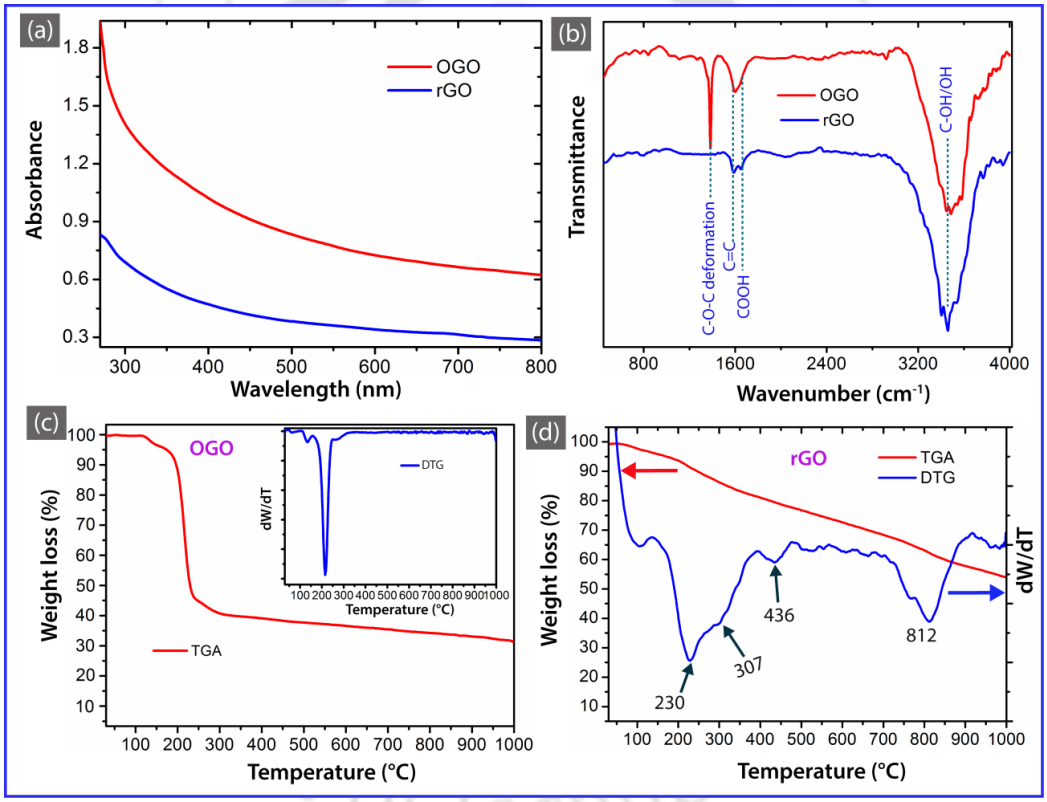

Figure 3.2: Comparison of (a) Optical UV-Vis absorption, (b) FTIR spectra of OGO and rGO. (c) TGA/DTG profile of OGO, showing the weight loss ~200 ℃ due loss of in-plane functional groups. (d) TGA/DTG profile of rGO. The multiple DTG peaks in rGO are due to the presence of epoxy/C-O (ether), COOH, C=O related functional groups and sp^2 hybridized carbon.

3.4. TEM and AFM Imaging

During the hydrothermal growth of GQDs, the morphological evolution and changes in basal plane of OGO were monitored by TEM analysis. **Fig. 3.3(a-e)** shows the TEM images of hydrothermal grown GQDs samples. **Fig. 3.3(a)** represents the TEM image of

S12 sample and its magnified view is shown in **Fig. 3.3(b).** It is apparent from **Fig. 3.3(a, b)** that the pore formation occurs in OGO during the hydrothermal reaction under high temperature (200 °C) and high pressure. **Fig. 3.3(c)** represents the TEM image of GQDs in S12, which shows small GQDs fragments that are separated from the OGO sheet after the hydrothermal reaction. During the hydrothermal reaction, in order to release the strain in the OGO lattice, the epoxy functional groups may form a closed/ quasi-ring type structure on the basal plane of OGO [30]. This implies an initiation of cutting of OGO sheets through which strain might be released and we believe that the epoxy pairs attached at the defective sites of GO may have a very important role in cutting of the OGO sheets. It is possible that the holes in OGO could form by oxidative widening of existing defects through attack on the internal edges of the OGO and epoxy ring like structure may not be essential for the cutting of the OGO sheets. However, our experiment on rGO does not support this hypothesis. In order to prove the necessity of the epoxy functional groups in GQD formation, we studied the effect of hydrothermal reaction on the rGO sheet. Interestingly, it was found that for hydrothermal reaction with rGO under similar conditions (12 h reaction), no distinct GQDs were formed. **Fig. 3.3(d)** shows the TEM image of GQDs obtained from the rGO precursor**.** Despite the strong presence of structural defects in rGO, oxidative cutting of rGO does not take place during the hydrothermal reaction. This establishes the critical role of epoxy functional groups on the basal plane of OGO in cutting of the OGO sheets to form GQDs. However, higher resolution TEM imaging including aberration–corrected TEM studies would be more helpful to gain better insight into the precise structure of these pores and the GQDs edges[31, 32]. The reaction for longer duration (24 h) yields smaller sized GQDs, as shown by the TEM image of S24 sample (**Fig. 3.3(e)**). The average size of GQDs is ~5 nm for S24 sample. **Fig. 3.3(f)** represents the AFM image (obtained with Agilent, Model 5500) of GQDs in S24 sample and the solid lines are drawn to obtain the height profile of the GQD layers, as shown in **Fig. 3.3(f)**. The AFM image of GQDs and its height profiles confirm that the GQDs consist of a few (1-5) layers of graphene.

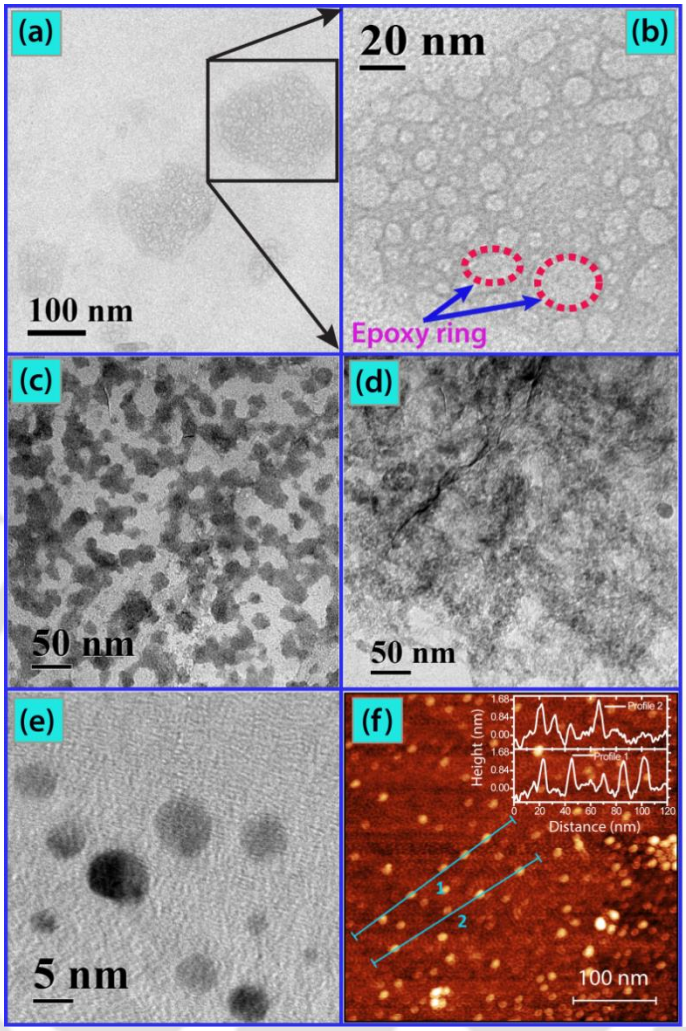

Figure 3.3: (a) A TEM image of early stage of growth of GQDs with pore structures in S12, and (b) a magnified view of a portion of the image in (a). Dotted circles in (b) represent the oxygen functional group ring formation on the basal plane of OGO sheet. (c-e) TEM images of GQDs in S12, GQDs synthesized from rGO precursor and GQDs in S24, respectively. (f) AFM image of GQDs in S24 and inset shows the height profile of GQDs measured along the line 1 and 2.

3.5. Formation Mechanism of GQDs

In the process of exfoliation of graphite flakes, and the preparation of GO, it involves chemical reactions that promote the distortion in the sp^2 conjugated carbon network. This implies that the GO has structural imperfections in contrast to the perfect sp^2 carbon in graphite. In other words, the attached oxygenated functional groups on the basal plane and edges alter the GO sp^2 conjugated carbon network. Generally, the epoxide (C-O-C) and hydroxyl groups (OH) are attached on the basal plane of GO and the carboxylic (COOH), carbonyl (C=O), lactone, pyrone and ether etc. are decorated at the edge sites [33-35].

An epoxide is cyclic ether with a three-atom ring. This ring approximates to an equilateral triangle, which makes it highly strained. The strained ring makes epoxides more reactive than other ethers. In the literature, the reported models and experimental results have mostly discussed about the unzipping of CNTs and cutting of GO that takes place along a C-C line [36-38]. However, this type of cutting results into the growth of 1-D structure (e.g., graphene nanoribbons) or a particular type of oriented structure of carbon (ziz-zag or armchair). The cutting of GO along the C-C line was shown in **Fig. 1.3(a), Chapter 1**. A proper understanding on the mechanism of formation of circular shaped GQDs is elusive.

In the present work, we propose that the epoxy functional groups attached at the sp^3 sites are believed to form a co-operative quasi-ring type closed structure along the C-C bond to yield nearly circular shaped GQDs by cutting of OGO, as confirmed from the TEM analysis. TEM imaging results of GQDs synthesised using two different precursor materials further supports the distinct role of in-plane epoxy functional groups for the formation of high quality GQDs. Based on our experimental evidences, we propose below a mechanism for the formation of GQDs. **Fig. 3.4** shows a schematic of the proposed formation mechanism for GQDs from the cutting of OGO sheet with the help of epoxy rings. Note that the degree of oxidation of GO, solvent, and reaction temperature will have strong influence on the structure and morphology of GQDs. OGO has epoxy functional groups on basal plane and OH functional groups on in-plane as well as at the edges (**Fig. 3.4(a)**). In the first step, the epoxy functional groups in OGO tend to appear at the C-C bond and form a quasi-ring type structure underlying the C-C bonds on the basal plane of OGO during the hydrothermal reaction (**Fig. 3.4(b)**). Formation of quasi-ring type epoxy functional groups and porous structure of OGO is proposed based on the evidence from the TEM imaging (**Fig. 3.3(a, b)**). In the second step, once the epoxy pairs form, it is energetically favourable to cut the OGO into small pieces, as shown (**Fig. 3.4(c)**), and finally small sized GQDs are formed (**Fig. 3.4(d)**). Note that this cutting need not be mediated by the defects or hydroxyls [35-37]. Further, the GQD fragments that are separated from OGO sheets have the size similar to that of the pore size, indicating that the GQDs are indeed formed due to the cutting of the OGO sheets, as apparent from **Fig. 3.3(b** and **c)**. Reaction duration of 24 h results in the smaller ~5 nm GQDs (**Fig. 3.3(e)**). The above proposed mechanism is fully consistent with the formation of nearly circular shaped GQDs with different edge states, oxygen functionalized and defective GQDs.

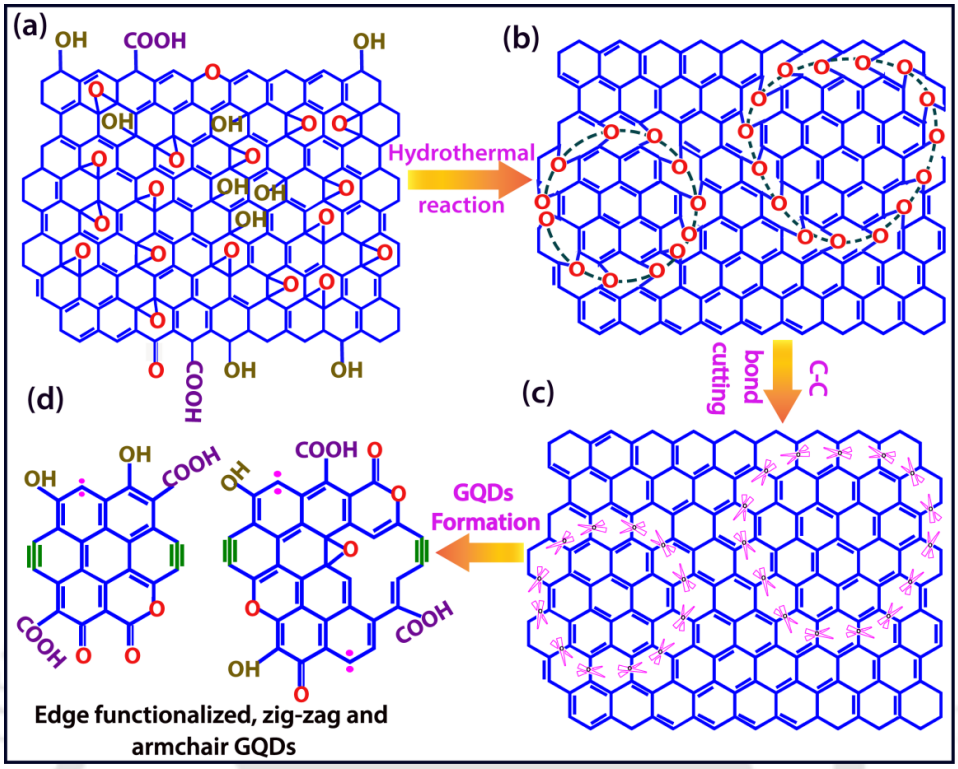

Figure 3.4: A schematic illustration of the proposed formation mechanism of GQDs from OGO sheets. (a) Schematic of in-plane epoxy (C-O-C) and OH functional groups on OGO sheet, and (b) dashed circle with oxygen atoms represents the epoxy quasi-ring formation underlying the C-C bonds during the hydrothermal reaction. (c) Cutting process of the C-C bonds in OGO sheet. (d) Formation of circular/quasi-circular GQDs through the cutting. Separated GQDs possess zigzag, armchair edges and functional groups. Magenta dot and olive colour bonds refer to the zig-zag and armchair sites, respectively.

3.6. Raman Study on the Edges and Functional Groups

In this section, we discuss the Raman bands and their evolution with annealing of GQDs thin films. **Fig. 3.5** shows a comparison of the Raman spectra of GQDs in S12, S12F and S24 before and after annealing. The as-grown samples show multiple Raman bands, some of which are characteristic modes of graphene, such as D, G and D' bands. After annealing, the peaks are broadened and the relative intensity of the D band is enhanced as compared to that of the G band. The characteristic G band is due to the in-plane vibrations of sp^2 carbon (E_{2g} mode), while D' band is attributed to the vacancies and/or pentagonal and octagonal defects, usually referred as zigzag 5-7 defects[39-41].

In order to gain a better insight into the edge states and functional group defects in GQDs, the broad Raman spectrum in the range 1000-1815 cm^{-1} is deconvoluted. The deconvolution of Raman spectrum is essential for understanding the disordered graphitic

materials [42]. Sadezky et al. [41] described a five peak model for the fitting of the Raman spectra of carbon soot and related carbonaceous materials, and Sergi et al. [40] proposed a five peak model for the fitting of Raman data of GO. Similarly, Rebelo et al. [43] recently proposed a multi-peak Raman fitting for the multiwalled CNTs and studied the covalent functionalization by diazonium chemistry and oxidation methodologies. In the present work, we find that six peaks were necessary to fit the broad Raman spectra of GQDs. Note that besides the well know D, G and D' Raman modes, new Raman modes D1, D2 and D3 are fitted to the experimental data (**Fig. 3.5**). The D1, D2 and D3 are well fitted with Gaussian peaks, while the characteristic D, G and D' bands are fitted with Lorentzian peaks. Generally, some of the Raman-inactive modes become active due to the presence of structural defects that are created during the cutting (growth) and/or attachment of various functional groups in GQDs. The edge is a special kind of disorder and the nature of edges can be probed by the intensity of Raman D band. The D band arises from the momentum conservation law due to the formation of edge states (zigzag and armchair). The intensity of Raman D band is very sensitive to the nature of edge states in GQDs. It has been reported that the D band is strongly present for the armchair edges and nearly absent for the zigzag edges [44-48]. The additional bands D1, D2, D3 may be related to functional group defects. The parameters of the fitted peaks are presented in **Table 3.1**. The ratio of intensity of the D to G band (I_D/I_G) is 0.70 for S12 sample. Interestingly, after annealing, the I_D/I_G ratio is increased by more than three times for S12H and S12O samples. Since the D band intensity is most sensitive to the armchair edge states, the increased D band intensity (ratio) after annealing, clearly reveals the conversion of the edges from zigzag to arm chair type. The low intensity of D band in S12 indicates the presence of both types of edges, zigzag as well as armchair, while the increased D band intensity in S12H and S12O suggests the dominance of armchair edges due to the conversion from zigzag to armchair sites after annealing. Similar trend in change in intensity ratios is observed for S12F and S24 before and after annealing, and the results are shown in **Fig. 3.5** and **Table 3.1.** These results strongly suggest that the zigzag edges of GQDs are converted to armchair edges and the annealed samples contain primarily the armchair edges. This result is consistent with the quantitative analysis of PL data (discussed later).

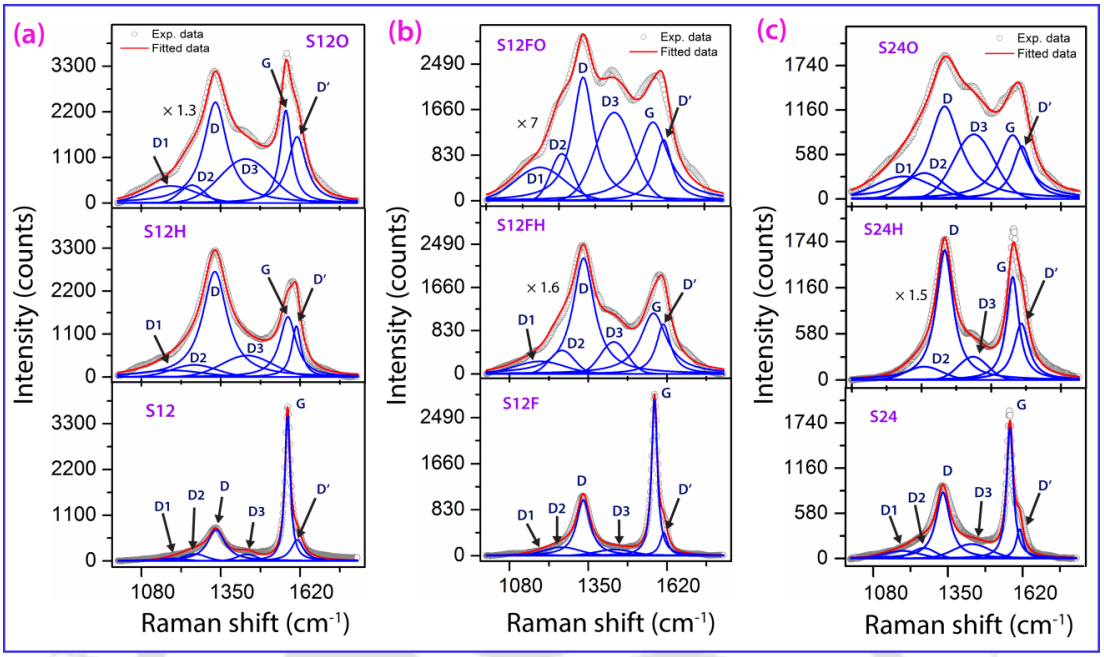

Figure 3.5: Raman spectra of various GQDs thin films fitted with Lorentzian and Gaussian peaks. Raman peak fitting; (a) S12, S12H and S12O, (b) S12F, S12FH and S12FO and (c) S24, S24H and S24O. To enable comparison of intensity, some of the spectra are magnified with appropriate factors, as mentioned in each case. Note that 632.8 nm laser excitation is used for the Raman measurements. The experimental data are shown with symbols and the fitted data are shown with red line. The new Raman bands D1, D2, and D3 correspond to the sp^2-sp^3 carbon, COOH/C-OH and C=O/C-O edge functional groups, respectively.

Next, we address the evolution of the edge oxygenated functional groups in GQDs after annealing. The edge carbon atoms are reconstructed during the annealing and the sp^2-sp^3 bonding changes in order to maintain the stability of edge carbon atoms [39, 49]. In S12, the I_{D1}/I_G ratio is increased by five-fold after H_2 annealing and by about ten-fold after O_2 annealing. Similar increment in the intensity ratio is observed for S12F and S24 (**see Table 3.1**). Thus, the D1 band at ~1185 cm^{-1} may be attributed to the sp^2-sp^3 bonded carbon atoms at the edges of the GQDs. The increased I_{D1}/I_G ratio after oxygen annealing is attributed to the increased density of sp^2-sp^3 bonds due to the covalent attachment of oxygen atoms at the sp^3 carbon sites. In the same way, we monitored the I_{D2}/I_G ratio for different GQDs samples before and after annealing. The ratio I_{D2}/I_G is marginally higher after both oxygen and hydrogen annealing. Since thermal stability of C-OH functional group is higher than that of C=O groups [50], the D2 band may be attributed to COOH/C-OH functional groups. This is in accordance with the FTIR and XPS analyses. In case of H_2 annealing, C-H bonds may be present at the GQD edges [51]. Thus, the increase in I_{D2}/I_G

value after H_2 annealing is expected due to the formation of C-H bonds or due to the residual C-OH functional group. Similar trend is observed in other samples (see **Table 3.1**). For the band D3 centred at ~1438 cm^{-1}, intensity ratio I_{D3}/I_G is remarkably increased after annealing in O_2 due to formation of the covalent bond between the oxygen and the edge carbon atoms, i.e., C=O/C-O bonds at the GQD edges. The I_{D3}/I_G ratio is only 0.16 for S12 sample, while it is 5.5 fold increased in S12FO after O_2 annealing. For S24, I_{D3}/I_G ratio is increased from 0.39 to 0.95 after O_2 annealing (see **Table 3.1**). These results strongly suggest that the oxygen functionalization takes place at the GQDs edge sites, which can be easily controlled through post growth annealing. On the other hand, H_2 gas annealing causes relatively smaller change in the I_{D3}/I_G ratio. The I_{D3}/I_G ratio changed from 0.39 to 0.35 for S24 after H_2 annealing. This might be due to the C=O functional groups that are thermally more stable than the COOH groups [50]. Finally, the D' band intensity is compared for GQDs thin films before and after annealing. The $I_{D'}/I_G$ ratio for S12 sample is 0.33, while it is 3.5-fold increased for the S12H and 1.4 times increased in S12O. Similar trend is observed in other samples (see **Table 3.1**). The marginally lower $I_{D'}/I_G$ ratio in oxygen annealed sample may be due to the fact that some of the oxygen atoms gets attached at the defect sites during the oxygen annealing. The high temperature (620 ℃) annealing may have resulted into the formation of vacancy and pentagon/heptagon (edge reconstruction) defects due to the loss of loosely bonded functional groups (ether) and the conversion of edge states. The stability of ether and lactone type functional groups is relatively lower than other functional groups. Annealing of graphene at high temperature causes the formation of pentagon/heptagon and reconstructed zigzag (5-7) defects[27,49]. Further, after annealing higher density of defects is observed in GQDs thin films. Thus, the increased $I_{D'}/I_G$ ratio in the annealed samples directly implies the formation of additional defects, such as vacancies, pentagon/heptagon defects and reconstructed zig-zag (5-7) defects in GQDs thin films. Similar trend is followed in other GQDs samples after annealing.

Table 3.1. Summary of fitting parameters for Raman bands of various GQDs thin films before and after annealing. The new Raman bands, D1, D2 and D3 are fitted with Gaussian peaks, while well-known D, G and D' bands are fitted with Lorentzian peaks.

Sample Code	Raman Bands Peak position in cm^{-1}						Intensity ratio				
	D1	*D2*	*D*	*D3*	*G*	*D'*	I_{D1}/I_G	I_{D2}/I_G	I_D/I_G	I_{D3}/I_G	$I_{D'}/I_G$
S12	1187	1260	1334	1438	1577	1610	0.05	0.13	0.70	0.10	0.33
S12H	1187	1260	1334	1438	1577	1610	0.28	0.36	2.27	0.72	1.18
S12O	1180	1253	1332	1436	1572	1610	0.57	0.28	2.59	1.44	0.48
S12F	1185	1260	1333	1440	1577	1609	0.19	0.22	0.83	0.16	0.19
S12FH	1185	1260	1334	1438	1574	1608	0.25	0.24	1.56	0.35	0.44
S12FO	1185	1260	1333	1440	1573	1610	0.45	0.28	1.08	0.91	0.43
S24	1185	1262	1332	1436	1574	1609	0.20	0.18	1.07	0.39	0.23
S24H	1185	1260	1333	1435	1577	1608	-	0.25	1.75	0.35	0.68
S24O	1185	1260	1333	1438	1577	1610	0.47	0.27	1.62	0.95	0.54
Peak Identity	***sp^2-sp^3 Carbon***	***COOH/ C-OH***	***Zig-zag/ armchair states***	***C=O/ C-O***	***C=C***	***Crystalline defects***					

Dippel et al. [52] and Sadezky et al. [41] observed a Raman peak at 1190 cm^{-1} in flame soot and attributed it to the sp^2-sp^3 bonds or C–C and C=C stretching vibrations of polyene-like structures. Claramunt et al. attributed the Raman band at ~1187 cm^{-1} to oxygen content in GO [40]. Thus, there is a controversy regarding the origin of the additional Raman bands near the D band. GQDs are a few nanometer sized sp^2-sp^3 bonded carbon atoms with plenty of edge defects. Due to the cleavage of OGO, the carbon atoms are rearranged and the attachment of oxygen functional groups takes place at the sp^2-sp^3 edge carbon sites. Indeed, the edge carbon atoms are more favourable to form the sp^2-sp^3 bonds due to the attachment of oxygen functional group moieties/ defects [39]. Thus, the Raman D1 band at ~1185 cm^{-1} can be assigned to the sp^2-sp^3 bonded carbon atoms at the edges of the GQDs. The Raman D2 band at ~1260 cm^{-1} may be assigned to COOH or ring type C-OH edge functional group, while the D3 band at ~1438 cm^{-1} is attributed to the C=O/C-O functional groups. The peak assignments are consistent with

the evolution of XPS, FTIR and PL spectra from GQDs. There are several theoretical [53, 54] and microscopic studies [1, 3, 10, 17] that confirm the presence of edge defects in GQDs, and our Raman analysis proves to be a powerful tool to monitor these defects more conveniently.

3.7. Ultraviolet-visible Absorption Study

In order to understand the optical transition in GQDs, ultraviolet (UV)-visible absorption measurements are performed. **Fig. 3.6** shows the UV-visible absorption spectra of different GQDs samples. All the samples show the characteristic π-π* transition peak at ~276 nm, which signifies the transition of sp^2 carbon atoms. The other absorption band at ~333 nm is relatively broad and it changes after PEG functionalization, along with the reduction of intensity of ~276 nm peak. The ~333 nm peak is referred as n- π* transition and it is mainly due to the attachment of oxygen functional groups (C=O/COOH) at the GQDs edges [11, 29]. Interestingly, S24 sample shows a distinct absorption peak at ~276 nm, revealing the ultrafine size of GQDs in the as-grown samples and it arises from the quantum confinement effect. Note that this feature is not prominent in other samples perhaps due to the larger size of the GQDs. This is strongly supported by HRTEM results that show a size of ~5 nm for the S24 sample. Besides the size, the attachment of edge

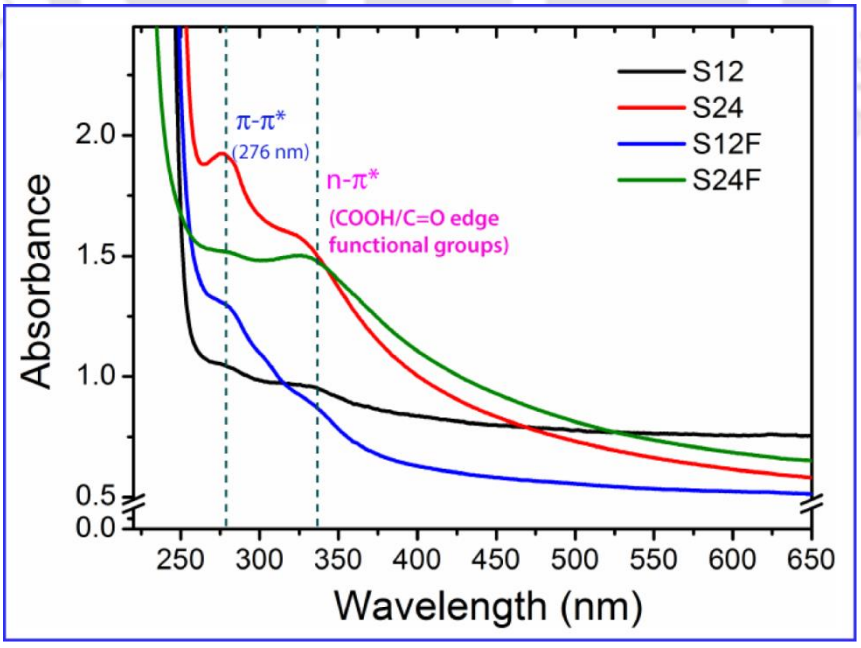

Figure 3.6: Comparison of the UV-Vis absorption spectra of hydrothermal grown GQDs before and after functionalization with PEG. The π- π* band originates from the band to band (π-π*) transition of sp^2 carbon and n- π* absorption band corresponds to the sub-band states arising from the COOH/C=O edge functional groups.

oxygenated functional groups is also evident from the absorption spectra. The absorption band corresponding to the oxygenated functional groups become broad after PEG functionalization. It is noted that the PEG is a polymer that contains branched COOH functional groups. During the reaction, the COOH functional groups attach at the GQDs edges resulting in the broad absorption band for the functionalized GQDs samples.

3.8. Photoluminescence Analysis

Room temperature steady state PL measurements were performed to understand the origin of visible PL emission from GQDs. **Fig. 3.7** shows the PL spectra excited with 355 nm laser for various GQDs thin films before and after annealing. **Fig. 3.7(a-c)** shows the PL spectra before and after annealing and the Gaussian peak fitting for S12, S12F and S24, respectively. All the samples clearly show the PL emission in the blue and green regions. It is clear from the asymmetry and shift in the PL spectra (after annealing) that multiple peaks contribute to the strong PL emission from the GQD thin films. A proper understanding of the various PL peaks is explored by the Gaussian peak fitting of each spectrum. Note that each PL spectrum is fitted with four Gaussians peaks (P1, P2, P3 and P4) and different samples show different intensities of these peaks based on the growth and annealing conditions. Typically, the blue and green PL emissions from GQDs have been assigned to edge defects and functional groups of GQDs, respectively [7, 21]. However, the nature of edge states has not been distinguished properly through PL analysis and it was found necessary to monitor the evolution of different PL peaks after functionalization and annealing to identify the exact origin of each peak. Interestingly, we found an intriguing correlation between the evolution of the PL peaks with annealing and the new Raman bands discussed in the section 3.6. Note that there is a drastic change in the relative intensities of peaks P1 (at ~407 nm) and peak P2 (at ~440 nm) after annealing in both H_2 and O_2 environment. The relative intensities of peak P1 is reduced significantly after annealing, while that of peak P2 is strongly increased after annealing, and there is a one to one correspondence between the intensities of the two peaks. At high temperatures the zigzag edges convert to the zigzag 5-7 and armchair edges [27], the armchair edges are the most prevalent edge structure among various edge configurations in graphene [55]. The high temperature annealing of GQDs results in the reduction in the zigzag edges and increase the armchair edges in GQDs through the inter-conversion of edges. Thus, the

drastic reduction in the intensity of peak P1 and the concomitant increase in the intensity of peak P2 after annealing clearly signify the conversion of edge states from zigzag to armchair and it allows us to unambiguously distinguish the PL peaks related to zigzag and armchair states.

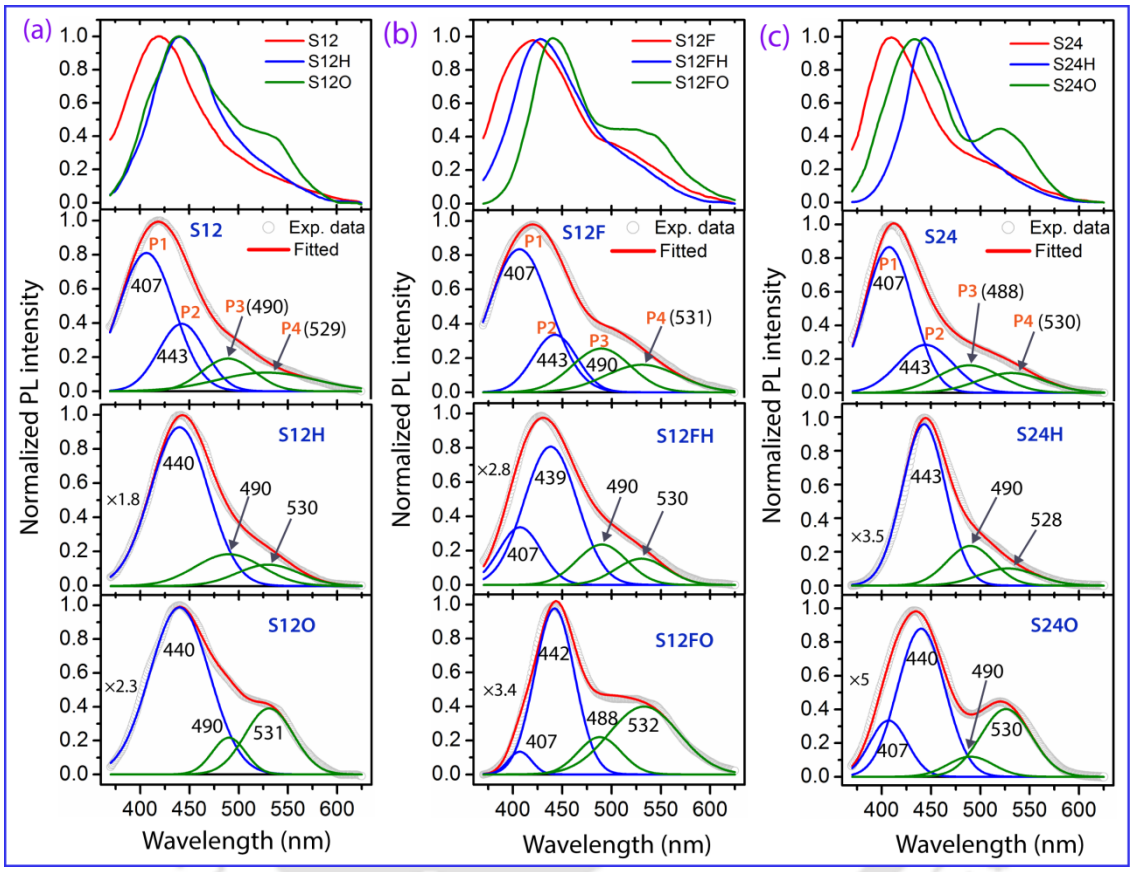

Figure 3.7: PL spectra for various GQDs thin films before and after (H_2 and O_2) annealing. (a-c) Comparison of the PL spectra of with Gaussian fitting before and after annealing of S12, S12F and S24, respectively. Note that the peaks P1 and P2 are significant for the zigzag and armchair edge states, while the P3 and P4 are significant for the COOH/C-OH and C=O/C-O edge functional groups, respectively. All the peak positions are in nm units. The experimental data are shown with symbols and the fitted data are shown with red line in each case.

In order to quantify the relative changes in the density of edge states and functional groups with annealing, we monitored the changes in integrated intensity of PL peak with annealing. **Fig. 3.8(a-c)** shows the relative percentage of each PL band before and after annealing. Importantly, we monitor the conversion of edge states due to the thermal annealing, while the edge functional groups are controlled by the annealing environment (H_2 and O_2). The decrease in the intensity of peak P1 and the concomitant increase in the intensity of peak P2 follow a trend similar to that of the changes in the

Raman D bands of GQDs. Since annealing at 620°C enables to convert the zigzag edges to armchair edges, the decrease in intensity of P1 is due to the decrease in the density/percentage of zigzag edges. Similarly, the strong increase in the intensity of P2 after annealing implies the enrichment of armchair edges in the GQDs. Thus, peaks P1 and P2 at ~407 nm and ~440 nm, respectively, are assigned to the zig-zag (carbene-like, with a triplet ground state being most common) and free armchair sites (carbyne-like, with a singlet ground state most common) in GQDs. At the same time, during the annealing the density of oxygen functional groups is altered, based on the annealing environment. Two green emissions P3 and P4 are attributed to the COOH/C-OH and C=O groups, respectively.

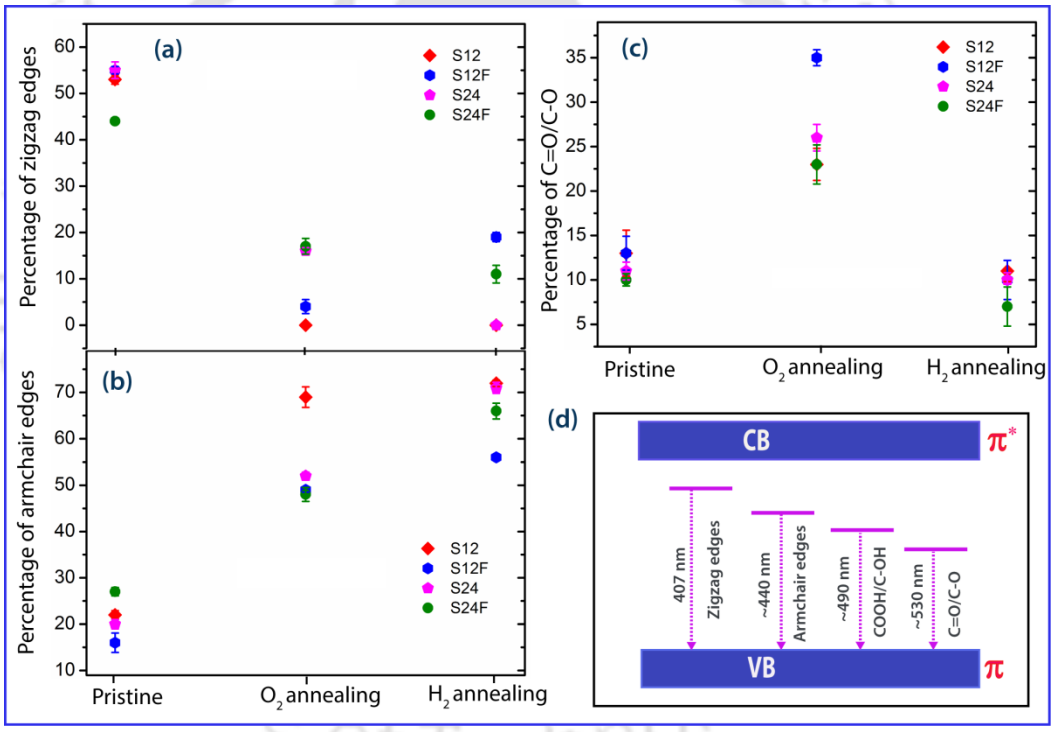

Figure 3.8: Quantitative analysis of edge states (zigzag and armchair) and oxygenated functional groups before and after annealing, as derived from the relative integrated intensities of PL. Relative percentage of (a) zigzag edges, (b) armchair edges, (c) C=O/C-O edge functional groups before and after annealing. (d) Schematic of the band diagram of GQDs showing the edge states and functional groups related transitions giving rise to two blue and two green PL emission bands.

Note that the overall PL intensity is reduced in annealed samples that might be due to the creation of additional defects, e.g., vacancies, pentagon/heptagon defects, and some of these defects may act as a nonradiative recombination centers. These results are consistent with the Raman analysis that showed increased $I_{D'}/I_G$ ratio in the annealed

samples. **Fig. 3.8(a)** shows change in the relative percentage of zigzag edges in pristine and annealed samples, while **Fig. 3.8(b)** shows change in the relative percentage of armchair edges in pristine and annealed samples. **Fig. 3.8(c)** represents that the concentration of C=O/C-O bonds is increased after O_2 annealing, as expected, and it again decreases upon H_2 annealing at 620 °C. We find from the PL analysis that the as-grown samples contain mostly zigzag edges, while the annealed samples contain mostly the armchair edges without any significant presence of zigzag states. The slight increment in the intensity of P3 may be due to the C-H bond formation. Based on these results, we provide a schematic of the energy band diagram of GQDs, as shown **Fig. 3.8(d).** It depicts the edge states and functional groups related transitions giving rise to two blue (P1, P2) and two green (P3, P4) PL emission bands.

3.9. X-ray Photoelectron Spectroscopy Study

In order to gain further insight into the identity of functional groups, XPS study was carried out on the GQDs samples. **Fig. 3.9** represents the XPS core level C1s and O1s spectra of S24 sample before and after annealing. **Fig. 3.9(a-c)** shows the C1s spectrum of S24, S24H and S24O samples, respectively. Each of the C1s spectra is fitted with five Gaussian peaks to extract the peak parameters properly and the fitted parameters are listed in **Table 3.2.** The peaks centered at 284.5, 286.14, 287.5, 290.0, and 293.7 eV are the characteristic peaks assigned to sp^2 bonded carbon (C=C), C-O (ether), carbonyl (C=O), carboxylic (COOH) and shake up satellite peak (π-π^*), respectively [7, 10]. It is evident from the **Table 3.2** that the relative percentages of C=C, C-O (ether), C=O and COOH in S24 sample are 39%, 22%, 13% and 16%, respectively. Interestingly, after annealing the percentage of edge functional groups in S24H and S24O is drastically changed with respect to that of S24. It implies that the functional groups in GQDs can be carefully tuned and monitored by the H_2 and O_2 gas annealing, which leads to the significant change in the green PL emission (P3, P4) discussed in the previous section. Further, we observed an increased concentration of C=C bonds in S24H, as expected. Since some of the edge functional groups are destroyed during the annealing, it results in the relative enhancement of C=C bonds. Similarly, there is a substantial change in the percentage of the C-O (ether) group in S24H and S24O as compared to that of S24. Note that the as-grown GQDs contain edge defect, ether and edge functional groups (**Fig. 3.4**).

The atomic percentage of C-O (ether) group in S24 is 22%, while it reduces by more than half to 9% and 7% for S24H and S24O, respectively. This is possibly due to the fact that ether functional group has a lower thermal stability than the other functional groups [56]. The high temperature (620 ℃) annealing results in the loss of oxygen atoms from the ether group and the vacancy defects are formed and/or edges reconstruct to the heptagon and pentagon defects, the so called stone-wall (S-W) defects [27, 49]. Thus, the formation of vacancy and/or heptagon and pentagon defects is more favorable in the annealed samples. This result is in good agreement with the Raman analysis that showed increased intensity ratio of I_D/I_G after annealing (see **Fig. 3.5** and **Table 3.1**). During the annealing, besides

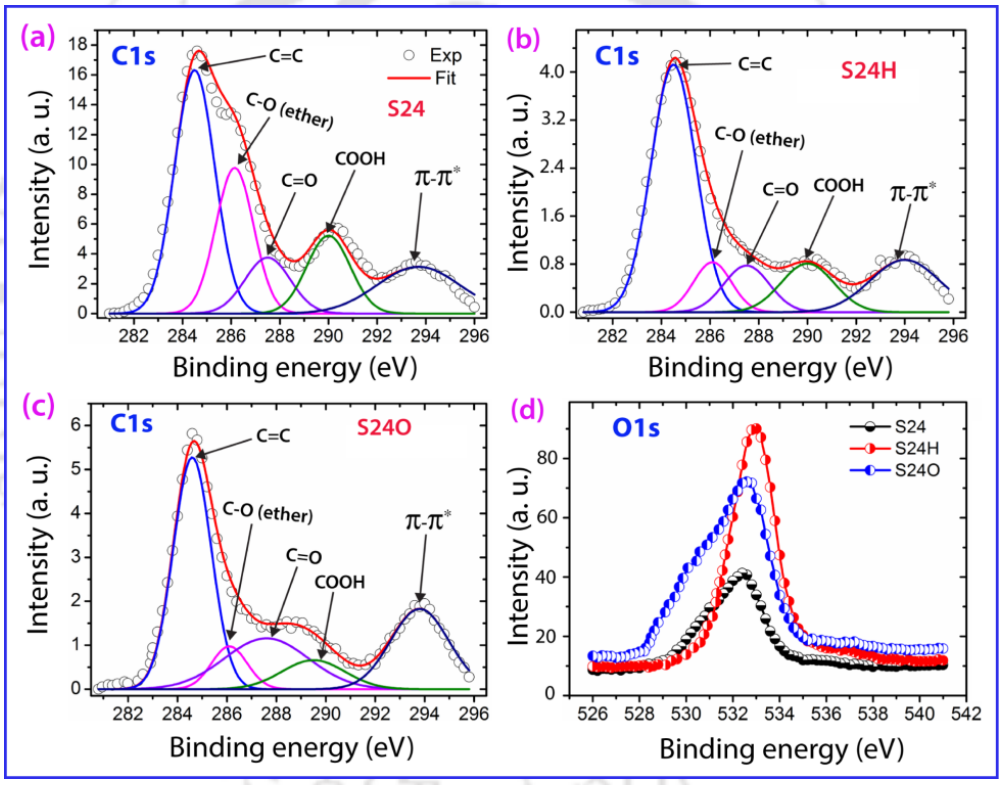

Figure 3.9: Core level XPS spectra for GQDs thin films. (a-c) C1s spectra with Gaussian peak fitting for S24, S24H, and S24O samples, respectively. (d) Comparison of the O1s spectra for S24 sample before and after O_2 and H_2 annealing.

the creation of crystalline defects, the conversion of edge states is very efficient in the GQDs, as evident from the Raman and PL analyses. Note that the percentage of C=O functional group in S24 sample is 10%, while it is doubled in S24O due to O_2 annealing. However, atomic percentage of C=O functional group in S24H sample does not show any substantial change, which might be due to the higher stability of C=O groups [50]. Note that H_2 (purity 99.9%) annealing may also cause partial removal of oxygen functional groups.

Besides the C1s spectrum, O1s XPS spectrum of GQDs samples further augmented the increased concentration of oxygen functional groups in GQDs after O_2 annealing. **Fig. 3.9(d)** shows the comparison of O1s spectra for S24 before and after annealing. The integrated intensity of O1s spectrum for the S24O sample is 1.78 times higher than that of pristine sample, which reveals the attachment of oxygen atoms at the edge/in-plane sites of GQDs. This is consistent with the enhanced intensity of green PL (530 nm) and enhanced intensity of FTIR band related to the oxygenated functional groups after the O_2 annealing. Note that the integrated intensity of O1s spectrum for the S24H sample is 1.56 times higher than that of pristine samples. This might be due to the impurity content in the H_2 gas, adsorbed moisture and residual (C=O) functional groups that strongly bind to the GQDs edge sites before the measurement. This is consistent with the considerable green PL (peak P3) emission after the hydrogenation.

Table 3.2: Summary of the results of Gaussian peak fitting of Core level C1s XPS spectrum for S24, S24H and S24O samples.

Sample Code	Peak Centre (eV)					Atomic percentage (%)				
	C=C	*Ether (C-O)*	*C=O*	*COOH*	*π-π**	*C=C*	*Ether (C-O)*	*C=O*	*COOH*	*π-π**
S24	284.50	286.14	287.50	290.00	293.70	39	22	10	13	16
S24H	284.50	286.10	287.50	290.00	293.99	52	9	10	12	17
S24O	284.59	286.10	287.60	289.80	293.80	42	7	20	9	22

3.10. FTIR Analysis

Fig. 3.10 shows the characteristic FTIR spectra of S12F before and after H_2 and O_2 annealing. It is evident from the spectra that substantial change in the intensity of various functional groups occurs after the annealing. All the samples show the characteristic IR active vibrational modes of sp^2 carbon and oxygenated functional groups that are attached at the edge sites of GQDs. Firstly, the vibrational mode at ~1000-1100 cm^{-1} is related to the C-O stretching vibrations [10]. The bands at ~1360 cm^{-1} and ~1580 cm^{-1} are attributed to the C-O epoxy deformation and in-plane stretching vibrations of sp^2 hybridized carbon atoms (C=C), respectively [9, 29]. Besides these, the edge functionalized oxygen functional groups can be clearly distinguished from the FTIR spectra. The vibrational modes at ~1650 and ~1700 cm^{-1} originate from the COOH and C=O edge functional groups [10, 29].

Interestingly, the intensity of C-O vibrational mode (1000-1100 cm^{-1}) is considerably increased for O_2 annealed sample, suggesting the covalent attachment of oxygen atoms at the edge sites in GQDs. Some of the low intense vibrational bands at 1067, 1104, 1122, 1159, 1237 and 1296 cm^{-1} may originate from single or bi vacancies in hexagonal ring structure of GQDs [35]. Note that our Raman analysis also suggested some crystal defects (vacancy and SW) in the GQDs samples. Note that the oxygenated GQDs thin films show considerable C-O epoxy bonds at the basal plane, although GQDs possess high ratio of edge to basal plane carbon atoms.

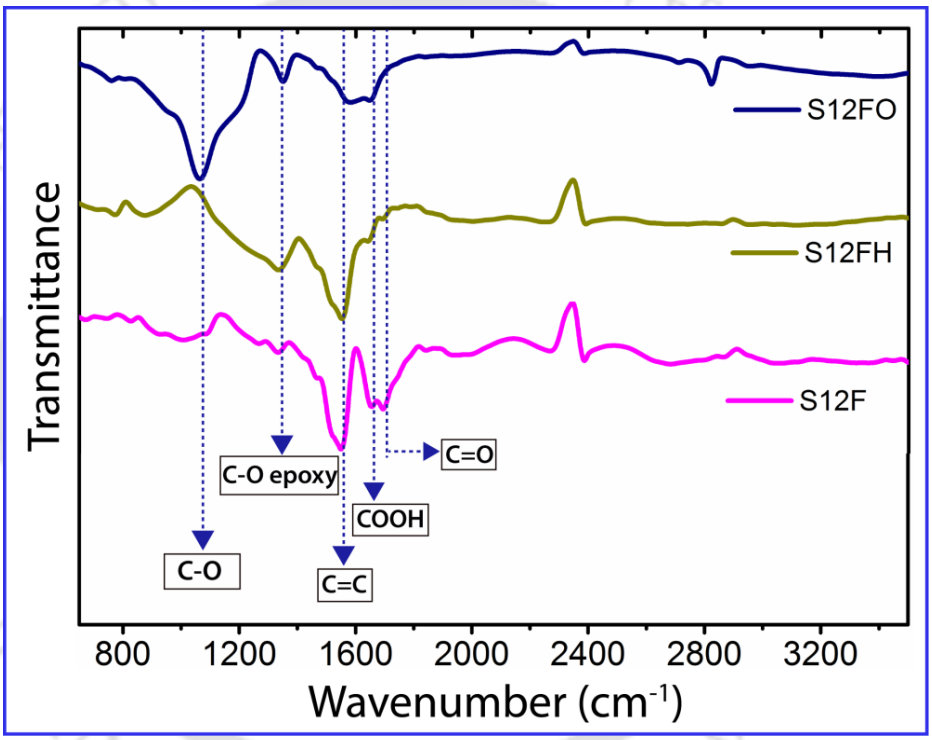

Figure 3.10: FTIR transmittance spectra and associated vibrational modes of S12F before and after annealing showing the sp^2 carbon (C=C) and oxygenated edge functional groups (COOH, C=O/C-O).

3.11. Summary & Conclusions

1. We have prepared GQDs by hydrothermal method using two different precursors.

2. We proposed a new mechanism for the formation of nearly circular/ quasi circular shaped GQDs from the TEM imaging of the GQDs formed at different stages of hydrothermal reaction.

3. In-plane epoxy (C-O-C) functional groups act as an active channel for the cutting of OGO into GQDs, which was corroborated from the TGA/DTG results of OGO and rGO materials.

4. In addition to the characteristic Raman bands, we observed two new Raman bands in GQDs at ~1260 and ~1440 cm^{-1} and these are assigned to COOH/C-OH and C=O/C-O edge oxygenated functional groups in GQDs, respectively, for first time.

5. The conversion of edge sites in GQDs by thermal annealing is reported for the first time. The blue PL emissions at ~407 and ~440 nm are assigned to the zigzag and armchair free edge states in GQDs, while the two green PL emissions peaked at ~490 and ~530 nm are attributed to the COOH/C-OH and C=O/C-O edge oxygenated functional groups attached to GQD edges, respectively.

6. We established a direct correlation between the Raman and PL analysis of GQDs for the first time, which is consistent with the XPS and FTIR analyses.

References

1. K. A. Ritter and J. W. Lyding, *Nature Materials*, 2009, **8**, 235-242.
2. L. R. Radovic and B. Bockrath, *Journal of the American Chemical Society*, 2005, **127**, 5917-5927.
3. K. Lingam, R. Podila, H. Qian, S. Serkiz and A. M. Rao, *Advanced Functional Materials*, 2013, **23**, 5062-5065.
4. M. A. Montes-Morán, D. Suárez, J. A. Menéndez and E. Fuente, *Carbon*, 2004, **42**, 1219-1225.
5. L. A. Ponomarenko, F. Schedin, M. I. Katsnelson, R. Yang, E. W. Hill, K. S. Novoselov and A. K. Geim, *Science*, 2008, **320**, 356-358.
6. L. R. Radovic, *Journal of the American Chemical Society*, 2009, **131**, 17166-17175.
7. S. Zhu, J. Zhang, X. Liu, B. Li, X. Wang, S. Tang, Q. Meng, Y. Li, C. Shi, R. Hu and B. Yang, *RSC Advances*, 2012, **2**, 2717-2720.
8. D. Pan, J. Zhang, Z. Li and M. Wu, *Advanced Materials*, 2010, **22**, 734-738.
9. Y. Sun, S. Wang, C. Li, P. Luo, L. Tao, Y. Wei and G. Shi, *Physical Chemistry Chemical Physics*, 2013, **15**, 9907-9913.

10. J. Peng, W. Gao, B. K. Gupta, Z. Liu, R. Romero-Aburto, L. Ge, L. Song, L. B. Alemany, X. Zhan, G. Gao, S. A. Vithayathil, B. A. Kaipparettu, A. A. Marti, T. Hayashi, J.-J. Zhu and P. M. Ajayan, *Nano Letters*, 2012, **12**, 844-849.
11. D. Qu, M. Zheng, L. Zhang, H. Zhao, Z. Xie, X. Jing, R. E. Haddad, H. Fan and Z. Sun, *Scientific Reports*, 2014, **4**, 5294.
12. L. Tang, R. Ji, X. Cao, J. Lin, H. Jiang, X. Li, K. S. Teng, C. M. Luk, S. Zeng, J. Hao and S. P. Lau, *ACS Nano*, 2012, **6**, 5102-5110.
13. M. W. Lee, J. Kim and J. S. Suh, *RSC Advances*, 2015, **5**, 67669-67675.
14. J. Kim and J. S. Suh, *ACS Nano*, 2014, **8**, 4190-4196.
15. J.-L. Li, K. N. Kudin, M. J. McAllister, R. K. Prud'homme, I. A. Aksay and R. Car, *Physical Review Letters*, 2006, **96**, 176101.
16. L. Wang, S.-J. Zhu, H.-Y. Wang, S.-N. Qu, Y.-L. Zhang, J.-H. Zhang, Q.-D. Chen, H.-L. Xu, W. Han, B. Yang and H.-B. Sun, *ACS Nano*, 2014, **8**, 2541-2547.
17. K. Habiba, V. I. Makarov, J. Avalos, M. J. F. Guinel, B. R. Weiner and G. Morell, *Carbon*, 2013, **64**, 341-350.
18. F. Liu, M.-H. Jang, H. D. Ha, J.-H. Kim, Y.-H. Cho and T. S. Seo, *Advanced Materials*, 2013, **25**, 3657-3662.
19. V. Gupta, N. Chaudhary, R. Srivastava, G. D. Sharma, R. Bhardwaj and S. Chand, *Journal of the American Chemical Society*, 2011, **133**, 9960-9963.
20. S. Zhu, J. Zhang, S. Tang, C. Qiao, L. Wang, H. Wang, X. Liu, B. Li, Y. Li, W. Yu, X. Wang, H. Sun and B. Yang, *Advanced Functional Materials*, 2012, **22**, 4732-4740.
21. G. Sandeep Kumar, R. Roy, D. Sen, U. K. Ghorai, R. Thapa, N. Mazumder, S. Saha and K. K. Chattopadhyay, *Nanoscale*, 2014, **6**, 3384-3391.
22. J. Du, H. Wang, L. Wang, S. Zhu, Y. Song, B. Yang and H. Sun, *Journal of Materials Chemistry C*, 2016, **4**, 2235-2242.
23. H. Yoon, Y. H. Chang, S. H. Song, E.-S. Lee, S. H. Jin, C. Park, J. Lee, B. H. Kim, H. J. Kang, Y.-H. Kim and S. Jeon, *Advanced Materials*, 2016, **28**, 5255-5261.
24. Y. Shin, J. Park, D. Hyun, J. Yang, J.-H. Lee, J.-H. Kim and H. Lee, *Nanoscale*, 2015, **7**, 5633-5637.

25. J. Chen, B. Yao, C. Li and G. Shi, *Carbon*, 2013, **64**, 225-229.
26. S. Stankovich, D. A. Dikin, R. D. Piner, K. A. Kohlhaas, A. Kleinhammes, Y. Jia, Y. Wu, S. T. Nguyen and R. S. Ruoff, *Carbon*, 2007, **45**, 1558-1565.
27. K. He, A. W. Robertson, Y. Fan, C. S. Allen, Y.-C. Lin, K. Suenaga, A. I. Kirkland and J. H. Warner, *ACS Nano*, 2015, **9**, 4786-4795.
28. S. Saxena, T. A. Tyson, S. Shukla, E. Negusse, H. Chen and J. Bai, *Applied Physics Letters*, 2011, **99**, 013104.
29. R. K. Biroju, G. Rajender and P. K. Giri, *Carbon*, 2015, **95**, 228-238.
30. T. Fan, W. Zeng, W. Tang, C. Yuan, S. Tong, K. Cai, Y. Liu, W. Huang, Y. Min and A. J. Epstein, *Nanoscale Research Letters*, 2015, **10**, 55.
31. C. Gómez-Navarro, J. C. Meyer, R. S. Sundaram, A. Chuvilin, S. Kurasch, M. Burghard, K. Kern and U. Kaiser, *Nano Letters*, 2010, **10**, 1144-1148.
32. S. H. Dave, C. Gong, A. W. Robertson, J. H. Warner and J. C. Grossman, *ACS Nano*, 2016, **10**, 7515-7522.
33. A. Lerf, H. He, M. Forster and J. Klinowski, *The Journal of Physical Chemistry B*, 1998, **102**, 4477-4482.
34. E. Fuente, J. A. Menéndez, M. A. Díez, D. Suárez and M. A. Montes-Morán, *The Journal of Physical Chemistry B*, 2003, **107**, 6350-6359.
35. M. Acik, G. Lee, C. Mattevi, A. Pirkle, R. M. Wallace, M. Chhowalla, K. Cho and Y. Chabal, *The Journal of Physical Chemistry C*, 2011, **115**, 19761-19781.
36. Z. Li, W. Zhang, Y. Luo, J. Yang and J. G. Hou, *Journal of the American Chemical Society*, 2009, **131**, 6320-6321.
37. D. V. Kosynkin, A. L. Higginbotham, A. Sinitskii, J. R. Lomeda, A. Dimiev, B. K. Price and J. M. Tour, *Nature*, 2009, **458**, 872-876.
38. T. Sun and S. Fabris, *Nano Letters*, 2012, **12**, 17-21.
39. K. N. Kudin, B. Ozbas, H. C. Schniepp, R. K. Prud'homme, I. A. Aksay and R. Car, *Nano Letters*, 2008, **8**, 36-41.
40. S. Claramunt, A. Varea, D. López-Díaz, M. M. Velázquez, A. Cornet and A. Cirera, *The Journal of Physical Chemistry C*, 2015, **119**, 10123-10129.
41. A. Sadezky, H. Muckenhuber, H. Grothe, R. Niessner and U. Pöschl, *Carbon*, 2005, **43**, 1731-1742.

42. A. C. Ferrari and J. Robertson, *Physical Review B*, 2000, **61**, 14095-14107.
43. S. L. H. Rebelo, A. Guedes, M. E. Szefczyk, A. M. Pereira, J. P. Araujo and C. Freire, *Physical Chemistry Chemical Physics*, 2016, **18**, 12784-12796.
44. L. G. Cançado, M. A. Pimenta, B. R. A. Neves, M. S. S. Dantas and A. Jorio, *Physical Review Letters*, 2004, **93**, 247401.
45. C. Casiraghi, A. Hartschuh, H. Qian, S. Piscanec, C. Georgi, A. Fasoli, K. S. Novoselov, D. M. Basko and A. C. Ferrari, *Nano Letters*, 2009, **9**, 1433-1441.
46. D. Bischoff, J. Güttinger, S. Dröscher, T. Ihn, K. Ensslin and C. Stampfer, *Journal of Applied Physics*, 2011, **109**, 073710.
47. Y. You, Z. Ni, T. Yu and Z. Shen, *Applied Physics Letters*, 2008, **93**, 163112.
48. R. Nishinakagawa, K. Matsuda, T. Arai, A. Sawada and T. Terashima, *AIP Advances*, 2013, **3**, 092111.
49. C. Hyun, J. Yun, W. J. Cho, C. W. Myung, J. Park, G. Lee, Z. Lee, K. Kim and K. S. Kim, *ACS Nano*, 2015, **9**, 4669-4674.
50. A. Ganguly, S. Sharma, P. Papakonstantinou and J. Hamilton, *The Journal of Physical Chemistry C*, 2011, **115**, 17009-17019.
51. R. Balog, B. Jorgensen, L. Nilsson, M. Andersen, E. Rienks, M. Bianchi, M. Fanetti, E. Laegsgaard, A. Baraldi, S. Lizzit, Z. Sljivancanin, F. Besenbacher, B. Hammer, T. G. Pedersen, P. Hofmann and L. Hornekaer, *Nat Mater*, 2010, **9**, 315-319.
52. B. Dippel, H. Jander and J. Heintzenberg, *Physical Chemistry Chemical Physics*, 1999, **1**, 4707-4712.
53. D. Wang, L. Zhu, J. F. Chen and L. Dai, *Nanoscale*, 2015, DOI: 10.1039/C5NR01734C.
54. M. Wimmer, A. R. Akhmerov and F. Guinea, *Physical Review B*, 2010, **82**, 045409.
55. B. Song, G. F. Schneider, Q. Xu, G. Pandraud, C. Dekker and H. Zandbergen, *Nano Letters*, 2011, **11**, 2247-2250.
56. D. R. Dreyer, S. Park, C. W. Bielawski and R. S. Ruoff, *Chemical Society Reviews*, 2010, **39**, 228-240.

Chapter 4

Solvent Dependent Growth of Luminescent Graphene Quantum Dots and Its Application in the Bio-Imaging of Cancer Cells

In this chapter, we discuss the effect of solvent on the synthesis of graphene quantum dots (GQDs) that are highly fluorescent and its application in bio-imaging of cancer cells. The edge site and functional groups of GQDs are controlled by the solvent assisted synthesis and monitored by the Raman spectroscopy. The oxygen functional groups attachment at the edge and in-plane sites of GQDs are probed by using thermogravimetric analyses. We elucidate the origin of visible photoluminescence (PL) emission from GQDs in liquid media. The charge recombination dynamics is probed from time resolved PL analysis. We have achieved a high PL quantum yield of 32% from the GQDs. GQDs are used as fluorescent markers to study the bio-imaging of different cancer cell lines A-375 and HeLa. The incorporation of GQDs into the cancer cells and their bio-compatibility are discussed.

4.1. Introduction

In recent years, research on GQDs have drawn massive attention due to their low toxicity, excellent biocompatibility, low cost, high resistance to photobleaching, and an abundance of raw materials in nature [1-5]. Due to these exceptional properties, GQDs are considered to be promising for replacing the conventional semiconductor QDs [6]. In addition, GQDs offer particular advantages over the other carbon nanomaterials due to the pronounced quantum confinement effect, plenty of edge states and functional groups [7-10]. The abundance of edge states and oxygenated functional groups play a major role in various applications ranging from sensors, bioimaging, memory, energy and environment [1, 11-16] and so on. The PL emission arises mainly from the size effect, edge sites and oxygenated functional group defects in GQDs. Generally, the PL mechanism from GQDs is explained on the basis of intrinsic states (blue PL) and defect states emission (green PL).The intrinsic states arise from the size/edge defects where the recombination of electron-hole

pairs takes place, while the defects states correspond to the attachment of functional groups [3, 9, 17-19]. The effect of solvent on the synthesis of GQDs and understanding the PL mechanism of GQDs are important for optoelectronic, drug delivery and bio-imaging applications. In this chapter, we present the synthesis of GQDs using three different solvents and studied its PL mechanism when dispersed in liquid media. We explore the bright blue emission of GQDs in confocal imaging of A-375 and HeLa cell lines and assess the bio-compatibility of GQDs.

4.2. Experimental Details

4.2.1. Synthesis and Functionalization of GQDs

For the synthesis of GQDs, oxidized graphene oxide (OGO) is used as precursor material and dimethyl formamide (DMF), dimethyl sulfoxide (DMSO) and water are used as solvents. The details of the synthesis of graphene oxide (GO) and OGO was discussed in **Chapter 3, section 3.1.** For the GQDs synthesis, 1mg of OGO is mixed with 0.1 mL of DMF and ultrasonicated for a few minutes to obtain the uniform dispersion. Further, this solution was transferred into a Teflon lined autoclave (100 mL) and heated at 200 °C for 7 h. The sample code is labelled as GQD-DMF. The synthesis procedure for GQDs using DMSO is similar to the DMF, except the reaction is performed in open atmosphere under the fume wood, since the vapour temperature of DMSO is higher than that of DMF. After filtration (PTFE, 0.22μm), and subsequent washing with DI water, the solution was dried. GQDs grown using DMSO solvent is labelled as GQD-DMSO. The synthesis procedure of GQDs and functionalization by using hydrothermal reaction were discussed in **Chapter 3, section 3.2.3** and **3.2.4**. The as-grown and PEG functionalized GQDs samples are denoted as S24 and S24F, respectively. In all the chemical reactions, temperature is fixed based on the TGA/DTG result of OGO, as discussed in **Chapter 3.**

4.2.2. Determination of PL Quantum Yield

PL quantum yield (QY) of the GQDs is calculated by comparing of the integrated PL intensity of the GQDs to that of the standard quinine sulphate (QS). QS was chosen as a standard dye for QY measurements due to the fact that the PL emission spectrum of QS is close to that of the GQDs and QY of QS is 0.54. For the QY measurements, QS in 0.1 M H_2SO_4 solution is prepared. The optical absorbance was kept below 0.05 to avoid inner filter effects. The QY of the GQDs was calculated using the following formula [20]:

$$\phi_x=\phi_{st}\left(\frac{I_x}{I_{st}}\right)\left(\frac{n_x^2}{n_{st}^2}\right)\left(\frac{A_{st}}{A_x}\right) \quad \ldots\ldots\ldots\ldots\ldots\ldots (4.1)$$

Where ϕ is the QY, I is the integrated PL intensity, A is the optical density and n is the refractive index of the solvent (water). The subscripts 'st' and 'x' refers to the standard reference and GQD sample, respectively. The PL measurements were carried out with a commercial fluorometer (Fluromax-4, Horiba)

4.2.3. Cell Culture

The cancer cell lines, such as A-375 (human malignant melanoma cells), HeLa (human cervical carcinoma) and normal cells HEK-293 (human embryonic kidney cells) were cultured in Dulbecco's modified Eagle's medium supplemented with L-glutamine (4 mM), 10,000 units penicillin, streptomycin (10 mg/mL), and 10% (v/v) fetal bovine serum (obtained from PAA Laboratories, Austria). This was incubated in 5% CO_2 humidified incubator at 37 °C for 24h.

4.2.4. Procedure for the Cell Viability Test

The viability effects of different GQDs on cancer cells lines were assessed by using a MTT (3-(4,5-dimethylthiazol-2-yl)-2,5-diphenyltetrazolium bromide) dye assay. For this study, 5×10^3 of A-375 cells/well were seeded in a 96-well microtiter plate. Further, these cells were allowed to grow overnight by maintaining the same medium and condition as discussed in the previous section. Then, different GQDs samples with different concentrations were added in each well in triplicates and incubated for 24 h. Afterwards, MTT dye was added in each well to find out the number of viable cells. The viable cells reduce the yellow tetrazolium MTT by the action of dehydrogenase enzymes, to an insoluble, coloured (dark purple) formazan product. The resulting intracellular purple formazan crystals are solubilized in DMSO. The solution has an absorbance (A) peak at 570 nm. Note that similar procedure is followed for MTT assay studies of HeLa cell lines using different GQDs samples. The % of cell viability is using the following equation.

$$\%\ \text{of cell viability}=\frac{(A_{570}-A_{655})_{\text{sample}}}{(A_{570}-A_{655})_{\text{control}}}\text{x}100 \quad \ldots\ldots\ldots\ldots\ldots\ldots (4.2)$$

Where the control data was obtained in the absence of GQDs and sample data was obtained in the presence of GQDs. Each experiment was performed three times and the average value is calculated and presented.

4.2.5. Preparation of Cells for Confocal Imaging

1×10^5 number of A-375 cells were grown on a coverslip in a 35 mm culture dish and incubated in a 5% CO_2 humidified incubator (37 °C for 24 h). After attachment of cells, the samples GQD-DMF, GQD-DMSO, S24 and S24F (concentration, 26.64 µg/mL) were added and incubated for 4h under similar conditions as mentioned above. Then, they were washed with phosphate-buffered saline for 2 times and were fixed with 4% formaldehyde (incubation at 37 °C for 10 min). The fixed samples on the cover slip were taken and mounted onto glass slides. The samples were then observed under a Zeiss LSM 880 confocal microscope with the excitation at 405 nm. Similarly the other cell lines such as HeLa, HEK-293 and control cells (without any addition of GQDs) were imaged under identical conditions.

4.3. XRD and TEM Analysis

Fig. 4.1(a-b) depicts the XRD pattern of GQD-DMSO and S24 samples. It is evident from the figure that both the samples exhibited the (002) reflection peak, which is a signature of hexagonal lattice structure of graphitic material. The (002) XRD peak is very strong evidence for graphitic structure and represents the inter layer distance variation in graphitic materials. We estimated the interlayer distance for GQD-DMSO and S24. The (002) peak centre for samples GQD-DMSO and S24 are at 2θ= 26.34 and 26.08°, respectively. The corresponding interlayer distance (d) of (002) peak is at 3.38 and 3.41 Å for samples GQD-DMSO and S24, respectively. The interlayer distance in graphite is 3.40 Å [1]. The difference in d spacing for the samples is possibly due to the strain. Besides, the emerging weak reflection peaks at 2θ= 43 and 45° in **Fig. 4.1(b)** and corresponding planes (100) and (110) are confirm the in-plane disorder structure in GQDs samples [21].

Next, the morphological features of GQDs were studied by TEM imaging. **Fig. 4.1(c-e)** shows the TEM images of the GQD samples. **Fig. 4.1(c)** shows the TEM image of GQD synthesized using DMF solvent and the average size of the GQDs in this sample is 5.2 nm**. Fig. 4.1(d)** shows the TEM image of GQD synthesized by using DMSO solvent and the average size of the GQDs is 8.2 nm. The TEM image of the hydrothermal process grown GQD (sample S24) TEM image is shown in **Fig. 4.1(e)** and the average size of the GQD is 5 nm.

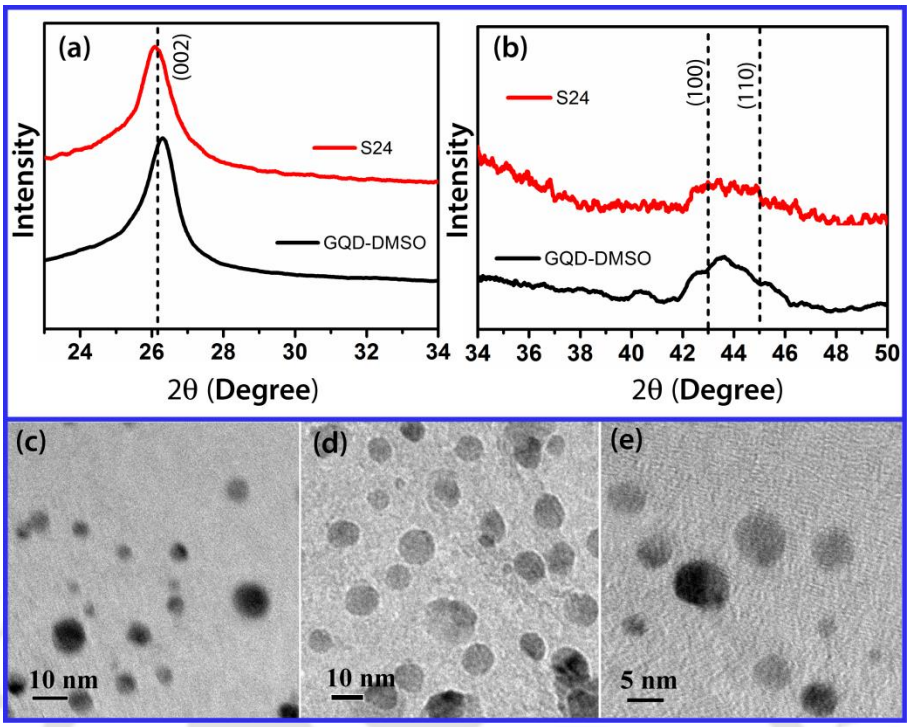

Figure 4.1: XRD pattern and TEM imaging of GQDs. (a,b) XRD pattern of GQD, GQD-DMSO and S24 samples. TEM images of (c) GQD, (d) GQD-DMSO and (e) S24 samples.

4.4. Raman Analysis

In order to understand the solvent dependent structural features of GQDs, we have performed the Raman measurements on GQDs samples using 488 nm laser. **Fig. 4.2** depicts the comparison of the Raman spectra of GQD-DMF, GQD-DMSO, S24 and S24F samples. All the GQD samples show the characteristic Raman bands such as G, D and D'. The D band is very sensitive to the graphene edges [22-26]. Note that the origin of bands was discussed in **Chapter 1**. In order to insight in to the nature of edges, we estimate the intensities of Raman D to G bands for all the samples. GQD synthesized by DMF solvent has the Raman I_D/I_G ratio of 1.08, while the GQD synthesized by DMSO solvent has ratio of 0.86. This indicates that both the samples have distinct edge configuration. Note that the D band intensity is high for armchair edges. Similarly the Raman I_D/I_G ratio for S24 is 0.35, which signifies the dominance of zigzag edge sites in S24. Interestingly, after in-situ functionalization (S24F), the Raman I_D/I_G ratio for S24F is increased to 0.53. This is because some of the zigzag edge sites are passivated by the PEG and results in the reduction of zigzag edges. It implies that the effect of chemical functionalization induces the structural changes in GQDs. Besides, D' band is due to the vacancies and/or pentagonal and octagonal defects, usually referred as zigzag 5-7 defects. [19-21] The relative

intensity ratio I_D/I_G values for GQD-DMF, GQD-DMSO, S24 and S24F are 1.07, 0.67, 0.34 and 0.43, respectively. These results suggest the presence of carbon vacancies and/or pentagonal and octagonal defects in the samples. The Raman I_D/I_G values of the samples are provided in **Table 4.1.** These results suggest that we can manipulate the edge defects of the GQDs by using different solvents during synthesis.

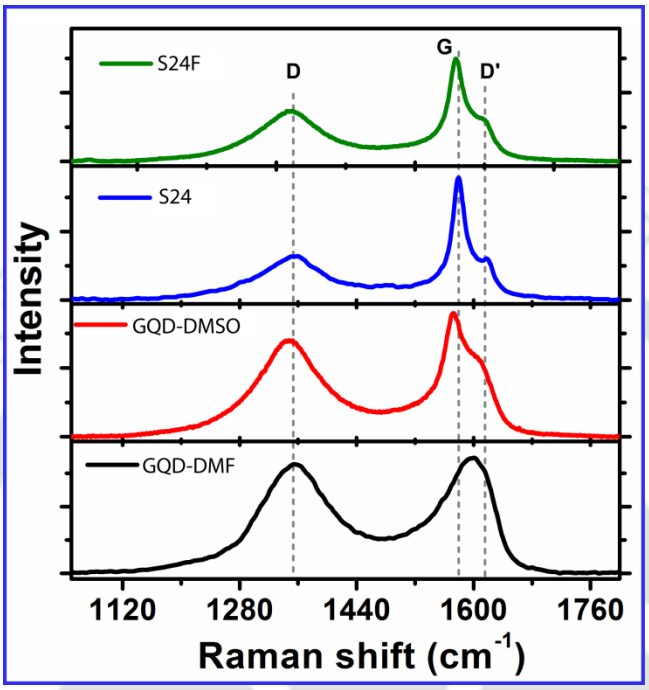

Figure 4.2: Raman spectra of GQD-DMF, GQD-DMSO, S24 and S24F samples. The characteristic Raman bands D, G, and D' are labelled in the figure.

4.5. Thermogravemetric Analysis

The structural changes of the GQDs due to the attachment of different oxygen functional groups are analysed by TGA/DTG profiles. **Fig. 4.3(a-c)** shows the TGA/DTG profiles of GQD-DMF, S24 and S24F respectively. **Fig. 4.3(a)** represents the TGA/DTG profiles of GQD-DMF and the multiple DTG peaks arises due to the loss of different oxygenated functional groups and different forms of carbon in GQD. First, low temperature DTG peaks at 193 and 265 ℃ suggests the loss of hydroxyl/ in-plane epoxy and C-O ether functional groups from GQDs, respectively [27]. The DTG peaks centred at 276 and 297 ℃ are due to the loss of COOH related functional groups from GQDs [27, 28]. The other DTG peaks at 352, 466 and 646 ℃ are due to the loss of C=O related functional groups, sp^3 and sp^2 carbon, respectively [27, 28]. In case of S24, low temperature peak at 258 ℃ is due to the loss of epoxy/C-O (ether) related functional group and other two peaks at 319, 360 ℃ are

due to the COOH and C=O functional groups, respectively [27, 28]. The DTG peaks at 476 and 715℃ signifies the loss of sp^3 and sp^2 carbon domains in S24, respectively. Further, chemical functionalized sample (S24F) exhibited the multiple DTG peaks due to the additional functional groups attachment due to the PEG functionalization. Here the DTG peaks are slightly modified from that of S24, indicating the attachment of functional

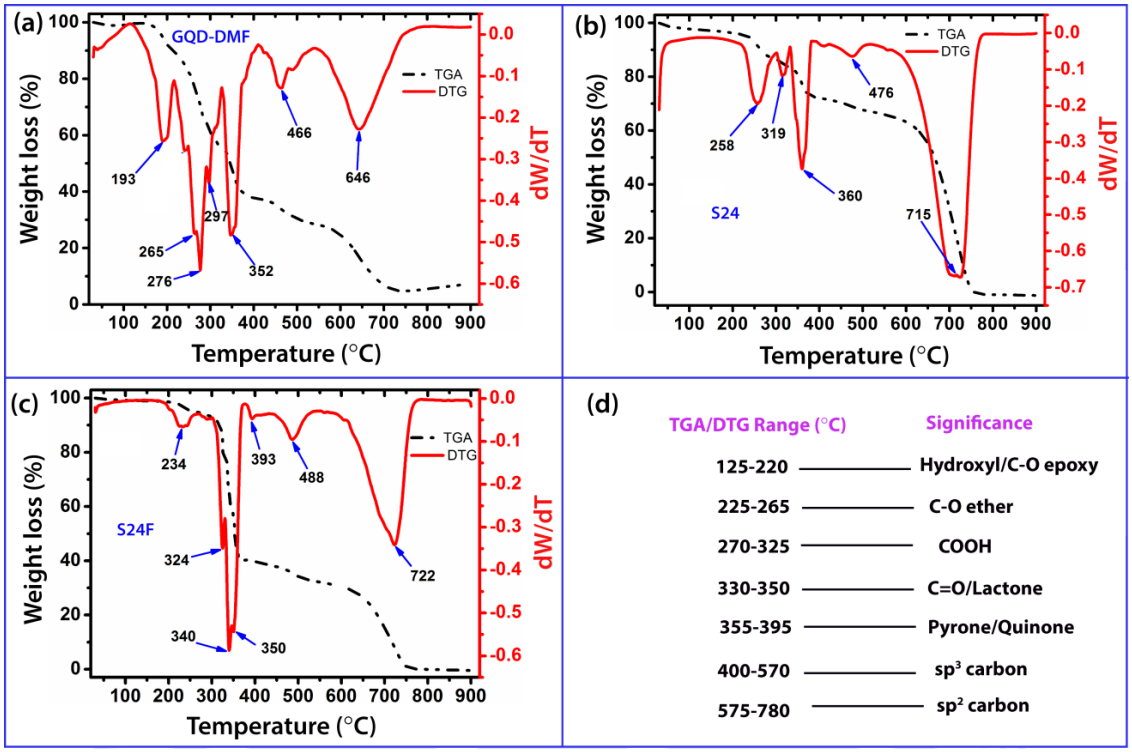

Figure 4.3: TGA/DTG profile of the samples; (a) GQD-DMF, (b) S24 and (c) S24F. (d) A summary of the TGA/DTG peaks and their significance.

groups at different position of carbon atom in GQDs. **Fig. 4.3(c)** depicts the TGA/DTG profiles of S24F sample. The DTG peak 234 ℃ is due to the loss of epoxy/C-O (ether) related functional group. This suggesting the epoxy/ ether functional groups is reduced in S24F as compare to the S24. In addition, however, there are major changes in the C=O related functional groups after PEG functionalization. The DTG peak at 324 ℃ is due to the COOH functional groups as discussed above [27, 28]. There are additional DTG peaks in the region 340-393 ℃, which are due to the loss of different form of highly stable C=O bonds in quinone, lactone and pyrone groups. Note that the quinone, lactone and pyrone groups are attached at the edges of GQDs. The other two DTG peaks at 488 and 722 ℃ are attributed to the sp^3 and sp^2 carbon, respectively [27, 28] . Based on our results, we propose a tentative range for loss of different oxygenated functional groups and different

form of carbon as shown in **Fig. 4.3(d)**. These results clearly suggest the effect of functionalization and distinct oxygen functional groups in GQDs. These results are consistent with the optical studies of the samples discussed in the below section.

4.6. Optical Properties

The optical absorption spectra of GQDs are shown in **Fig. 4.4(a-b).** It shows the two main optical absorption bands; one is in the ultra-violet (UV) region 261-288 nm is due to the π-π* transition of sp^2 C=C skeletal framework and other absorption tail extending from UV to visible region is attributed to the n- π* transitions of oxygen functional groups in GQDs [28, 29]. Although the average size of the GQD-DMF and S24 is comparable, the π-π* transition peak center is different. For GQD-DMF and S24 the π-π* transition peaks appeared at ~268 and ~276 nm, respectively. This might be due to the effect of solvents on the GQDs synthesis [4].

In **Chapter 3**, we have elucidated the origin of PL emission from GQDs thin films. The PL measurements of GQDs thin film allowed us to study the origin of PL emission from GQDs, where the effect of solvent on resulting PL is easily discarded. The PL of GQDs is strongly dependent on the defects state of the GQDs. In this chapter, in order to understand the origin of PL from GQDs in liquid media, we perform the PL measurement in different solvents which are having different dielectric constants (ε). The liquid samples are excited with a Xe lamp at 350 nm wavelength. **Fig. 4.4(c)** shows the PL spectra of S24 in water, DMSO and THF solvents. Interestingly, the PL spectra of S24 shows distinctly different spectrum in different solvents, indicating the PL of GQDs strongly depends on the solvent. This further elucidate that one of the origin of PL from the GQDs is indeed the surface state, which means that the reactive sites; edges and oxygen functional groups are initiated the interaction with the solvent. Note that the edge sites and oxygen functional groups have the free electrons at the carbon edges. The line width of the PL in solvent can be explained on the basis of dielectric media of the solvent. In case of the THF which have the dielectric constant value of ε=7.58 is smaller than that of water (ε=80) and DMSO (ε=47). The lower line width of the PL spectra in THF could be due to efficient charge transfer from GQDs to solvent. Since THF is solvent with a low dielectric and the GQDs are enriched with edge sites and functional groups, the solvation process is faster than the fluorescence. This is also consistent with the TRPL analysis

(discussed later). The shift of the PL peak of GQDs in different solvents indicates that the surface states of GQDs are primarily responsible for visible PL. **Fig. 4.4(d)** represents comparative PL spectra of different GQD samples measured in aqueous water. Note that all the PL spectra were corrected by the background subtraction (PL spectrum of the bare solvent). All the GQDs samples show the bright blue PL emission. For a quantitative assessment of PL emission of GQDs, we measured the QY of GQDs by using the QS as a standard dye, which has the QY of 0.54. For each GQD sample, we measured the integrated intensity of PL spectrum and the QY is calculated using equation 4.1. The PL QY for the GQD-DMF, GQD-DMSO, S24 and S24F are found to 32%, 27%, 15% and 21%, respectively. The GQD-DMF shows the highest PL QY among all the GQDs samples due the enrichment of edges and oxygen functional groups. Note that the *in-situ* chemical functionalization (S24F) showed improved PL QY as compared to the bare S24. The QY of the samples is listed in **Table 4.1.**

In order to understand the charge transfer process of GQDs in solvents, we measured the life time of carriers in GQDs using the TRPL measurements. **Fig. 4.4(c, e)** shows the TRPL spectra of S24 in DMSO and THF. The TRPL spectra are well fitted with the tri-exponential decay equation. The carrier life times and their amplitudes are summarised in **Table 4.1**. The three different life times can be attributed to the recombination of electrons from the edge sites and functional groups defects in GQDs [30-32]. The average life time of S24 in DMSO is 6.74 ns, while it reduces to 3.84 ns in THF. As discussed above the THF has lower dielectric constant than the DMSO: Thus, during the light irradiation the charge from enriched edges and functional groups of GQDs is transferred to the THF through the solvation process [33]. We noticed shorter life time of carriers in THF, this indicates the efficient charge transfer from GQDs to THF.

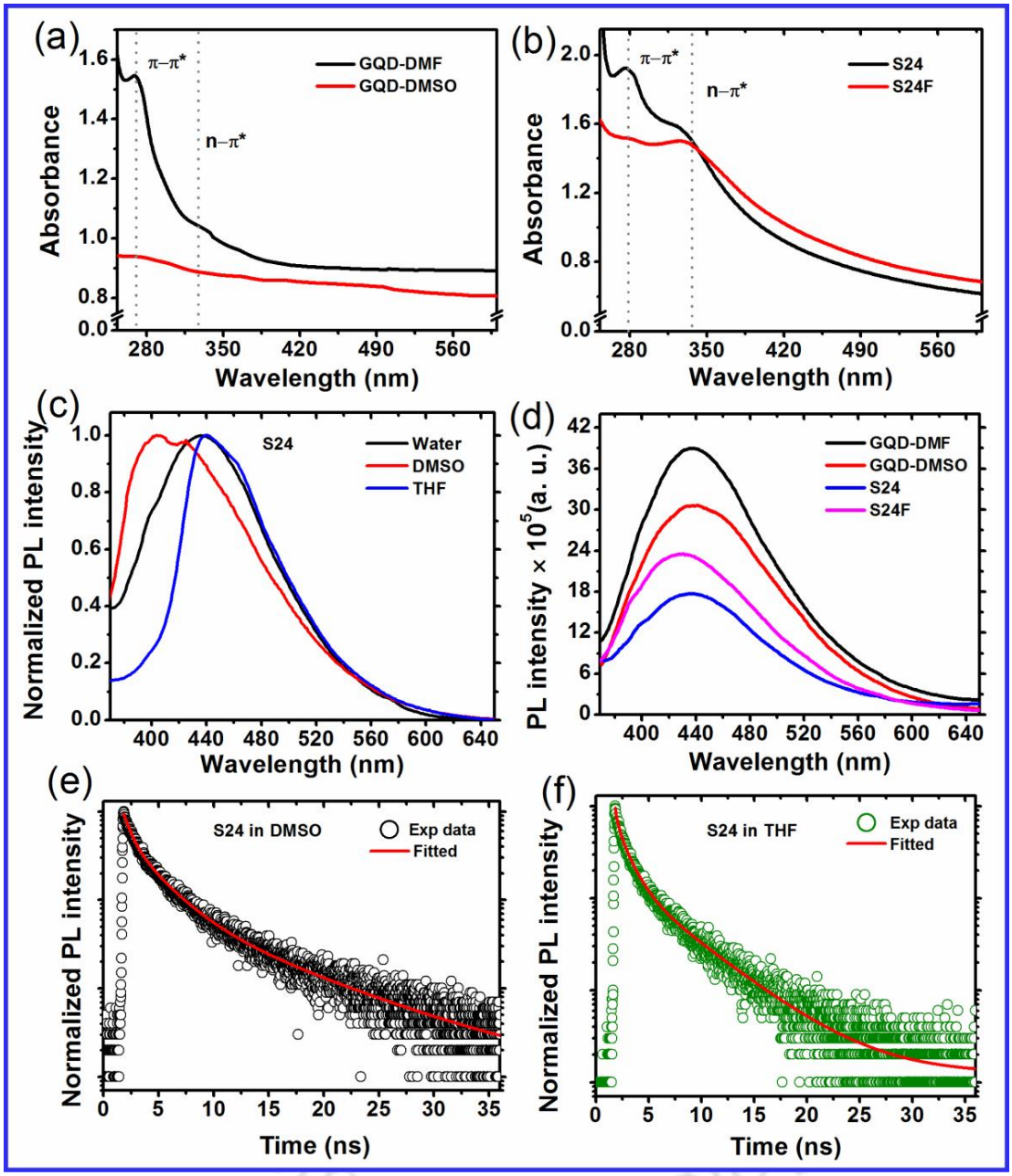

Figure 4.4: Optical absorption and emission characteristic of the GQD samples. (a, b) UV-Vis absorption spectra of GQD-DMF, GQD-DMSO, S24 and S24F. (c) PL spectra of S24 in water, DMSO and THF solvents. (d) PL spectra of GQD-DMF, GQD-DMSO, S24 and S24F. (e,f) TRPL spectrum of S24 measured in DMSO and THF, respectively.

Table 4.1: Summary of Raman band intensity ratio, PL quantum yield and life time constants of the samples.

Sample Code	Raman intensity ratio (I_D/I_G)	PL QY (%)	Sample code	τ_1 (ns) (A_1%)	τ_2 (ns) (A_2%)	τ_3 (ns) (A_3%)	τ_{av} (ns)
GQD-DMF	1.08	32	S24 in DMSO	0.65 (22.41)	2.61 (46.90)	8.92 (30.68)	6.74
GQD-DMSO	0.86	27	S24 in THF	0.15 (11.16)	1.15 (37.84)	4.88 (51.00)	3.84
S24	0.35	15	$\tau_{av} = \sum_{i=1}^{3} \frac{A_i \tau_i^2}{A_i \tau_i}$				
S24F	0.53	21					

4.7. Cell Viability and Bio-Imaging Studies

The advantage of bright blue PL emission of GQDs is used to study the bio-imaging application. Prior to the confocal imaging of cell lines using GQDs as fluorescent markers, we have checked the bio-compatibility of GQDs on the cell lines. In order to find out the cellular toxicity, the cell viability test was conducted using the MTT assay. The cytotoxicity of GQD-DMF, GQDs-DMSO, S24 and S24F was evaluated with varied concentration from 0-44.4μg/mL on two different cancer cell lines A-375 and HeLa. The cell viability results of the four GQDs samples on A-375 and HeLa are shown in **Fig. 4.5(a-d)**. **Fig. 4.5(a)** shows the comparison of cell viability of the GQD-DMF sample on A-375 and HeLa cells for the GQD concentration of 44.4 μg/mL. The cell viability by GQD-DMF on A-375 and HeLa are 92% and 78%, respectively. **Fig. 4.5(b)** shows the comparison of cell viability of the GQD-DMSO up to the concentration of 44.4 μg/mL on the A-375 and HeLa cells and respective cell viabilities are 90% and 80%. Further, the cell viability of S24 and S24F on A-375 and HeLa is shown in **Fig. 4.5(c)** and **(d)**, respectively. Note that in case of S24 sample, its shows the 79% cell viability for both the cell lines A-375 and HeLa. On the other hand, for S24F sample the cell viability on the A-375 and HeLa are 80% and 82%, respectively for the concentration of 44.4μg/mL. From these results, we demonstrate that despite the presence of oxygenated functional groups in GQDs, the difference in the edge structure and PL QY of GQDs are the responsible for difference in the cell viability of the cell lines. These results indicate that the GQDs are quite viable for both cell lines and useful for bio-imaging and drug delivery

applications. In case of A-375 cells, highest cell viability indicates it better bio-compatibility with the as prepared GQDs.

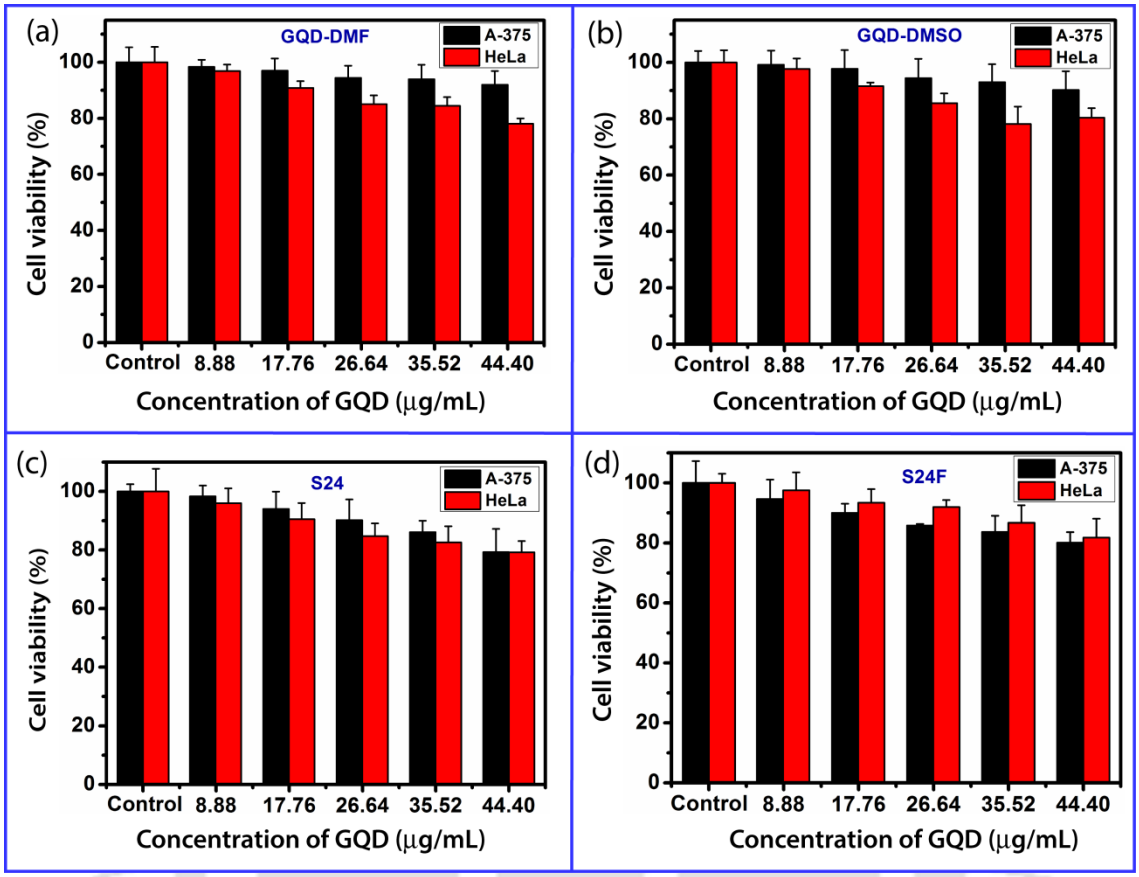

Figure 4.5: Comparison of cell viability of A-375 and HeLa cell lines in GQDs samples; (a) GQD-DMF, (b) GQD-DMSO, (c) S24 and (d) S24F.

Since the GQDs showed less toxicity on A-375 and HeLa cell lines, we have carried out the confocal imaging of the cell lines using GQDs as a labelling agent. For this, the confocal imaging was carried out for four different GQDs on HeLa, A-375 cells and HEK-293. **Fig. 4.6** shows bright filed and fluorescence images of the A-375, HeLa and HEK-293 cell lines. **Fig. 4.6(a_1-a_4), (b_1-b_4), (c_1-c_4)** and **(d_1-d_4)** shows the confocal images of A-375 and HeLa cell lines with GQD-DMF, GQD-DMSO, S24 and S24F samples, respectively. The first column and third column represents the bright filed images, while the second column and fourth column represents the fluorescence images of the images of the different GQDs. The bright blue luminescence is observed inside the cells, indicating that the GQDs have been internalized by the A-375 and HeLa cells and are mainly localized in the cytoplasm region. **Fig. 4.6 (e_1 and e_2)** depicts the bright field and fluorescence images of the HeLa cell without any addition of GQDs. Further, we

have also the performed the confocal imaging on normal cell lines (HEK-293). **Fig. 4.6** **Fig. 4.6** (**f_1 and f_2**) depicts the bright field and fluorescence images of the HEK-293 using the S24F as bio-markers. We did not find any considerable fluorescence from the confocal imaging of HEK-293. These results suggest the GQDs are internalized by the cancer cells and show the blue PL. These results prove that the strong blue PL emission, with low cytotoxicity, and ease of labelling of cells with GQDs enables its promising applications for biological imaging, disease diagnosis and biosensors.

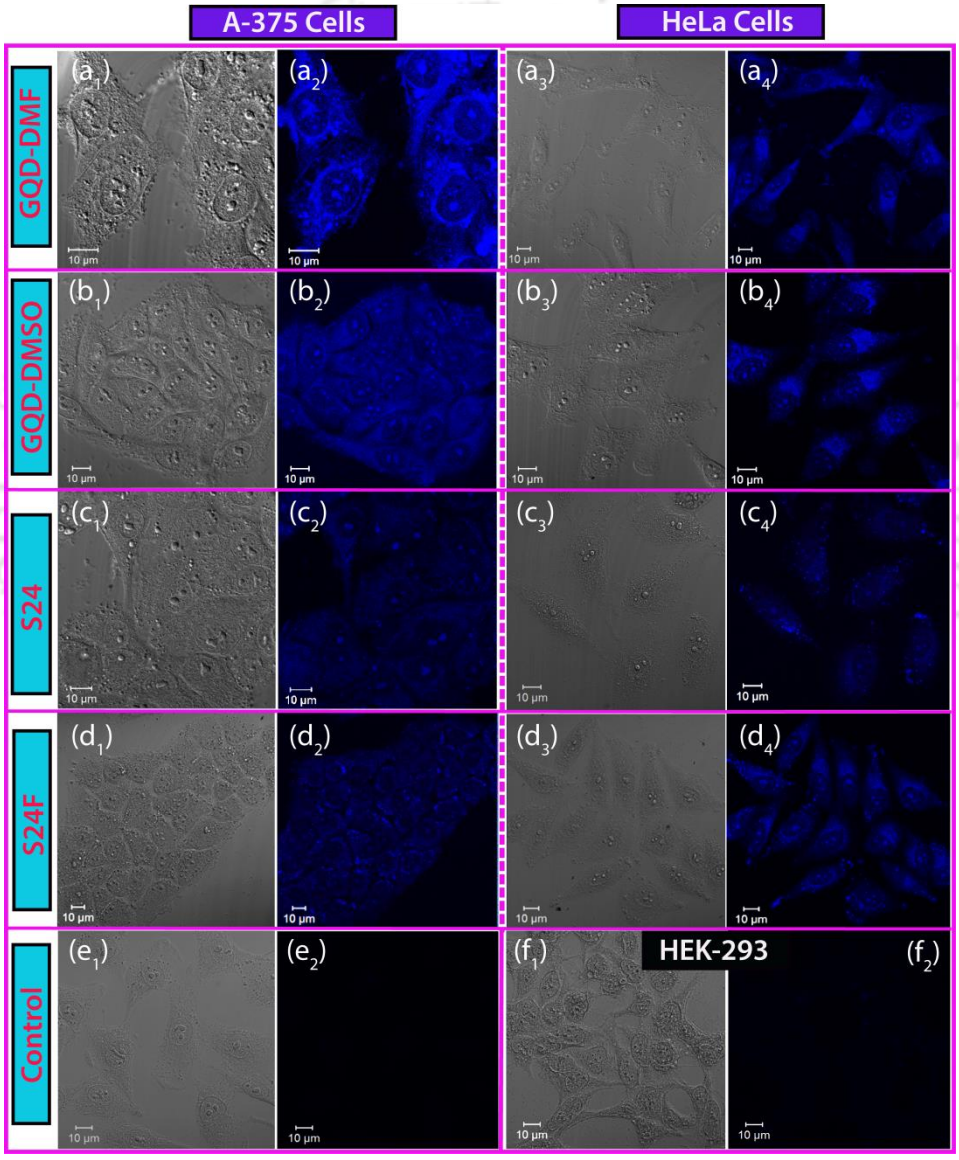

Figure 4.6: Confocal microscopy images of GQDs in different cell lines. A-375 and HeLa cell lines imaging using: (a_1-a_4) GQD-DMF; (b_1-b_4) GQD-DMSO; (c_1-c_4) S24; and (d_1-d_4) S24F. (e_1 and e_2) the confocal microscopy images of the control sample without any addition of GQDs. (e_3 and e_4) the confocal microscopy images of S24F sample by HEK-293 cell lines. The first column (a_1-e_1) and third column (a_3-e_3) represents the bright filed images, while the second column (a_2-e_2) and fourth column (a_4-e_4) represents the fluorescence images of the different GQDs.

4.8. Summary & Conclusions

1. In this chapter, we presented the solvent assisted synthesis of GQDs using three different solvents and compared the structural and optical properties of resulting GQDs.

2. Raman intensity ratio of different GQDs suggested that the edge site and functional groups of the GQDs can be controlled by using different solvents during the synthesis of GQDs.

3. TGA/DTG analyses reveal the various oxygenated edge functional groups in GQDs.

4. We elucidated the origin of PL emission of GQDs in liquid media. The strong PL emission of GQDs arises primarily from the surface defect states in GQDs. We have achieved a high 32% PL QY from the GQDs. The charge recombination dynamics is probed from the TRPL analysis.

5. Confocal imaging of GQDs showed very bright PL inside the cancer cell lines, such as A-375 and HeLa and showed its good bio-compatibility.

References

1. Y. Sun, S. Wang, C. Li, P. Luo, L. Tao, Y. Wei and G. Shi, *Physical Chemistry Chemical Physics*, 2013, **15**, 9907-9913.
2. S. Wang, I. S. Cole and Q. Li, *RSC Advances*, 2016, **6**, 89867-89878.
3. J. Peng, W. Gao, B. K. Gupta, Z. Liu, R. Romero-Aburto, L. Ge, L. Song, L. B. Alemany, X. Zhan, G. Gao, S. A. Vithayathil, B. A. Kaipparettu, A. A. Marti, T. Hayashi, J.-J. Zhu and P. M. Ajayan, *Nano Letters*, 2012, **12**, 844-849.
4. G. W. Lingling Li, Guohai Yang, Juan Peng, Jianwei Zhao and Jun-Jie Zhu, *Nanoscale*, 2013, **5**, 4015-4039.
5. R. Ye, C. Xiang, J. Lin, Z. Peng, K. Huang, Z. Yan, N. P. Cook, E. L. G. Samuel, C.-C. Hwang, G. Ruan, G. Ceriotti, A.-R. O. Raji, A. A. Martí and J. M. Tour, *Nat Commun*, 2013, **4**.
6. Z. Wang, H. Zeng and L. Sun, *Journal of Materials Chemistry C*, 2015, **3**, 1157-1165.
7. K. A. Ritter and J. W. Lyding, *Nature Materials*, 2009, **8**, 235-242.
8. L. R. Radovic and B. Bockrath, *Journal of the American Chemical Society*, 2005, **127**, 5917-5927.

9. K. Lingam, R. Podila, H. Qian, S. Serkiz and A. M. Rao, *Advanced Functional Materials*, 2013, **23**, 5062-5065.
10. M. A. Montes-Morán, D. Suárez, J. A. Menéndez and E. Fuente, *Carbon*, 2004, **42**, 1219-1225.
11. Z. Zhang, J. Zhang, N. Chen and L. Qu, *Energy & Environmental Science*, 2012, **5**, 8869-8890.
12. H. Yue, Z. Yang, L. Gewu, C. Nan, Z. Zhipan, L. Hui, S. Huibo and Q. Liangti, *Nanotechnology*, 2013, **24**, 195401.
13. V. Gupta, N. Chaudhary, R. Srivastava, G. D. Sharma, R. Bhardwaj and S. Chand, *Journal of the American Chemical Society*, 2011, **133**, 9960-9963.
14. L. Li, G. Wu, T. Hong, Z. Yin, D. Sun, E. S. Abdel-Halim and J.-J. Zhu, *ACS Applied Materials & Interfaces*, 2014, **6**, 2858-2864.
15. B. Wang, S. Zhuo, L. Chen and Y. Zhang, *Spectrochimica Acta Part A: Molecular and Biomolecular Spectroscopy*, 2014, **131**, 384-387.
16. L. Kou, F. Li, W. Chen and T. Guo, *Organic Electronics*, 2013, **14**, 1447-1451.
17. S. Zhu, J. Zhang, S. Tang, C. Qiao, L. Wang, H. Wang, X. Liu, B. Li, Y. Li, W. Yu, X. Wang, H. Sun and B. Yang, *Advanced Functional Materials*, 2012, **22**, 4732-4740.
18. G. Sandeep Kumar, R. Roy, D. Sen, U. K. Ghorai, R. Thapa, N. Mazumder, S. Saha and K. K. Chattopadhyay, *Nanoscale*, 2014, **6**, 3384-3391.
19. S. Zhu, J. Zhang, X. Liu, B. Li, X. Wang, S. Tang, Q. Meng, Y. Li, C. Shi, R. Hu and B. Yang, *RSC Advances*, 2012, **2**, 2717-2720.
20. W. Shi, H. Fan, S. Ai and L. Zhu, *New Journal of Chemistry*, 2015, **39**, 7054-7059.
21. M. S. Seehra, V. Narang, U. K. Geddam and A. B. Stefaniak, *Carbon*, 2017, **111**, 380-385.
22. L. G. Cançado, M. A. Pimenta, B. R. A. Neves, M. S. S. Dantas and A. Jorio, *Physical Review Letters*, 2004, **93**, 247401.
23. C. Casiraghi, A. Hartschuh, H. Qian, S. Piscanec, C. Georgi, A. Fasoli, K. S. Novoselov, D. M. Basko and A. C. Ferrari, *Nano Letters*, 2009, **9**, 1433-1441.
24. D. Bischoff, J. Güttinger, S. Dröscher, T. Ihn, K. Ensslin and C. Stampfer, *Journal of Applied Physics*, 2011, **109**, 073710.

25. Y. You, Z. Ni, T. Yu and Z. Shen, *Applied Physics Letters*, 2008, **93**, 163112.
26. R. Nishinakagawa, K. Matsuda, T. Arai, A. Sawada and T. Terashima, *AIP Advances*, 2013, **3**, 092111.
27. G. Rajender and P. K. Giri, *Journal of Materials Chemistry C*, 2016, **4**, 10852-10865.
28. R. K. Biroju, G. Rajender and P. K. Giri, *Carbon*, 2015, **95**, 228-238.
29. D. Qu, M. Zheng, L. Zhang, H. Zhao, Z. Xie, X. Jing, R. E. Haddad, H. Fan and Z. Sun, *Scientific Reports*, 2014, **4**, 5294.
30. S. Zhu, J. Shao, Y. Song, X. Zhao, J. Du, L. Wang, H. Wang, K. Zhang, J. Zhang and B. Yang, *Nanoscale*, 2015, **7**, 7927-7933.
31. L. Lin and S. Zhang, *Chemical Communications*, 2012, **48**, 10177-10179.
32. R. Gone, C. Biswajit and P. K. Giri, *Nanotechnology*, 2017, **28**, 395703.
33. S. K. Cushing, M. Li, F. Huang and N. Wu, *ACS Nano*, 2014, **8**, 1002-1013.

Chapter 5

In-Situ Decoration of Plasmonic Au Nanoparticles on Graphene Quantum Dots- Graphitic Carbon Nitride Hybrid and Its Photocatalytic Activity

In this chapter, a ternary hybrid consisting of Au nanoparticles (NPs) decorated graphene quantum dots (GQDs)-graphitic carbon nitride (GCN) system was prepared through an *in-situ* chemical method. A series of characterization was performed to probe the structural quality and characteristics features of the pristine as well as the hybrid samples. A striking enhancement in the intensity of Raman G band is observed in Au functionalized GQD-GCN due to the surface plasmon resonance of Au NPs. A systematic study on the visible light photocatalytic degradation of methylene blue (MB) was studied and we have achieved an improved 86% degradation of MB in the Au NPs decorated GQD-GCN. The enhanced photocatalytic degradation of MB by the ternary hybrid is due to the efficient interfacial charge transfer between the GQD-GCN to Au. We present the evidence for free radical generation in the MB degradation and dominance of hydroxyl radical involvement as compared to the superoxide radical in the MB degradation.

5.1. Introduction

Photocatalytic (PC) activity based on the conventional semiconductor materials have been studied for the last few decades. Among these, the most commonly known PC material is TiO_2 [1]. It is important to note that the presence of dye effluents cannot be discarded, as it greatly affects the environmental eco system[2, 3]. It is well known that the conventional metal oxide semiconductor materials, such as TiO_2 and ZnO etc. have the band gap in UV region. It needs to be emphasized that the solar spectrum consists of only 3 to 5 % of UV and 44% of visible light. In addition, the high recombination rate of photogenerated charge carries is another cause of concern for the low PC efficiency of conventional materials [4]. Therefore, for efficient utilization of visible solar light and charge carrier separation, and the design of a proper hybrid material is necessary. Besides, plasmonic

NPs based hybrids are gaining enormous attention in recent times due to the surface plasmon resonance (SPR) effect. Similar to the graphene analogy in sp^2 hybridized graphitic structure, graphitic carbon nitride (GCN), have been considered as a promising material for photocatalysis due to possession of bandgap [5, 6]. An integration of graphene quantum dots (GQDs), Au NPs and GCN hybrid is expected to show superior PC activity as compare to their individual counterparts.

In the following sections, we discuss the experimental details, characterization results and visible light PC degradation of methylene blue (MB) by the GQD based hybrid catalysts.

5.2. Experimental Details

5.2.1 Sample Preparation

5.2.1.1. Preparation of GCN

The synthesis details of GQD using DMF solvent was discussed in **Chapter 4, section 4.2.1.** GCN was prepared using urea as the starting precursor. 10 g of urea was taken in a silica crucible and was covered with a lid. The crucible was placed at the centre of the muffle furnace and heated at 550 °C for 3 h at the ramping rate of 5 °C /min [10]. After cooling naturally to the room temperature the crucible was taken out. The final powder sample is used for further studies.

5.2.1.2. Synthesis of Au NPs

Au NPs were prepared by a citrate reduction method [7]. Typically, 0.5 mM gold (III) chloride was prepared in 300 mL water and heated to boiling. Further, 30 mL of 0.1 M trisodium citrate dehydrate (TSC) was added to the boiling gold chloride solution with continuous monitoring of colour changing. When the colour of solution became purple red, the reaction was stopped and it was cooled down to room temperature. This gave rise to the colloidal Au NPs.

5.2.1.3. Preparation of GQD-GCN Hybrid

For the preparation of GQD-GCN hybrid system, equal weight ratio (1:1) of GQD and GCN was taken and added to 100 mL water in two separate beakers. Both beakers were kept for ultrasonic treatment for 1 h to allow complete dispersion in water. GCN solution was kept in stirring condition. After 15 min, the GQDs dispersion was added to the GCN

solution and the mixture was stirred for another 1 h. After completion of stirring, the mixture was centrifuged and dried at 60 °C in a hot air oven to collect the dried product.

5.2.1.4. *In-Situ* Decoration of Au NPs on GQD, GCN and GQD-GCN

An *in-situ* decoration of Au NPs over GQD, GCN, and GQD-GCN hybrid was performed by directly adding the powder samples in the gold chloride solution. Typically, 30 mg of GQD-GCN was taken in 300 mL of double distilled water in a 500 mL beaker and subjected to ultrasonication for 30 min. The large volume of water was taken for better dispersion of GQD-GCN and to prevent agglomeration of Au NPs over the hybrid nanosystem. The gold solution containing GQD-GCN was then heated at 90 °C. 30 mL of 38.8 mM TSC was added dropwise to the gold solution containing GQD-GCN. After 30 min of stirring, the final mixture got a purple-white colour. At this point, the reaction was stopped and cooled down to room temperature. The solution was centrifuged three times with water and then dried at 60 °C. The obtained product was Au NPs decorated GQD-GCN hybrid and was named as Au@GQD-GCN. Similar procedure is followed for Au decoration on 15 mg of GQD or GCN and the samples are denoted as Au-GQD and Au-GCN, respectively.

5.2.2. Visible Light Photocatalytic Measurements

5.2.2.1. Photodegradation of MB

For the PC degradation, we have considered non-biodegradable MB dye as the model organic pollutant. PC experiment was performed by adding 6 mg of catalyst to 100 mL aqueous MB solution with an initial MB concentration of 8 mg/L. Aqueous MB solution with catalyst was stirred in dark for 45 min in order to obtain an equilibrium condition between dye and the catalyst. The solution was irradiated under visible light (λ>400 nm, 450 Watt Xe arc lamp, ORIEL instruments) with external UV cut off filter (Hoya Filter, Japan) and mirror for beam reflection. During light irradiation, cold water was circulated throughout the reactor to maintain the temperature of the system near room temperature. After every 15 min, 2 mL of solution was taken and centrifuged. The irradiation was continued up to 180 min. Photo degradation of MB was monitored by the decrease of its absorption intensity (peak at ~665 nm) with irradiation time. To understand the free radical involvement in the MB degradation, we have performed the scavenger experiments discussed below.

5.2.2.2. Hydroxyl Radical Test

In a typical experiment, a solution was prepared with 2 mM of NaOH and 5 mM of terephthalic acid (TA) in 100 mL DI water [8]. After a few min of stirring, 6 mg catalyst was added to the solution. The irradiation time and sample collection after each step of irradiation were similar to the earlier case. After centrifugation, the solution containing the TA was taken and its PL intensity was measured. Fluorescence measurements of the sample were carried out with excitation at 312 nm using a PL spectrometer (Fluromax-4, Horiba).

5.2.2.3. Superoxide Radical Test

In this test, 10 μM nitro blue tetrazolium chloride (NBT) was dissolved into 100 mL of DI water and stirred [9]. During the stirring, 6 mg of catalyst was added and this was further stirred for 1 h. The irradiation time and sample collection after irradiation was similar to that of hydroxyl radical test. After centrifugation, the solution containing the NBT was taken and its UV-Vis absorbance was measured.

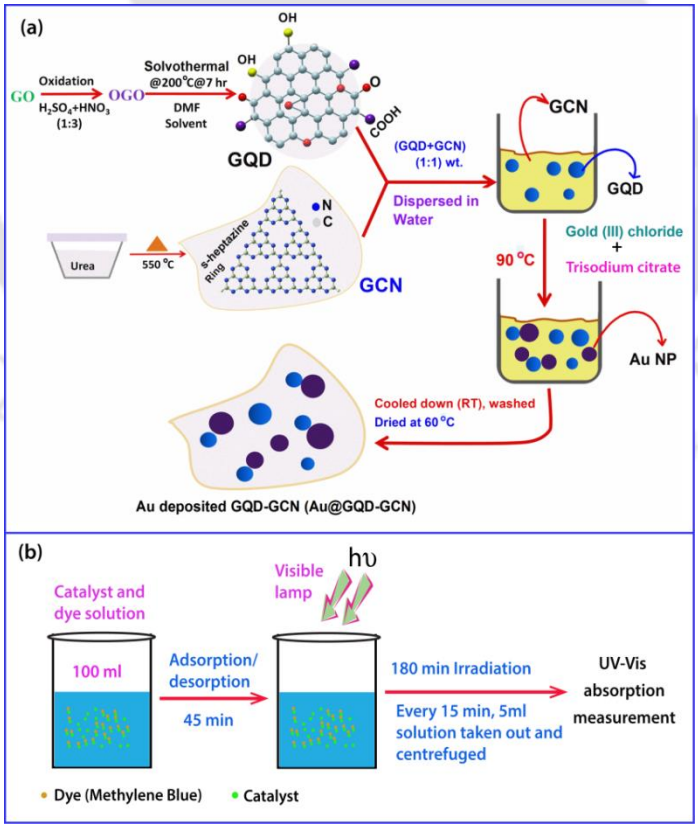

Figure 5.1: (a) Schematic illustration of the procedure for synthesis of GQD and GCN and *in-situ* deposition of Au NPs on nanosystem of GQD-GCN by citrate reduction method. (b) Schematic of PC degradation measurements of MB.

The details of the sample preparation and PC experiments are schematically shown in **Fig. 5.1. Fig. 5.1(a)** shows the steps involved in the synthesis of GQD, GCN and Au NPs decoration on GQD-GCN. Au NPs are shown with purple ball, and GQDs are shown with blue ball over the sheet of GCN. **Fig. 5.1(b)** shows the schematic of steps involved in the PC degradation measurements of MB.

5.3. Morphology, Composition and Structural Analyses

Fig. 5.2 shows the TEM images of GCN, GQDs, Au NPs and their hybrids. **Fig 5.2(a)** shows the TEM image of GCN. The GCN appears as buckled porous nanosheets. **Fig. 5.2(b)** shows the TEM image of GQD. The size of the GQDs is in the range 3-10 nm. The inset shows the size distribution of GQDs and the average diameter of GQD is 5.2 ±0.1 nm. **Fig. 5.2(c)** shows the TEM image of Au NPs and inset shows their size distribution with average diameter of 10.7±0.3 nm. **Fig. 5.2(d)** shows the TEM image of Au decorated GCN (Au-GCN) sample. **Fig. 5.2(e)** shows the TEM image of Au decorated GQD-GCN. Note that some of the Au NPs are isolated from the GCN surface that can be seen from the **Fig. 5.2(d).** Similar picture is also evident from the TEM image of

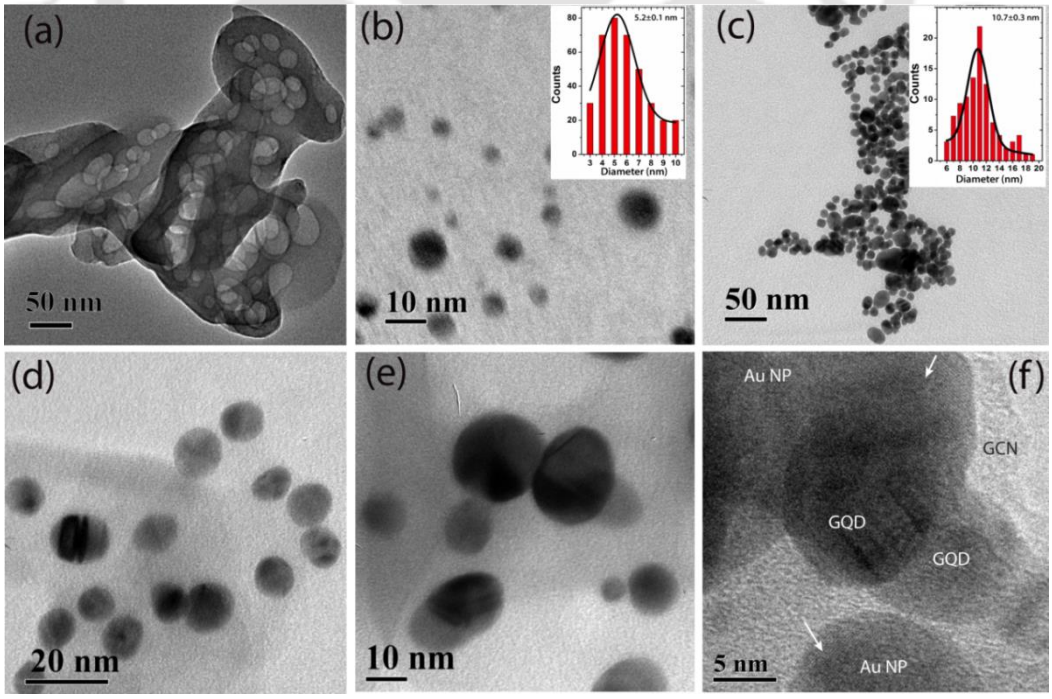

Figure 5.2: TEM images of (a) GCN, (b) GQD, (c) Au NPs, (d) Au-GCN and (e) Au@GQD-GCN. The inset in (b&c) shows the size distribution of GQDs and Au NPs, respectively. (f) High magnification TEM image of Au@GQD-GCN hybrid system. The arrows indicate the lattice plane of

Au@GQD-GCN (see **Fig. 5.2(e)**), where only about 50% of Au NPs are attached to GCN and GQD and some of the Au NPs are lying isolated. For a clear view of the interface between Au NPs and GQD-GCN, a high resolution TEM image of the plasmonic hybrid nanosystem was taken and it is shown in **Fig. 5.2(f)**. The lattice planes of Au NPs are indicated with an arrow. Note that the lattice fringes are not evident at the junction of Au decorated GQD-GCN. We speculate that the GQDs are attached to Au NPs as well as distributed over GCN nanosheets.

For further confirmation of the presence of Au in the hybrid system, we performed elemental mapping on Au@GQD-GCN. **Fig. 5.3(a)** shows the FESEM image of Au NPs decorated GQD-GCN and **Fig. 5.3(b-e)** represents its elemental mapping of C, N, O and Au. The different contrast mappings of C, N, O and Au show their distribution in the hybrid photocatalyst. Presence of O Kα reveals that the hybrid system contains many oxygenated functional groups resulting from GQDs and these are attached at the edges/in-plane sites of GQDs. **Fig. 5.3(f)** shows the XRD pattern of GCN, GQD-GCN and Au@GQD-GCN. The diffraction peak at 2θ = 27.5° in GCN appears due to the (002) crystallographic plane [10]. In the GQD-GCN hybrid system, the major peak at 2θ = 26.3° corresponds to the (002) crystallographic plane of GQD [11] and the shoulder peak

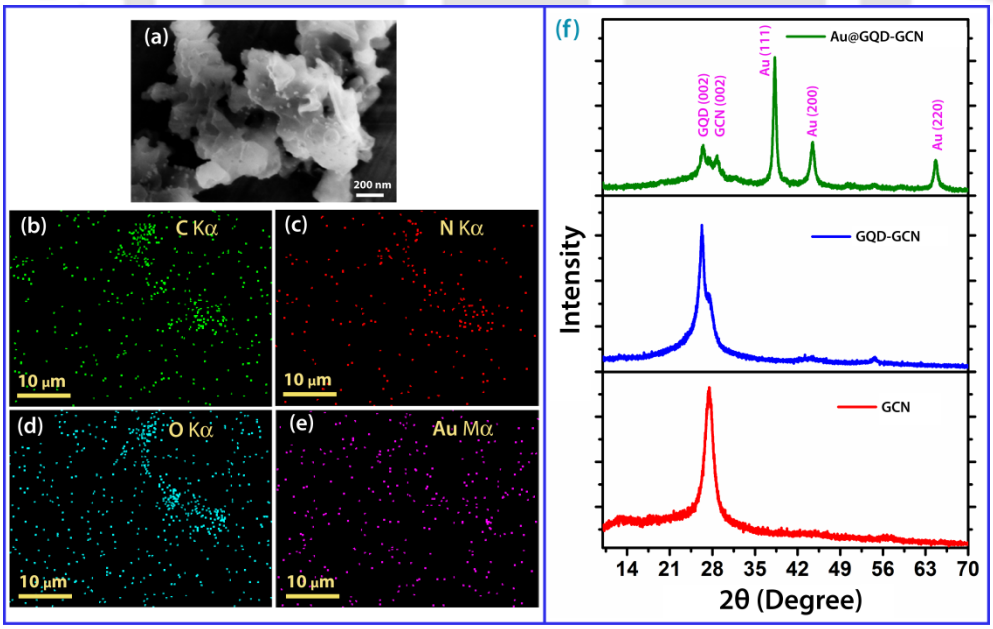

Figure 5.3: (a) FESEM image of Au@GQD-GCN. Elemental mapping for (b) C (c) N (d) O and (e) Au. (f) X-ray diffraction pattern of GCN, GQD-GCN and Au@GQD-GCN.

corresponds to (002) plane of GCN. Presence of (002) planes in these samples strongly suggest the sp^2 graphitic nature. Along with the diffraction peaks of GQD and GCN, the reflection lines of face-centered-cubic (fcc) Au are clearly observed in the XRD pattern of Au@GQD-GCN. The diffraction peaks at 38.2, 44.4 and 64.4° reveals the fcc phase structure of Au NPs ((JCPDS 04-0784)[12].

5.4. Raman Studies

Fig. 5.4(a) depicts the Raman spectra of GQD, GQD-GCN and Au@GQD-GCN samples obtained with a 488 nm laser excitation. All the samples show the characteristic Raman bands of GQD [13, 14]. The standard G and D bands appeared at ~1580, and ~1350 cm^{-1}, respectively. The weak Raman band at 2730 cm^{-1} is the 2D band, which is the overtone of D-band. This band results from the double resonance transition producing two phonons of opposite momentum [15]. We estimated the relative intensity of D to G bands (I_D/I_G), which is nearly 1 for all the samples, which signifies that the prepared GQDs contain unsaturated carbon on the edges and functional groups. There is a slight modification of Raman bands of GQD in the hybrid GQD-GCN. This might be due to the van der Waals interactions between the GQD and GCN [16].

Further, to understand the role of SPR effect on Raman spectra, we have performed the Raman measurements using 514.5 nm laser, which is close to the SPR absorption of the Au NPs and the results are shown in **Fig. 5.4(b).** From **Fig. 5.4(b)**, it is apparent that due to the presence of Au NPs, the G and 2D band intensity is enhanced. This might be caused by the Au plasmon induced surface enhanced Raman scattering (SERS). The enhancement factor (EF) is determined by the ratio of intensity, EF = $I_{Au}/I_{Pristine}$ for both G and 2D bands [17]. It is found that the G band intensity is enhanced by a factor of 1.3 and the 2D band intensity is enhanced by a factor of 7 after Au deposition. This implies that the incident radiation of λ = 514.5 nm is close to the SPR band of Au NPs seen at 539 nm (discussed later) results the changes in the Raman intensities. With the close proximity of the resonant bands of Au NPs with the excitation laser wavelength, there is an enhancement of electromagnetic field intensity at the Au NPs and GQD-GCN interface and this strong electromagnetic coupling results in the SERS enhancement [17]. Note that there is a decrease in D band intensity in GQD-GCN after Au deposition. This might be due to the reduction in the numbers of unsaturated carbon sites (edges) and

changes in the functional groups in GQDs. Note that both the materials have graphitic structure (pi electron system) and both are highly fluorescent in nature. Incorporation of Au NPs on to GQD-GCN hybrid facilitates the strong coupling between surface plasmon and fluorescent material [18].

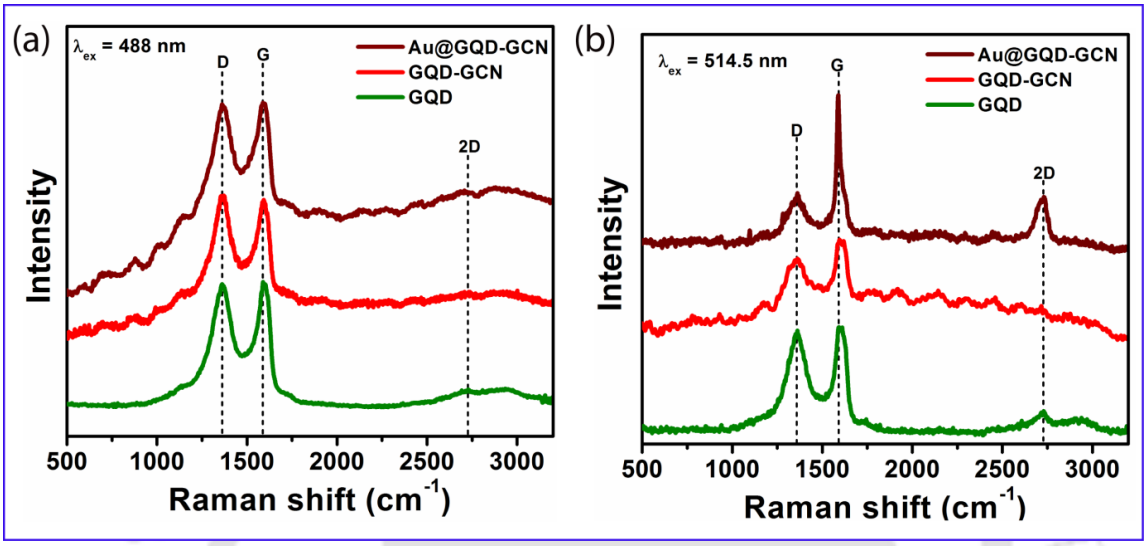

Figure 5.4: Characteristic Raman features of GQD, GQD-GCN and Au@GQD-GCN for excitation wavelength of (a) 488 nm and (b) 514.5 nm

5.5. FTIR Studies

Fig. 5.5 depicts the FTIR spectra of the plasmonic hybrid system and their associates. In GQD, the bonds at 1081 cm^{-1} is assigned to C-O stretching mode in epoxide and a peak at 1410 cm^{-1} can be assigned to C-H bending vibration mode [19, 20]. The FTIR absorption in the range 1560-1700 cm^{-1} is due to the presence of aromatic C=C bond (sp^2 hybridized carbon) and the COOH, C=O oxygenated functional groups in GQD [21]. The broad region 3000-3600 cm^{-1} in the FTIR spectrum of GQD is associated with the stretching vibrations of C–OH moiety. On the other hand, GCN shows several strong absorption bands. The band at 812 cm^{-1} is the breathing mode of aromatic ring (*s*-heptazine) of GCN [6, 10]. The weak absorption band at 887 cm^{-1} is attributed to C, N out of plane rocking mode in *s*-heptazine unit [22]. The broad absorption band covering 3000-3600 cm^{-1} is a contribution from N-H stretching vibration of any uncondensed amine groups [23]. Further, the absorption bands at 1238, 1323, 1410, 1462, 1572 and 1636 cm^{-1} are typically associated with symmetric, asymmetric stretching and bending vibrations of different C-N (or C=N)

bonds in the heptazine derived repeating units and correspond to either trigonal C-N(-C)-C (full condensation) or bridging C-NH-C units (partial condensation) [13, 22, 23]. In GQD-GCN, the vibrational modes corresponding to C=O and C=C of GQD are incorporated with *s*-heptazine ring vibrational mode in C_3N_4 in the range 1100-1650 cm^{-1}. We noticed that the GQD functional groups, in particular C-O and C-OH, are drastically reduced, indicating the change in functional groups in GQD hybrid. These results are in agreement with Raman analysis discussed in the previous section. In Au decorated GQD-GCN sample, the FTIR vibrational modes of the GQD or GCN are merged with the FTIR spectrum of Au@GQD-GCN.

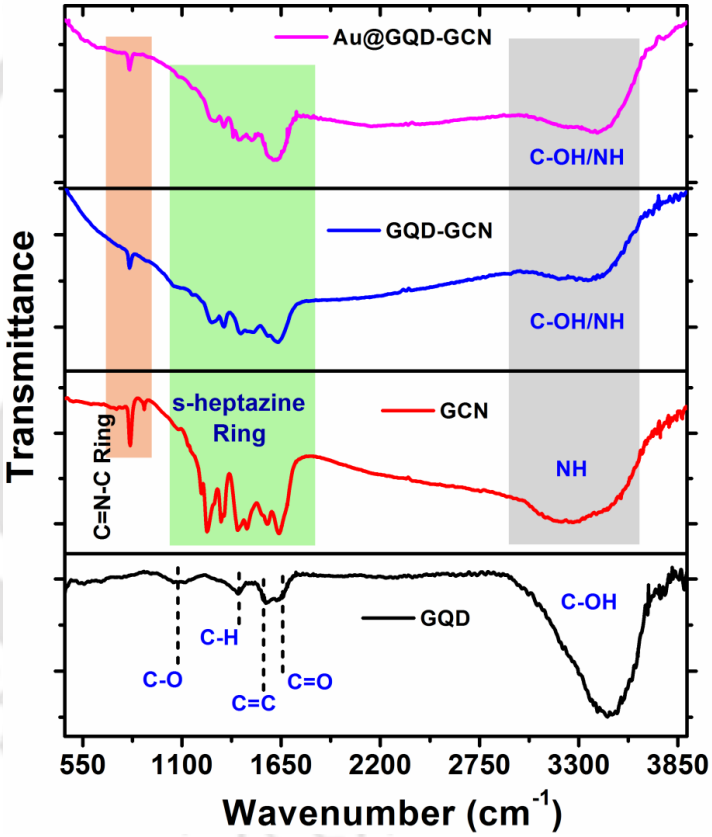

Figure 5.5: FTIR spectra of GQD, GCN, GQD-GCN and Au@GQD-GCN. The characteristic vibrations of the GQD and GCN are significant from the spectra.

5.6. Optical Properties

5.6.1. Optical Absorption

Fig. 5.6(a) shows the UV-visible absorption spectra of the samples. GQD exhibits two absorption bands peaked at ~268 nm and ~332 nm are due to the π-π^* transition of sp^2 C=C skeletal framework and n-π^* transitions involving the non-bonding electrons present

on oxygen (C=O or C-O) of the attached functional groups (COOH/C=O) at carbon edges, respectively [12, 24]. GCN has a strong absorption peak at 370 nm. This peak is attributed to *n*-*π** electronic transition involving lone pair electrons on nitrogen 2*p* orbital[4]. GQD-GCN contains π-π* absorption transition due to sp^2 carbon domains, two small humps at 326 nm and 387 nm and an absorption tail extended to the visible region. The humps at 326 nm and 387 nm correspond to *n*-*π** transition involving oxygen lone pair electrons in GQD and nitrogen lone pair electrons in GCN, respectively. The absorption tail appears because of the presence of disordered states (oxygenated functional groups and/or nitrogen vacancies) in the GQD-GCN. The absorption spectrum of Au@GQD-GCN has two significant absorption bands. The higher energy band correspond to *n*-*π** transition in GCN (at 370 nm) and the lower energy band refers to the SPR band (at 539 nm) of embedded Au NPs [25]. The expected UV absorption bands of GQDs are merged with the broad absorption spectrum of the plasmonic hybrid system. For the pristine Au NPs, a narrow SPR band is observed at 527 nm (see inset in **Fig. 5.6(a))**. The change in the absorption feature of Au NPs in Au@GQD-GCN is possibly due to the different dielectric media and formation of Au-C bonds in the hybrid system [25].

5.6.2. Steady State Photoluminescence

Fig. 5.6(b) depicts the steady-state PL spectra of plasmonic Au NPs decorated GQD-GCN and individual components. The samples show blue-green emission with the Xenon lamp (Fluromax-4, Horiba) excitation at 375 nm. The most intense emission peak appears in the blue region. The emission spectrum of GQD shows a peak at 423 nm and an emission tail extended to the visible region. The blue and green PL emission in GQD is originated from the edge states and oxygen functional groups, respectively [12]. These states are localized in the π-π* energy gap of GQD [12]. GCN displays a strong emission at 460 nm. Unlike GQD, the emissions in GCN are due to various electronic transitions in the *s*-heptazine ring. Band gap states of GCN consist of sp^2 (C=N) π bond, sp^3 (C-N) σ bond and lone pair (LP, *n*) electrons present on bridging N atom in *s*-heptazine ring [26]. On photoexcitation, electrons are excited to the highest energy states in the conduction band and then finally relax to the lowest occupied molecular orbital (LUMO), which is the C 2*p* *π** state. From π* states, the electrons undergo *π**-*π*, *π**-*n* transition giving rise to the

various emission peaks. Emissions at longer wavelength are mostly due to the presence of intra-gap electronic states in GCN [27]. The GQD-GCN hybrid displays emission peak at 432 nm with reduction in the green emission region. With first principle calculations, Ma et al. showed that GQD and GCN are bonded by the van der Waals interactions [16]. We speculate that the oxygen functional groups in GQDs are bonded with GCN by van der Waals forces. These results are consistent with the Raman and FTIR studies discussed in the above section. Similar PL observation was made from the Au decorated GQD-GCN. The blue and green PL from GQDs is originated from the edge sites and functional group defects [12]. The shift in the PL peak of hybrids of GQD suggests that there are some modifications in edge sites of GQD.

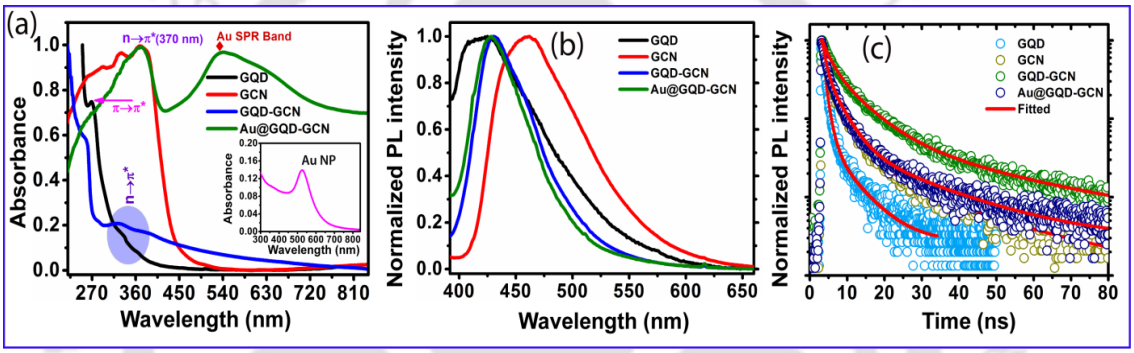

Figure 5.6: Optical characteristic of the samples: (a) UV-Vis absorption spectra of GQD, GCN, GQD-GCN and Au@GQD-GCN. Inset shows the UV-Vis absorption spectrum of Au NPs. (c) Steady state PL spectra of GQD, GCN, GQD-GCN and Au@GQD-GCN excited at 375 nm. (b) TRPL spectra of the samples obtained at an excitation of 375 nm.

5.6.3. Time Resolved Photoluminescence

In order to understand the carrier recombination dynamics in pristine and hybrid samples, we performed the time resolved (TR) PL measurement with the 375 nm laser excitation. The TRPL spectra of the samples are portrayed in **Fig. 5.6(c)**. Lifetime of the charge carriers and their relative abundances are obtained after tri-exponential fitting of the decay spectrum. The fitted parameters are shown in **Table 5.1.** The shortest lifetime (τ_1 ~ 0.46 ns) in GQD is due to the transition of charge carrier from π^*-π of the sp^2 bonded carbon. Various sources might contribute to the extended lifetimes (τ_2 and τ_3) in GQD. These include presence of armchair or zigzag edges and functional groups[12, 28, 29]. GCN has a short carrier lifetime of 0.86 ns (τ_1) which is due to π^*→n transition. Long lifetime components 4.23 ns (τ_2) and 21.45 ns (τ_3) can be associated with the presence of intra-

gap states in GCN. These intra-band gap states form both shallow and deep trap states in the band gap of GCN. The carriers are relaxed for a sufficiently longer period in these traps before they undergo recombination. The average carrier lifetimes (τ_{av}) in GQD and GCN are 4.3 ns and 16.3 ns, respectively. The hybrid GQD-GCN has the longest average carrier lifetime of 20.8 ns. The interface developed between GQD and GCN could be responsible for the prolonged charge carrier lifetime in GQD-GCN. Note that after Au decoration, the average carrier lifetime of the hybrid system reduces to 16.2 ns. The reduction in the carrier lifetime is due to enhanced charge transfer interaction in plasmonic hybrid system.[30, 31] The charge transportation occurs from hybrid to Au NPs, where Au acts as electron reservoir.

Table 5.1: Carrier lifetime components (τ_1, τ_2, τ_3) and their relative abundances (A_1, A_2, A_3) and the average carrier lifetime (τ_{av}) for GQD, GCN, GQD-GCN and Au@GQD-GCN.

Sample	τ_1 (ns) (A_1%)	τ_2 (ns) (A_2%)	τ_3 (ns) (A_3%)	τ_{av} (ns)
GQD	0.46 (30.4)	1.42(39.8)	6.73(29.8)	4.3
GCN	0.86 (26.8)	4.23(48.2)	21.45(25.0)	16.3
GQD-GCN	1.60(13.0)	6.66(51.6)	26.37(35.4)	20.8
Au@GQD-GCN	0.82(21.3)	3.87(49.0)	20.6(29.7)	16.2

$$\tau_{av} = \sum_{i=1}^{3} \frac{A_i \tau_i^2}{A_i \tau_i}$$

5.7. X-ray Photoelectron Spectroscopy Analysis

Fig. 5.7(a-c) shows the XPS core level C 1s, N 1s and Au $4f_{5/2}$ spectra of Au@GQD-GCN. **Fig. 5.7(a)** shows the C 1s spectrum, which is deconvoluted into four components with peaks centred at 284.4, 286.0, 287.5 and 288.6 eV. The intense peak at 284.4 eV is attributed to sp^2 C=C bonding of graphitic domain [12, 32]. The second intense peak at 287.5 eV can be attributed to aromatic sp^2 C-N=C linkages in the aromatic ring of g-C_3N_4 in hybrid [33, 34]. The peak at 286.0 eV originates from the presence of sp^3 carbon attached with functional groups C-O (ether) [35, 12]. One more peak appears at 288.6 eV, which is associated with C-NH-C linkages formed by the attachment of hydrogen on the bridging N atom coordinating the aromatic rings in the hybrid system. **Fig. 5.7(b)** shows the

deconvoluted N 1s spectrum showing the peaks at 398.0, 399.4 eV and these are due to aromatic sp^2 (C=N-C) bonding in the *s*-heptazine ring and bridging N atom (N-C3), respectively [32]. **Fig. 5.7(c)** represents the Au 4*f* spectrum of having two strong doublets at 83.0 eV (Au $4f_{7/2}$) and 86.6 eV (Au $4f_{5/2}$). These peaks signify the presence of metallic Au^0 in the hybrid system [36-38]. There is a negative shift (-0.8 eV) of the doublets of Au in the hybrid system with respect to the positions reported for pristine metallic Au, which are at 83.8 and 87.4 eV, respectively [37, 39]. The negative shift of the XPS peak is identified with electron transfer occurring from GQD-GCN to Au NPs [37, 38]. There are two shoulder peaks in Au 4*f* spectra, which are at the higher binding energy sides of the strong doublets. These peaks are at 84.5 and 88.1 eV, and attributed to the presence of cationic gold species ($Au^{\delta+}$). The appearance of charged species might be due to the formation of Au-C bonding at the interface of Au and GQD-GCN [40].

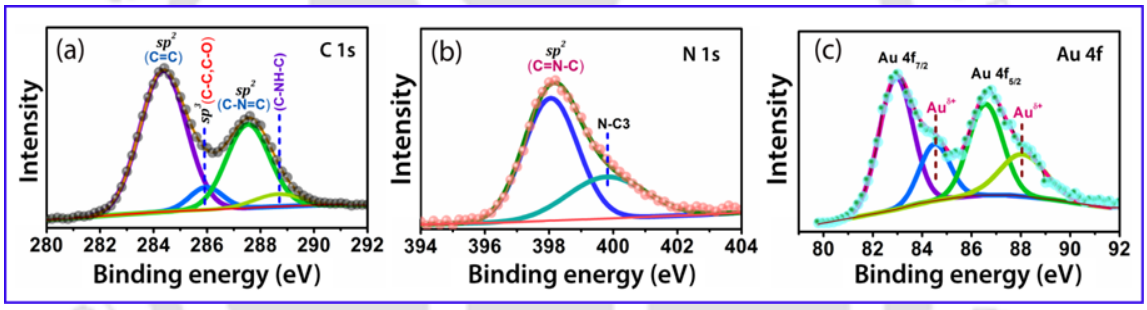

Figure 5.7: XPS spectra of (a) C 1s, (b) N 1s and (c) Au 4f for Au@GQD-GCN.

5.8. Visible light Photocatalytic Degradation of MB

5.8.1. Degradation and Reaction Kinetics

MB is considered as the model organic compound to study the PC activities of the different catalytic systems. **Fig. 5.8** shows the UV-vis absorption spectra of MB irradiated for different time in presence of catalysts GQD, GCN, Au-GCN, GQD-GCN and Au@GQD-GCN. MB shows the maximum absorbance of light at 665 nm. After irradiation of MB in presence of any catalyst, the intensity of absorption peak at 665 gradually goes down. This indicates that MB is degrading by visible light in presence of catalysts. **Fig. 5.8(a)** shows the change in absorption intensity of only MB as a function of irradiation time in absence of any catalyst. **Fig. 5.8(b,c)** shows the change in the absorption intensity of MB when GQD and GCN act as catalysts, respectively and PC is evaluated with respect to initial concentration of the MB. Further, decoration of Au NPs

on GQD or GCN shows small improvement in the PC performance. **Fig. 5.8(d))** shows the change in absorption intensity of MB in presence of Au-GCN. Hybrid of GQD and GCN shows marginally improved change in absorption intensity than GCN, as shown in **Fig. 5.8(e)**. This is possibly due to the van der Waals interaction between the GQD and GCN. The reduction in absorption intensity is most prominent when irradiation is performed in presence of Au@GQD-GCN (see **Fig. 5.8(f)**). The degradation (%) and reaction kinetics of MB in different catalyst samples are discussed below.

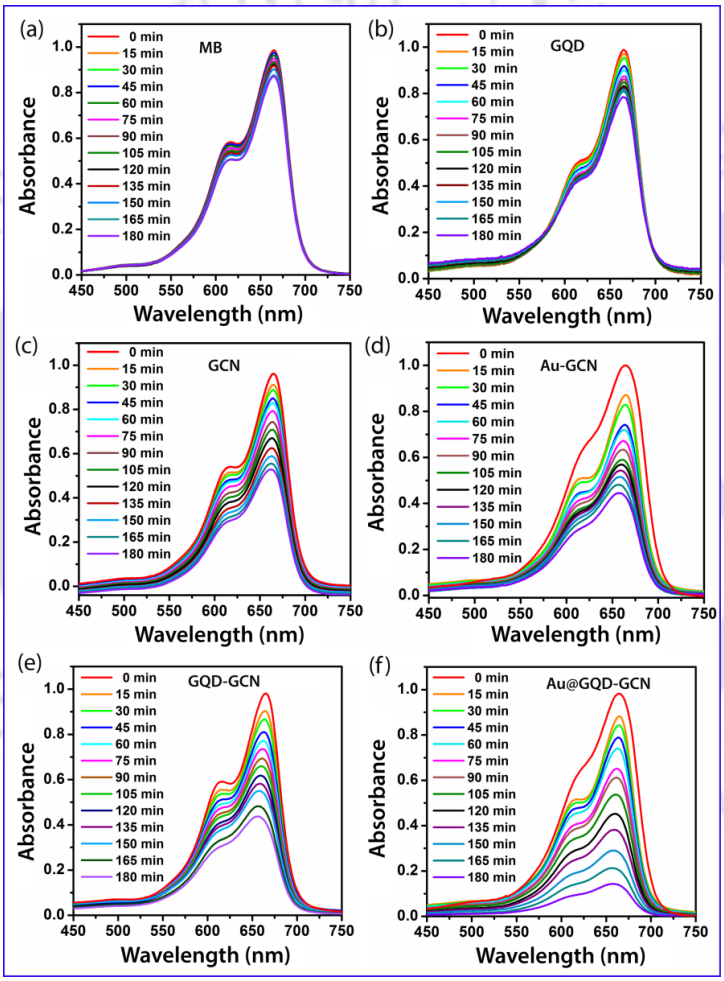

Figure 5.8: Absorption spectra of MB after irradiation under visible light for 0-180 min. (a) MB, (b) GQD, (c) GCN, (d) Au-GCN, (e) GQD-GCN and (f) Au@GQD-GCN.

The degradation percentage of the MB in each catalyst is assessed form the ratio of final (each interval of time) and initial value of its absorption intensity. **Fig. 5.9(a)** shows the change in concentration ratio of MB (% degradation) in catalyst samples for the dark reaction (45 min) and visible light irradiation up to 180 min. The dark reaction is performed in order to achieve the adsorption-desorption equilibrium between the dye and

catalyst solution. Note that there is no remarkable degradation of MB noticed in dark reaction (see **Fig. 5.9(a)**).

It is seen that in the absence of catalyst, MB molecule itself is inactive to undergo self-degradation under visible light and only 12% degradation occurs after 180 min of irradiation. When GQD is added as a catalyst and photoactivity is evaluated, 22% of MB degradation is achieved. With Au NPs are added as a catalyst, the MB degradation is improved to 28%, owing to the SPR absorption of Au. Further, GCN shows superior PC activity than GQD and a 48% of MB degradation is obtained. Next, GQD-GCN hybrid shows 54% degradation of MB. Decoration of Au NPs on GQD-GCN hybrid yields immensely high degradation (86%) of MB as compared to the other hybrids over the irradiation time of 180 min, as evident from **Fig. 5.9(a)**.

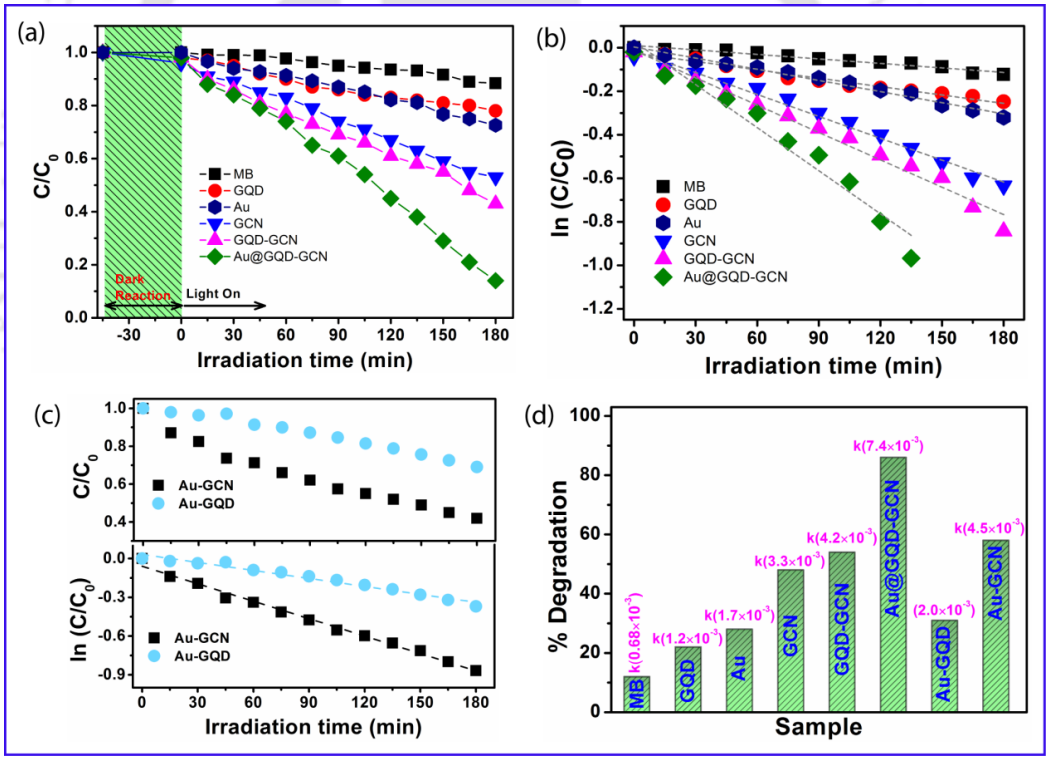

Figure 5.9: (a) Changes in the concentration of MB under dark and irradiation under visible light in presence of catalysts GQD, Au, GCN, GQD-GCN and Au@GQD-GCN. (b) Pseudo first order rate kinetics of MB photodecomposition. (c) Photodegradation and reaction kinetics of MB decomposition in presence of catalysts Au-GCN and Au-GQD. (d) Percentage degradation and rate constant values for different samples in MB degradation.

The kinetics of the PC reactions, which generally follows a pseudo first order process is expressed by $\ln(C/C_0) = -kt$, where C and C_0 are the concentration at certain time (t) and initial concentration of MB, respectively, and t is time, *k* is the reaction rate

constant, which is obtained from the slope of the linear plot. **Fig. 5.9(b)** shows the $\ln(C/C_0)$ verses irradiation time (t) plot for different catalyst samples. The symbols represent the experimental data and dotted line represents the fitted data. To understand the role of Au NPs with hybrid of GQD or GCN and its effect in PC activity, we performed photocatalysis of MB in presence of Au-GQD and Au-GCN. It is apparent from the **Fig. 5.9(c),** that the MB degradation in Au-GQD and Au-GQD catalysts is 31% and 58%, respectively, which showed better degradation performance than bare GQD and GCN. The low PC activity of Au NPs on the GQD or GCN might be due to the weak attachment or isolated Au NPs with the GQD or GCN surfaces. Our TEM images show the evidence for isolated Au NPs on GCN surface and GQD-GCN (see **Fig. 5.2(d, e)**). The details of the % degradation of MB and rate constants in different catalyst samples are depicted by a bar chart in **Fig. 5.9(d).** In **Fig. 5.9(d),** the value in the parenthesis bracket represents the rate constant of MB in different catalyst samples. Note that the unit of the rate constant (k) is in min^{-1}. In absence of any catalyst, MB is degraded to only 12% and the corresponding rate constant is 0.68×10^{-3} min^{-1}. The rate constants of degradation in GQD, Au and GCN are 1.2×10^{-3}, 1.7×10^{-3} and 3.3×10^{-3} min^{-1}, respectively. On the other hand the rate constant of MB in hybrid of GQD-GCN is 4.2×10^{-3} min^{-1}, which is marginally higher than the GQD and GCN. Interestingly, Au NPs decorated

GQD-GCN hybrid boosts the MB degradation up to 86% and rate constant obtained from this catalyst is 7.4×10^{-3} min^{-1}, which is most efficient catalyst among all the catalysts studied here. Note that integration of Au NPs on GQD or GCN shows smaller improvement in MB degradation as well as rate constant (see **Fig. 5.9(d)**). Xue *et al.*[41] reported 97 % degradation of MB for irradiation time of 240 min with 100 mg catalyst with the MB concentration of 10 mg/L. In the present study, we have achieved 86 % degradation of MB with 6 mg catalyst in 8 mg/L MB solution with irradiation time of 180 min. Thus, the present hybrid catalysts are much more efficient than that reported by Xue *et al.* [41]. The rate kinetics shown by Au@GQD-GCN is nearly 6 fold higher than that of GQD and 2.2, 1.7 times higher than GCN and GQD-GCN, respectively. The possible reason for different PC activity of MB in presence of different catalyst samples are summarized below.

Despite the presence of reactive oxygenated functional groups, GQD alone exhibits very poor PC activity. As revealed by the TRPL analysis, the oxygenated functional groups in GQD act as carrier recombination centres. Therefore, available density of free carriers is low to take part in the photocatalysis. Moreover, its poor absorption in the visible region could be another factor behind its low PC activity. Unlike GQD, GCN shows a better PC activity. The better PC activity of GCN can be attributed to its extended visible absorption and prolonged carrier lifetime. TRPL analysis of GQD-GCN shows a longer carrier lifetime implying a superior interfacial charge separation. Presence of sufficient numbers of free electrons and holes at the interface can readily interact with adsorbed MB molecule and could speed up the photodegradation of MB. The GQD-GCN hybrid system also shows broad absorption tail extended to ~720 nm in the visible region. Extended visible absorption and efficient interfacial charge separation can enhance the PC degradation of dye.

Au-GQD, Au-GCN and Au@GQD-GCN: It is observed that after the deposition of Au NPs, the PC activities of GQD, GCN and GQD-GCN hybrids are enhanced. Au NPs may act as electron traps and might enable hole separation on the material/substrate where it is attached. Further, because of the SPR effect, plasmonic Au NPs will enhance the localized electric field surrounding the Au NPs. [42, 43] This enhancement of optical field at the proximity of the attached semiconductor will provide facile electron-hole separation. When Au is deposited over GQD-GCN, the Au NPs may get attached with both GCN and GQD. Because of SPR effect, Au NPs are able to concentrate high light intensity (optical field enhancement) at the interface of GCN-Au-GQD. This will trigger photoexcitation of electrons in both GQD and GCN. Photoexcitation is followed by charge transfer from hybrid system to Au NPs. However, in case of Au-GCN and Au-GQD, the deposited Au NPs will trigger photoexcitation on GQD or GCN. The optical field enhancement for carrier excitation and separation are expected to be weaker in Au-GCN or Au-GQD as compared to those in Au@GQD-GCN.

5.8.2. Free Radical Detection and Degradation Mechanism

In order to understand free radical involvement and their contribution in the MB degradation, we have performed the free radical scavenger experiments on the Au@GQD-GCN, since it showed better efficiency of MB degradation. TA and NBT

compounds are used for the detection of free radicals [44, 45]. **Fig. 5.10** shows the evidence for the free radicals and formation of secondary compounds**. Fig. 5.10(a**) shows the PL spectra of the TA for the irradiation of 180 min. The PL spectra imply that with increasing the irradiation time the intensity of the TA continuously increases. This further implies that with irradiation time the amount of hydroxyl radical ($^{\bullet}OH$) increases. This is because that there is an irreversible reaction between TA and $^{\bullet}OH$ radical to form 2-hydroxy TA. **Fig. 5.10(b**) shows the schematic for the conversion of TA in to 2-hydroxy TA in presence of $^{\bullet}OH$. Other primary and secondary radicals, such as $^{\bullet}H$, $HO_2^{\bullet}$ and H_2O_2 do not significantly affect the induced PL [32]. Further, evidence of superoxide radical ($O_2^{\bullet-}$) in aqueous solution is probed from the UV-vis absorption measurments of

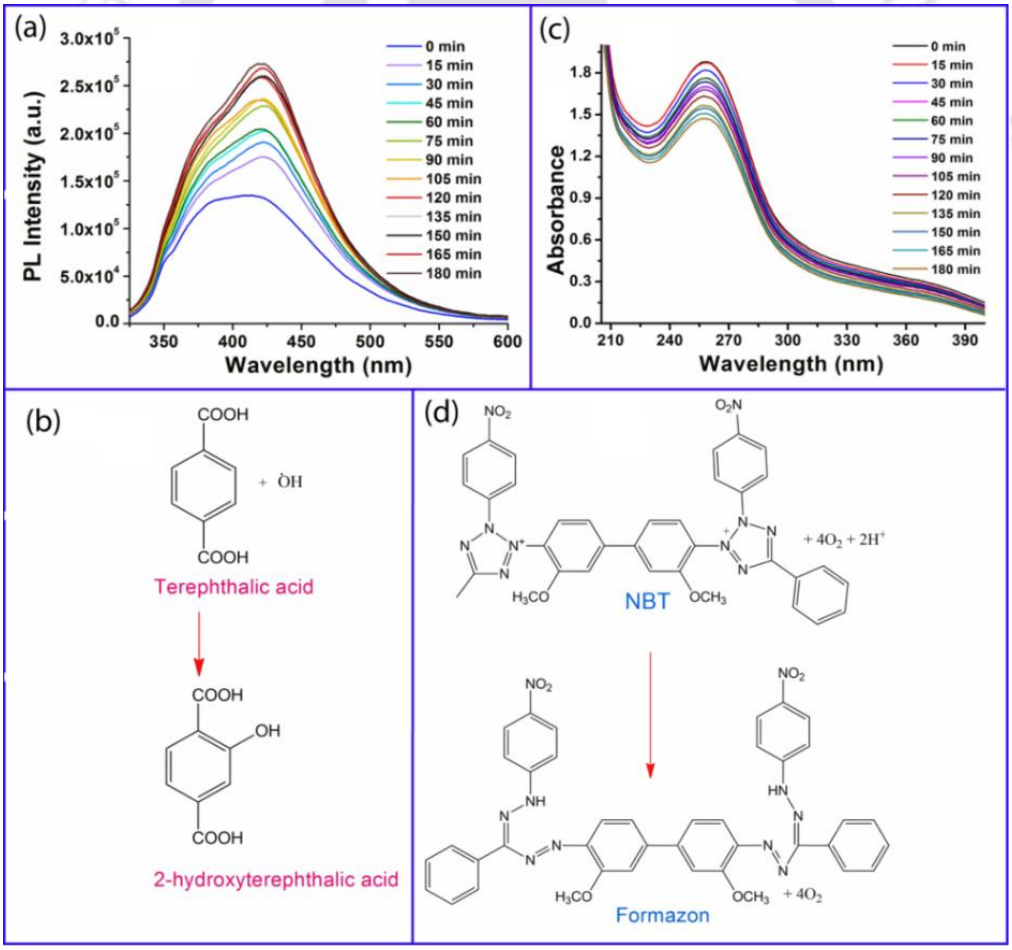

Figure 5.10: (a) PL spectra of TA up to the irradiation time of 180 min and (b) schematic showing the conversion of TA to 2hydroxy TA. (c) UV-Vis absorption spectra of NBT up to the irradiation time 180 min and (d) schematic showing the conversion of NBT to Formazon. Note that the TA and NBT tests are for the detection of hydroxyl and superoxide radicals, respectively.

NBT for irradiation of 0 to 180 min and absorption spectra is depicted in the **Fig. 5.10(c**). NBT shows an absorption maximum at 255 nm and it is very sensitive to electron donor, and therefore, in presence of $O_2^{\bullet-}$ NBT is reduced to its formazon form producing its characteristic purple colour. [33] If there is large concentration of $O_2^{\bullet-}$ radicals in solution, the absorption peak intensity will eventually decrease with irradiation time. **Fig. 5.10(d**) shows a schematic of the conversion of NBT to formazon. However, $^{\bullet}OH$ shows better response to TA test than $O_2^{\bullet-}$ to NBT test confirming that $^{\bullet}OH$ is the major species involved in the photocatalysis.

One important issues with the visible light absorbing dye molecule is its self-sensitization effect. Under the visible light illumination, MB molecule undergoes photoexcitation to a higher energy state. However, from the position of conduction band of MB, it is clear that transfer of electrons from photo excited MB* to GQD or GCN is not feasible. Electron transfer from MB* to Au, however, might take place. Therefore, the photodegradation of MB is initiated only in presence of plasmonic hybrid catalyst with negligible possibility of self- sensitized photodegradation. Therefore, the PC processes can be summarized as follows. Under photoexcitation of visible light, GQD-GCN absorbs mostly in the near visible region (λ<460 nm). However, longer wavelength (λ>530 nm) light exposure stimulates SPR absorption in the Au NPs. **Fig. 5.11(a)** shows the schematic representation for the illumination of light on hybrid of Au decorated GQD-GCN, where plasmon excitation will generate enhancement of optical field in the vicinity of Au NPs at the interface with GQD-GCN. This optical field will trigger energetic electron generation in the neighbourhood of GQD-GCN. Photoexcited carriers, generated in the hybrid as a result of plasmonic absorption, will migrate to Au NPs and participate in PC reaction.

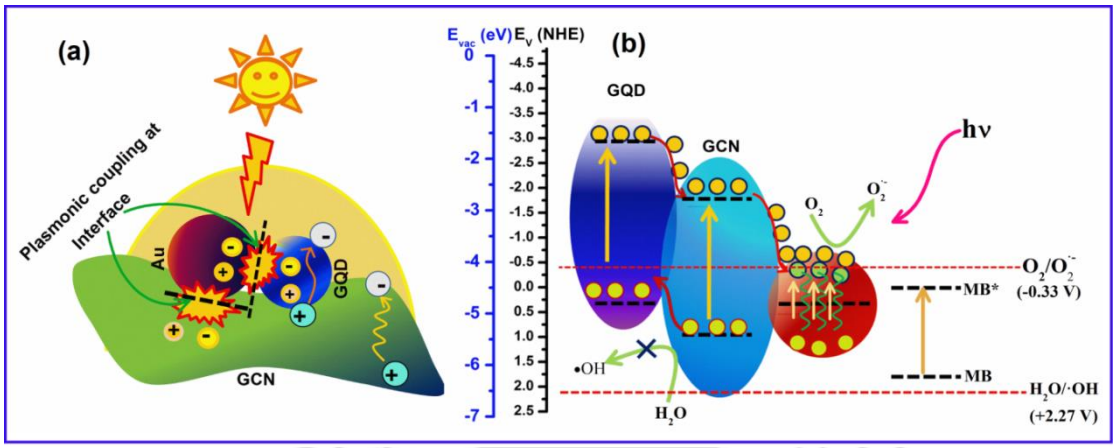

Figure 5.11: (a) Schematic of SPR absorption under visible light and carrier photoexcitation at the interface between Au-GQD-GCN in the plasmonic hybrid photocatalyst. (b) Schematic of band structure of plasmonic hybrid nanosystem with generation of radical species.

In order to understand the mechanism for the enhanced PC activity in Au@GQD-GCN, we need to understand the charge separation, charge transfer and charge accumulation process in the plasmonic hybrid. Carrier separation and charge transfer depends on the band structure of the hybrid. A schematic band diagram of the plasmonic hybrid system is drawn based on the band structure of GQD, GCN, Au and MB.[5, 46-50] The conduction band and valence band position of GQD is drawn at -1.57 and -4.8 eV, for GCN these positions are -2.82 and -5.47 eV, Au NPs have a work function of -4.75 eV, and for MB the band positions are at -4.55 and -6.26 eV *versus* (*vs.*) vacuum scale. The relation between redox potentials vs. normal hydrogen electrode and work functions *vs.* vacuum scale is given by E = -4.5 eV-E_{NHE} (V). [49] The standard redox potential of $O_2/O_2^{\bullet-}$ and $H_2O/{}^{\bullet}OH$ are -0.33 V and +2.27 V *vs.* normal hydrogen electrode. The schematic band diagram is shown in **Fig. 5.11(b)**. Electrons reached to Au forms $O_2^{\bullet-}$ by interacting with surface adsorbed O_2. It is evident from **Fig. 5.11(b)** that valence band holes cannot oxidize H_2O to ${}^{\bullet}OH$. This process can be explained in another way for hydroxyl radical formation. In aqueous solution $O_2^{\bullet-}$ is unstable and this is prone to form stable ${}^{\bullet}OH$. Note that our TA test also showed evidence for higher amount of ${}^{\bullet}OH$ in solution. The formation of ${}^{\bullet}OH$ through $O_2^{\bullet-}$ formation can be explained with the following reaction steps. [4] Finally, these free radicals degrade the MB into CO_2, water and other inorganic compounds.

$$O_2 + e^- \rightarrow O_2^{\bullet -}$$

$$H_2O \rightarrow H^+ + OH^-$$

$$O_2^{\bullet -} + 2H^+ + e^- \rightarrow H_2O_2$$

$$H_2O_2 \rightarrow {}^{\bullet}OH + OH^-$$

$$OH^- + h^+ \rightarrow {}^{\bullet}OH$$

$${}^{\bullet}OH + \text{dye} \rightarrow \text{water} + CO_2$$

5.9. Summary & Conclusions

1. In this chapter, an *in-situ* chemical method was used to prepare the hybrid of Au NPs decorated GQD and GCN.

2. A striking enhancement in the intensity of Raman G band is observed in Au functionalized GQD-GCN due to the SPR of Au.

3. We have achieved 86% of MB degradation in Au decorated GQD-GCN.

4. Evidence for the free radicals ($O_2^{\bullet -}$ and ${}^{\bullet}OH$) was studied by spectroscopic techniques and ${}^{\bullet}OH$ played the major role in the MB degradation.

5. The coupling between the Au-GQD-GCN and efficient charge transfer between the GQD-GCN to Au facilitated the enhanced photodegradation of MB.

References

1. A. Fujishima and K. Honda, *Nature*, 1972, **238**, 37-38.
2. R. S. Blackburn, *Environmental Science & Technology*, 2004, **38**, 4905-4909.
3. D. Özer, G. Dursun and A. Özer, *Journal of Hazardous Materials*, 2007, **144**, 171-179.
4. D. Friedmann, C. Mendive and D. Bahnemann, *Applied Catalysis B: Environmental*, 2010, **99**, 398-406.
5. S. Chu, Y. Wang, Y. Guo, J. Feng, C. Wang, W. Luo, X. Fan and Z. Zou, *ACS Catalysis*, 2013, **3**, 912-919.
6. X. She, H. Xu, Y. Xu, J. Yan, J. Xia, L. Xu, Y. Song, Y. Jiang, Q. Zhang and H. Li, *Journal of Materials Chemistry A*, 2014, **2**, 2563-2570.

7. M.-J. Lee, S.-H. Lim, J.-M. Ha and S.-M. Choi, *Langmuir*, 2016, **32**, 5937-5945.
8. S. A. Bakar, G. Byzynski and C. Ribeiro, *Journal of Alloys and Compounds*, 2016, **666**, 38-49.
9. L. Ye, J. Liu, Z. Jiang, T. Peng and L. Zan, *Applied Catalysis B: Environmental*, 2013, **142**, 1-7.
10. B. Choudhury and P. K. Giri, *RSC Advances*, 2016, **6**, 24976-24984.
11. Z. Zhang, J. Zhang, N. Chen and L. Qu, *Energy & Environmental Science*, 2012, **5**, 8869-8890.
12. C. C. Li, L. B. Chen, Q. H. Li and T. H. Wang, *CrystEngComm*, 2012, **14**, 7549-7551.
13. A. C. Ferrari and D. M. Basko, *Nat Nano*, 2013, **8**, 235-246.
14. C. Casiraghi, A. Hartschuh, H. Qian, S. Piscanec, C. Georgi, A. Fasoli, K. S. Novoselov, D. M. Basko and A. C. Ferrari, *Nano Letters*, 2009, **9**, 1433-1441.
15. A. C. Ferrari and J. Robertson, *Physical Review B*, 2000, **61**, 14095-14107.
16. Z. Ma, R. Sa, Q. Li and K. Wu, *Physical Chemistry Chemical Physics*, 2016, **18**, 1050-1058.
17. H.-B. Sun, J. Wu, J.-J. Zhu, D.-F. Pan, G.-H. Wang and J.-G. Wan, *Applied Physics Letters*, 2015, **106**, 211603.
18. P. Törmä and W. L. Barnes, *Reports on Progress in Physics*, 2015, **78**, 013901.
19. D. H. K. Sung Hwan Jin, Gwang Hoon Jun, Soon Hyung Hong, and Seokwoo Jeon, *ACS Nano*, 2013.
20. L. Wang, S.-J. Zhu, H.-Y. Wang, S.-N. Qu, Y.-L. Zhang, J.-H. Zhang, Q.-D. Chen, H.-L. Xu, W. Han, B. Yang and H.-B. Sun, *ACS Nano*, 2014, **8**, 2541-2547.
21. G. Rajender and P. K. Giri, *Journal of Materials Chemistry C*, 2016, **4**, 10852-10865.
22. W. Zheng, N.-B. Wong, G. Zhou, X. Liang, J. Li and A. Tian, *New Journal of Chemistry*, 2004, **28**, 275-283.
23. P. Niu, G. Liu and H.-M. Cheng, *The Journal of Physical Chemistry C*, 2012, **116**, 11013-11018.
24. D. Qu, M. Zheng, L. Zhang, H. Zhao, Z. Xie, X. Jing, R. E. Haddad, H. Fan and Z. Sun, *Scientific Reports*, 2014, **4**, 5294.
25. R. Jiang, B. Li, C. Fang and J. Wang, *Advanced Materials*, 2014, **26**, 5274-5309.

26. J. Bian, J. Li, S. Kalytchuk, Y. Wang, Q. Li, T. C. Lau, T. A. Niehaus, A. L. Rogach and R.-Q. Zhang, *ChemPhysChem*, 2015, **16**, 954-959.
27. P. Wu, J. Wang, J. Zhao, L. Guo and F. E. Osterloh, *Journal of Materials Chemistry A*, 2014, **2**, 20338-20344.
28. S. Zhu, J. Shao, Y. Song, X. Zhao, J. Du, L. Wang, H. Wang, K. Zhang, J. Zhang and B. Yang, *Nanoscale*, 2015, **7**, 7927-7933.
29. L. Lin and S. Zhang, *Chemical Communications*, 2012, **48**, 10177-10179.
30. N. T. Khoa, S. W. Kim, D.-H. Yoo, S. Cho, E. J. Kim and S. H. Hahn, *ACS Applied Materials & Interfaces*, 2015, **7**, 3524-3531.
31. J. Lee, H. S. Shim, M. Lee, J. K. Song and D. Lee, *The Journal of Physical Chemistry Letters*, 2011, **2**, 2840-2845.
32. S. Park, J. An, R. D. Piner, I. Jung, D. Yang, A. Velamakanni, S. T. Nguyen and R. S. Ruoff, *Chemistry of Materials*, 2008, **20**, 6592-6594.
33. Z. Zhou, Y. Shen, Y. Li, A. Liu, S. Liu and Y. Zhang, *ACS Nano*, 2015, **9**, 12480-12487.
34. X. Li, G. Hartley, A. J. Ward, P. A. Young, A. F. Masters and T. Maschmeyer, *The Journal of Physical Chemistry C*, 2015, **119**, 14938-14946.
35. S. Zhu, J. Zhang, X. Liu, B. Li, X. Wang, S. Tang, Q. Meng, Y. Li, C. Shi, R. Hu and B. Yang, *RSC Advances*, 2012, **2**, 2717-2720.
36. A. Y. Klyushin, M. T. Greiner, X. Huang, T. Lunkenbein, X. Li, O. Timpe, M. Friedrich, M. Hävecker, A. Knop-Gericke and R. Schlögl, *ACS Catalysis*, 2016, **6**, 3372-3380.
37. R. Wang, Z. Wu, G. Wang, Z. Qin, C. Chen, M. Dong, H. Zhu, W. Fan and J. Wang, *RSC Advances*, 2015, **5**, 44835-44839.
38. J. Li, C.-y. Liu and Y. Liu, *Journal of Materials Chemistry*, 2012, **22**, 8426-8430.
39. D. Briggs, *Surface and Interface Analysis*, 1981, **3**, v-v.
40. Y. Enbo, C. Han, T. Shun and N. Masaaki, *Journal of Physics D: Applied Physics*, 2016, **49**, 185304.
41. J. Xue, S. Ma, Y. Zhou and Q. Wang, *RSC Advances*, 2015, **5**, 88249-88257.
42. Z. Xuming, C. Yu Lim, L. Ru-Shi and T. Din Ping, *Reports on Progress in Physics*, 2013, **76**, 046401.
43. S. V. Boriskina, H. Ghasemi and G. Chen, *Materials Today*, 2013, **16**, 375-386.

44. Y. Nosaka, S. Komori, K. Yawata, T. Hirakawa and A. Y. Nosaka, *Physical Chemistry Chemical Physics*, 2003, **5**, 4731-4735.

45. M. Hayyan, M. A. Hashim and I. M. AlNashef, *Chemical Reviews*, 2016, **116**, 3029-3085.

46. Q. Lu, Y. Zhang and S. Liu, *Journal of Materials Chemistry A*, 2015, **3**, 8552-8558.

47. K. A. Ritter and J. W. Lyding, *Nat Mater*, 2009, **8**, 235-242.

48. H.-Z. Wu, L.-M. Liu and S.-J. Zhao, *Physical Chemistry Chemical Physics*, 2014, **16**, 3299-3304.

49. Z. Xiong, L. L. Zhang, J. Ma and X. S. Zhao, *Chemical Communications*, 2010, **46**, 6099-6101.

50. H.-J. Li, B.-W. Sun, L. Sui, D.-J. Qian and M. Chen, *Physical Chemistry Chemical Physics*, 2015, **17**, 3309-3315.

Chapter 6

Interfacial Charge Transfer in Oxygen Deficient TiO2–Graphene Quantum Dot Hybrid and Its Influence on the Enhanced Visible Light Photocatalysis

In this chapter, we discuss the formation of heterojunction between TiO_2 and graphene quantum dots (GQDs) and its visible light photocatlytic activity. We explain the formation of TiO_2-GQD heterojunction through the bonding between oxygen vacancy sites of TiO_2 and in-plane oxygen functional (epoxy) groups in GQDs possibly through the C-O-Ti bonds proposed, for the first time. Our FTIR, XPS and Raman results lend support to the proposed mechanism of heterojunction formation. In the TiO_2/GQD hybrid, the Raman $E_g(1)$ peak of anatase TiO_2 is blue shifted indicating the strong interaction between the GQD and TiO_2. Further, we performed the density functional theory (DFT) calculation to calculate its optical spectrum and to support the hybrid formation. Interestingly, the calculated results for the hybrid structure show strong optical absorption in the visible to near infrared region, which is in close agreement with the experimental results. The TiO_2-GQD heterojunction exhibits enhanced photocatalytic degradation (97%) of methylene blue (MB) due to the facile interfacial charge separation, as revealed from the steady state and time resolved photoluminescence studies. The degradation rate constant (first order) for TiO_2-GQD hybrid is 9.2 and 5.2 times higher than that of the GQD and TiO_2, respectively. Free radical scavenger test revealed that $^{\bullet}OH$ radicals played a major role in the MB degradation as compared to $O_2^{\bullet-}$ radical.

6.1. Introduction

In the previous chapter, we have discussed about motivation behind the visible light photocatalysis study. TiO_2 has different polymorph structures, such as anatase, rutile and brookite. Regardless of different phases of TiO_2, the band gap of these material falls in the UV region, which limits the efficiency of visible light photocatalytic (PC) activity. Among the different polymorphs of TiO_2, anatase TiO_2 is preferable for PC studies due to its highly oxidizing power, high surface area, ability to generate more free radicals and

charge carrier transport etc. [1-4]. There are a few reports that discuss about the TiO_2-graphene hybrid formation. Xing et al studied the graphene and TiO_2 hybrid formation through the OH functional groups [5]. Umrao et al. proposed the C-O-Ti bond formation in TiO_2-graphene system due to the free electron interaction of both the materials [6]. However, the actual pathway that leads to the formation of the TiO_2-graphene hybrid has not been addressed. Graphene quantum dots (GQDs) are known to be ultrafine size pieces of graphene materials. Due to the ultrafine size and high ratio of edge to basal plane carbon atoms, GQDs possess the edge states and edge oxygen functional groups [7-10]. In this regard, GQDs have meagre in-plane oxygen functional groups than that of other graphene materials. Thus, we believe that in GQDs mostly the edge oxygen functional groups rearrangement or in-plane epoxy disorder is necessary in order to form the hybrid. In this case, an ultrasonication method is used to construct the heterojunction of TiO_2 and GQDs and the role of GQDs in the charge carrier separation and PC degradation of methylene blue (MB) was studied.

6.2. Experimental and Computational Details

Details of the precursor and hybrid sample preparation and the experimental details for the PC degradation of MB as well as free radical scavenger test are elaborated in this section. The computational details are provided at the end.

6.2.1. Sample Preparation

6.2.1.1 Fabrication of GQDs and TiO_2 Nanoparticles

The synthesis details of GQD using DMF solvent was discussed in **Chapter 4, section 4.2.1.** TiO_2 nanoparticles (NPs) are prepared by mechanical ball milling. Commercially procured anatase TiO_2 powder (purity >99%) with average particle size ~80 nm was used as the starting material for the mechanical ball milling process. Ball-milling was performed under ambient condition at 350 rpm for the duration of 16 h in a Zirconia vial using Zirconia balls. The ball to powder weight ratio was taken as 10:1. The vial and balls (diameter 5 mm) are made of the ZrO_2. The use of ZrO_2 containers ensures the contamination free preparation of TiO_2 NPs through the ball-milling process. The pristine and ball milled (16 h) samples are denoted as T0 and T16, respectively.

6.2.1.2. Fabrication of GQDs and TiO_2 NPs Hybrids

Equal amount (weight ratio 1:1) of TiO_2 NPs (pristine or ball milled) and GQDs are mixed together and dispersed in DI water. Next, the mixture was ultrasonicated (40 kHz) for 1h and subsequently centrifuged, and dried to get the solid powder. The hybrid samples of T0 and T16 each mixed with GQDs and ultrasonicated are denoted as T0/GQD and T16/GQD, respectively. To understand the interaction between the GQDs and TiO_2 NPs, one set of hybrid sample is prepared only by mixing and stirring method without any ultra-sonication, and the sample is termed as T16/GQDM. Schematic of the sample preparation procedure is shown in **Fig. 6.1(a)**.

6.2.2. Visible Light Photocatalysis

6.2.2.1. Photodegradation of methylene blue

The details about the light source and arrangements for the photodegradation of methylene blue (MB) was discussed in **Chapter 5, section 5.2.2.1.** In this case 20 mg of catalyst was mixed with 100 mL of aqueous solution with an initial MB concentration of 8 mg/L. Next the MB with catalyst was stirred in dark for 1 h to reach the adsorption-desorption equilibrium between dye and catalyst. Further, the solution was irradiated with visible light for 120 min. At an interval of 10 min, 5 mL aliquot was taken out and centrifuged. Photodegradation of MB was measured from the UV-Vis absorption spectrum of its maximum absorption peak intensity at 665 nm after each 10 min of light irradiation.

6.2.2.2. Free Radicals Scavenger Test

To determine the contribution of reactive species that are involved in the photodegradation of MB, we have performed the free radical scavenger experiment. For this experiment, Ammonium oxalate (AO), tert-butyl alcohol (t-BA) and p-benzoquinone (BQ) scavengers were used to study the influence of hole (h^+), hydroxyl radical ($^{\bullet}OH$) and superoxide radical ($O_2^{\bullet-}$), respectively. In each experiment, 1 mM of scavenger is added to the catalyst–dye solution (20 mg, 8 mg/L) [11]. Afterwards, the dye-catalyst-quencher solution was irradiated and the sample collection and UV-Vis absorption measurements conditions are identical to that mentioned in the previous section.

6.2.3. Computational Methodology

In order to lend support to the experimental results and the proposed mechanism of TiO_2-GQD heterojunction, we have carried out the theoretical calculations by CASTEP code

based on density functional theory (DFT) in *Materials Studio* program [12]. The exchange correlation interaction is implemented by generalized gradient approximation (GGA) functional in Perdew-Burke-Ernzerhof (PBE) format, using the ultrasoft pseudopotentials [13, 14]. Grimme dispersion corrected density functional theory (DFT-D) has been employed for the interaction of GQD and TiO_2 surface. The system contains hybrid structure of a 2×2 supercell of TiO_2 (110) surface with two oxygen vacancies and overlapping GQD of size 1.27×1.27 nm^2 with oxygen functional groups. The GQD contained nine hexagonal rings with two epoxy functional groups out of the GQD plane. A vacuum space of 20 Å is placed to avoid the interaction between the adjacent layers in the direction perpendicular to the GQD plane. Geometry optimization of hybrid structure is performed until the maximum force was less than 0.05 eV/Å. Spin unrestricted calculation is performed with the Brillouin zone integration by setting a 3×3×2 Monkhorst-Pack k-point grid for geometry optimization and optical properties. The cut off energy of 600 eV is used with 2×10^{-5} eV/atom self-consistent filed convergence tolerance limit. Note that 0.1 eV smearing is used for the calculation of the absorption spectrum in each case. For comparison, we have calculated the absorption spectrum of bare anatase TiO_2 (110). Computational results are compared with that of the experimental results of bare TiO_2 and hybrid structures.

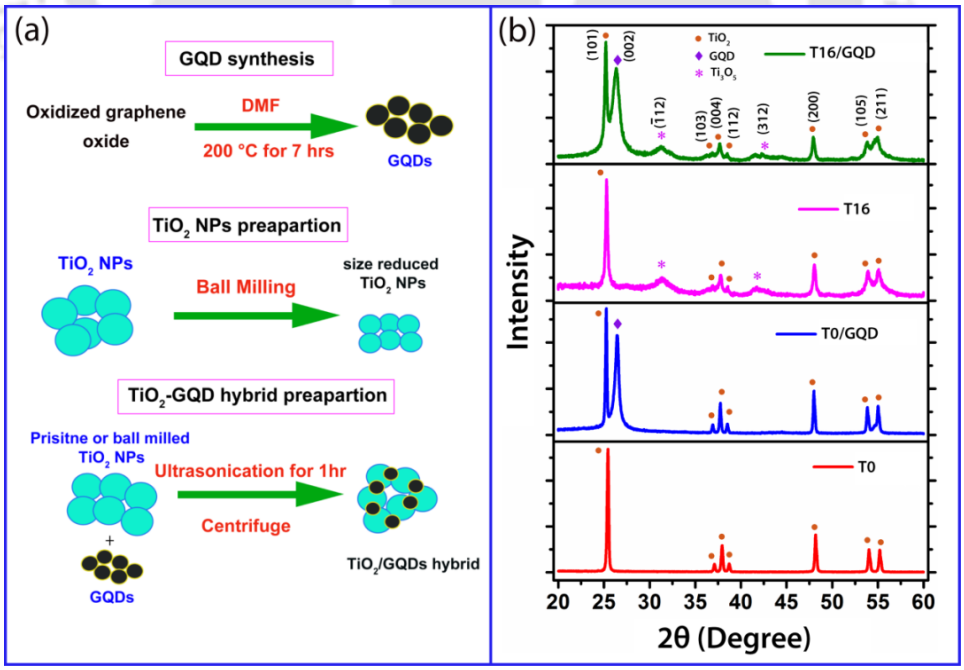

Figure 6.1: (a) Schematic representation of sample preparation. (b) XRD pattern of T0, T16, T0/GQD and T16/GQD hybrids. Note that the peaks corresponding to the anatase TiO_2, Ti_3O_5 and GQDs are labelled with different symbols.

6.3. X-ray Diffraction and TEM Studies

The structural and morphological properties of bare and hybrids of GQD and TiO_2 NPs are studied by X-ray Diffraction (XRD) and transmission electron microscopy (TEM) analyses. **Fig. 6.1(b)** shows the XRD pattern of T0, T16, T0/GQD and T16/GQD. All the samples shows the characteristic reflection peaks related to the antase phase of TiO_2. In **Fig. 6.1(b)** the major intense XRD peak at 2θ~ 25° corresponds to the anatase phase (101) plane of TiO_2 [15]. As compared to the pristine TiO_2 (T0), ball milled sample (T16) exhibited additional XRD peaks at 2θ~31.28 and 41.6°, which correspond to the (T12) and (312) planes of Ti_3O_5 (JCPDS No. 74-0819), respectively [15]. Additionally, as compared to T0, the crystallinity of T16 is reduced, presumably due to the mechanical milling that causes high density of defects/disorder in the system [15]. In hybrid samples, the major intense XRD peak is due to the anatase TiO_2 and other intense peak at 2θ~26.3° is originated from the (002) plane of sp^2 hybridized, hexagonal graphitic structure of GQDs [16]. The (002) peak is very intense for the hybrid sample prepared with equal weight ratio of TiO_2 and GQDs. Note that in **Fig. 6.1(b),** XRD peaks related to the anatase TiO_2, Ti_3O_5 and GQDs are labelled with the '•', '*' and '♦' symbols, respectively. The role of oxygen vacancies in the formation of TiO_2-GQD hybrid is discussed later. These results indicate the successful preparation of TiO_2-GQD hybrids with crystalline phases.

The size and morphological features of the TiO_2 NPs, GQDs and their hybrids were analysed by TEM and high resolution (HR) TEM imaging, as displayed in **Fig. 6.2(a-i)**. **Fig. 6.2(a)** shows the TEM image of T0 and the average TiO_2 particle size is ~80 nm. **Fig. 6.2(b)** represents the HRTEM inverse fast Fourier transform (IFFT) lattice image of T0 showing a lattice spacing (d) of 3.25 Å, which corresponds to the TiO_2 (101) planes. **Fig. 6.2(c)** shows the TEM image of GQDs and the average size of GQDs is ~5.2 nm. The inset shows the HRTEM lattice image showing the lattice spacing of 3.34 Å (002) plane [17, 18]. Presence of this plane in GQDs confirms the sp^2 hybridized, hexagonal graphitic structure. **Fig. 6.2(d)** represents the TEM image of T16 sample and the inset shows the HRTEM lattice image, where the lattice spacing (d) 3.29 Å corresponds to the TiO_2 (101) plane. The dotted oval shape in inset of **Fig. 6.2(d)** represents the strained region of lattice fringes in TiO_2. The lattice spacing in T16 is marginally higher than that of the T0, due to the tensile strain in the TiO_2 NPs caused by ball milling [15]. The formation of TiO_2/GQD hybrid is noticeable from the TEM/HRTEM lattice images

shown in **Fig. 6.2(e-h)** for T0/GQD and T16/GQD. **Fig. 6.2(e)** shows the TEM image of T0/GQD and decoration of the GQDs on the surface of the TiO_2 NPs is clear from this image. **Fig. 6.2(f)** shows the HRTEM lattice image of T0/GQD sample, where the lattices of both TiO_2 and GQDs are discernible. The lattice spacing's of TiO_2 and GQD are 3.32 and 3.40 Å, respectively and their respective planes are (101) and (002). Similarly, the GQD distribution over the T16 surface in T16/GQD hybrid can be clearly seen from the

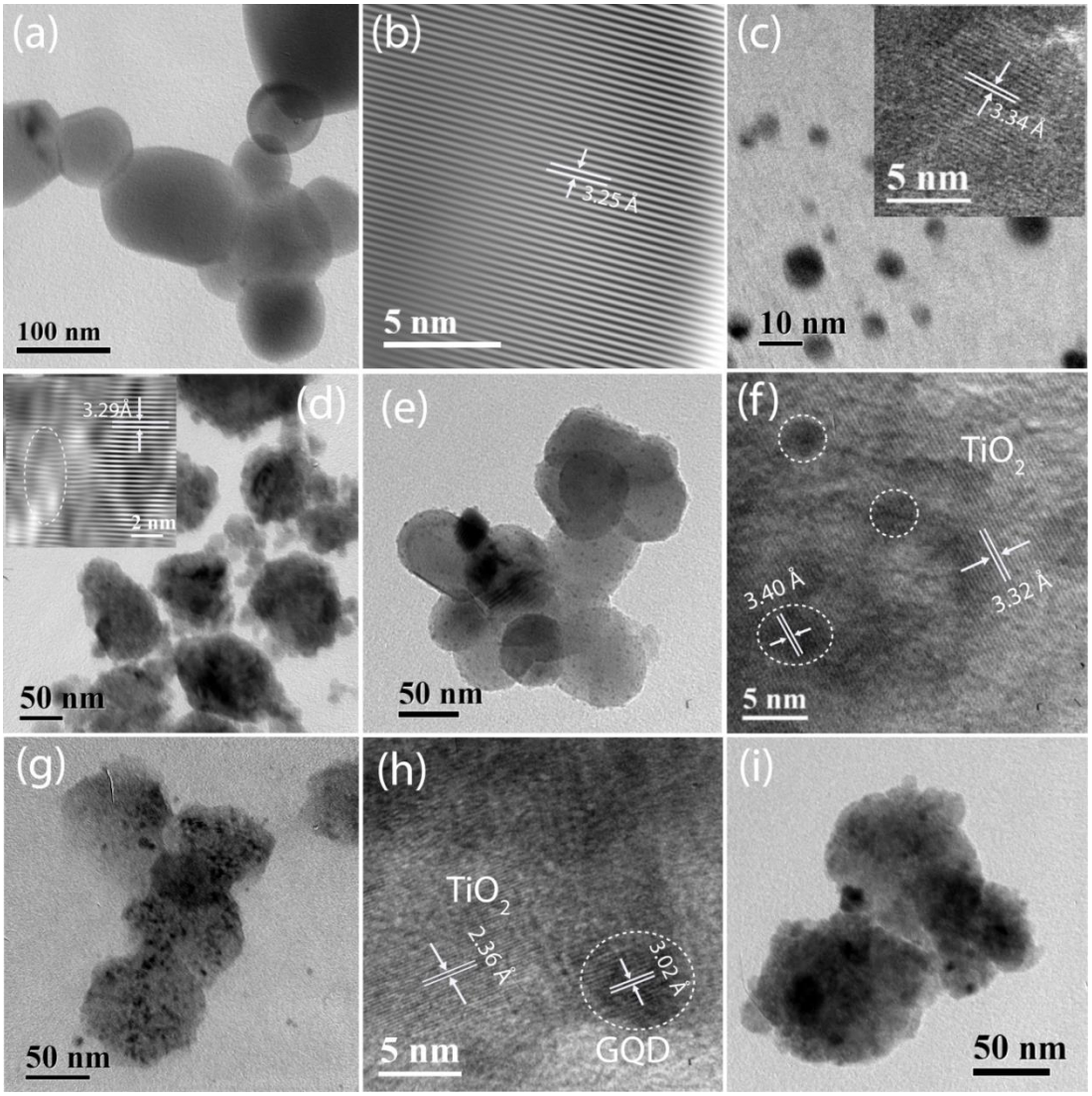

Figure 6.2: (a, b) TEM and HRTEM lattice images of TiO_2 NPs in sample T0. (c) TEM image of GQDs and the inset shows its HRTEM image. (d) TEM image of TiO_2 NPs in T16. The inset shows the HRTEM lattice image of single TiO_2 NP with the strained region marked with oval shaped dotted line. (e-f) TEM and HRTEM lattice images of T0/GQD hybrid, respectively. (g) The TEM image of T16/GQD hybrid, (h) the HRTEM lattice image of T16/GQD showing simultaneous presence of TiO_2 and GQDs lattices. Note that the GQDs are shown with the dotted line in (f, h). (i) TEM image of T16/GQD hybrid after 3 cycles of photocatalysis experiment.

TEM images in **Fig. 6.2(g,h). Figs. 6.2(g)** and **(h)** show the TEM and HRTEM lattice image of T16/GQD. The simultaneous presence of both TiO_2 and GQD lattices are evident from the image and it reveals the strong attachment of the GQDs over the TiO_2 surface. Note that in HRTEM lattice images of TiO_2-GQDs hybrid in **Fig. 6.2(f, h)**, the GQDs are shown with dotted circles. In T16/GQD, the lattice spacing 2.36 Å corresponds to the (004) plane of anatase TiO_2 (JCPDS No. 21-1272) and that of 3.02 Å corresponds to the GQDs. TEM image of T16/GQD hybrid after three repeated cycles of photocatalysis is shown in **Fig. 6.2(i)**, which reveals the stable structure of the hybrid after photocatalysis experiment. These results clearly demonstrate the formation of TiO_2/GQD heterojunction.

6.4. Raman Spectroscopy Analysis

Raman spectroscopy is an established tool for the characterization of semiconductor nanostructures and graphitic materials. **Fig. 6.3** shows the Raman spectra of pristine and hybrid samples of TiO_2 and GQDs. All the TiO_2 and TiO_2/GQD hybrid samples display the characteristic Raman bands of anatase TiO_2, such as three E_g, two B_{1g}, and one A_{1g} modes, which are consistent with the literature reports [19, 20]. In case of GQDs, the characteristic Raman G and D bands are evident. The D band is present due to the edge sites of GQDs. Besides the G and D band, another defect band, known as the D' band, appears as result of crystalline defects, such as vacancies, pentagon/heptagon or so called stone-walls (S-W) defects [21, 22]. In addition to the characteristic Raman features of anatase TiO_2 and GQDs as labelled in **Fig. 6.3(a)**, we noticed new peaks with low intensity (marked with * symbol) related to the phase of Ti_3O_5 in T16 and T16/GQD samples [15]. This is consistent with the XRD analysis (discussed in the above section). In case of TiO_2-GQD hybrid, due to the introduction of additional covalent bond (i.e., possible C-O-Ti) results in broadening in Raman line shape. In order to understand the broad Raman peak in the region 350-480 cm^{-1} of T16/GQD spectrum, we have deconvoluted it into three peaks. The inset in **Fig. 6.3(a)** shows a magnified view of the Raman spectrum in the region 240-480 cm^{-1} and Lorentzian peak fitting of T16/GQD. The fitted Lorentzian peaks are centred at 395 (peak1), 410 (peak2) and 425 cm^{-1}(peak3). Note that the peak1 and peak3 are the related to the $B_{1g}(1)$ (Raman mode of TiO_2) and Ti_3O_5 phase (denoted by "*" symbol), respectively. The peak2 and one more peak at ~267 cm^{-1} are the

possiblydue to the C-O-Ti bonds. The C-O-Ti related peaks are shown in the inset of **Fig. 6.3(a)**. Fernandes et al. reported that the Raman modes at ~264, ~407 and ~620 cm^{-1} are due to the C-O-Ti bonds in the hybrid structure of TiO_2 and TiC [23]. Further, the linkage of oxygen deficient TiO_2 and GQD through the possible C-O-Ti bonds can be understood by the blue shift of $E_g(1)$ Raman mode in the hybrid samples. **Fig. 6.3(b)** shows a comparison of the Raman $E_g(1)$ peak profiles of TiO_2 and TiO_2-GQD hybrid samples. The centre of the Raman $E_g(1)$ for T0/GQD and T16/GQD are at 148.0 and 149.8 cm^{-1}, respectively, which are upshifted by 5 and 6 cm^{-1} from that of the T0 and T16. The shift in $E_g(1)$ peak in T16/GQD is 1.8 cm^{-1} higher than that of T0/GQD. These results indicate a strong interaction between GQD and TiO_2 through defects in TiO_2. The shift in the Raman peak in hybrid samples is possibly due to the formation of possible C-O-Ti- bond, when GQD and TiO_2 come in contact with each other or due to the strain.

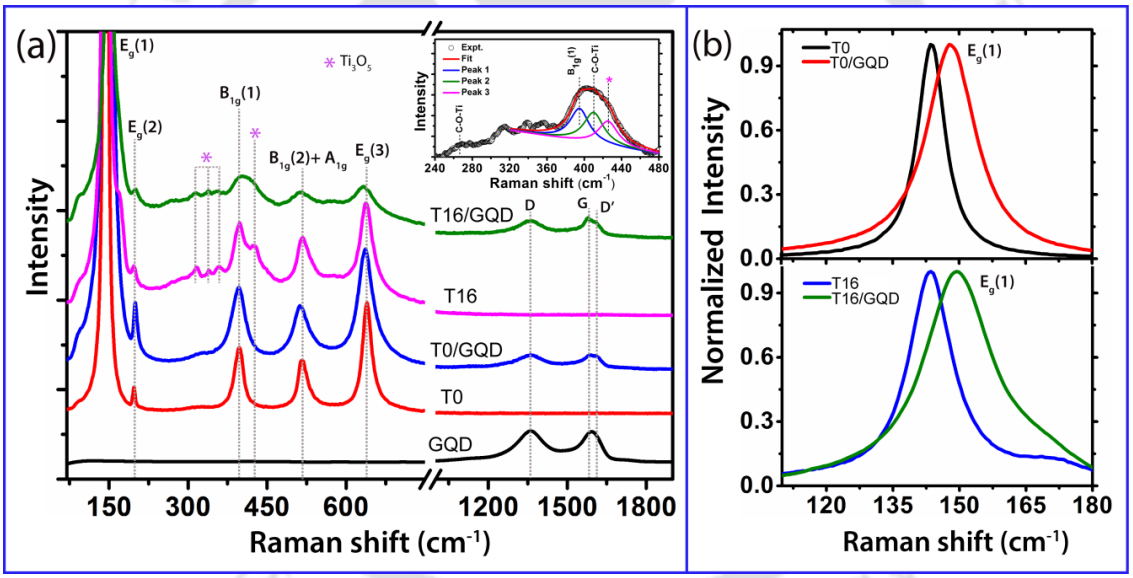

Figure 6.3: (a) Characteristic Raman spectra of TiO_2 NPs and GQDs and their hybrid samples. The characteristic Raman signatures of anatase TiO_2 and GQDs are labelled by standard notations. Note that the curves are vertically shifted for clarity. The inset shows the magnified view of the spectrum region 240-480 cm^{-1} fitting for T16/GQD showing C-O-Ti modes, besides the other modes. (b) Comparison of the Raman $E_g(1)$ peak profile for the T0 and T16 samples before and after decoration of GQDs. 488 nm laser excitation is used for Raman measurements.

With the first principle calculations, Long at el. proposed that the central part of GQDs is mostly intact with TiO_2 surface and resultant GQDs is slightly bent [24]. We believe that the central part, most likely the in-plane epoxy functional groups, is directly connected to the defect sites in TiO_2 through the possible C-O-Ti bonds during the hybrid formation. As a result, the in-plane part of GQD is more favourable to form the hybrid

with TiO_2. These results further indicate the change in the oxygenated functional groups, without significant change in the edge configuration. To estimate the relative contribution of in-plane functional groups and edge states, we have calculated the intensity ratio of Raman D band to G band (I_D/I_G) in GQDs and TiO_2-GQD hybrid. The I_D/I_G ratios are 1.08, 1.01 and 0.97 for GQDs, T0/GQD and T16/GQD, respectively. The negligible change in I_D/I_G ratio for different samples indicates the uniform edge configuration of GQDs. It is important to note that despite the formation of the TiO_2-GQD hybrids, the edge sites (zigzag and armchair) configuration of GQDs is unaltered [5]. Our results imply that the changes take place mostly at the in-plane oxygenated functional groups of GQDs. The oxygenated functional groups may have been formed during the ultrasonication to facilitate the hybrid formation [25]. We speculate that edge and in-plane oxygenated functional groups are re-distributed and provides the in-plane disorder (in-plane epoxy C-O) to facilitate the hybrid/junction formation. The basal plane disorder has direct connection with the TiO_2 bonding through the linking of basal plane C-O to the Ti in TiO_2. The stability of edge sites in GQDs is higher than that of the edge oxygenated functional groups [17]. Note that our XPS results (discussed below) suggest the decrease in some of the edge oxygenated functional groups after hybrid formation. As a result, the oxygen functional groups in GQDs can rearrange due to its weak bonding. Note that the ratio of in-plane to edge carbon atoms is relatively small in GQDs as compared to that of graphene oxide. Thus, we believe that the ultrasonication induced in-plane epoxy disorder enables the formation of the possible C-O-Ti bonds in TiO_2-GQD hybrid. In order to form sufficient C-O-Ti- bonds, some of the functional groups might be supplied from the atmospheric oxygen during the hybrid formation [25].

6.5. X-ray Photoelectron Spectroscopy Study

In order to understand the chemical composition and bonding environment in different samples, XPS measurements were conducted. **Fig. 6.4(a,b)** represents the core level C1s spectra for GQD and T16/GQD. The C 1s spectrum is fitted with four Gaussian peaks centred at 284.5 (P1), 286.1 (P2), 287.5 (P3) and 290.1 eV (P4). The peak P1 signifies the honeycomb lattice structure of sp^2 hybridized carbon atoms, while the other peaks (P2, P3, and P4) correspond to the oxygen related edge functional groups in GQDs, such as C-O (ether), C=O, and COOH, respectively [22, 26]. It is evident from the fitted data that the C-

O (ether) and COOH functional groups are significantly reduced in the hybrid sample, which implies that some of the oxygen related functional groups may be converted to in-plane epoxy group to facilitate the formation of possible C-O-Ti bonds in the TiO_2-GQD hybrid. The edge carbon atoms are bonded with C-O (ether), COOH and C=O oxygen functional groups, among which the C=O is highly stable [22, 27]. Due to less sta bility, the C-O (ether) and COOH functional groups may relocate during the hybrid formation. Note

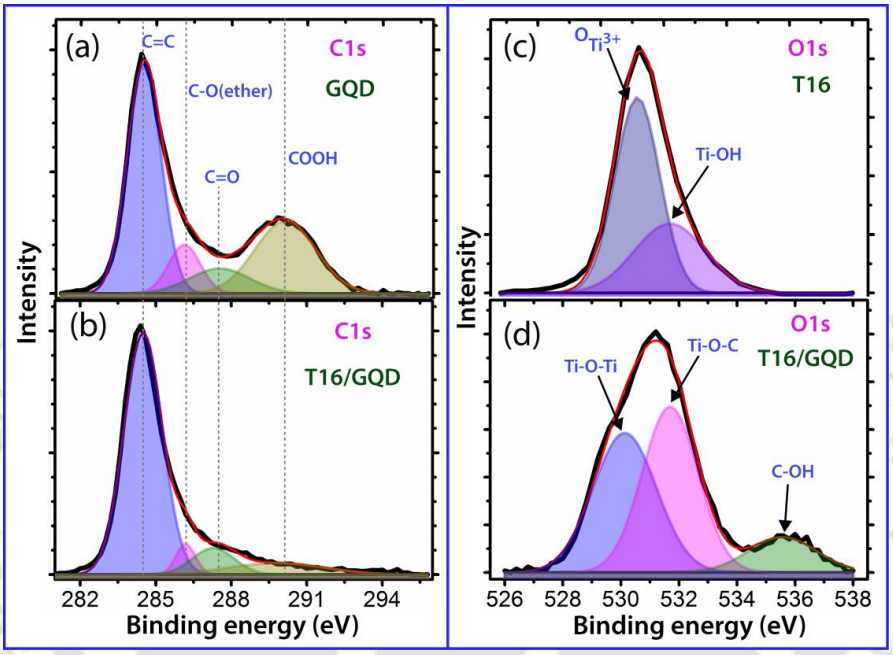

Figure 6.4: Core level XPS spectra of different samples: (a - b) C1s spectra for GQD and T16/GQD, (c-d) O1s spectra for T16 and T16/GQD, respectively.

that we have not noticed any peak related to Ti-C bond in the C 1s XPS spectrum of T16/GQD. This further implies that the Ti and C may be bonded through the oxygen atom in ordered to form the C-O-Ti bond. Some studies indicated the Ti-C bond formation in TiO_2 and carbon hybrid [6, 28]. Further, the change in surface states in T16 and T16/GQD samples is understood from the core level O 1s XPS spectra, as shown in **Fig. 6.4(c,d)**. Based on the nature of the O 1s XPS spectrum, the XPS spectrum of T16 is fitted with two Gaussian peaks centred at 531.1 and 532.2 eV, which are attributed to the Ti-O bonds (O_{Ti}^{3+}) and organic impurities, respectively [6, 29]. In contrast, the O 1s XPS spectrum of T16/GQD shows asymmetry and distinctly different peaks. Accordingly, the XPS spectrum is fitted with three Gaussian peaks. The peak centred at 530.1eV is referred to the oxygen in crystal lattice (O_L) [29] and the other two peaks at 531.7 and 535.5 eV are due to the Ti-O-C and hydroxyl functional group (C-OH) [6, 30], respectively. In the literature,

XPS peaks lying in the range 530.0-532.1 eV are assigned to the Ti-O-C [5, 6, 31]. In our study, the strong peak at 531.7 eV is believed to result from the Ti-O-C bond. These results confirm the hybrid formation through the possible Ti-O-C bonds in TiO_2-GQD.

6.6. UV-visible Absorption and FTIR Studies

The UV-visible absorption characteristics of the T0, T16 and T16/GQD samples are depicted in **Fig. 6.5**. **Fig. 6.5(a)** shows the diffused reflectance spectra, and the corresponding Kubelka-Munk plots (absorption spectra) are shown in **Fig. 6.5(b),** for T0, T16 and T16/GQD samples. The UV-Vis absorption characteristic of GQDs was discussed in C**hapter 4, section 4.6.1.** The band edge of T16 is clearly red shifted with respect to that of the T0, due to the combined effect of strain and oxygen vacancy defects [15]. This clearly implies a narrowing of the band gap in the T16 sample. Further it shows enhanced absorption in the visible region as compared to that of T0. Interestingly, the T16/GQD hybrid sample shows very strong absorption in the entire visible to near-infrared (NIR) region. This extended range absorption is highly advantageous for the visible-NIR light photocatalysis and related applications. The extended absorption is due to the hybrid formation through the coupling of GQDs to TiO_2 via possible C-O-Ti covalent bonds. An intimate contact between the TiO_2 and GQDs through this bond facilities the efficient interfacial charge transfer from GQDs to TiO_2 [24].

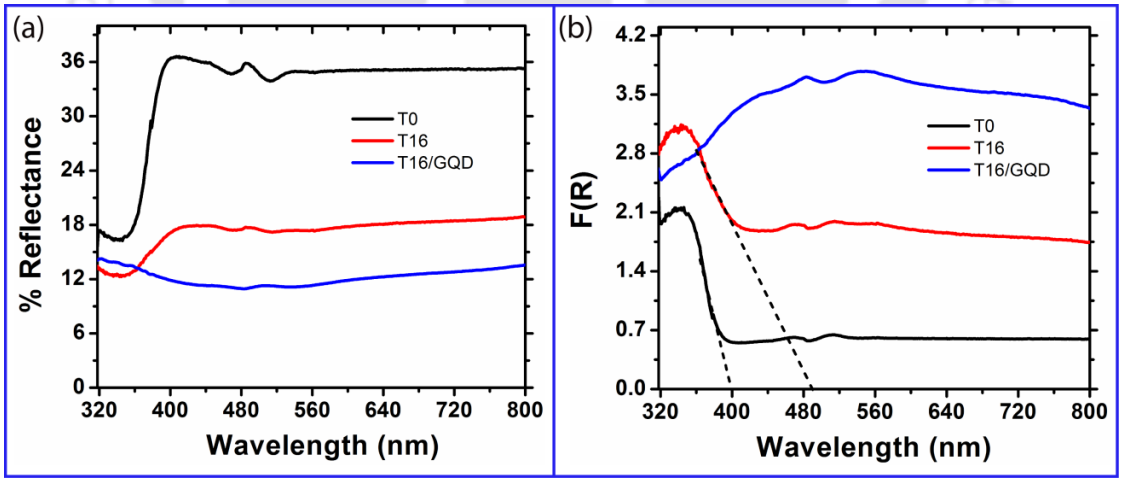

Figure 6.5: (a) Diffuse reflectance spectra and (b) corresponding Kubelka-Munk plot (F(R)) of absorbance of T0, T16 and T16/GQD samples in the powder form.

The characteristics of anatase TiO_2 and formation of TiO_2/GQD heterojunction is further confirmed from the FTIR analysis. **Fig. 6.6** shows the FTIR spectra for T16 and T16/GQD. The TiO_2 vibrational modes lying in the range 600-800 cm^{-1} can be attributed

the Ti-O and O-Ti-O bonds [29, 32]. Note that the characteristic vibration modes of GQDs was described in **Chapter 5, section 5.5.** In case of T16/GQD, the O-Ti-O vibrational peak is shifted to lower wavenumber as compared to that of T16. This red shift is a signature of the formation of hybrid through the possible C-O-Ti- bond formation [32]. In addition, a vibrational band at ~1400 cm^{-1} is observed in T16 and it is due to the Ti-O-Ti vibration in TiO_2 [33]. Notably, this mode becomes prominent in GQDs/T16 probably due to the lattice distortion caused by the formation of possible C-O-Ti- bond or oxygen vacancy rearrangement during the hybrid formation. The peak at 1620 cm^{-1} in T16 could be due to the adsorption of water/OH on TiO_2 [34], whereas two weak vibrational modes at 1590 and 1650 cm^{-1} in T16/GQD are due to the C=C and COOH bond vibrations of GQD, respectively [22, 35]. Further, we observed an additional broad band centred at ~2131 cm^{-1} in T16/GQD sample, as shown in the inset of **Fig. 6.6**. This band is attributed to C-O-Ti bond (C-O attachment at oxygen deficient sites in TiO_2 [36]. From this result, it is believed that the oxygen in GQDs may bind to the oxygen deficient sites in TiO_{2-x}, which result in the formation of possible C-O-Ti bonds in the T16/GQD hybrid samples. A broad vibrational band in the range from 3000-3900 cm^{-1} is due to OH vibrations [22, 32].

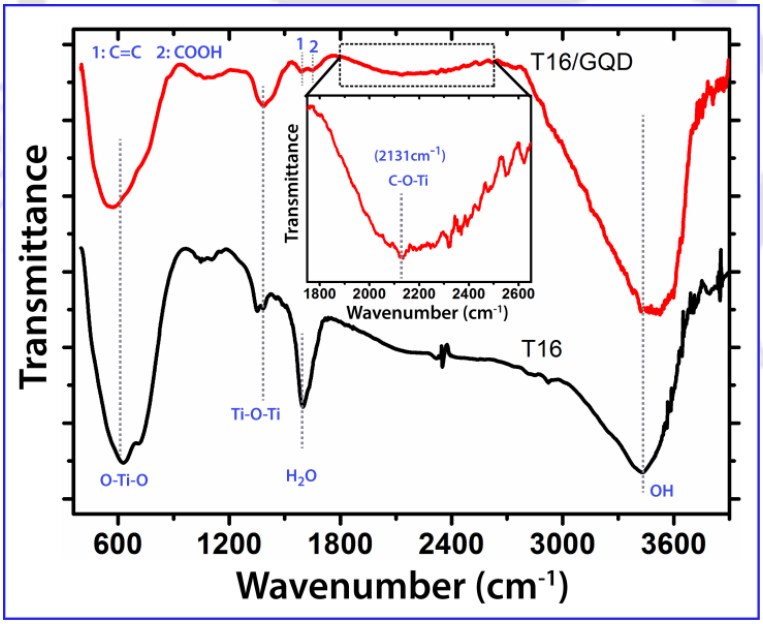

Figure 6.6: Comparison of FTIR spectra for T16 and T16/GQD. The inset shows the magnified view of a portion of the spectrum showing the presence of C-O-Ti bonds.

6.7. Steady State and Time resolved Photoluminescence Studies

To understand the nature of defects and their role in hybrid formation, we have carried out the steady state PL measurements on the pristine and hybrid samples. The PL spectra

of T0, T16, GQD and T16/GQD obtained with 405 nm laser excitation are portrayed in **Fig. 6.7(a)**. The broad PL spectra from T0 and T16 result from the transition of electrons from different defect states; particularly the green PL emission (~520 nm) is due to oxygen vacancy defects in TiO_2 [29]. Note that the PL intensity of T16 is substantially higher than that of the T0 due to the introduction of additional oxygen vacancy defects during the ball milling process [15]. On the other hand, PL spectrum of GQDs shows strong blue-green emission; the blue PL emission arises from the edge states and the green PL emission arises from the oxygenated functional groups in GQDs [22, 26, 37]. Interestingly, the PL spectrum of T16/GQD shows a much lower intensity than that of the individual components. In particular, the intensity of green PL emission is significantly reduced as compared to that of the blue PL in the hybrid sample. For T16/GQD hybrid, the green PL (~518 nm) intensity is 5.6 times lower than that of pristine T16. This may indicates the reduction/passivation of oxygen vacancies in the hybrid system due to the bonding of GQDs to oxygen vacant sites in TiO_2, possibly through the C-O-Ti bonds. The partial quenching of PL intensity is also indicative of the electron transfer from GQDs to TiO_2. In order to ascertain that the additional oxygen vacancies are indeed formed during the ultrasonication, we compare the PL intensities of sample T0 before and after ultrasonication (T0S), as shown in **Fig. 6.7(b)**. It's evident that the visible PL intensity of T0 is increased by four fold after ultrasonication, which implies the creation of additional oxygen vacancies during the ultrasonication of bare TiO_2 NPs.

To gain an insight into the mechanism of the interfacial charge transfer in TiO_2-GQD hybrid, we have performed the TRPL measurements on T16 and T16/GQD. For the TRPL measurements, the samples are excited with the 405 nm laser source and the PL emission is monitored at 518 nm, based on the steady state PL spectrum (**Fig. 6.7(a)**). **Fig. 6.7(c)** shows the TRPL spectra for T16 and T16/GQD. Each spectrum is well fitted with a bi-exponential decay, indicating that two life time components contribute in the carrier dynamics. The carrier life time values for T16 are 0.82 (τ_1) and 2.08 ns (τ_2), possibly due to the prompt recombination of charge carries at the defect states in TiO_2. On the other hand, the carrier life time values for T16/GQD are 0.82 ns (τ_1) and 4.5 ns (τ_2), indicating a slower decay in the hybrid sample. The average life time values in T16 and T16/GQD are 1.08 and 2.42 ns, respectively. This prolonged life time value in the hybrid sample signifies the efficient charge separation at the TiO_2-GQD interface. These

separated charge carriers play a vital role in the free radical generation and dye degradation process, which is illustrated later. These results are consistent with the steady state PL analysis, which showed lower PL intensity in the hybrid sample. Through density functional theory calculations, R. Long [24] reported on the efficient electron transfer and charge separation at the TiO_2/GQD interface where the GQDs were chemisorbed on to TiO_2 (110) surface. The visible light irradiation can excite the electrons of GQD to be injected into the TiO_2 surface due to band-gap narrowing of GQD/TiO_2 composites relative to pure TiO_2 [24].

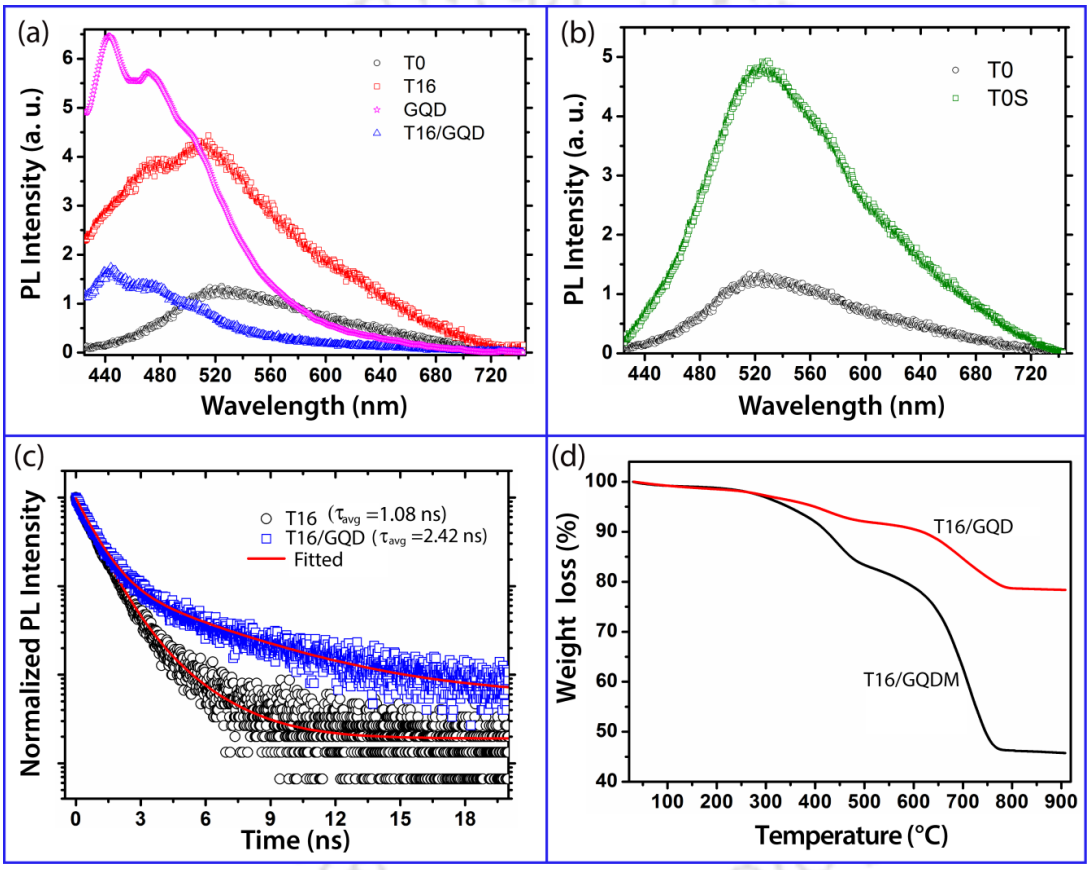

Figure 6.7: (a) Comparison of PL spectra excited with 405 nm laser for T0, T16, GQD and T16/GQD hybrid showing reduced PL intensity in the hybrid sample. (b) PL spectra of T0 before and after ultrasonication. (c) TRPL spectra excited with 405 nm pulsed laser for T16 and T16/GQD showing longer life time of photo-generated carriers in the hybrid sample. (d) Comparison of TGA profiles of T16/GQD and T16/GQDM showing higher thermal stability of T16/GQD.

6.8. Thermogravimetric Analysis

In order to ascertain the role of oxygen vacancies in the hybrid formation, we prepared two different hybrid samples: (i) mixing of GQDs and TiO_2 under simple stirring (T16/GQDM), and (ii) mixing of GQDs and TiO_2 under ultrasonication (T16/GQD). To

understand the interaction and thermal stability of these two samples, we have performed Thermogravimetric Analysis (TGA). Interestingly, the TGA analyses of these two samples showed quite different weight loss characteristics due to the difference in hybrid formation. **Fig. 6.7(d)** shows the TGA profiles of T16/GQDM and T16/GQD. The results can be understood as follows. In case of the hybrid prepared under stirring (T16/GQDM), the faster weight loss characteristics indicates that the GQDs may be loosely attached to the TiO_2 surface, perhaps physisorbed onto the TiO_2 surface due to insufficient energy to change local structure (e.g., oxygen vacancies) in TiO_2, and negligible rearrangement in the functional groups in GQDs. On the other hand, in case of the hybrid prepared by ultrasonication (T16/GQD), the slower and low weight loss characteristic indicate strong bonding between the TiO_2 and GQDs through some changes in the local structure (e.g., oxygen vacancies) in TiO_2 and functional groups rearrangement in GQDs. It is likely that the in-plane epoxy (C-O) functional groups in GQDs are transferred to the oxygen deficient sites in TiO_2 and form a hybrid through the possible C-O-Ti bond. This type of bonding may strongly couples the GQDs and TiO_2. Thus, ultrasonication of the hybrid mixture results in a kind of chemisorption of GQDs on to TiO_2, instead of physisorption. The chemisorption is believed to be responsible for the high thermal stability and low weight loss (only ~20%) in T16/GQD. These results clearly demonstrate the role of oxygen vacancies in TiO_2 in the formation of TiO_2/GQD hybrid. Note that T16 contains high density of oxygen vacancies and during ultrasonication, more vacancy sites of TiO_2 are available for chemisorption of GQDs with in-plane C-O functional groups and it results in the hybrid formation with covalent bonding. It is likely that the hybrid sample prepared only under stirring leads to the van der Waals interactions between GQD and TiO_2, which is likely to yield physisorption.

6.9. Electron Paramagnetic Resonance Study

In order to understand the nature of defects in pristine and TiO_2-GQD heterojunction, we have performed the electron paramagnetic resonance (EPR) measurements. **Fig. 6.8** shows the EPR spectra of T16, GQD and T16/GQD samples. The intensity of EPR signal for T16 is very high as compared to other samples, which could be due to the large density of defects in T16 [38]. This result is consistent with the PL analysis, which showed high density of oxygen vacancy defects in T16. The EPR signal at g value 1.9905 is due to the oxygen defects related to the F^+ centres in TiO_2 [38]. On the other hand, the EPR

signal at g value 1.9975 in GQD is due to the free electron sites (edge sites) [39]. The possible reason for lower g-value and reduction of EPR intensity in the GQD sample could be due to the large density of oxygenated functional groups attached at the edge sites of carbon. Presence of various functional groups, such as -OH, -CO, and –O etc. in GQDs strongly influence the EPR signal [39]. Note that broad PL (blue-green) emission from GQDs (see **Fig. 6.7(a)**) results from the edge states and functional groups, as discussed above. In addition, our XPS results from GQDs further supports the evidence for edge oxygenated functional groups. Thus, the results of XPS and EPR analysis are consistent with each other. In the hybrid sample, the g-value of 1.9961 is due to the F^+ centres in TiO_2 [38]. In addition, the EPR signal intensity of T16/GQD is reduced, probably due to the passivation of the defects in TiO_2 by the GQDs. Note that we observed a reduced intensity of peaks related to functional group in XPS C1s spectrum of the hybrid sample. Thus, the reduced EPR signal indicates the formation of TiO_2-GQD hybrid possibly through the C-O-Ti covalent bonding. These results are consistent with the PL analysis of the hybrid sample.

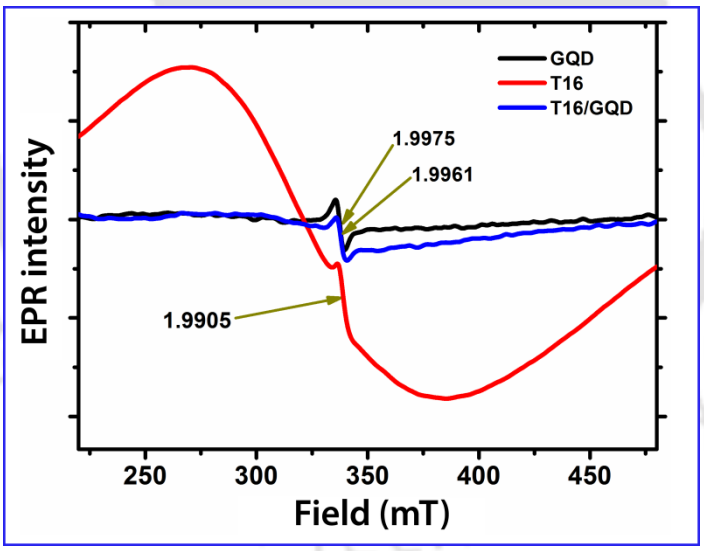

Figure 6.8: EPR spectra of GQD, T16 and T16/GQD hybrid. The corresponding g-values are marked in each case.

6.10. Computational Study on the Optical Spectra of TiO_2/GQD Hybrid

In order to verify the physical validity of possible C-O-Ti bonds for the hybrid formation and to compute its optical spectra, we have performed the DFT calculations on the anatase TiO_2 and oxygen deficient TiO_2-GQD hybrid structure. The atomistic structures of the bare TiO_2 and TiO_2-GQD hybrid without and with energy optimization are shown

in **Fig. 6.9(a, b, c)**. The corresponding optical absorption spectra for different structures are shown in **Fig. 6.9(d)**. Interestingly, as compared to bare the TiO_2, the oxygen deficient TiO_2-GQD hybrid without and with optimization show much stronger absorption in the visible region and the absorption tail is extended to NIR region. The computed absorption spectra are fully consistent with our experimental absorption data shown in **Fig. 6.5(b)**. For the hybrid of TiO_2-graphene, Gao et al. reported a red-shift of absorption edge and greatly improved absorption intensity in the visible region [40]. In the present case, the coupling of functionalized GQD with oxygen deficient TiO_2 through possible Ti-O-C bonds gives rise to extended absorption in the visible-NIR region. This results in highly improved PC performance of the hybrid under visible-NIR light irradiation.

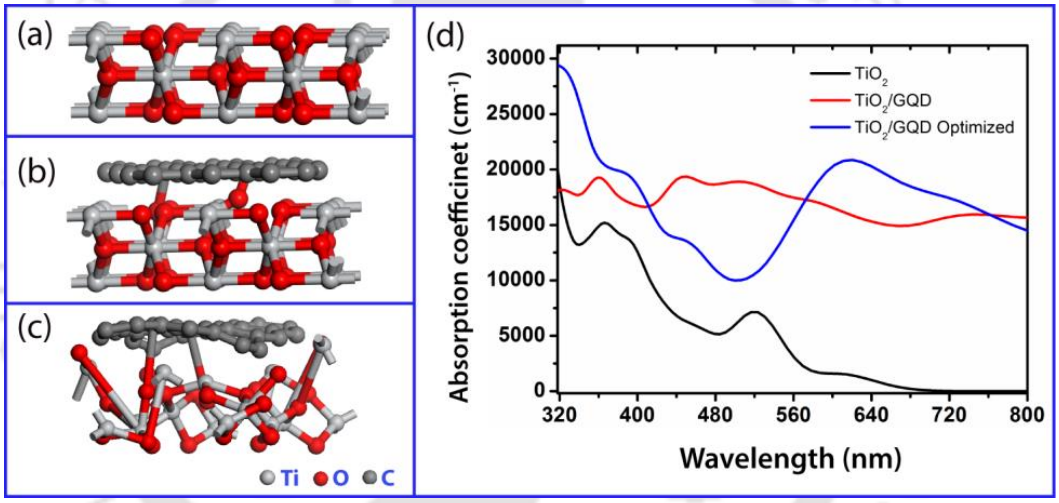

Figure 6.9: DFT simulation images of structure of (a) anatase TiO_2, (b) oxygen deficient TiO_2-GQD hybrid without optimization, (c) optimized oxygen deficient TiO_2-GQD hybrid structure, and (d) comparison of optical absorption spectrum of anatase TiO_2 and oxygen deficient TiO_2-GQD hybrids.

Based on our finding, a schematic model for the structural arrangement in TiO_2-GQD hybrid is presented in **Fig. 6.10**, which is performed in the *Materials Studio* software. It depicts the structural changes taking place in TiO_2 and GQD to form TiO_2-GQD hybrid through the possible C-O-Ti bonds during ultrasonication. Note that the edge sites in GQD contain various oxygenated functional groups, such as COOH, C-O (ether) and C=O. After ultrasonication of TiO_2, more oxygen vacancy defects are created, as shown in **Fig. 6.10(a,b)**. The ultrasonication of mixture of TiO_2 and GQD (**Fig. 6.10(c)**) results in creation of oxygen vacancies in TiO_2 and redistribution of oxygen functional groups in GQDs. The resultant hybrid structure of TiO_2-GQD bonded through the

possible C-O-Ti covalent bonds is shown in **Fig. 6.10(d)**. In recent report, Umrao et al. proposed the C-O-Ti bond formation in hybrid of TiO_2-graphene oxide [6]. They proposed the C-O-Ti bond formation through the bonding between the free electrons on the surface of TiO_2 with unpaired π electrons of graphene.

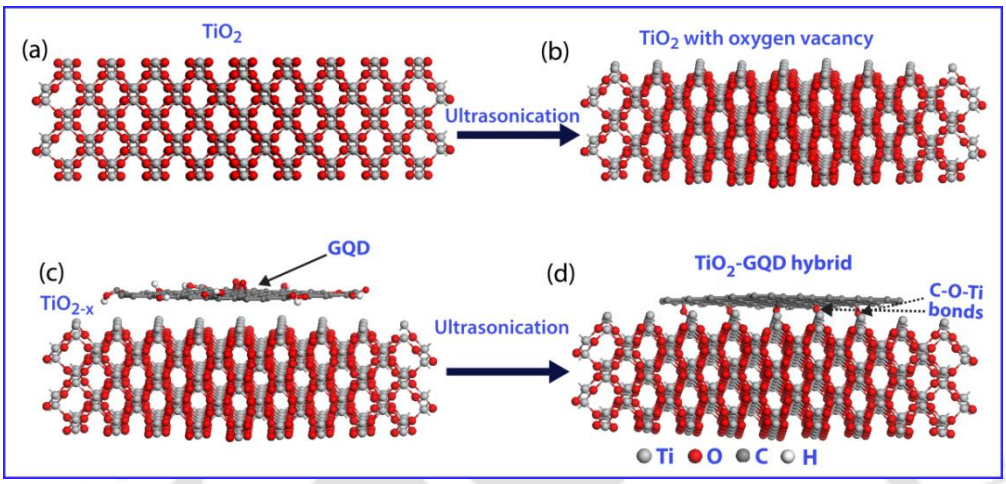

Figure 6.10: (a, b) Schematic illustration of structural transformation in TiO_2 NPs by ultrasonication that creates additional oxygen vacancy defects in TiO_2. (c, d) TiO_2-GQD hybrid formation through the possible C-O-Ti bonds aided by ultrasonication of TiO_2 NPs and GQDs mixture. The images are simulated in *Materials Studio* software.

6.11. Visible light Photocatalytic Degradation of MB

The oxygen vacancy and in-plane epoxy functional group mediated TiO_2-GQD heterojunction formation, interfacial charge transfer and its influence on the visible light photodegradation of MB is studied in details. In this section we will discuss the reaction kinetics, free radical scavenger test and MB degradation mechanism.

6.11.1. Degradation and Reaction Kinetics

Fig. 6.11 depicts the change in absorption intensity of MB in catalyst samples and its reaction kinetics. **Fig. 6.11(a-d)** represents the UV-vis absorption spectra of MB up to 120 min irradiation using GQD, T16, T16/GQDM and T16/GQD catalysts, respectively. It is evident from figure that the variation in absorption intensity of MB as a function of irradiation time in T16/GQD is higher than that of other catalyst samples subjected to visible light irradiation up to 120 min. **Fig. 6.11(e)** shows the concentration ratio (final to initial concentration, C/C_0) of MB and MB in different catalyst samples. MB is only 6% self-catalysed after irradiation of 120 min. Although the GQD catalyst amount is high as compared to the PC studies of GQD discussed in **Chapter 5**, here MB is degraded to only 31%. This is due to the very poor visible absorption characteristic of GQD, as discussed

in **Chapter 5.** On the other hand, the degradation of MB in T16 is increased to the 44%, while it is dramatically high (97%) for T16/GQD hybrid. The photo degradation of MB in T16 is primarily due the effect of band gap narrowing. Note that the band gap narrowing in T16 is the combined effect of strain and oxygen vacancies induced by milling process[15, 41]. On the other hand, due to the band bending at the heterojunction of T16/GQD hybrid, the degradation efficiency is vastly improved. We believe that the chemisorption of GQDs on TiO_2 and possible C-O-Ti bond formation are responsible for the efficient interfacial charge transfer and enhanced PC performance of the hybrid sample. Note that, our degradation studies on the T16/GQDM sample prepared by simple

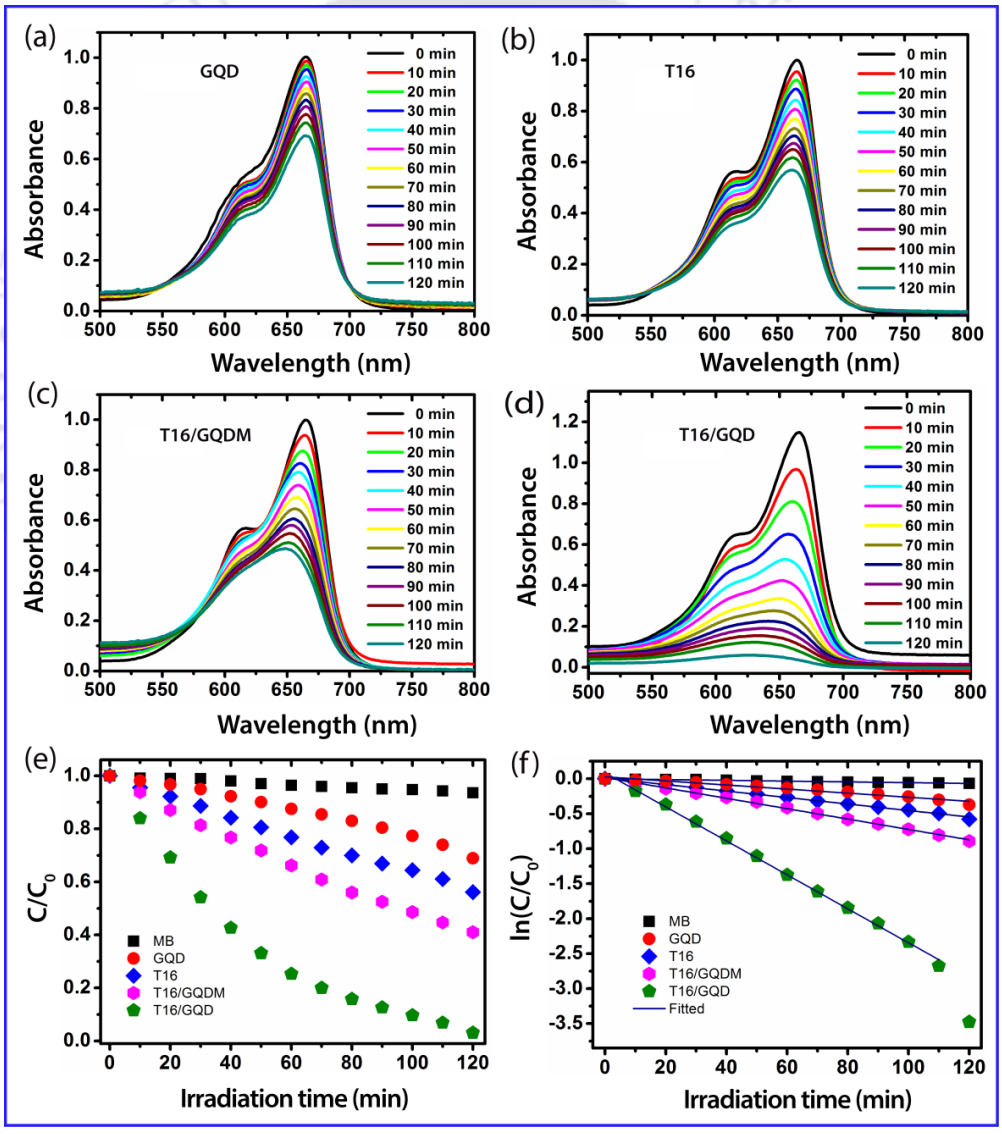

Figure 6.11: UV-Vis absorption spectra of MB in catalysts: (a) GQD, (b) T16, (c) T16/GQDM and (d) T16/GQD. (e) Change in relative concentration (C/C_0) of MB in different catalysts as a function of irradiation time up to 120 min. (c) Plot of $\ln(C/C_0)$ vs. irradiation time (t) for MB degradation in different catalysts.

stirring showed only 59% degradation in contrast to the 97% degradation in case of T16/GQD. The lower degradation in case of T16/GQDM is believed to be due to the weak van der Waals interaction between the GQD and TiO_2 during the stirring. In contrast, during ultrasonication, oxygen vacancy mediated bond formation takes place through the possible C-O-Ti bonding and due to strong interaction between TiO_2 and GQD, the efficient charge carrier separation at the interface takes place, which results in high degradation rate. Besides the interfacial charge transfer process, the hot charge carrier injection from GQDs to TiO_2 [42] is another considerable factor for the difference in the PC of hybrid sample. Considering the T16/GQD sample, GQDs are strongly coupled to the TiO_2 as compared to that in T16/GQDM. As a result, the interfacial charge separation and hot carrier generation is higher in T16/GQD as compared to that of T16/GQDM.

Next, we estimated the degradation rate constants for MB in different catalysts. The kinetics of the PC reaction follows a pseudo first order reaction process, which is expressed by $\ln(C/C_0) = -kt$, where 'k' is the apparent reaction rate constant, C and C_0 are the concentration of MB after irradiation time 't' and initial concentration, respectively. The rate constants are obtained from the slope of the linear plots. **Fig. 6.11(f)** shows a plot of $\ln(C/C_0)$ vs irradiation time for degradation of MB in different catalysts. The symbols represent the experimental data and the line represents the fitted data. The % of MB degradation and rate constants are shown in **Fig. 6.12(a)**. The value in the parenthesis indicates the rate constant. The rate constant for MB and GQD are 0.61×10^{-3} and 0.26×10^{-2} min^{-1}, respectively. In case of T16 the rate constant is 0.46×10^{-2} min^{-1} and that of T16/GQDM is 1.47×10^{-2} min^{-1}. The rate constant in T16/GQD is 2.40×10^{-2} min^{-1}, which is 9.2 fold and 5.2 fold higher than that of the GQD and T16, respectively. Thus, the hybrid sample shows much improved degradation rate constant than the pristine samples. These results signify the influence of interaction of GQDs and TiO_2 for enhanced PC degradation of MB.

Further, we studied the reusability of the T16/GQD catalyst, since it has shown the highest efficiency photodegradation of MB as compared to the other catalysts. The relative concentrations of MB in T16/GQD catalyst for three repeated cycles of photocatalysis are shown in **Fig. 6.12(b)**. It's evident from the data that the hybrid catalyst is quite stable up to three repeated cycles. Furthermore, in order to assess the

structural stability of the catalyst, we recorded the XRD pattern of the samples before and after three cycles of catalysis. **Fig. 6.12(c)** shows the XRD pattern of T16/GQD before and after catalysis. Note that the anatase TiO_2, Ti_3O_5 phase and GQD reflection planes are marked with different symbols in **Fig. 6.12(c)**. These results indicate that crystalline phase of the TiO_2 and GQD is unchanged even after three repeated cycles of photocatalysis. These results are consistent with the TEM results shown in **Fig. 2(i)**. The degradation mechanism and the nature of free radical species involved in the degradation of MB are elucidated in the following section.

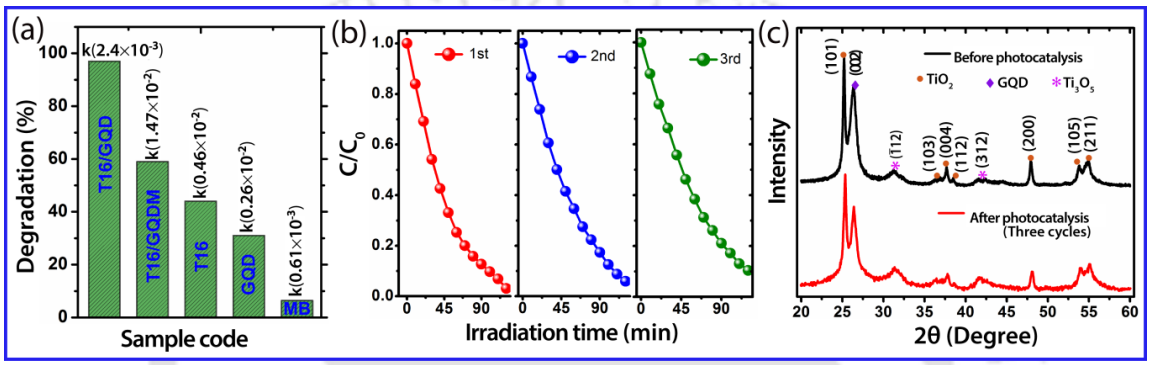

Figure 6.12: (a) Percentage degradation and rate constant values for different catalysts in MB degradation. (b) Change in relative concentration of MB as a function of irradiation time for T16/GQD catalyst for three repeated cycles. (c) XRD pattern of T16/GQD catalyst before and after three cycles of

6.11.2. Free Radical Detection and Degradation Mechanism

To investigate the free radical generation and their contribution in visible light photocatalysis, a series of scavenger test was performed on T16/GQD catalyst. Ammonium oxalate (AO), tert-butyl alcohol (t-BA) and p-benzoquinone (BQ) scavengers were used to study the roles of hole (h^+), hydroxyl radical ($^{\bullet}OH$) and superoxide radical ($O_2^{\bullet-}$), respectively [43, 44]. **Fig. 6.13(a-c)** shows the change in absorption intensity of MB after the scavenger's experiments such as BQ, AO and t-BA test, respectively. **Fig. 6.13(d)** represents the evolution of the relative concentration of MB in different scavengers, and **Fig. 6.13(e)** shows the degradation (%) of MB in presence of different catalyst-scavenger combination. As compared to the bare T16/GQD, the degradation efficiency of MB is reduced /quenched after addition of any scavenger. This indicates the contribution of all the oxidative species to the MB degradation. Note that without any quencher, the MB is degraded by 97%. It can be understood from the scavenger test that the MB is degraded by 76% in BQ, and it is quenched to 46% in t-BA. Interestingly, high quenching of MB degradation (38%) is observed in presence of AO. These results

indicate the significant role of holes (h^+) in the MB degradation. Further, t-BA scavenger studies show the second highest quenching of MB degradation. This demonstrates that $^{\bullet}OH$ radical is a major reactive species in MB degradation. Indeed, in the photocatalysis process the photo-generated holes are the sources for $^{\bullet}OH$ radicals emerging. On the other hand, the electrons from GQDs are transferred to the TiO_2 conduction band and

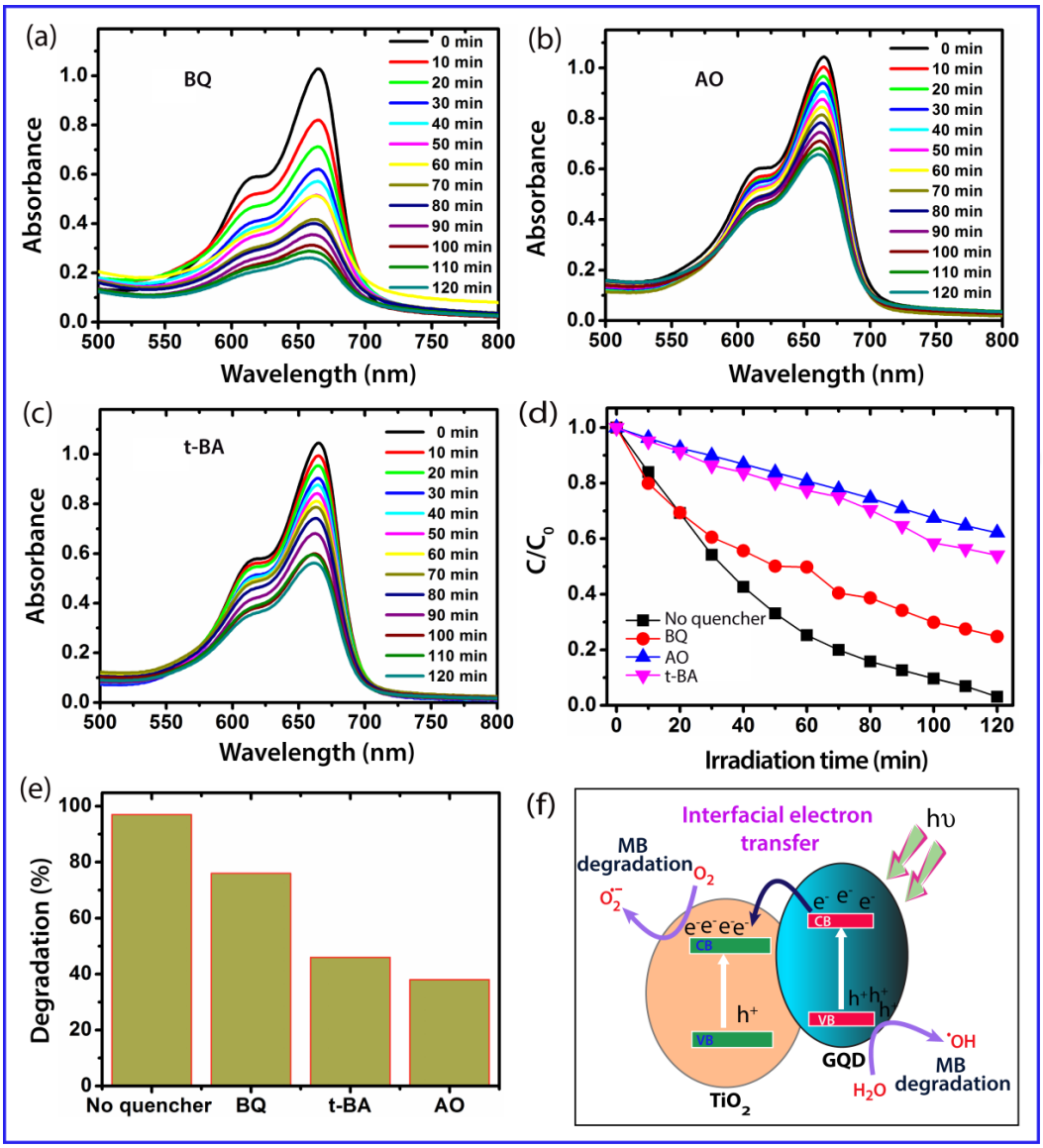

Figure 6.13: UV-Vis absorption spectra of MB after scavenger experiments: (a) BQ, (b) AO and(c) t-BA. (d) Relative MB concentration as a function of irradiation time in absence and in presence of different catalyst-scavengers (scavengers: BQ, t-BA, and AO). (e) Degradation (%) of MB in without quencher and in presence of scavengers. (f) Schematic illustration of interfacial charge separation at the TiO_2-GQD heterojunction and free radical generation for MB degradation.

they trap the molecular oxygen (O_2) and convert it to the $O_2^{\bullet-}$ radicals. This process enables efficient utilization of holes for the generation of the $^{\bullet}OH$ radicals. The high

degradation of MB in BQ can be interpreted as conversion of superoxide radical in to the $^{\bullet}OH$ radical, as detailed below.

Based on the above results, we can discuss about the mechanism of enhanced charge separation and enhanced PC activity of TiO_2-GQD hybrid. The TiO_2-GQD heterojunction forms a type-II band alignment, which is thermodynamically more favourable [45, 46]. **Fig. 6.13(f)** shows a schematic representation of interfacial charge transfer and free radical generation in TiO_2-GQD hybrid during the photocatalysis process. The superoxide free radicals are unstable in aqueous solution and these are immediately converted to the $^{\bullet}OH$ radicals [11]. Since the band gap of TiO_2 is narrowed in T16 as evident from the absorption spectrum, part of the visible light is absorbed by T16 and gives rise to the MB degradation up to ~44%. Note that the anatase phase of TiO_2 surface is more facile and versatile for generation of mobile $^{\bullet}OH$ radical [1, 4]. However, the charge separation is the one of the major factor influencing the MB degradation efficiency. In case of the TiO_2-GQD hybrid, the band alignment at the heterojunction facilitates the charge separation at the interface, where GQD act as a donor and the TiO_2 as an acceptor. Our TRPL results (**Fig. 6.7(c)**) lend strong support to the fact that there is efficient charge separation at the heterojunction giving rise to the enhanced photocatalysis. Once the charges are separated, the $^{\bullet}OH$ and $O_2^{\bullet-}$ radicals are formed, which are highly energetic to decompose the MB into water, CO_2 and other inorganic compounds. However, as compared to the $O_2^{\bullet-}$, $^{\bullet}OH$ radical contribution is more in the present case, as described earlier. The possible degradation pathways for MB can be expressed by the following reactions.

$$O_2 + e^- \rightarrow O_2^{\bullet-}$$
$$H_2O \rightarrow H^+ + OH^-$$
$$O_2^{\bullet-} + 2H^+ + e^- \rightarrow H_2O_2$$
$$H_2O_2 \rightarrow {}^{\bullet}OH + OH^-$$
$$OH^- + h^+ \rightarrow {}^{\bullet}OH$$
$$^{\bullet}OH + \text{dye} \rightarrow \text{water} + CO_2$$
$$O_2^{\bullet-} + \text{dye} \rightarrow \text{water} + CO_2$$

6.12. Summary & Conclusions

1. In this chapter, we discussed the fabrication of the TiO_2-GQD heterojunction using an ultrasonication process and studied the role of oxygen vacancies in TiO_2-GQD hybrid formation through the possible C-O-Ti bond, for the first time.

2. We introduced the concept of oxygen functional groups rearrangement in GQD and the consequence of the in-plane epoxy disorder in TiO_2-GQD hybrid formation, for the first time.

3. Raman, FTIR and XPS results suggest the existent of possible C-O-Ti bonds in TiO_2-GQD hybrid. DFT based simulation results support the hybrid formation.

4. The role of oxygen vacancies and binding of GQD on TiO_2 was probed form the PL and TGA results.

5. The TiO_2-GQD hybrid sample exhibited 97% degradation of MB under visible light illumination and the degradation rate constant is 9.2 and 5.2-fold enhanced as compared to that of bare GQD and TiO_2, respectively.

6. Our free radical studies reveal that the $^{\bullet}OH$ played a major role in the MB degradation.

References

1. W. Kim, T. Tachikawa, G.-h. Moon, T. Majima and W. Choi, *Angewandte Chemie International Edition*, 2014, **53**, 14036-14041.
2. T. Luttrell, S. Halpegamage, J. Tao, A. Kramer, E. Sutter and M. Batzill, *Scientific Reports*, 2014, **4**, 4043.
3. T. A. Kandiel, A. Feldhoff, L. Robben, R. Dillert and D. W. Bahnemann, *Chemistry of Materials*, 2010, **22**, 2050-2060.
4. J. Zhang and Y. Nosaka, *The Journal of Physical Chemistry C*, 2014, **118**, 10824-10832.
5. M. Xing, F. Shen, B. Qiu and J. Zhang, *Scientific Reports*, 2014, **4**, 6341.
6. S. Umrao, S. Abraham, F. Theil, S. Pandey, V. Ciobota, P. K. Shukla, C. J. Rupp, S. Chakraborty, R. Ahuja, J. Popp, B. Dietzek and A. Srivastava, *RSC Advances*, 2014, **4**, 59890-59901.
7. L. R. Radovic, *Journal of the American Chemical Society*, 2009, **131**, 17166-17175.

8. L. A. Ponomarenko, F. Schedin, M. I. Katsnelson, R. Yang, E. W. Hill, K. S. Novoselov and A. K. Geim, *Science*, 2008, **320**, 356-358.
9. J. Park, J. Moon, C. Kim, J. H. Kang, E. Lim, J. Park, K. J. Lee, S.-H. Yu, J.-H. Seo, J. Lee, J. Heo, N. Tanaka, S.-P. Cho, J. Pyun, J. Cabana, B. H. Hong and Y.-E. Sung, *NPG Asia Mater*, 2016, **8**, e272.
10. Y. Li, Y. Zhao, H. Cheng, Y. Hu, G. Shi, L. Dai and L. Qu, *Journal of the American Chemical Society*, 2012, **134**, 15-18.
11. B. Choudhury and P. K. Giri, *RSC Advances*, 2016, **6**, 24976-24984.
12. M. D. Segall, J. D. L. Philip, M. J. Probert, C. J. Pickard, P. J. Hasnip, S. J. Clark and M. C. Payne, *Journal of Physics: Condensed Matter*, 2002, **14**, 2717.
13. J. P. Perdew, K. Burke and M. Ernzerhof, *Physical Review Letters*, 1996, **77**, 3865-3868.
14. J. P. Perdew and W. Yue, *Physical Review B*, 1986, **33**, 8800-8802.
15. G. Rajender and P. K. Giri, *Journal of Alloys and Compounds*, 2016, **676**, 591-600.
16. Z. Zhang, J. Zhang, N. Chen and L. Qu, *Energy & Environmental Science*, 2012, **5**, 8869-8890.
17. T. Liu, K. Yu, L. Gao, H. Chen, N. Wang, L. Hao, T. Li, H. He and Z. Guo, *Journal of Materials Chemistry A*, 2017, **5**, 17848-17855.
18. D. B. Shinde and V. K. Pillai, *Chemistry – A European Journal*, 2012, **18**, 12522-12528.
19. W. F. Zhang, Y. L. He, M. S. Zhang, Z. Yin and Q. Chen, *Journal of Physics D: Applied Physics*, 2000, **33**, 912.
20. T. Ohsaka, F. Izumi and Y. Fujiki, *Journal of Raman Spectroscopy*, 1978, **7**, 321-324.
21. K. N. Kudin, B. Ozbas, H. C. Schniepp, R. K. Prud'homme, I. A. Aksay and R. Car, *Nano Letters*, 2008, **8**, 36-41.
22. G. Rajender and P. K. Giri, *Journal of Materials Chemistry C*, 2016, **4**, 10852-10865.
23. A. C. Fernandes, L. Cunha, C. Moura, F. Vaz, P. Carvalho, E. Le Bourhis, P. Goudeau, J. P. Rivière and N. M. G. Parreira, *Surface and Coatings Technology*, 2007, **202**, 946-951.

24. R. Long, *ChemPhysChem*, 2013, **14**, 579-582.
25. T. Skaltsas, X. Ke, C. Bittencourt and N. Tagmatarchis, *The Journal of Physical Chemistry C*, 2013, **117**, 23272-23278.
26. S. Zhu, J. Zhang, X. Liu, B. Li, X. Wang, S. Tang, Q. Meng, Y. Li, C. Shi, R. Hu and B. Yang, *RSC Advances*, 2012, **2**, 2717-2720.
27. A. Ganguly, S. Sharma, P. Papakonstantinou and J. Hamilton, *The Journal of Physical Chemistry C*, 2011, **115**, 17009-17019.
28. X.-Y. Zhang, H.-P. Li, X.-L. Cui and Y. Lin, *Journal of Materials Chemistry*, 2010, **20**, 2801-2806.
29. B. Santara, P. K. Giri, K. Imakita and M. Fujii, *Nanoscale*, 2013, **5**, 5476-5488.
30. J. Zhang, Z. Dong, X. Wang, X. Zhao, J. Tu, Q. Su and G. Du, *Journal of Power Sources*, 2014, **270**, 1-8.
31. X. Yan, Y. Li, M. Li, Y. Jin, F. Du, G. Chen and Y. Wei, *Journal of Materials Chemistry A*, 2015, **3**, 4180-4187.
32. A. Qu, H. Xie, X. Xu, Y. Zhang, S. Wen and Y. Cui, *Applied Surface Science*, 2016, **375**, 230-241.
33. C. H. Huang, H. L. Bai, Y. L. Huang, S. L. Liu, S. I. Yen and Y. S. Tseng, *International Journal of Photoenergy*, 2012, **2012**, 1-8.
34. A. Trapalis, N. Todorova, T. Giannakopoulou, N. Boukos, T. Speliotis, D. Dimotikali and J. Yu, *Applied Catalysis B: Environmental*, 2016, **180**, 637-647.
35. R. K. Biroju, G. Rajender and P. K. Giri, *Carbon*, 2015, **95**, 228-238.
36. L. F. Liao, C. F. Lien, D. L. Shieh, M. T. Chen and J. L. Lin, *The Journal of Physical Chemistry B*, 2002, **106**, 11240-11245.
37. R. Gone, C. Biswajit and P. K. Giri, *Nanotechnology*, 2017, **28**, 395703.
38. B. Santara, K. Imakita, M. Fujii and P. K. Giri, *Journal of Alloys and Compounds*, 2016, **661**, 331-344.
39. S. P. Jovanovic, Z. Syrgiannis, Z. M. Markovic, A. Bonasera, D. P. Kepic, M. D. Budimir, D. D. Milivojevic, V. D. Spasojevic, M. D. Dramicanin, V. B. Pavlovic and B. M. T. Markovie, *Acs Applied Materials & Interfaces*, 2015, **7**, 25865-25874.
40. H. Gao, B. Lu, D. Li, F. Guo, D. Dai, C. Si, G. Liu and X. Zhao, *RSC Advances*, 2016, **6**, 65315-65321.

41. X. Pan, M.-Q. Yang, X. Fu, N. Zhang and Y.-J. Xu, *Nanoscale*, 2013, **5**, 3601-3614.

42. K. J. Williams, C. A. Nelson, X. Yan, L.-S. Li and X. Zhu, *ACS Nano*, 2013, **7**, 1388-1394.

43. C. Zhou, J. Yan, B. Chen, P. Li, X. Dong, F. Xi and J. Liu, *RSC Advances*, 2016, **6**, 108955-108963.

44. W. Li, D. Li, Y. Lin, P. Wang, W. Chen, X. Fu and Y. Shao, *The Journal of Physical Chemistry C*, 2012, **116**, 3552-3560.

45. D. Pan, J. Jiao, Z. Li, Y. Guo, C. Feng, Y. Liu, L. Wang and M. Wu, *ACS Sustainable Chemistry & Engineering*, 2015, **3**, 2405-2413.

46. P. Sudhagar, I. Herraiz-Cardona, H. Park, T. Song, S. H. Noh, S. Gimenez, I. M. Sero, F. Fabregat-Santiago, J. Bisquert, C. Terashima, U. Paik, Y. S. Kang, A. Fujishima and T. H. Han, *Electrochimica Acta*, 2016, **187**, 249-255.

Chapter 7
Summary and Conclusions

This chapter provides the highlights and important contributions of the present thesis work. The new mechanisms proposed on the formation of GQDs, and GQD-TiO_2 hybrid and the origin of visible PL emission are highlighted. The advantageous bright blue PL emission of GQDs and its bio-imaging application of cell lines are demonstrated. The charge transfer mechanism in GQDs based hybrids and its role in the visible light photocatalytic degradation of methylene blue is presented. The specific role of free radical generation and its influence on the dye degradation is presented. The recommendations for future studies are provided at the end of the chapter.

7.1. Summary and Highlights of the Thesis Contribution

In this thesis, we presented a systematic study on the controlled synthesis of GQDs, understanding the formation mechanism of GQDs & its heterostructures, understanding the origin of visible PL emission from the GQDs. We explored the GQDs in bio-imaging application and GQDs based heterostructures for visible light photocatalysis application. We proposed a new formation mechanism of circular shaped GQDs and revealed the role of in-plane epoxy functional groups on the formation of high quality GQDs. We elucidated the origin of blue and green PL emission from GQDs and assigned the blue PL in GQDs is due to the edge sites such as zigzag and armchair edges, and the green PL to the COOH and C=O functional groups. For the first time, we made a correlation between the PL and Raman features of GQDs. Further, we studied the effect of solvents on the GQDs synthesis and the evolution of PL in different liquid media. We have achieved a high PL quantum yield of 32% from the GQDs. The bright blue PL emission of GQDs were used to study the bio-imaging application of A-375 and HeLa cancer cell lines and GQDs showed good bio-compatibility on the cell lines. The plasmonic Au NPs functionalized GQD-GCN hybrid nanostructures are fabricated to study the visible light photocatalytic activity of methylene blue (MB). We have achieved enhanced degradation of MB after Au NPs decoration on the GQD-GCN hybrid system due the interfacial charge transfer between the GQD-GCN hybrids to Au NPs. Next, a hybrid of GQD and TiO_2 NPs is prepared using an ultrasonication process and the photocatalytic degradation of MB in different catalyst

samples was studied. We proposed the formation mechanism of TiO_2-GQD hybrid through the C-O-Ti bonds, for the first time, and the conclusions are supported by DFT calculation.

The important contributions of the present thesis work are summarized below.

A. Controlled Synthesis of Graphene Quantum Dots and Its Formation Mechanism

In the present thesis, top down approach of synthesis of GQDs was adopted using hydrothermal and solvothermal methods. Hydrothermal reactions are performed for two different reaction durations, such as 12 and 24 h. To understand the role of in-plane oxygen functional groups on the formation mechanism of circular shaped GQDs, we compared the reactions of hydrothermal reaction on the GO and rGO. We proposed a new mechanism of formation of circular shaped GQDs. Our proposed mechanism is corroborated by the TEM imaging and our results suggest the essential role of in-plane epoxy functional groups in obtaining a high quality GQDs. In order to improve the optical properties of GQDs, *in-situ* chemical functionalization of GQDs was performed by using the polyethelenglycol (PEG). Solvent dependent growth of the GQDs was performed using the solvothermal reactions using dimethylformamide (DMF) and dimethyl sulfoxide (DMSO) as organic solvent. Our controlled synthesis results show that the size and quality GQDs can be controlled by reaction duration and GO precursor materials. In addition, the edge sites and oxygened functional groups of GQDs can be tailored by the solvent assisted synthesis.

B. Elucidating the Origin of Visible Photoluminescence from Graphene Quantum Dots

In order to understand the origin of visible PL emission from GQDs, we fabricated the GQDs as thin films and annealed in controlled gas flow of oxygen or hydrogen to monitor the structural changes of GQD thin films. The thermal annealing enables the conversion of edge sites and functional groups in GQDs thin films. To distinguish the particular PL emissive species from the GQDs, we deconvoltued the PL spectrum of GQDs. From these studies, we identified each of the PL bands to specific states of GQDs, for the first time. It is concluded that the blue PL emissions (~407 and ~442 nm) arise from the edge sites and the green PL bands (~490 and ~529 nm) originate from the oxygenated functional groups of GQDs. Next, in order to understand the broad Raman spectrum from the GQDs samples, we have deconvoluted the spectra and the significance of different new peaks is studied in

details. We have made a correlation between the PL signatures and the Raman modes of GQDs, for the first time. The origin of PL evolution in liquid medium suggested that the PL from GQDs strongly depends on the solvent and visible PL mainly from surface defects of GQDs. The dielectric medium of the solvent and free electrons sites in edges and oxygen functional groups of the GQDs are responsible for the changes in the PL spectrum of the GQDs. We probed the charge carries dynamics in solvent media by time resolved PL analysis. We have achieved a high PL quantum yield of 32% from the GQDs.

C. Cell Viability and Bio-Imaging Studies by Graphene Quantum Dots

The bright blue PL emissions of GQDs were used to study the bio-imaging of cancer cells using GQDs as bio-markers. The GQDs synthesised from the water, DMF and DMSO solvents show good bio-compatibility on the A-375 and HeLa cell lines. Cell viability studies reveal that the GQDs grown using DMF and DMSO solvent have very good bio-compatibility on A-375 cell as compare to that of HeLa cell lines. GQDs showed bright blue PL emission inside the cell lines. The bio-imaging of cancer cell lines by the GQDs as bio-markers and its high bio-compatibility are very promising for the future applications.

D. In-situ Decoration of Au NPs on GQD-GCN Hybrids and its Visible Light Photocatalytic Activity

An in-situ chemical method was employed to prepare the GQDs hybrids with Au nanoparticles (NPs) and graphitic carbon nitride (GCN). A striking enhancement in the intensity of Raman G band was identified in Au functionalized GQD-GCN due to the surface plasmon resonance of Au. The SPR absorption in the hybrid of Au decorated GQD-GCN was shown to very broad in the visible region and red shift in Au NP absorption peak suggests the formation of Au-C bonds in the hybrid, which was further corroborated with the XPS analysis. Further, we studied the application of hybrids asphotocatalysts for the degradation of MB under irradiation of visible light. We have achieved a significantly high ~86% degradation of MB in presence of the hybrid Au decorated GQD-GCN catalyst even at ultra-low concentration. The SPR played a significant role on the MB degradation. The interfacial charge transfer from Au NPs to GQD-GCN enhances the MB degradation, which was studied by time resolved PL analysis. Free radical scavenger tests suggested the major contribution of the hydroxyl radical in MB degradation. The conversion of superoxide radical in to hydroxyl radical was discussed.

E. Graphene Quantum Dots-TiO_2 NPs Heterojunction and Its Visible Light Photocatalysis

The GQD-TiO_2 hybrids were prepared by ultrasonication process. We proposed a mechanism for the formation of GQD-TiO_2 NPs heterojunction based on controlled experiments and density functional theory (DFT) based simulation results. We proposed that the ultrasonication induced oxygen vacancies in TiO_2 and in-plane functional groups in GQDs allowed the C-O-Ti bond formation in GQD-TiO_2 hybrid, for the first time. In the TiO_2/GQD hybrid, we noticed a blue shift of the Raman $E_g(1)$ peak of anatase TiO_2, indicating the strong interaction between the GQD and TiO_2. Further, the binding of GQDs and TiO_2 was explained by TGA results. To support the proposed mechanism of heterojucntion formation, DFT based simulation was performed to obtain the optical spectrum on the hybrid between oxygen deficient TiO_2 and oxygen functionalized GQDs. The calculated results for the hybrid structure showed strong optical absorption in the visible to near infrared region, which is in close agreement with the experimental results. The evidence for the existence of C-O-Ti bond in the hybrid of GQD-TiO_2 was probe by the FTIR, XPS and Raman results. The TiO_2-GQD heterojunction exhibits enhanced photocatalytic degradation (97%) of MB due to the facile interfacial charge separation, as revealed from the steady state and time resolved PL results. Interestingly, the photoluminescence intensity of the TiO_2-GQD heterojunction was partially quenched indicating the electron transfer from GQDs to TiO_2. The first order rate constant for TiO_2-GQD hybrid is 5.2 times higher than that of bare TiO_2. The mechanism of heterojunction formation of GQDs and TiO_2 NP hybrid system and its application in photocatalytic degradation of MB is investigated. Free radical scavenger experiment proved that the $^{\bullet}OH$ radical played a major role in MB degradation as compared to $O_2^{\bullet-}$ radical. These results provide important clue to the development of hybrid nanocatalysts based on non-metallic GQD and metal oxide semiconductor nanostructures for ensuing optoelectronic, energy and environmental applications.

7.2. Recommendations for Future Work

Present thesis is focused on the controlled synthesis and photo-physical properties of GQDs and GQD based hybrid nanostructures. The present work can be extended in several ways. Tthe recommendations for future works are listed below.

1. The present work has attempted to provide the new formation mechanism of circular shaped GQDs by the top down synthesis approach. Higher resolution imaging, in particular, the aberration-corrected TEM imaging is recommended to study the edge sites of GQDs and pores structure of GO to pin point the formation mechanism.

2. Synthesis of GQDs by the bottom up approach from the organic precursor materials through the solution chemistry may provide better control of size and optoelectronic properties of GQDs.

3. The bright PL emission of GQDs can be exploited to use it as a sensor for the detection of toxic metal ions, chemicals and biomolecules.

4. GQDs and plasmonic NPs hybrid may have new technological importance in sensing applications.

5. Because of the robust edge sites and oxygen functional groups in GQDs, it may offer to form the hybrid nanostructure with organic materials through the strong π- π interactions.

6. Recently the GCN and other 2D based materials are gaining a considerable attention and the hybrids of GQDs with the 2D materials may exhibit new properties for ensuing applications.

7. For bio-imaging applications, low energy photon excitation is desirable. For this purpose, doping of GQDs with heteroatom may give the near infrared PL emission, which could be better used for the bio-imaging.

8. Hybrid structures made of GQDs and QDs derived from the other 2D materials possess interesting properties, which is worthy of investigation.

.